# Model electrodes for the electrooxidation of simple alcohols: a DEMS study

**Dissertation**
zur
Erlangung des Doktorgrades (Dr. rer.nat)
der
Mathematisch-Naturwissenschaftlichen Fakultät
der
Rheinischen Friedrich-Wilhelms-Universität Bonn

vorgelegt von

## Abd-El-Aziz Ali Abd-El-Latif Abd-El-Salehin

aus

Kairo, Ägypten

Bonn, 2011

Angefertigt mit Genehmigung der Mathematisch-Naturwissenschaftlichen Fakultät
der
Rheinischen Friedrich-Wilhelms-Universität Bonn

**Promotionskommission**

Erster Gutachter: Prof. Dr. Helmut Baltruschat
Zweiter Gutachter: Prof. Dr. Klaus Wandelt
Fachnaher Gutachter: Prof. Dr. Siegfried Waldvogel
Fachfremder Gutachter: Prof. Dr. Karl Maier

Tag der mündlichen Prüfung:

10 . 08 .2011

Ich versichere, dass ich diese Arbeit selbständig verfasst und keine anderen als die angegebenen
Quellen und Hilfsmittel benutzt sowie die Zitate kenntlich gemacht habe.

Bonn, 08.06.2011

Abd-El-Aziz Abd-El-Salehin

For my Motherland (Egypt),
Martyrs of El-Tahrir Square,
My Parents,
My Family

# Contents

## Chapter 1: Introduction

## Chapter 2: Experimental work

## Chapter 3: Electrooxidation of methanol and the mechanism of methylformate formation

# Chapter 4: Electrooxidation of ethanol

# Chapter 5: Cu UPD at Ru quasi single crystal

# Chapter 6: New DEMS cell applicable to different electrode sizes

**Chapter 7: Summary and outlook**

# Notations

| | | | |
|---|---|---|---|
| A | Current efficiency | N | Step density |
| $A_{Geom}$ | Geometric surface area | n | Terrace width |
| $A_{real}$ | Real surface area | $Q_F$ | Faradaic charge |
| C | Concentration | $Q_H$ | Charge of $H_{ad}$ at Pt surface |
| $C_0$ | Initial concentration | $Q_i$ | Ionic charge |
| $C_{eq}$ | Concentration at equilibrium state | r | Atomic radius |
| E | Potential | t | Time |
| e | Elemental charge, $1602 \times 10^{-19}$ C | u | Electrolyte flow rate |
| $E_0$ | Initial potential | z | The number of electrons transferred |
| $E_{ads}$ | Adsorption potential | $\alpha$ | Angle between terrace plane and surface plane |
| $E_u$ | Final potential | $\Gamma_{CO}$ | CO concentration at Pt surface |
| F | Faraday constant, $96485$ C·mol$^{-1}$ | $\Gamma_H$ | Number of surface active sites |
| $I_F$ | Faradaic current | $\Delta d$ | Inter-planer spacing |
| $I_i$ | Ionic current | $\theta_{step}$ | Coverage at step |
| j | Current density | $\vartheta_{CO}$ | Relative coverage of CO |
| $K^*$ | Calibration const. of DEMS | $\nu$ | Potential scan rate |
| $k_{-1}$ | Rate constant of ester formation | $\tau$ | Time constant |
| $k_1^`$ | Rate constant of ester hydrolysis | $\Phi$ | Work function |
| $K_{eq}$ | Equilibrium constant | $\Psi$ | Binding energy |

# Abbreviations

| | | | |
|---|---|---|---|
| AES | Auger electron spectroscopy | PAFC | Phosphoric acid fuel cell |
| AFC | Alkaline fuel cell | PEMFC | Polymer electrolyte membrane fuel cell, Proton exchange membrane fuel cell |
| CE | Counter electrode | Ph | Potential hold |
| CN | Coordination number | Ps | Potential step |
| $CO_{ad}$ | CO adsorbed layer | Pt(pc) | Polycrystalline platinum |
| CV | Cyclic voltammetry | rds | Rate determining step |
| DAFC | Direct alcohol fuel cell | RE | Reference electrode |
| DAM | Dipped adcluster model | RHE | Reversible hydrogen electrode |
| DEMS | Differential electrochemical mass spectrometry | SCE | Saturated calomel electrode |
| DFT | Density functional theory | SEIRAS | Surface enhanced IR absorption spectroscopy |
| DMFC | Direct methanol fuel cell | SERS | Surface enhanced raman spectroscopy |
| EMS | In-situ electrochemical mass spectrometry | SK | Stranski-Krasanov growth mode |
| fcc | Face centered cubic | SOFC | Solid oxide fuel cell |
| FCs | Fuel cells | STM | Scanning tunnelling microscope |
| FM | Frank-van der Merwe growth mode | SXS | Surface X-ray scattering |
| FTIR | Fourier transform infrared spectroscopy | TDS | Thermal deposition spectroscopy |
| hcp | Hexagonal close packed | UHV | Ultrahigh vacuum |
| LEED | Low energy electron diffraction | UPD | Underpotential deposition |
| LH | Langmuir-Hinshelwood | VW | Volmer-Weber growth mode |
| MCFC | Molten carbonate fuel cell | WE | Working electrode |
| MSCV | Mass spectrometric cyclic voltammetry | XPS | X-ray photoelectron spectroscopy |
| ML | Monolayer | | |

# Chapter 1: Introduction

## 1.1 Fuel cells

### 1.1.1 History of fuel cell

A fuel cell is an electrochemical cell that converts chemical energy from a fuel into electric energy through a clean and efficient electrochemical reaction. Although fuel cells were discovered in 1839 by the British Sir William Grove (1811 – 1896) who is considered to be "the father of fuel cell" [1], it took 120 years until NASA demonstrated some of their potential applications in providing power during space flight.

Grove had established that, when running an electric current through water, it would split this into hydrogen and oxygen. Using this hypothesis, he developed a device which would combine hydrogen and oxygen to produce electricity. Grove had developed the world's first gas battery. It was this gas battery which has become known as the fuel cell.
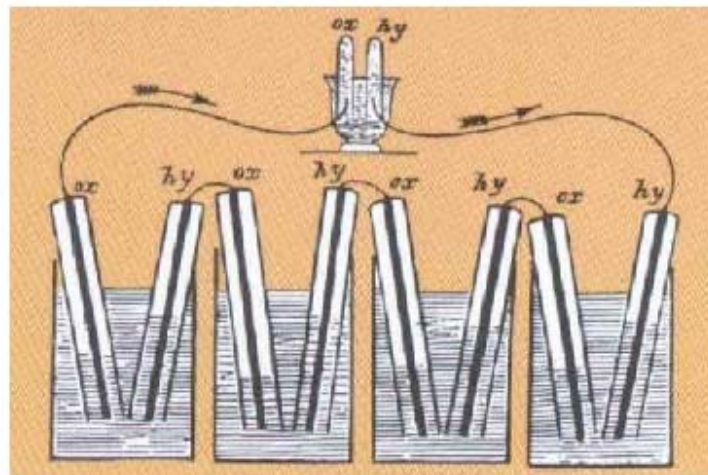


Figure 1-1: Sketch of Grove's experiment of separating oxygen and hydrogen from water.

### 1.1.2 Importance of fuel cell

Because of their potential to reduce the environmental impact and geopolitical consequences of the use of fossil fuels, fuel cells have emerged as important alternatives to combustion engines. Like a combustion engine, a fuel cell uses some sort of chemical

fuel as its energy source; but like a battery, the chemical energy is directly converted to electrical energy. In addition to high efficiency and low emissions, fuel cell systems are characterized by low noise and low environmental pollution. These benefits were responsible for attracting the interest of the scientific and engineering communities to fuel cells starting in the late 1950s and early 1960s for transportation applications.

### 1.1.3 Basics of fuel cell

Similar to a battery, fuel cells have a negative charged anode and a positive charged cathode separated by an ion-conducting material called an electrolyte and connected in an external circuit. The principle of hydrogen/oxygen fuel cell is shown in Fig. 1-2. Hydrogen passes over the anode and oxygen over the cathode, generating electricity, water and heat. Hydrogen is oxidized at the anode and protons diffuse the electrolyte and are transported to the cathode. Oxygen is reduced at the cathode to form oxide or hydroxide ions, which recombine with protons to form water, the electrons flow in the external circuit during these reactions.
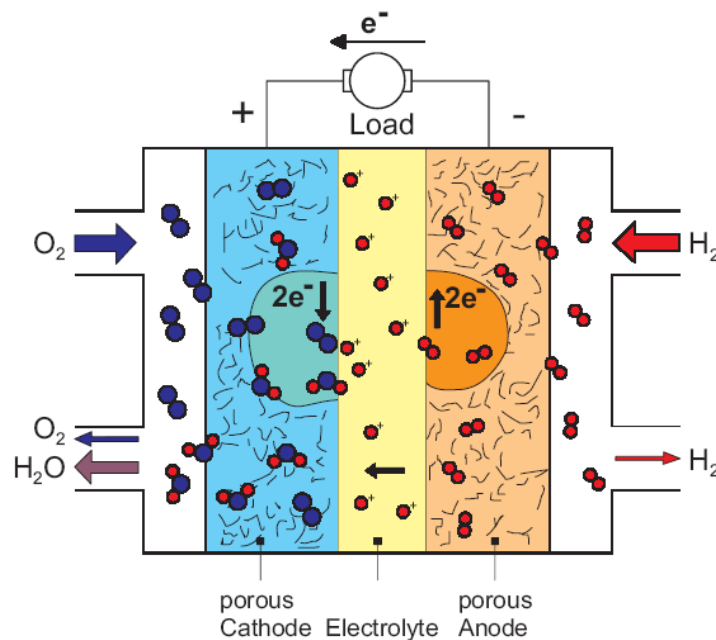


Figure 1-2: Schematic drawing of a hydrogen/oxygen fuel cell and its reactions based on the proton exchange membrane fuel cell (PEMFC). The overall chemical reaction is $H_2 + 1/2\ O_2 \rightarrow H_2O$. Reprint from ref. [2].

## 1.1.4 Types of fuel cell [3, 4]

The main characteristic that distinguishes fuel cell types is the electrolyte. The five principal types are shown in table 1-1.

Table 1-1: The main five types of fuel cell.

| Fuel Cell | Electrolyte | Operating temperature (°C) | Electrochemical reactions | Potential uses | Advantages | Disadvantages |
|---|---|---|---|---|---|---|
| Membrane (PEM) | Solid organic polymer poly-perfluorosulfonic acid | 60 - 110 | Anode: $H_2 => 2H^+ + 2e^-$<br>Cathode: $1/2\ O_2 + 2H^+ + 2e^- => H_2O$<br>Cell: $H_2 + 1/2\ O_2 => H_2O$ | electric utility portable power transportation | • Solid electrolyte reduces corrosion & management problems<br>• Low temperature<br>• Quick start-up | • Expensive removal of $CO_2$ from fuel and air streams required.<br>• Poisoning the catalyst with $CO_{ad}$. |
| Alkaline (AFC) | Aqueous solution of potassium hydroxide soaked in a matrix | 100 - 250 | Anode: $H_2 + 2(OH)^- => 2H_2O + 2e^-$<br>Cathode: $1/2\ O_2 + H_2O + 2e^- => 2(OH)^-$<br>Cell: $H_2 + 1/2\ O_2 => H_2O$ | Military space | • Cathode reaction faster in alkaline electrolyte — so high performance | • Expensive removal of $CO_2$ from fuel and air streams required |
| Phosphoric Acid (PAFC) | Liquid phosphoric acid soaked in a matrix | 150 - 250 | Anode: $H_2 => 2H^+ + 2e^-$<br>Cathode: $1/2\ O_2 + 2H^+ + 2e^- => H_2O$<br>Cell: $H_2 + 1/2\ O_2 => H_2O$ | electric utility transportation | • Up to 85 % efficiency in co-generation of electricity and heat<br>• Impure $H_2$ as fuel | • Pt catalyst<br>• Low current and power<br>• Large size/weight |
| Molten Carbonate (MCFC) | Liquid solution of lithium, sodium and/ or potassium carbonates, soaked in a matrix | 500 - 700 | Anode: $H_2 + CO_3^{2-} => H_2O + CO_2 + 2e^-$<br>Cathode: $1/2\ O_2 + CO_2 + 2e^- => CO_3^{2-}$<br>Cell: $H_2 + 1/2\ O_2 + CO_2 => H_2O + CO_2$ | electric utility | • High temperature advantages | • High temperature enhances corrosion and breakdown of cell components |
| Solid Oxide (SOFC) | Solid zirconium oxide to which a small amount of ytrria is added | 700 -1000 | Anode: $H_2 + O^{2-} => H_2O + 2e^-$<br>Cathode: $1/2\ O_2 + 2e^- => O^{2-}$<br>Cell: $H_2 + 1/2\ O_2 => H_2O$ | electric utility | • High temperature advantages*<br>• Solid electrolyte advantages | • High temperature enhances breakdown of cell components |

### 1.1.5 Fuel of PEM fuel cell

The advantage of using pure hydrogen as a fuel for PEMFC is that higher electric efficiency and performance than with alcohols are obtained. The difficulty of clean production, storage and distribution of hydrogen are the obstacles that limited hydrogen gas [5, 6]. The use of hydrogen rich molecules like alcohols (methanol, ethanol, etc.), in a direct alcohol fuel cell (DAFC), therefore appears to be advantageous for two main reasons: they are liquids (allowing easy storage) and their theoretical specific energy density is rather high, close to that of gasoline [1]. Alcohols (mainly methanol and ethanol) have often been considered as fuels [1, 7-9], but as a consequence of the acidic environment of the ionomeric conducting membrane and because of the low working temperatures of DAFCs (80–120 ºC), the kinetics of electrooxidation is rather poor. The complete electrooxidation of ethanol to $CO_2$ is more difficult to achieve than that of methanol because in ethanol the breaking of C–C bond is required. In addition, the formation of a strongly adsorbed species such as $CO_{ad}$ [10] poisons the Pt surface as in the case of methanol [11]. In order to improve the catalytic activity of Pt and in sequence the reaction kinetics, a deep understanding of the mechanisms of the electrooxidation reactions of these alcohols is a key issue.

## 1.2 Platinum as electrocatalyst in fuel cell

Many metal elements crystallize in the face-centered cubic (fcc) structure. Among them are the coinage metals copper (Cu), silver (Ag), gold (Au), as well as the catalytic important metals nickel (Ni), rhodium (Rh), palladium (Pd), iridium (Ir) and platinum (Pt). Since Platinum is the best non-alloy fuel cell electrocatalyst known, so far, this work is focused entirely on the studies of pure Pt and the effect of surface orientation on the catalytic activity towards methanol and ethanol electrooxidation and the effect of surface modification with a foreign metal at Pt.

### 1.2.1 Pt single crystals

A well-characterized and clean Pt(hkl) single crystal electrode can be prepared either by ultra high vacuum (UHV) sample preparation [12], or by annealing the single crystal in a hydrogen-air flame [13] for the study of the electrochemical surface.

### *1.2.1.1 Pt basal plane*

Three low-index planes (111), (100) and (110) of fcc systems are shown in Fig. 1-3 with hexagonal, square and rectangular arrangement of the surface atoms, respectively [14, 15]. Fcc metals, like Pt, can provide a variety of surface structures with well-ordered atomic arrangements, depending on their orientation.
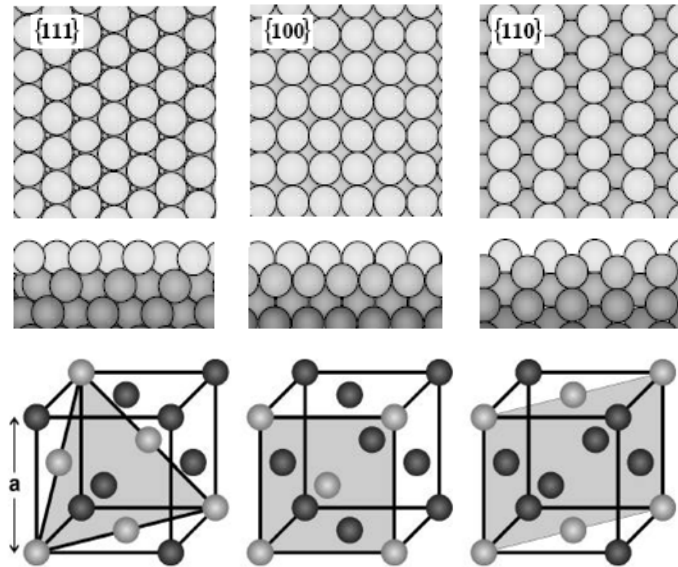


Figure 1-3: (111), (100) and (110) surfaces of fcc-crystals; bottom row displays side views. Ball models of the three low-index faces of an fcc-crystal. Reprinted from ref. [15].

The stereographic triangle (Fig. 1-4) is commonly used to illustrate the coordinates of different crystal planes [16, 17]. The atomic arrangement models of several typical planes are also shown in Fig. 1-4. Three vertexes of the triangle represent the three low-index planes or basal planes, i.e., (111), (100), and (110). Among them, the (111) and (100) planes are flat on the atomic-scale with closely packed surface atoms, whereas the (110) plane is rough with step atoms. The coordination numbers of surface atoms are 9, 8 and 7 for the (111), (100) and (110) surfaces [15].

Other planes lying in the sidelines and locating inside the triangle are high-index planes. The three sidelines of the triangle represent [01$\bar{1}$], [1$\bar{1}$0], and [001] crystallograph-

ic zones, in which the planes exhibit terrace-step structure and are thus also called stepped surfaces.

### 1.2.1.2 High index surfaces of metals

High index surfaces are those for which one or more of the Miller indices are relatively large numbers. The most commonly studied surfaces of this type are vicinal surfaces which are cut at a relatively small angle to one of the low index surfaces. The ideal surfaces can then be considered to consist of terraces which have an atomic arrangement identical with the corresponding low index surface, separated by monatomic steps (steps which are a single atom high).
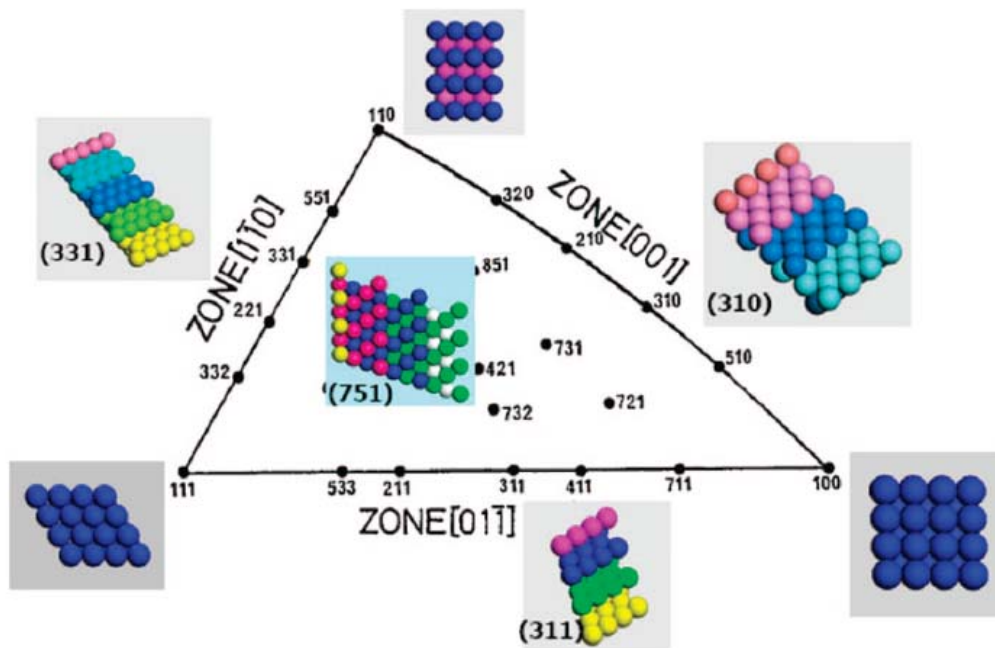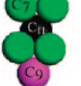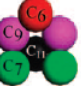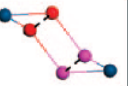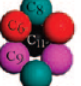


Figure 1-4: The stereographic triangle of fcc metal single-crystal and models of some Pt high index planes present between the low index planes. Reprinted from ref. [16, 17].

Table 1-2: Densities of step atoms and configuration of steric sites on Pt stepped surfaces. Reprinted from ref. [16].

| Zone | Miller index (n≥2) | Microfacet notation | Step density[†] | Steric sites[‡] | |
|------|------|------|------|------|------|
| [01$\bar{1}$] | $(n+1, n-1, n-1)$ | $n(111) \times (100)$ | $\dfrac{4}{a^2\sqrt{3(n-1)^2+4n}}$ | | |
| | $(2n-1, 1, 1)$ | $n(100) \times (111)$ | $\dfrac{4}{a^2\sqrt{4n(n-1)+3}}$ | | |
| [1$\bar{1}$0] | $(n+1, n+1, n-1)$ | $n(111) \times (110)$ | $\dfrac{4}{a^2\sqrt{3(n-1)^2+8n}}$ | | |
| | $(2n-1, 2n-1, 1)$ | $n(110) \times (111)$ | $\dfrac{4(n-1)}{a^2\sqrt{8n(n-1)+3}}$ | | |
| [001] | $(n, n-1, 0)$ | $n(110) \times (100)$ | $\dfrac{2(n-1)}{a^2\sqrt{2n(n-1)+1}}$ | | |
| | $(n, 1, 0)$ | $n(100) \times (110)$ | $\dfrac{2}{a^2\sqrt{n^2+1}}$ | | |

[†] $a$ is lattice constant. For Pt, $a$ = 0.3924 nm. [‡] CN is the coordination number.

It has been well established that the electrosorption of hydrogen and oxygen is found to be highly sensitive to the surface crystallography of an electrode surface [18-22]. For example, Furuya et al. have provided a series of voltammograms of Pt single-crystal planes including low and high index planes in both acidic (as shown in Fig. 1-5) and basic solutions and shown that the features of hydrogen desorption varied regularly with Miller indices [21, 23]. Each voltammogram acts as a fingerprint for the plane studied and may be used to ascertain the extent of long range order present. Step density and average terrace length can be calculated from the integration of the hydrogen desorption region between appropriate potential limits.
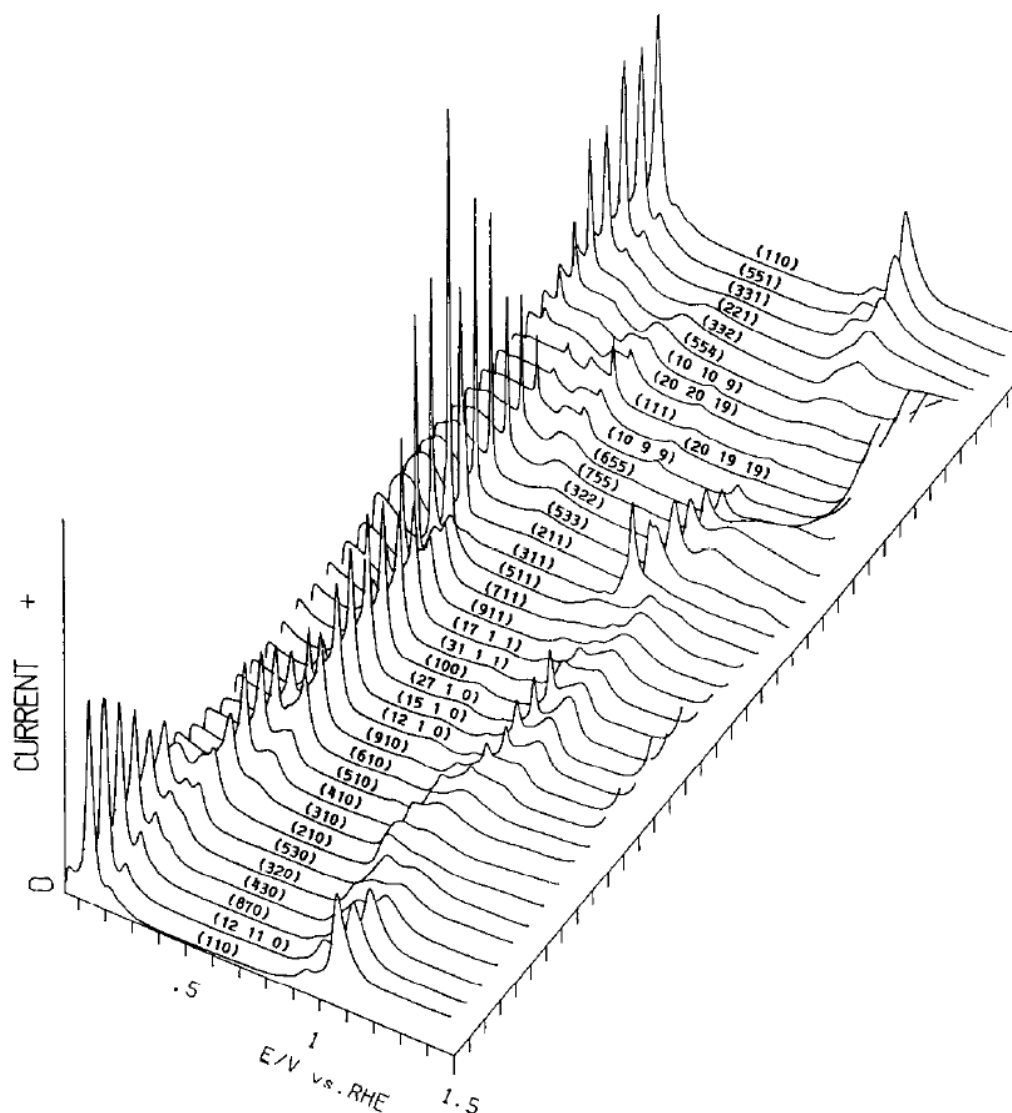
Figure 1-5: Voltammograms for the surfaces of low and higher Miller indices in 0.5 M $H_2SO_4$ at a scan rate 50 mV s$^{-1}$. Reprinted from ref. [21].

## 1.2.2 Relaxation and reconstruction of clean single crystal surfaces

Modern surface crystallographic studies on the atomic scale have shown that the clean metals tend to reduce their surface energy by two types of atomic surface rearrangements associated with the decrease of the coordination number of the surface atoms: a) perpendicular (relaxation) and b) parallel (reconstruction) to the plane.

### *1.2.2.1 Relaxation*

The phenomenon of small interlayer spacing changes (perpendicular displacement) relative to the ideal bulk lattice of metal surfaces is called "layer relaxation" [24-26]. The low coordination number of surface atoms (the deficient of the neighbour bonds number) is the main driving force for fcc metals relaxation. The surface atoms have lost 5, 4 and 3 for (110), (100) and (111) respectively compared to high coordination number (12) for atoms in the bulk. So, the relaxation is very small (1-2%) for the (100) and (111) surfaces and it is larger for the (110) surfaces, and even the distance between the second and the third layer differs notably from the bulk. For example, the first layer atoms contract towards the second layer atoms in order to increase their interaction and third layer atoms respond by expanding away from the second layer atoms, to compensate for the over-coordination in the second layer (Fig. 1-6). This oscillation in inter-planar spacing ($\Delta d$) penetrates deeper into the surface until it is eventually completely dampened [27]. In the case of relaxation, there is no change of the surface periodicity; still the surface possesses the crystal structure pertinent to the bulk.
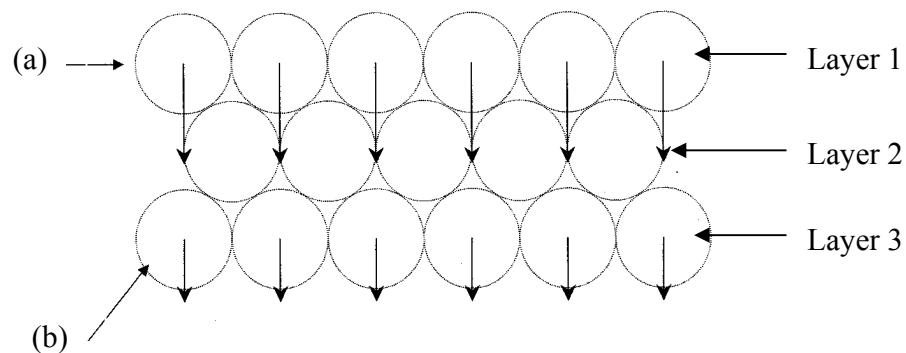


Figure 1-6: Schematic presentation of clean single crystal surfaces relaxation: (a) The first layer / second layer distance contracts and (b) The second layer / third layer distance increases.  Reprinted from ref. [27].

### *1.2.2.2 Reconstruction*

If the surface energy is sufficiently high, not only surface relaxation will occur but also dense restructuring of the surface plane, usually to enhance the coordination number of the surface atoms and, hence, to achieve a lower surface energy. Most surfaces of the 5d-

transition metals like Ir, Pt and Au reconstruct [15, 28]. The nature of the reconstruction is such that the surface plane of the reconstructed surface contains more atoms per area than an unreconstructed surface. Such "reconstruction" leads to significant changes in all surface properties.

The hexagonal fcc (111) surface of Pt (surface density of $1.53 \times 10^{15}$ atoms $cm^{-2}$), has no tendency to reconstruct [29] (cited from [30]). The fcc (100) and (110) have a high tendency to reconstruct. Pt(100)-(1x1) surface (surface density of $1.28 \times 10^{15}$ atoms $cm^{-2}$) reconstruct to Pt(100)-hex with a surface density of $1.55 \times 10^{15}$ atoms $cm^{-2}$. Pt(110) exhibits a (1x2) reconstruction at room temperature resulting in the "missing row" structure shown in Fig. 1-8.
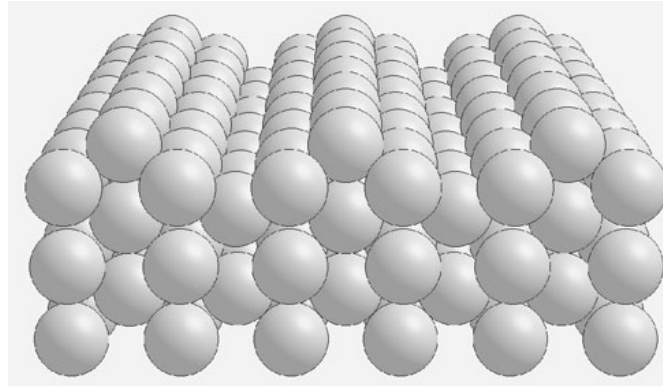


Figure 1-8: The (1×2) reconstruction on (110) surfaces of Ir, Pt and Au. Reprinted from ref. [15].

## 1.3 Fundamentals of metal deposition

Generally, there are three possible modes for the nucleation and growth of metal deposit layer on the substrate: Volmer–Weber, Frank–van der Merwe, Stranski–Krastanov growth, and as shown in Fig. 1-9. The growth mode of thin films deposited on a metal substrate depends on the strength of interaction (binding energy) between adatoms and the substrate and crystallographic misfit.

In the first case, the binding energy ($\Psi_{Me-Me}$) between 2 adatoms are stronger than those of the adatom with the substrate ($\Psi_{Me-S}$), leading to 3D adatom clusters formation according to Volmer-Weber (VW) growth mode, or islands formation independent of

crystallographic misfit [31]. Growth of this type produces rough multi-layer films on the substrate.
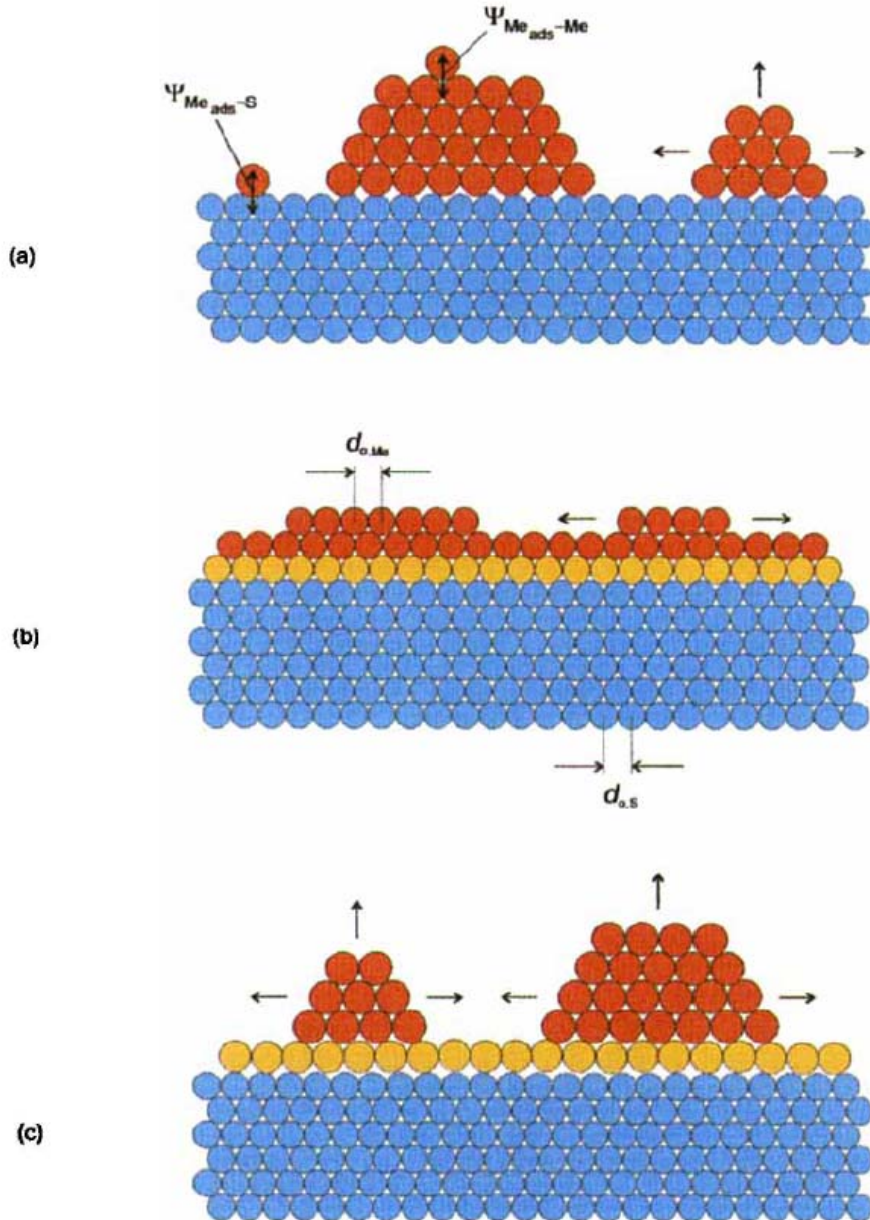


Figure 1-9: schematic representation of different growth modes in metal deposition on the foreign substrate. Cross-section views of (a) Volmer-Weber (VW: island formation), (b) Frank-van der Merwe (FM: layer by layer), and (c) Stranski-Krastanov (SK: layer plus island) model for the film growth. Reprinted from ref. [32].

In the second case, the interactions between adatom-substrate are stronger than those of the adatom–adatom. The layer-by-layer growth is 2D, indicating that complete films are formed before starting the subsequent layers to grow [31, 33]. If the system has a negligible crystallographic misfit, the adatoms attach preferentially to substrate sites resulting in atomically smooth (homo-epitaxial growth), fully formed layers [Frank-van der Merwe (FM) growth mode]. Otherwise, the Stranski-Krastanov (SK) growth mode is predominant. The SK mode is characterized by a two step process: a complete 2D monolayer contains internal strain is formed; then followed by unstrained 3D islands above the first layer [27, 31-33].

## 1.3.1 Cu underpotential deposition (Cu UPD)

The UPD of a metal is defined as the electrodeposition of a metal monolayer or more on a dissimilar metal substrate at a potential that is more positive than the Nernst potential for bulk deposition [34-36]. UPD is sensitive to surface structure; the catalytic activity of electrode surface can be increased or inhibited by UPD.

Cu UPD is currently used to determine the active surface area for Pt, Ru and Pt-Ru alloy [37-39] because the UPD peak and even bulk deposition takes place in potential range before hydrogen evolution or oxygen adsorption in addition to the atomic radii of Cu (0.128 nm) is relatively like Pt(0.138 nm) and Ru (0.134 nm).

### *1.3.1.1 Cu UPD on Pt basal planes*

The voltammetry of Cu UPD on Pt basal planes and adlayer structure depends on the base electrolyte and surface structure. The cyclic voltammetry of Cu UPD on Pt(111) electrode shows two sharp peaks for deposition and stripping in sulfuric acid over a narrow potential region [40-42]. The suggested sequence of steps for Cu UPD on Pt(111) during the cathodic going sweep starting from 0.85 V vs. RHE to 0.25 V in the presence of sulfuric acid is: first at high potential, bisulfate anions are adsorbed on Pt surface to form a honeycomb structure $(\sqrt{3} \times \sqrt{3})R30°$ [43]. As Cu atoms start to be deposited in the first UPD peak, $HSO_4^-$ is converted to $SO_4^{-2}$ [44]. After further Cu deposition, a complete monolayer (pseudomorphic (1x1)) of Cu UPD is formed and sulfate is adsorbed on $Cu_{ML}$ [30, 36].

The cyclic voltammetry of Cu UPD on Pt(100) depends on the surface structure of Pt(100) (i.e. the possible reconstruction). On a (1x1) surface, a sharp reversible peak is formed [42, 45] with a stripping charge density of 446 $\mu$C cm$^{-2}$ [45]. On reconstructed Pt(100)-hex-R0.7º structure, the deposition/stripping peaks are less reversible and the stripping peak is present at more positive potential [45, 46].

The formation of Cu UPD monolayer at Pt(110) takes places in two separate steps in sulfuric acid [47, 48]. The first one is the deposition into the grooves with (1x2) structure until half monolayer is formed, followed by the deposition on the resulting troughs to reach the complete monolayer.

### *1.3.1.2 Cu UPD on Pt stepped surfaces*

Cu UPD on stepped surfaces helps us to determine the number of surface active sites of different geometry. Usually the electrodeposition is initiated at the step sites, (the most active site at the surface) because the step site atoms have lower coordination number than terraces and it works as linear template for deposition process (the deposit is a one-dimensional line array) [49].

Scortichini and Reilley were the first who studied the behaviour of Cu UPD on stepped surfaces [50-53]. Cu UPD at Pt stepped surfaces with different orientation of steps and terraces (Pt(s)[n(111)x(110)] and Pt(s)[n(111)x(100)]) show that the deposition of Cu first starts at (110) and (100) step sites [54-56]. Then, after complete coverage of steps, the deposition is continuous at terraces.

On Pt(s)[n(100)x(111)], Cu deposition is preferentially (100) sites at terraces. Francke et al. [57] explained the stability of Cu on terraces sites relative to step sites by the higher coordination number of Cu atom by four Pt atoms at (100) terraces, while on (111) step it is only three due to the hexagonal symmetry.

### 1.3.2 Ru deposition at Pt surfaces

Ru sub-monolayer deposit on Pt has a synergistic effect for the electrooxidation of carbon monoxide (Pt poisoning) and organic molecules. Different preparation methods are available for Ru sub-monolayers deposition on Pt surfaces [58], including spontane-ous deposition [59, 60], forced deposition [61, 62], electrodeposition [63-65], vacuum

13

deposition by evaporation [66], chemical vapor deposition [67, 68] and deposition from a variety of organic and inorganic Ru precursors dissolved in non-aqueous solvents [69, 70]. In the following section, the first three methods will be discussed in details (cf. Ref. [58] and references therein).

### 1.3.2.1 Spontaneous deposition

Spontaneous deposition of Ru has been reported on Pt nanoparticles and bulk Pt surfaces [59, 71, 72]. Wieckowski and co-workers were found the spontaneous deposition of Ru from $RuCl_3$ dissolved in 0.1 $MHClO_4$ solutions yield reproducible Ru coverage. They are quantified the Ru coverage using electrochemical techniques, as well as Auger electron spectroscopy (AES) and scanning tunneling microscopy (STM) [59, 73, 74].

### 1.3.2.2 Forced deposition

Ru spontaneously decorates a Pt surface that has a layer of pre-adsorbed hydrogen by immersion of Pt electrode in $RuCl_3$ or $Ru_2(SO_4)_3$ solutions [61] or on $Ru(NO)(NO_3)_3$ solution at 50 mV [75]. The presence of hydrogen is necessary in case of the last solution because the high stability of this compound and it has poor adsorption at Pt surface.

Ru forced deposition can also be established by immersion of a Pt electrode in a solution of $RuCl_3$ that is either initially saturated with $H_2$ gas [62] or subsequently exposed to a stream of $H_2$ [76-78]. More details about forced deposition of Ru on Pt stepped single crystals to form epitaxial multi-layer (Ru quasi-single crystalline film) on these surface and their characterization by Cu UPD will present in chapter 5.

### 1.3.2.3 Electrodeposition

Commonly $RuCl_3$ bath is used for the electrodeposition of Ru on Pt surface. Baltruschat and co-workers, using potential sweep technique, found that the Ru is initially deposited at defects and step sites on vicinal Pt(111), followed by deposition at (111) terraces [79, 80]. Stimming and coworkers studied the deposited Ru surface on Pt(111) using a variety of surface study techniques, including STM, X-ray photoelectron spectroscopy (XPS), surface X-ray scattering (SXS), and Fourier transform infrared spectroscopy

(FTIR) of adsorbed CO, and they found Ru forming commensurate islands with diameter of 2 to 5 nm [81-85].

## 1.4 Differential electrochemical mass spectrometry (DEMS) setup and DEMS cells

The differential electrochemical mass spectrometry (DEMS) has become an indispensable tool for the qualitative and quantitative detection of volatile products and intermediates which are formed during the electrooxidation of organic molecules at electrode surface using potential sweep, potentiostatic and galvanostatic methods. Different types of electrode surfaces such as lacquer, sputtered, smooth and supported nanoparticles are applied on DEMS. Two important factors are necessary for DEMS: the first one is the transfer of the volatile species which are produced at an electrode surface to vacuum system. The second one is the detection of these species shortly after their formation. DEMS has some obstacles such as the overlapping between the mass signals of many products, low applied sweep rate ( $< 50$ mV s$^{-1}$), non-volatile products not detected and it is limited to liquid electrolytes [86].

### 1.4.1 DEMS history

In 1971, Bruckenstein and Gadde [87] were the first to qualitatively detect the electrochemical generated gaseous products using a hydrophobic porous electrode by in-situ electrochemical mass spectrometry (EMS) with a time constant about 20 s. In order to use EMS for quantitative studies (current efficiency and kinetic information) Wolter and Heitbaum [88, 89] improved the vacuum system of the EMS and reduced the delay time of detection. At the same time, they used differential pumping system to pump down the residual gases and large amount of solvent inside the system. In the last two decades, DEMS cells were developed and improved as reviewed in ref. [90] and references therein. Baltruschat et al. [91-93] introduced a thin layer cell to use smooth and single crystals massive electrodes, and quartz crystal microbalance [94]. The dual thin layer flow through cell was introduced by Baltruschat and co-workers [94]. In this cell the electrochemistry compartment is separated from a mass spectrometry thin layer cell compartment. The product species are transferred from the upper compartment to the lower

compartment through six capillaries by constant convection, then they diffuse through the Teflon membrane, which is supported by a steel frit, to the mass spectrometer. This flow cell could be used for a single crystal electrodes without the hanging meniscus arrangement or for a high large surface area electrode (supported nanoparticles) [95]. In 2003, Abruna et al. [96] presented a DEMS cell setup in which the single crystal electrode was pressed into a Teflon plunger in order to isolate the desired single crystal face. This assembly was then laid on top of a Teflon membrane supported by a steel frit, so that the electrode formed a thin-layer configuration against the membrane. Kita et al. [97] applied a hanging meniscus configuration for massive electrodes, using a pinhole as the gas inlet, located at the hemispherical end of a glass tube, which is covered by Teflon film. Recently, Koper et al. [98] developed on-line EMS based on a small inlet Teflon tip that applied for bead single crystal electrodes in a hanging meniscus arrangement. A disadvantage of this setup is a long delay time of $10 - 15$ s and it does not work under convection condition.

Details of the DEMS cells used in this study will be given in chapter 2.

## 1.5 Electrooxidation of simple molecules

### 1.5.1 Electrooxidation of adsorbed CO

Adsorbed carbon monoxide (CO) is a catalyst-poisoning intermediate during methanol oxidation, and it has been widely studied on platinum electrodes by spectroscopic methods [99, 100]. The catalytic oxidation of CO heterogeneously in the gas phase and electrochemically in solution are important reactions for the removal of CO from reactant stock gases in PEMFC applications, since CO poisons Pt-based anode catalysts in direct methanol fuel cell (DMFC) [30, 101]. Almost a monolayer of CO is adsorbed if traces of CO (about 10 ppm) are present in the feedstock gas hydrogen at the PEMFC anode at temperatures below 100 ºC [102].

The electrochemistry of adsorbed CO on Pt(hkl) and the effect of surface orientation, step density, foreign metal and many other parameters were studied. The mechanism of $CO_{ad}$ oxidation and the determination of the rate determining step (rds) have been a subject of many studies.

It is known that the electrooxidation of CO follows the Langmuir-Hinshelwood (LH) mechanism as suggested firstly by Gilman [103], where the adsorbed CO reacts with adsorbed oxygen species (OH from water). Now the LH mechanism for this reaction is widely accepted for polycrystalline as well as single-crystal Pt surfaces [30, 104]. The overpotential for the surface reaction is associated with activation of water to produce the surface oxidant, and the surface reaction may take place through a hydroxyl carbonyl intermediate according to the following reactions [105].

$CO + * \rightarrow CO_{ad}$

$H_2O + * \rightarrow OH_{ad} + H^+ + e^-$

$CO_{ad} + OH_{ad} \rightarrow COOH_{ad}$     (rds)

$COOH_{ad} \rightarrow CO_2 + H^+ + e^- + 2*$
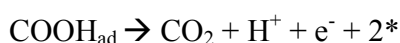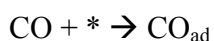
where * denotes a free surface site

The cyclic voltammetry for the electrooxidation of $CO_{ad}$ shows two stripping peaks, the main peak is present at high potential and the pre-peak "pre-ignition" is present at lower overpotential [106]. Ertl et al. reported that the heat of adsorption of CO on Pt(hkl) is dependent on the surface coverage using low energy electron diffraction (LEED) technique [107]. At high $CO_{ad}$ coverage ($\theta_{CO} > 0.65$ ML), the pre-peak is due to the electrooxidation of the weakly adsorbed CO, which has a low heat of adsorption, whereas the main peak is due to the electrooxidation of the strongly adsorbed CO, that has a high heat of the adsorption [106]. At high coverage, all of $CO_{ad}$ molecules on the surface is in the weakly adsorbed state due to the repulsive interactions between CO molecules. During the oxidation of $CO_{ad}$, the $\theta_{CO}$ decreases and the rest of $CO_{ad}$ on the surface relax and thus are strongly adsorbed at the surface [30].

The alloying of a second or even third, metal component in Pt has been the favored method of providing CO-tolerant anode catalysts, and to date the most active catalytic system for both applications is Pt/Ru alloy [86]. It is interested to study the electrooxidation of $CO_{ad}$ at Pt surface and the effect of step density and Ru coverage on the catalytic activity of CO oxidation.

The high catalytic activity of a second metal as alloy or adlayer element on platinum, toward methanol oxidation, have been attributed to lowering of the overpotential for CO electrooxidation and oxidation of CO through (a) a bifunctional mechanism (cf. Fig. 1-10

a) [63, 108]. Oxygen-containing species prefer to adsorb at Ru sites at potentials 0.2 – 0.3 V lower than at a pure platinum surface, and the adsorbed CO on platinum sites are preferentially oxidized by oxygen-containing species formed on neighboring Ru atoms [63, 109]. (b) Electronic effect or ligand effect (cf. Fig. 1-10 b). The second metal modifies the electronic nature of the surface of the base metal [110-112] e.g. Ru on Pt that reduces the CO binding energy on the Pt [113-116].

Figure 1-10: The mechanisms of Ru effect on the electrooxidation of CO at Pt surface a) Bifunctional effect and b) Ligand field effect (electronic effect).

## 1.5.2 Electrooxidation of methanol

Due to the importance of methanol as a fuel for low temperature direct methanol fuel cells (DMFC), the electrooxidation of methanol on different Pt-catalysts has been extensively studied in the last decades [7, 8, 117, 118]. The mechanism of methanol oxidation at Pt surfaces was studied using different techniques. Besides $CO_2$, the formation of formaldehyde, formic acid, methylformate and dimethoxymethane were found [119-124].

The dual path mechanism for the electrooxidation of methanol was originally suggested by Bagotzky [125] and later by Parsons [101]. Here the decomposition of methanol to form $CO_{ad}$ is identified as the indirect pathway, while the formation of soluble intermediates is referred to as the direct pathway [101]. The identification of adsorbed formate as an intermediate in the non-CO pathway [126] has been possible only recently using in situ surface-enhanced IR absorption spectroscopy (SEIRAS) technique.

$$CH_3OH \longrightarrow \text{adsorbed intermediates} \begin{cases} CO_{ad} \longrightarrow CO_2 \\ HCHO + HCOOH \end{cases}$$
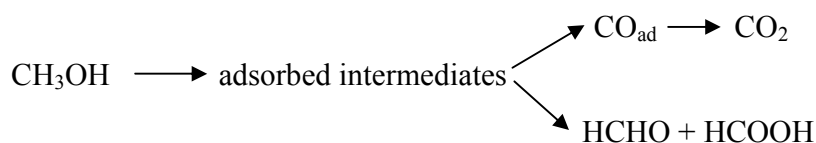
Bagotzky et al. [125] postulated that the rate-determining step (rds) during methanol electrooxidation is the rupture of the C–H bond in a methyl group to yield a $CH_2OH$ intermediate. Using the electrochemical and UHV techniques combined with an isotope substitution method, Franaszczuk et al. [127] have shown that, in the electrochemical environment, the first step is the cleavage of a C–H bond whereas the reaction rate is 3 times in $CD_3OH$ lower than that in $CH_3OH$ and the Tafel slope is equivalent to 1 $e^-$ process at low potential. In contrast, they are suggested that the first step of methanol decomposition in the UHV is the cleavage of an O–H bond to yield a methoxy intermediate whereas the reaction rate ratio is 1.6 between $CH_3OH$ and $CD_3OH$. Recently, Watanabe et al. [128] suggested that the reaction pathway starting with C–H bond cleavage has a larger activation barrier and, therefore, is kinetically less favorable using the dipped adcluster model (DAM) combined with density-functional theory (DFT) calculations.

Based on ab initio DFT calculations combined with chronoamperometry, fast scan cyclic voltammetry, Cao et al. suggested that the dual pathway is already initiated at the first methanol dehydrogenation step [129]: C–H bond cleavage leads to an adsorbed hydroxymethyl ($CH_2OH$) intermediate, which is further dehydrogenated to $CO_{ad}$, while O–H bond cleavage leads to adsorbed methoxy, $CH_3O$, which binds to Pt via the oxygen. The adsorbed methoxy intermediate is further dehydrogenated to $H_2CO_{ad}$, which can subsequently desorb as formaldehyde. The C–H cleavage, however, is not the rds. Jusys et al. [130] only found a very small kinetic isotope effect. Rather, the oxidation of adsorbed CO is assumed to be the rds.

A general problem in the detection of intermediates in methanol oxidation is their small amount. Therefore, in many of the above cited experiments, prolonged electrolysis was used. In such experiments, however, the intermediates are likely to react further, in particular since formaldehyde and formic acid are more reactive than methanol. In this respect, DEMS is very useful, as it allows the online detection of volatile products simultaneously to a cyclic voltammogram.

Iwasita and Vielstich [120] were the first to detect the formation of methylformate by DEMS. They attributed its formation to the further reaction between formic acid with the excess of methanol [119, 120, 131-133]. Formaldehyde and formic acid are not volatile enough at room temperature to be detected by DEMS. Instead, many authors assumed

that the detection of methylformate is an indirect measure of the amount of formic acid formed [132, 133]. Using DEMS with a pinhole inlet, Lai et al. [133] found that the methylformate/$CO_2$ ionic current ratio during the electrooxidation of methanol at the Pt basal planes surfaces decreases in the order Pt(111) > Pt(110) > Pt(100).

For a quantitative evaluation of product (or intermediate) formation rates, it is necessary to examine the effect of convection. Using a flow through cell coupled to a mass spectrometer, Baltruschat and co-workers thus found that the flow rate (between 1.1 and 30 $\mu$L s$^{-1}$) had no influence on the current efficiency of $CO_2$, which in all experiments was below 50% dependent on methanol concentration and potential [134, 135]. Baltruschat and co-workers concluded that no further oxidation of the intermediately formed formaldehyde and formic acid is occurring in the range of the flow rates used, because otherwise the current efficiencies for $CO_2$ should increase with decreasing flow rate because of the larger residence time. In other words, at the flow rates used, diffusion of the intermediates away from the surface is faster than further oxidation. If the oxidation only occurred via dissolved intermediates, the current efficiency of zero at high flow rates would be expected. The non-zero, but flow rate independent value can thus be taken as a proof for the above mentioned parallel pathway. On the other hand, at rough electrodes or model gas diffusion electrodes, current efficiency is lager and approaches 100 % for high Pt loadings because of the probability for intermediately formed species to react further within the catalyst layer [123]. A systematic study of the effect of catalyst thickness corroborated these results [132].

Crucial for a detailed understanding is the determination not only of the current efficiency for $CO_2$, but also those of formaldehyde and formic acid. As shown in ref. [134] the rate of $CO_2$, formic acid and formaldehyde formation can be determined from the ion current for $CO_2$, the decrease of the ion current for methanol during oxidation and the faradaic current. In a very detailed study, Behm and co-workers determined the amount of the three species from the faradaic current, the ion current for $CO_2$ and that for methylformate, assuming that formic acid is quantitatively converted to methylformate [132].

My work in chapter 3 aims at determining the role of methylformate as a product of methanol electrooxidation. Whereas old data on the equilibrium constant of methylformate were available, astonishingly I found no kinetic data [136, 137]. I investigated the

effect of methanol concentration (0.1 M and 0.2 M) and electrolyte flow rate on the current efficiency with respect to $CO_2$ and methylformate formation during the electrooxidation of methanol at smooth polycrystalline Pt. The steady state coverages of $CO_{ad}$ as a function of potential and flow rate are determined using a potential step program.

By comparing the kinetic parameters of methanol esterification and hydrolysis, a new pathway for direct methylformate formation at Pt surface/electrolyte interface is assumed. As well as the effect of step density of Pt surfaces vicinal to (111) terraces and Ru coverage on the specific catalytic activity of the electrooxidation of adsorbed monolayer of CO and bulk 0.01 M methanol were studied.

## 1.5.3 Electrooxidation of formaldehyde

Since formaldehyde is one of the main soluble intermediate products during the partial electrooxidation of methanol in fuel cells, knowing details of its electrooxidation is one important key step to understand the mechanism of methanol oxidation [122]. Formaldehyde in acidic solution is hydrated to methylene glycol ($K_{eq}$ = 2280), that is oxidized via the dual pathway according to the following equations:

$$CH_2(OH)_2 \longrightarrow CO_2 + 4H^+ + 4e^- \text{ (direct pathway)}$$

$$CH_2(OH)_2 \longrightarrow CO_{ad} + H_2O + 2e^- \text{ (indirect pathway)}$$
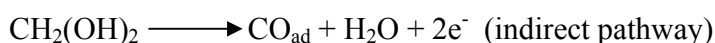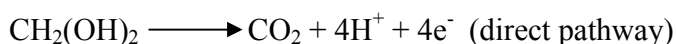
The adsorbed CO is further oxidized to $CO_2$ at high potential by a reaction with oxygen containing adsorbed species at the surface (OH or $H_2O_{ad}$).

Olivi et al. [138] observed the complete blockage of Pt(100) at E < 0.7 V for 0.1 M HCOH in 0.5 M $HClO_4$ solution due to the strongly adsorbed CO in that potential region. The oxidation peak in positive going sweep is at 0.8 V and in the negative going sweep at 0.55 V. Batista and Iwasita [139] found a small shift in the anodic and the cathodic peaks at 0.85 and 0.75 V respectively for 0.5 V HCOH at Pt(100) in perchloric acid. The catalytic activity for formaldehyde oxidation at the platinum basal planes are in the order of Pt(111) > Pt(100) > Pt(110).

## 1.5.4 Electrooxidation of ethanol

The oxidation of ethanol on metal surfaces is of special interest for the use in fuel cells. Ethanol could be the fuel of future; compared to methanol, ethanol can be directly obtained from fermentation of biomass (renewable nature), it is non-toxic, ease in storage and transportation and it has a high energy content of 8 kWh kg$^{-1}$, corresponding to 12 e$^-$ per molecule for its total oxidation to $CO_2$.

Ethanol oxidation on the other hand, at moderate temperatures is even more difficult than that of methanol; in addition to C–H bond, the C–C bond has to be cleaved. Similarly to methanol [111, 123, 134], there are two oxidation pathways for ethanol [140, 141]; one pathway via adsorbed intermediates and one via dissolved intermediates.

The final product of the route via acetaldehyde is acetic acid, which itself is unreactive, whereas in the case of methanol, the corresponding product (formic acid) is oxidized further to $CO_2$ if the residence time in proximity of the surface is high enough [123]. Therefore the route via adsorbed intermediates is even more important.

Many authors discussed the mechanism of ethanol electrooxidation at different surfaces and using different techniques. $CH_4$ formed during the electrooxidation of ethanol or the ethanol adsorbate was first observed by Vielstich and co-workers [142] and Iwasita [143]. For the adsorbed intermediates, Baltruschat and co-workers [144] reported on the formation of $CO_{ad}$ and $CH_{x,ad}$ species at polycrystalline platinum and Pt(110) using DEMS. The formation of the adsorbed $CH_x$ species was only postulated based on the finding of an adsorbate which can be desorbed either in the hydrogenation as $CH_4$ or oxidized in the oxygen region. Recently Koper et al. [145] found the same intermediates at low potential in the electrooxidation of ethanol using surface enhanced raman spectroscopy (SERS) technique.

Many authors have studied the effect of surface structure on the electrooxidation of ethanol. Feliu et al. studied the electrooxidation of ethanol on Pt basal plane surfaces [146] whereas the effect of step density of Pt(s)[n(111)x(111)] was studied by Koper et al. [147]. Tarnowski and Korzeniewski [148] studied the effect of step density of surfaces vicinal to the (111) plane on the amount of acetic acid formed by ion chromatography. They found that acetic acid formation decreases with increasing the step density and with increasing the potential, whereas the potential dependence was not explicitly discussed.

The dependence on step density was ascribed to more poison formation and shift of the pathway towards $CO_2$ formation via C–C bond splitting.

The effect of ethanol concentration on product species was studied at polycrystalline platinum [141], and it was found that at high ethanol concentration the main product is acetaldehyde and at low concentration is acetic acid. Using FTIR technique, Giz and Camara found that, the production of acetic acid takes place at potential lower than that of acetaldehyde during the electrooxidation of ethanol at Pt(111) surface [149].

The effect of bimetallic surfaces (foreign metal on Pt) on the electrooxidation of ethanol was demonstrated at many co-catalyst surfaces. The optimum surface concentration of Ru on Pt for ethanol electrooxidation is in the range of $0.3 - 0.4$ at low temperature; at high temperature it decreases to 0.15 [150-152]. Ru partially decorating the step sites of Pt stepped surfaces promotes the cleavage of the C–C bond, but at high coverage it inhibits the ethanol oxidation [153]. Whereas the main products are acetic acid and acetaldehyde during the oxidation of ethanol at PtSn electrodes prepared by thermal decomposition [154], the presence of rhodium on Pt electrode enhances the $CO_2$ route [155, 156]. Santos et al. found the mechanistic pathways for ethanol oxidation depend on the osmium coverage on Pt(100) using in situ FTIR spectroscopy. Thus, for low osmium coverage ($\theta_{Os}$ up to 0.15) the formation of CO as an intermediate was favored. For $\theta_{Os}$ up to 0.33, the more the direct ethanol oxidation to acetaldehyde and acetic acid is favored. For osmium coverage degree of 0.40, the catalytic activity of the electrode for ethanol oxidation decreases [157].

In all the papers cited above, in particular those on the effect of monoatomic steps, high concentrations of ethanol and a stagnant electrolyte were used. Whereas such conditions apply to practical conditions, this may lead to complications in the interpretation, when one is interested in the main fundamental questions: slow follow up reactions cannot be separated from the initial process, and poison formation becomes more important at high concentrations. My work in chapter 4 is consider the study of the catalytic activity of Pt stepped single crystals and polycrystalline platinum towards ethanol oxidation under controlled convection using the dual thin layer flow through cell combined with DEMS. Also the effect of Ru decorating the Pt step sites on ethanol oxidation is investigated. The

current efficiencies with respect to the volatile products formed during the electrooxidation of ethanol (acetaldehyde and carbon dioxide) are estimated.

## References:

[1]     F. Vigier, S. Rousseau, C. Coutanceau, J. M. Leger, and C. Lamy, Topics in Catalysis 40:111 (2006).

[2]     L. Carrette, K. A. Friedrich, and U. Stimming, Fuel Cells 1:5 (2001).

[3]     S. M. Haile, Acta Materialia 51:5981 (2003).

[4]     E. G. S. P. Inc., ed., Fuel Cell Handbook, U.S. Department of Energy, Office of Fossil Energy, National Energy Technology Laboratory, 2004.

[5]     R. Strbel, M. Oszcipok, M. Fasil, B. Rohland, L. Jrissen, and J. Garche, Journal of Power Sources 105:208 (2002).

[6]     J. W. Gosselink, International Journal of Hydrogen Energy 27:1125.

[7]     T. Iwasita-Vielstich, in Advances in Electrochemical Science and Engineering, Vol. 1 (H. Gerischer and C. W. Tobias, eds.), VCH, Weinheim, New York, 1990, p. 127.

[8]     A. Hamnett, Catalysis Today 38:445 (1997).

[9]     E. Peled, T. Duvdevani, A. Aharon, and A. Melman, Electrochemical and Solid State Letters 4:A38 (2001).

[10]    F. Vigier, C. Coutanceau, F. Hahn, E. M. Belgsir, and C. Lamy, Journal of Electroanalytical Chemistry 563:81 (2004).

[11]    B. Beden, S. Juanto, J. M. Leger, and C. Lamy, Journal of Electroanalytical Chemistry 238:323 (1987).

[12]    A. T. Hubbard, Chemical Reviews 88:633 (1988).

[13]    J. Clavilier, R. Faure, G. Guinet, and R. Durand, Journal of Electroanalytical Chemistry 107:205 (1980).

[14]    L. A. Kibler, Preparation and Characterization of Noble Metals Single Crystal Electrodes, University of Ulm, 2003.

[15]    H. Ibach, Physics of Surfaces and Interfaces, Springer, Berlin, 2006.

[16]    N. Tian, Z.-Y. Zhou, and S.-G. Sun, The Journal of Physical Chemistry C 112:19801 (2008).

[17]    J. F. Nicholas and H. M. Otte, Physics Today 18:67 (1965).

[18]    A. Rodes, K. El Achi, M. A. Zamakchardi, and J. Clavilier, Journal of Electroanalytical Chemistry 284:245 (1990).

[19]   J. Clavilier, K. E. Achi, and A. Rodes, Journal of Electroanalytical Chemistry 272:253 (1989).

[20]   R. Parsons and G. Ritzoulis, Journal of Electroanalytical Chemistry 318:1 (1991).

[21]   N. Furuya and S. Koide, Surface Science 220:18 (1989).

[22]   J. Solla-Gullon, F. J. Vidal-Iglesias, A. Lopez-Cudero, E. Garnier, J. M. Feliu, and A. Aldaz, Physical Chemistry Chemical Physics 10:3689 (2008).

[23]   N. Furuya and M. Shibata, Journal of Electroanalytical Chemistry 467:85 (1999).

[24]   K. Christmann, Introduction to surfaces physical chemistry Springer-Verlag New York, 1991.

[25]   G. A. Somorjai and M. A. Vanhove, Progress in Surface Science 30:201 (1989).

[26]   G. A. Somorjai, Introduction to surface chemistry and catalysis WILEY INTERSCIENCE JOHN WILEY & SONS, INC. New York, 1994.

[27]   G. Attard and C. Barnes, Surfaces Oxford university Press, 1998.

[28]   B. Lang, R. W. Joyner, and G. A. Somorjai, Surface Science 30:440 (1972).

[29]   M. A. Van Hove, Physics of covered solid surfaces., Springer, Berlin, 1999.

[30]   N. M. Markovic and P. N. Ross, Surface Science Reports 45:117 (2002).

[31]   K. Oura, V. G. Lifshits, A. A. Saranin, A. V. Zotov, and M. Katayama, Surface Science: An Introduction, Springer: Berlin, 2003.

[32]   E. Budevski, G. Staikov, and W. J. Lorenz, Electrochemical Phase Formation and Growth, VCH, Weinheim, 1996.

[33]   A. Pimpinelli and J. Villain, Physics of Crystal Growth, Cambridge: Cambridge University Press, 1998.

[34]   D. M. Kolb, M. Przasnyski, and H. Gerischer, Journal of Electroanalytical Chemistry 54:25 (1974).

[35]   D. Kolb, Advances in Electrochemistry and Electrochemical Engeneering, Wiley, New York, 1978.

[36]   E. Herrero, L. J. Buller, and H. D. Abruña, Chemical Reviews 101:1897 (2001).

[37]   S. A. S. Machado, A. A. Tanaka, and E. R. Gonzalez, Electrochimica Acta 36:1325 (1991).

[38]   T. Nagel, N. Bogolowski, and H. Baltruschat, Journal of Applied Electrochemistry 36:1297 (2006).

[39]   N. Bogolowski, T. Nagel, B. Lanova, S. Ernst, H. Baltruschat, K. Nagabhushana, and H. Boennemann, Journal of Applied Electrochemistry 37:1485 (2007).

[40]   K. Varga, P. Zelenay, and A. Wieckowski, Journal of Electroanalytical Chemistry 330:453 (1992).

[41]   H. S. Yee and H. D. Abruna, Journal of Physical Chemistry 97:6278 (1993).

[42]   N. Markovic and P. N. Ross, Langmuir 9:580 (1993).

[43]   C. A. Lucas, N. M. Markovic, and P. N. Ross, Physical Review B-Condensed Matter 56:3651 (1997).

[44]   Y. Shingaya, H. Matsumoto, H. Ogasawara, and M. Ito, Surface Science 335:23 (1995).

[45]   A. Alakl, G. Attard, R. Price, and B. Timothy, Journal of the Chemical Society-Faraday Transactions 91:3585 (1995).

[46]   D. Aberdam, Y. Gauthier, R. Durand, and R. Faure, Surface Science 306:114 (1994).

[47]   D. M. Kolb, R. Kotz, and D. L. Rath, Surface Science 101:490 (1980).

[48]   R. Michaelis and D. M. Kolb, Journal of Electroanalytical Chemistry 328:341 (1992).

[49]   F. Hernandez and H. Baltruschat, Journal of Solid State Electrochemistry 11:877 (2007).

[50]   C. L. Scortichini and C. N. Reilley, Journal of Electroanalytical Chemistry 152:255 (1983).

[51]   C. L. Scortichini and C. N. Reilley, Journal of Electroanalytical Chemistry 139:233 (1982).

[52]   C. L. Scortichini and C. N. Reilley, Journal of Electroanalytical Chemistry 139:247 (1982).

[53]   C. L. Scortichini, F. E. Woodward, and C. N. Reilley, Journal of Electroanalytical Chemistry 139:265 (1982).

[54]   L. J. Buller, E. Herrero, R. Gomez, J. M. Feliu, and H. D. Abruna, Journal of the Chemical Society, Faraday Transactions 92:3757 (1996).

[55]   C. Nishihara and H. Nozoye, Journal of Electroanalytical Chemistry 396:139 (1995).

[56]   C. Nishihara and H. Nozoye, Journal of Electroanalytical Chemistry 386:75 (1995).

[57]   R. Francke, V. Climent, H. Baltruschat, and J. M. Feliu, Journal of Electroanalytical Chemistry and Interfacial Electrochemistry 624:228 (2008).

[58]   J. S. Spendelow, P. K. Babu, and A. Wieckowski, Current Opinion in Solid State & Materials Science 9:37 (2005).

[59]   W. Chrzanowski and A. Wieckowski, Langmuir 13:5974 (1997).

[60]   A. Crown, I. R. Moraes, and A. Wieckowski, Journal of Electroanalytical Chemistry 500:333 (2001).

[61]   M. M. P. Janssen and J. Moolhuysen, Electrochimica Acta 21:869 (1976).

[62] T. Iwasita, H. Hoster, A. John-Anacker, W. F. Lin, and W. vielstich, Langmuir 16:522 (2000).

[63] M. Watanabe and S. Motoo, Journal of Electroanalytical Chemistry 60:267 (1975).

[64] E. Herrero, K. Franaszczuk, and A. Wieckowski, Journal of Electroanalytical Chemistry 361:269 (1993).

[65] K. A. Friedrich, K. P. Geyzers, A. Marmann, U. Stimming, and R. Vogel, Zeitschrift Fur Physikalische Chemie-International Journal of Research in Physical Chemistry & Chemical Physics 208:137 (1999).

[66] J. C. Davies, B. E. Hayden, D. J. Pegg, and M. E. Rendall, Surface Science 496:110 (2002).

[67] C. Lu and R. I. Masel, Journal of Physical Chemistry B 105:9793 (2001).

[68] A. Lamouri, Y. Gofer, Y. Luo, G. S. Chottiner, and D. A. Scherson, Journal of Physical Chemistry B 105:6172 (2001).

[69] D. X. Cao and S. H. Bergens, Journal of Electroanalytical Chemistry 533:91 (2002).

[70] E. R. Fachini, R. Diaz-Ayala, E. Casado-Rivera, S. File, and C. R. Cabrera, Langmuir 19:8986 (2003).

[71] K. Franaszczuk and J. Sobkowski, Journal of Electroanalytical Chemistry 327:235 (1992).

[72] P. Waszczuk, J. Solla-Gullon, H. S. Kim, Y. Y. Tong, V. Montiel, A. Aldaz, and A. Wieckowski, Journal of Catalysis 203:1 (2001).

[73] W. Chrzanowski, H. Kim, and A. Wieckowski, Catalysis Letters 50:69 (1998).

[74] E. Herrero, J. M. Feliu, and A. Wieckowski, Langmuir 15:4944 (1999).

[75] C. L. Green and A. Kucernak, Journal of Physical Chemistry B 106:11446 (2002).

[76] A. A. El-Shafei, R. Hoyer, L. A. Kibler, and D. M. Kolb, Journal of the Electrochemical Society 151:F141 (2004).

[77] S. E. Huxter and G. A. Attard, Electrochemistry Communications 8:1806 (2006).

[78] N. Bogolowski, S. Huxter, A.-E.-A. A. Abd-El-Latif, G. A. Attard, and H. Baltruschat, Journal of Electroanalytical Chemistry 646:68 (2010).

[79] H. Massong, H. S. Wang, G. Samjeske, and H. Baltruschat, Electrochimica Acta 46:701 (2000).

[80] G. Samjeské, X.-Y. Xiao, and H. Baltruschat, Langmuir 18:4659 (2002).

[81] K. A. Friedrich, K. P. Geyzers, A. J. Dickinson, and U. Stimming, Journal of Electroanalytical Chemistry 524:261 (2002).

[82] K. A. Friedrich, K. P. Geyzers, F. Henglein, A. Marmann, U. Stimming, W. Unkauf, and R. Vogel, Electrochemical Society Proceedings 96-8:119 (1996).

[83] K. A. Friedrich, K.-P. Geyzers, U. Linke, U. Stimming, and J. Stumper, Journal of Electroanalytical Chemistry 402:123 (1996).

[84] F. Maillard, M. Eikerling, O. V. Cherstiouk, S. Schreier, E. Savinova, and U. Stimming, Faraday Discussions 125:357 (2004).

[85] F. Maillard, G. Q. Lu, A. Wieckowski, and U. Stimming, Journal of Physical Chemistry B 109:16230 (2005).

[86] S. Wasmus and A. Küver, Journal of Electroanalytical Chemistry 461:14 (1999).

[87] R. R. Bruckenstein and J. Gadde, Journal of the American Chemical Society 93:793 (1971).

[88] O. Wolter and J. Heitbaum, Ber. Bunsenges. Phys. Chem. 88:2 (1984).

[89] O. Wolter and J. Heitbaum, Ber. Bunsenges. Phys. Chem. 88:6 (1984).

[90] H. Baltruschat, Journal of the American Society for Mass Spectrometry 15:1693 (2004).

[91] T. Hartung and H. Baltruschat, Langmuir 6:953 (1990).

[92] T. Hartung, U. Schmiemann, I. Kamphausen, and H. Baltruschat, Analytical Chemistry 63:44 (1991).

[93] H. Baltruschat and U. Schmiemann, Ber. Bunsenges. Phys. Chem. 97:452 (1993).

[94] Z. Jusys, H. Massong, and H. Baltruschat, Journal of the Electrochemical Society 146:1093 (1999).

[95] Z. Jusys, J. Kaiser, and R. J. Behm, Electrochimica Acta 47:3693 (2002).

[96] S. P. E. Smith, E. Casado-Rivera, and H. D. Abruna, Journal of Solid State Electrochemistry 7:582 (2003).

[97] Y. Gao, H. Tsuji, H. Hattori, and H. Kita, Journal of Electroanalytical Chemistry 372:195 (1994).

[98] A. H. Wonders, T. H. M. Housmans, V. Rosca, and M. T. M. Koper, Journal of Applied Electrochemistry 36:1215 (2006).

[99] B. Beden, C. Lamy, A. Bewick, and K. Kunimatsu, Journal of Electroanalytical Chemistry 121:343 (1981).

[100] S.-C. Chang, L.-W. H. Leung, and M. J. Weaver, Journal of Physical Chemistry 94:6013 (1990).

[101] R. Parsons and T. VanderNoot, Journal of Electroanalytical Chemistry 257:9 (1988).

[102] Q. F. Li, R. H. He, J. A. Gao, J. O. Jensen, and N. J. Bjerrum, Journal of the Electrochemical Society 150:A1599 (2003).

[103] S. Gilman, Journal of Physical Chemistry 68:70 (1964).

[104] C. McCallum and D. Pletcher, Journal of Electroanalytical Chemistry 70:277 (1976).

[105] E. Herrero, J. M. Feliu, S. Blais, Z. Radovic-Hrapovic, and G. Jerkiewicz, Langmuir 16:4779 (2000).

[106] N. M. Markovic, B. N. Grgur, C. A. Lucas, and P. N. Ross, Journal of Physical Chemistry B 103:487 (1999).

[107] G. Ertl, M. Neumann, and K. M. Streit, Surface Science 64:393 (1977).

[108] M. Watanabe and S. Motoo, Journal of Electroanalytical Chemistry 60:275 (1975).

[109] H. A. Gasteiger, N. Markovic, P. N. Ross, and E. J. Cairns, Journal of Physical Chemistry 97:12020 (1993).

[110] R. Parsons and T. VanderNoot, Journal of Electroanalytical Chemistry 257:9 (1988).

[111] H. Wang and H. Baltruschat, Journal of Physical Chemistry C 111:7038 (2007).

[112] P. Waszczuk, A. Wieckowski, P. Zelenay, S. Gottesfeld, C. Coutanceau, J. M. Leger, and C. Lamy, Journal of Electroanalytical Chemistry 511:55 (2001).

[113] B. Hammer and J. K. Norskov, Surface Science 343:211 (1995).

[114] B. Hammer, Y. Morikawa, oslash, and J. K. rskov, Physical Review Letters 76:2141 (1996).

[115] T. E. Shubina and M. T. M. Koper, Electrochimica Acta 47:3621 (2002).

[116] M. Tsuda and H. Kasai, Physical Review B 73 (2006).

[117] V. S. Bagotzky and Y. B. Vassilyev, Electrochimica Acta 12:1323 (1967).

[118] T. Iwasita, Electrochimica Acta 47:3663 (2002).

[119] K.-I. Ota, Y. Nakagawa, and M. Takahashi, Journal of Electroanalytical Chemistry 179:179 (1984).

[120] T. Iwasita and W. Vielstich, Journal of Electroanalytical Chemistry 201:403 (1986).

[121] S. Wasmus, J. T. Wang, and R. F. Savinell, Journal of the Electrochemical Society 142:3825 (1995).

[122] C. Korzeniewski and C. L. Childers, Journal of Physical Chemistry 102:L489 (1998).

[123] H. S. Wang, C. Wingender, H. Baltruschat, M. Lopez, and M. T. Reetz, Journal of Electroanalytical Chemistry 509:163 (2001).

[124] E. A. Batista, G. R. P. Malpass, A. J. Motheo, and T. Iwasita, Journal of Electroanalytical Chemistry 571:273 (2004).

[125] V. S. Bagotzky, Y. B. Vassiliev, and O. A. Khazova, Journal of Electroanalytical Chemistry 81:229 (1977).

[126] Y. X. Chen, A. Miki, S. Ye, H. Sakai, and M. Osawa, Journal of the American Chemical Society 125:3680 (2003).

[127] K. Franaszczuk, E. Herrero, P. Zelenay, A. Wieckowski, J. Wang, and R. I. Masel, Journal of Physical Chemistry 96:8509 (1992).

[128] T. Watanabe, M. Ehara, K. Kuramoto, and H. Nakatsuji, Surface Science 603:641 (2009).

[129] D. Cao, G. Q. Lu, A. Wieckowski, S. A. Wasileski, and M. Neurock, Journal of Physical Chemistry B 109:11622 (2005).

[130] Z. Jusys and R. J. Behm, Journal of Physical Chemistry B 105:10874 (2001).

[131] M. Krausa and W. Vielstich, Journal of Electroanalytical Chemistry 379:307 (1994).

[132] Z. Jusys, J. Kaiser, and R. J. Behm, Langmuir 19:6759 (2003).

[133] S. C. S. Lai, N. P. Lebedeva, T. H. M. Housmans, and M. T. M. Koper, Topics in Catalysis 46:320 (2007).

[134] H. Wang, T. Löffler, and H. Baltruschat, Journal of Applied Electrochemistry 31:759 (2001).

[135] H. Wang, Beijing Normal University, Beijing, 2001.

[136] R. F. Schultz, Journal of the American Chemical Society 61:1443 (1939).

[137] B. Indu, W. R. Ernst, and L. T. Gelbaum, Industrial & Engineering Chemistry Research 32:981 (1993).

[138] P. Olivi, L. Bulhoes, J. M. Leger, F. Hahn, B. Beden, and C. Lamy, Electrochimica Acta 41:927 (1996).

[139] E. A. Batista and T. Iwasita, Langmuir 22:7912 (2006).

[140] J. Willsau and J. Heitbaum, Journal of Electroanalytical Chemistry 194:27 (1985).

[141] G. A. Camara and T. Iwasita, Journal of Electroanalytical Chemistry 578:315 (2005).

[142] B. Bittins-Cattaneo, S. Wilhelm, E. Cattaneo, H. W. Buschmann, and W. Vielstich, Ber. Bunsenges. Phys. Chem. 92:1210 (1988).

[143] T. Iwasita and E. Pastor, Electrochimica Acta 39:531 (1994).

[144] U. Schmiemann, U. Müller, and H. Baltruschat, Electrochimica Acta 40:99 (1995).

[145] S. C. S. Lai, S. E. F. Kleyn, V. Rosca, and M. T. M. Koper, The Journal of Physical Chemistry C 112:19080 (2008).

[146] F. Colmati, G. Tremiliosi-Filho, E. R. Gonzalez, A. Berna, E. Herrero, and J. M. Feliu, Faraday Discussions 140:379 (2008).

[147] S. C. S. Lai and M. T. M. Koper, Faraday Discussions 140:399 (2008).

[148] D. J. Tarnowski and C. Korzeniewski, Journal of Physical Chemistry B 101:253 (1997).

[149] M. J. Giz and G. A. Camara, Journal of Electroanalytical Chemistry 625:117 (2009).

[150] G. A. Camara, R. B. de Lima, and T. Iwasita, Journal of Electroanalytical Chemistry 585:128 (2005).

[151] G. A. Camara, R. B. d. Lima, and T. Iwasita, Electrochemistry Communications 6:812 (2004).

[152] N. Fujiwara, K. A. Friedrich, and U. Stimming, Journal of Electroanalytical Chemistry 472:120 (1999).

[153] V. Del Colle, A. Berna, G. Tremiliosi-Filho, E. Herrero, and J. M. Feliu, Physical Chemistry Chemical Physics 10:3766 (2008).

[154] F. C. Simões, D. M. dos Anjos, F. Vigier, J. M. Léger, F. Hahn, C. Coutanceau, E. R. Gonzalez, G. Tremiliosi-Filho, A. R. de Andrade, P. Olivi, and K. B. Kokoh, Journal of Power Sources 167:1 (2007).

[155] J. P. I. de Souza, S. L. Queiroz, K. Bergamaski, E. R. Gonzalez, and F. C. Nart, Journal of Physical Chemistry B 106:9825 (2002).

[156] K. Bergamaski, E. R. Gonzalez, and F. C. Nart, Electrochimica Acta 53:4396 (2008).

[157] V. P. Santos, V. Del Colle, R. B. De Lima, and G. Tremiliosi-Filho, Langmuir 20:11064 (2004).

# Chapter 2: Experimental

This chapter provides a description of the experimental setup that was employed in the present work. The first section gives an overview of the experimental techniques (Sect. 2.1) followed by the chemicals and cleaning of the glassware, electrochemical cells and DEMS cells, in addition to the short description for the cleaning and the preparation of Pt-single crystals (working electrodes) (Sect. 2.2). The third section (Sect. 2.3) describes the differential electrochemical mass spectrometry (DEMS) setup and types of DEMS cell which were used within the framework of this work. The last section describes the calibration of DEMS and the calibration for some compounds, in particular for the soluble intermediates that are produced during the oxidation of methanol and ethanol (Sect. 2.4).

## 2.1 Experimental techniques

### 2.1.1 Cyclic voltammetry (CV)

A triangular potential sweep is applied to the working electrode (Fig. 2-1). The applied potential rises from the initial value $E_0$ to a final value $E_u$ then returns back to the initial potential at a constant potential sweep rate. The applied sweep rate can vary from a few microvolts per second to a hundred volts per second. The current measured during this process is plotted vs. the applied potential, and the result is referred to as a cyclic voltammogram (CV).
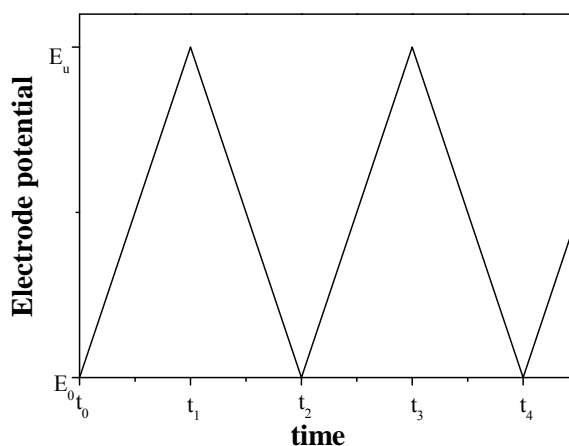


Figure 2-1: The cyclic voltammetry potential waveform.

### 2.1.2 Potential step

The potential step experiments were done according to the potential program shown in Fig. 2-2 for the adsorption and oxidation of alcohols: the potential was first held in the supporting electrolyte at 0.05 V, then the supporting electrolyte was replaced by alcohol containing solution. Afterwards, the potential was stepped to a more positive potential ($E_{ads}$), at which alcohol could adsorb, for 100 s, and then the potential was stepped back to 0.05 V. The potential was swept in the anodic direction after exchanging the alcohol containing solution with supporting electrolyte to oxidize $CO_{ad}$ (alcohol adsorbate species).
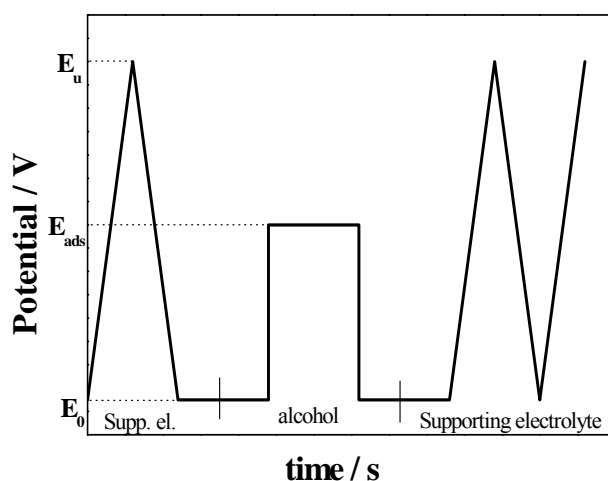


Figure 2-2: The potential program for potential step experiments and electrooxidation of adsorbed alcohol.

### 2.1.3 Deposition of Ru sub-monolayer at Pt stepped single crystals

A stock solution of 0.1 M $RuCl_3$ in 0.1 M $HClO_4$ is prepared and kept in a refrigerator, from which the actual deposition solution of 5 mM $RuCl_3$ in 0.1 M $H_2SO_4$ + 0.5 M $HClO_4$ is prepared freshly for each deposition.
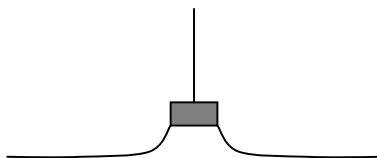


Figure 2-3: Hanging meniscus configuration of Pt single crystal in H-cell.
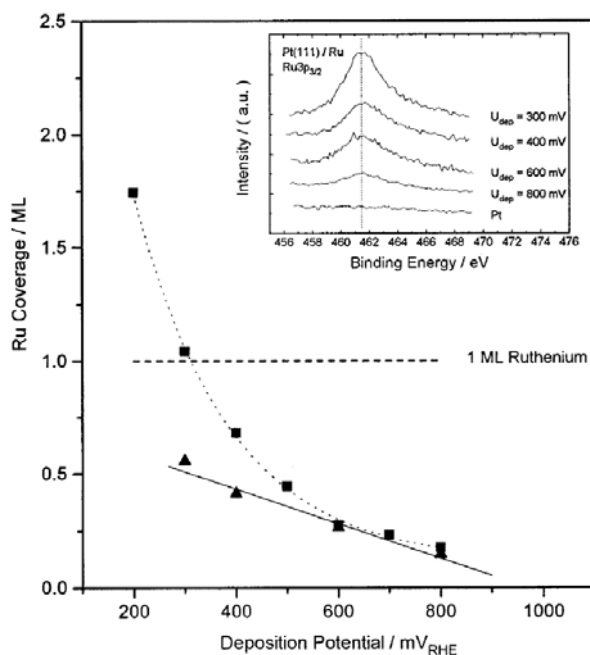
Figure 2-4: Ru coverage determined by XPS as a function of deposition potential for polycrystalline Pt (*squares*) and Pt (111) (*triangles*). The insert shows the XPS spectra (Ru $3p_{3/2}$ emission) of Ru-modified Pt(111) at various deposition potentials. The dotted line indicates the value of 461.4 eV. Reprinted from ref. [1].

After preparation and checking of the Pt stepped single crystal surface in the H-cell, the crystal is transferred to another H–cell containing the deposition solution (5 mM RuCl$_3$). Potential control is insured at a potential of 0.35 V, after this a hanging meniscus contact (Fig. 2-3) is established at 0.6 V. Since, according to the results of Stimming and co-workers [1], the amount of Ru deposited on the surface depends on the applied potential (see Fig. 2-4), the crystal stays in contact with the solution at 0.6 V for 5 minutes, resulting in coverage of about 20% of the total surface area. This corresponds to the amount of ruthenium needed to completely cover the steps of Pt(332) but not the terraces (Fig. 2-5a) and to cover the steps of Pt(331) to 50% (Fig. 2-5b). After removing the crystal from the Ru solution containing cell, it is rinsed with Milli-Q water and transferred back to an H-cell containing supporting electrolyte to check the surface coverage by comparing of the H$_{ad/des}$ charges at the step sites before and after Ru deposition. In this case, the peak for hydrogen desorption from Pt(332) step sites should completely disappear. In the present experiments, after Ru deposition on Pt(331) for 5 min at 0.4 V, the

residual Pt step sites in Pt(331) supply about 10% of the original faradaic charge, which means that 90% of step sites are covered with ruthenium.
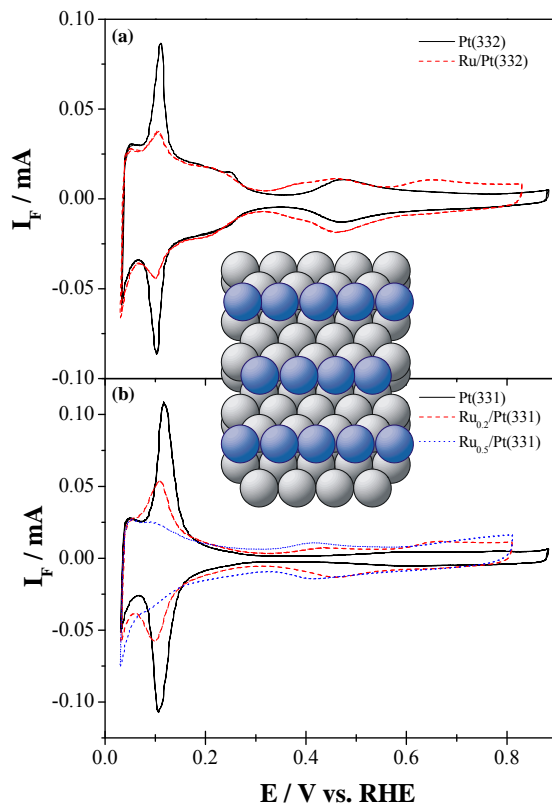


Figure 2-5: Cyclic voltammograms for (a) Pt(332) and (b) Pt(331) electrodes before and after Ru deposition at step sites in 0.1 M $H_2SO_4$ + 0.5 M $HClO_4$ solution. Scan rate: 50 mV $s^{-1}$. Inset: model for Ru deposition at the step sites of Pt(331).

### 2.1.4 Preparation of Ru quasi single crystals

These experiments were carried out in Cardiff University. Preparation of the Ru quasi single crystal film electrodes was performed according to the procedure of Huxter and Attard [2], as described here briefly. After preparation, the voltammetric profile of the single crystal surface in 0.1 M $H_2SO_4$ with a sweep rate of 50 mV $s^{-1}$ was recorded to confirm the surface order of the bead crystal and the cleanliness of the electrolyte. Then, the electrode was rinsed with Milli-Q water and ruthenium was deposited on the Pt surface by reduction of Ru ions from a droplet of $10^{-2}$ M $Ru(NO)(NO_3)_3$ attached to the single crystal surface in a hydrogen atmosphere for 5 or 10 seconds. The forced deposition

procedure was repeated 8 times. The Ru quasi single crystal surface structure was obtained after resistive heating of the Ru modified Pt single crystal to 800 - 900 K for 15 seconds in a nitrogen atmosphere by means of a homebuilt low voltage – high current power supply. Covered by a droplet of nitrogen containing Milli-Q water, the cooled Ru-film electrode was brought into contact with a 0.1 M $H_2SO_4$ electrolyte at a potential of 50 mV vs. Pd/H in an electrochemical cell. The success of the film preparation procedure was monitored by recording a voltammetric profile in the potential range from -0.1 to 0.8 V with a scan rate of 50 mV s$^{-1}$ and comparing this result with the reference profiles given in [2].
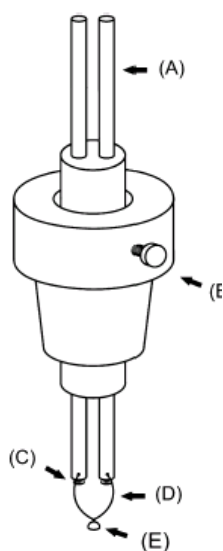


Figure 2-6: Diagram of the holder used for resistive heating of the single crystal electrode, (A) steel rods for electrical contact with the crystal, (B) Teflon screw and holder to vary height of the crystal above electrolyte, (C) steel screws to secure the Pt wires, (D) Pt wire for making contact with the crystal and to complete the electrical circuit, (E) single crystal. Reprinted from ref. [2].

### 2.1.5 Cu UPD

The single crystal protected by a droplet of hydrogen saturated water was transferred to a cell containing $10^{-3}$ M $CuSO_4$ in 0.1 M $H_2SO_4$. In case of Ru quasi single crystal, the electrode was brought into contact with the electrolyte at a potential of around 0 mV vs. Cu/Cu$^{2+}$ in a hanging meniscus configuration for approximately 15 seconds to reduce first the oxygen adsorbed species at Ru film. Cyclic voltammograms with a scan rate of 10 mV s$^{-1}$ in the potential range of 0 to 500 mV vs. Cu/Cu$^{2+}$ were recorded to characterize the surface of the Ru-film electrode. For diffusion controlled progressive deposition of copper, a $10^{-5}$ M $CuSO_4$ in 0.1 M $H_2SO_4$ was used as an electrolyte and the electrode was immersed at a potential of approximately -200 mV vs. Cu/Cu$^{2+}$ in a hanging menis-

cus configuration. Cyclic voltammograms in the potential range from -200 to 100 mV vs. $Cu/Cu^{2+}$ with a scan rate of 50 mV s$^{-1}$ were recorded to observe the suppression of the oxide/hydrogen adsorption peaks. After this, the potential window was set to 400 - 500 mV vs. $Cu/Cu^{2+}$ in order to characterize the surface of the Ru-film electrode, using a scan rate of 10 mV s$^{-1}$.

### 2.1.6 Galvanic replacement

A Sub-monolayer of Pt on Ru quasi single crystal film was created by the galvanic replacement of a less noble metal like Cu by Pt as shown in Fig. 2-7 [3].

First a Cu monolayer at Ru film was created by Cu UPD and the potential was kept positive of the bulk deposition of Cu, then the electrode was immersed into 1 mM hex-achloroplatinate solution where the replacement took place.
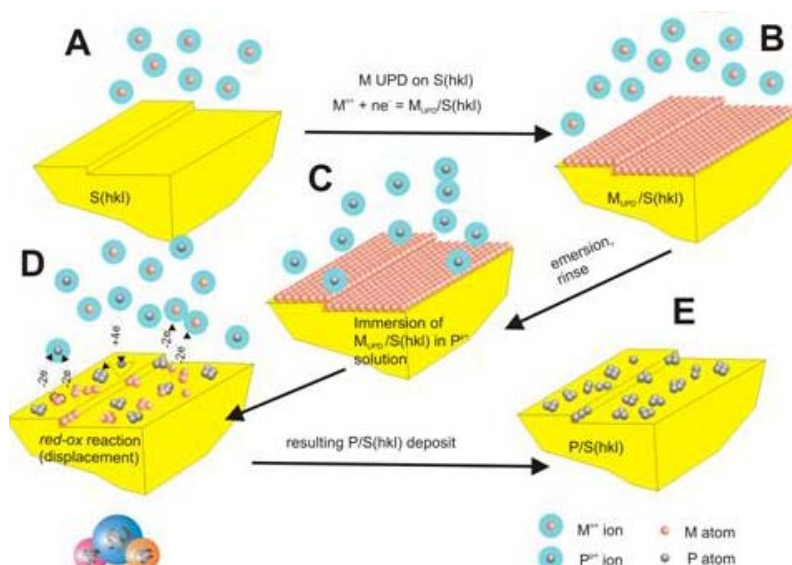


Figure 2-7: Galvanic replacement of Cu monolayer by more noble metal (Pt). A-B: Monolayer of Cu is placed on a Pt substrate by UPD, C-D: Sub-monolayer of Pt replaced Cu (ML). From http://www2.egr.uh.edu/~ecnfg/Electrochemical%20phase.htm.

## 2.2 Chemicals, cleaning and electrodes

### 2.2.1 Chemicals

Tables 2-1 – 2-3 summarize the gases, chemicals used for the electrolytes and cleaning baths preparation and the working electrodes were used in this work. All solutions

were prepared from 18.2 MΩ Milli-Q water with TOC less than 3 ppb and deaerated with high purity argon, nitrogen or hydrogen gas.

Table 2-1: List of chemicals and materials used in this work.

| Name | Formula | Company | Purity (degree) |
|---|---|---|---|
| Acetaldehyde | $CH_3COH$ | Fluka | >99.5% |
| Acetic acid | $CH_3COOH$ | KMF laborchemie | 96% |
| Ammonium solution | $NH_3OH$ | Chem solute | 25% |
| Argon | $Ar$ | Praxair | 5.0 |
| Carbon monoxide | $CO$ | Praxair | 4.7 |
| Copper sulphate | $CuSO_4$ | KMF laborchemie | 99% |
| Deuterated ethanol | $CD_5OD$ | Aldrich | 99.5% D |
| Ethanol | $CH_3CH_2OH$ | Merck | 99.9% |
| Ethylacetate | $CH_3COOCH_2CH_3$ | KMF laborchemie | 99.5% |
| Formaldehyde* | $HCOH$ | Merck | 37% |
| Formic acid | $HCOOH$ | Merck | 90% |
| Hexachloroplatinate | $H_2PtCl_6$ | Acros organics | 40% Pt |
| Hydrogen | $H_2$ | Air Liquide | 5.0 |
| Hydrogen peroxide | $H_2O_2$ | Merck | 30% |
| Methanol | $CH_3OH$ | Merck | 99.9% |
| Methylformate | $HCOOCH_3$ | Merck | 97% |
| Nitrogen | $N_2$ | – | – |
| Perchloric acid | $HClO_4$ | Fluka | 70% |
| Ruthenium chloride | $RuCl_3$ | Acros organics | 35-40% Ru |
| Ruthenium(III) nitrosylnitrate | $Ru(NO)(NO_3)_3$ | Alfa Aesar | 31.3% |
| Sulphuric acid | $H_2SO_4$ | Merck | Suprapure, 95-97% |

* Stabilized by 10% methanol.

Table 2-2: List of disc working electrodes used in this work.

| Crystal  type | Company | Diameter |
|---|---|---|
| Pt(pc) | Metal crystals | 1 cm |
| Pt(111) | MaTeck | 1 cm |
| Pt(332) = Pt(s)[6(111)x(111)] | Goodfellow | 1 cm |
| Pt(331) = Pt(s)[3(111)x(111)] | Metal crystals & oxides | 1 cm |
| Pt(100) | Kristallhandel Kelpin | 0.9 cm |
| Pt(19 1 1) = Pt(s)[10(100)x(111)] | Metal crystals & oxides | 1 cm |

Table 2-3: List of Pt bead crystal electrodes used in this work.

| Crystal type | Company (exp. in Bonn) | A / cm$^2$* | Company (exp. in Cardiff)** | A / cm$^2$ |
|---|---|---|---|---|
| Pt(pc) | Lab made | | Pt crystals were | |
| Pt(110) | icryst | | prepared and | |
| Pt(100) | icryst | 0.032 | oriented at Cardiff. | 0.089 |
| Pt(311) =Pt(s)[2(100)x(111)] | icryst | | | |
| Pt(511) =Pt(s)[3(100)x(111)] | icryst | 0.053 | | 0.0304 |
| Pt(711) =Pt(s)[4(100)x(111)] | icryst | 0.038 | | 0.0281 |
| Pt(911) =Pt(s)[5(100)x(111)] | icryst | | | 0.0384 |
| Pt(11 1 1) =Pt(s)[6(100)x(111)] | icryst | 0.032 | | |
| Pt(13 1 1) =Pt(s)[7(100)x(111)] | icryst | | | 0.0411 |
| Pt(15 1 1) =Pt(s)[8(100)x(111)] | icryst | 0.038 | | |
| Pt(19 1 1) =Pt(s)[10(100)x(111)] | icryst | 0.047 | | |
| Pt(111) | icryst | 0.053 | | 0.028 |

* In order to determine the geometrical surface area (A) of the bead crystals using GIMP 2.6 software, the crystal next to a sheet of 2D-scale paper were fixed at the scanner, then both areas were magnified and scanned both area. The surface area of the crystal was calculated relative to the area of 2D-scale paper.

** The Pt metals were supplied by Goodfellow metals Ltd. (>99.995%).

### 2.2.2 Cleaning of laboratory glassware

To remove the attached oil (degreasing), the glassware and DEMS cells were kept for one day in concentrated potassium hydroxide (5 M KOH) bath. To clean the experimental tools from the attached metal ions (cations), they were immersed in chromic acid (640 ml of concentrated $H_2SO_4$ + 360 ml $H_2O$ + 21.4 g $CrO_3$) bath overnight. Due to the carcinogenic and toxic properties of hexavalent chromium compounds, another strong oxidizing reagent was used like green acid ($KMnO_4$ + $H_2SO_4$) or the cleaning of laboratory glassware in a water steam system for at least four hours is an alternative choice.

### 2.2.3 Electrolytes

Sulphuric acid (at a concentration of 0.1 and 0.5 M) was used as a supporting electrolyte, because the hydrogen adsorption peaks are sharper and more characteristic in the presence of sulfate than on perchloric acid; this helps in the control of cleanliness and surface structure. During ethanol electrooxidation, 0.1 M $H_2SO_4$ + 0.5 M $HClO_4$ was used as supporting electrolyte. The reasoning behind this choice is the need for a high conductivity in the thin layer flow through cell and avoiding a high concentration of sulfate, which reduces the reactivity of the Pt surface due to its strong specific adsorption.

### 2.2.4 Adsorption test

The cleanliness of the supporting electrolyte, glassware and DEMS cell was checked by adsorption test. In this test the applied potential on polycrystalline Platinum electrode was cycled between 0.05 and 1.5 V at a sweep rate of 50 mV s$^{-1}$.

When the cyclic voltammogram reaches a stable shape, the cleanliness of the surface is checked by holding the potential in the beginning of double layer region at 0.34 V in anodic direction (where there is no hydrogen or oxygen adsorption or desorption taking place) for 3 minutes, then the potential sweep was started again.

If the CVs before and after the potential hold are the same (Fig. 2-8), this means the system is clean. If this not the case, the DEMS cell and the glassware have to be cleaned again and a fresh electrolyte has to be prepared. This procedure applies for pure sulfuric acid as base electrolyte. In some experiments, a solution of 0.1 M $H_2SO_4$ and 0.5 M

HClO$_4$ was used. In these cases, the CVs before and after the stop at 0.34 V were not completely identical, which might be due to some impurities in HClO$_4$ like Cl$^-$ ions.
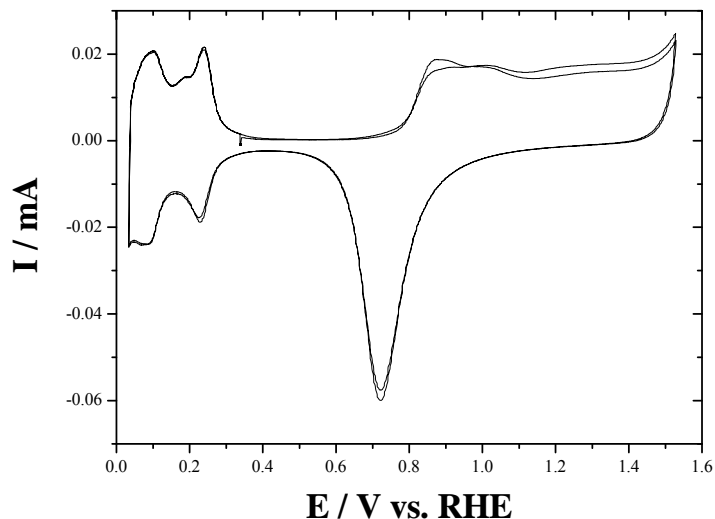


Figure 2-8: Typical cyclic voltammogram recorded during the adsorption test on Pt(pc) in 0.1 M H$_2$SO$_4$ + 0.5 M HClO$_4$ at 50 mV s$^{-1}$.

### 2.2.5 Cleaning and preparation of single crystals

Since the stepped Pt single crystal electrodes might contain impurities, they must be cleaned before any measurement carried out.

#### *2.2.5.1 Electrochemical cleaning*

The Pt surface has to be cleaned first by sweeping the potential between 0.05 V and 1.5 V at 50 mV s$^{-1}$ several times in H-cell containing the supporting electrolyte (Fig. 2-9). Once the CV does not change anymore, the steps of Pt single crystals preparation (annealing, cooling and characteristic CV) were done. If the characteristic CV does not correspond to the CVs known from literature, the surface should be cleaned chemically.
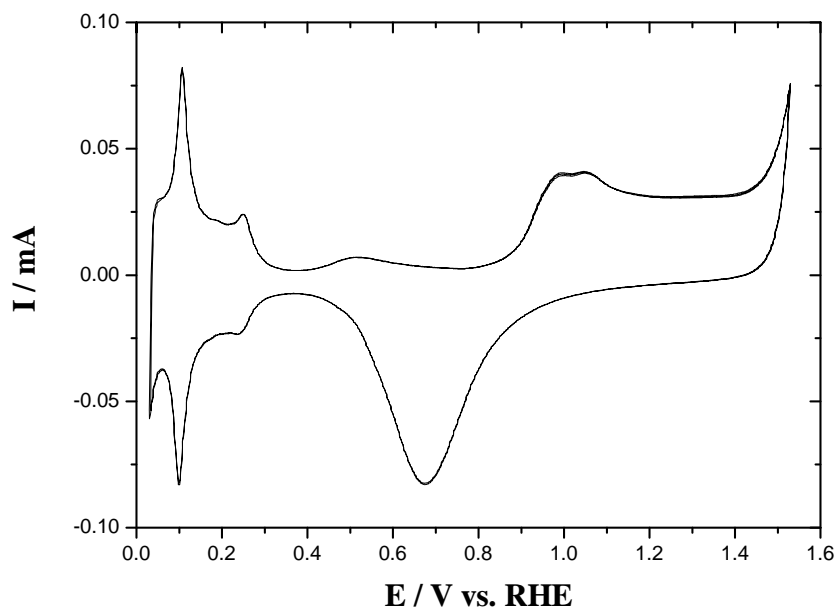
Figure 2-9: Cyclic voltammogram for Pt(332) roughening in 0.1 M $H_2SO_4$ + 0.5 M $HClO_4$.

### 2.2.5.2 Chemical treatment

The single crystal electrode was immersed first in conc. $HNO_3$ then in conc. $NH_3/H_2O_2$ (1:1) solution for 5 min followed by electrochemical cleaning and annealing. This procedure is repeated many times until the characteristic CV obtained for the annealed single crystal surface.

### 2.2.5.3 Preparation of Pt single crystals

Stepped Pt single crystal electrodes were prepared according to Clavilier's method [4]: annealing was achieved by heating the Pt single crystal over a butane flame ($\approx$ 1750 $^o$C, melting point of Pt is 1768 $^o$C); after it turned to a cherry red color it was left over the flame for about 30 s and then transferred it into a glass cell, where it was allowed to cool down to room temperature for 4 min in a $H_2/Ar$ mixture atmosphere [5].

The crystal was kept in contact with the supporting electrolyte deaerated with highly pure argon (99.999%) in a hanging meniscus configuration (Fig. 2-3), and the quality of the single crystal surface after preparation was checked by cyclic voltammetry in the potential range of 0.05 to 0.85 V. The potential may not exceed 0.9 V, because at higher

potentials adsorbed oxygen destroys the arrangement of the Pt atoms at the surface. The crystal was then (or after deposition of Ru) transferred quickly to the DEMS cell while being protected by a droplet of electrolyte.
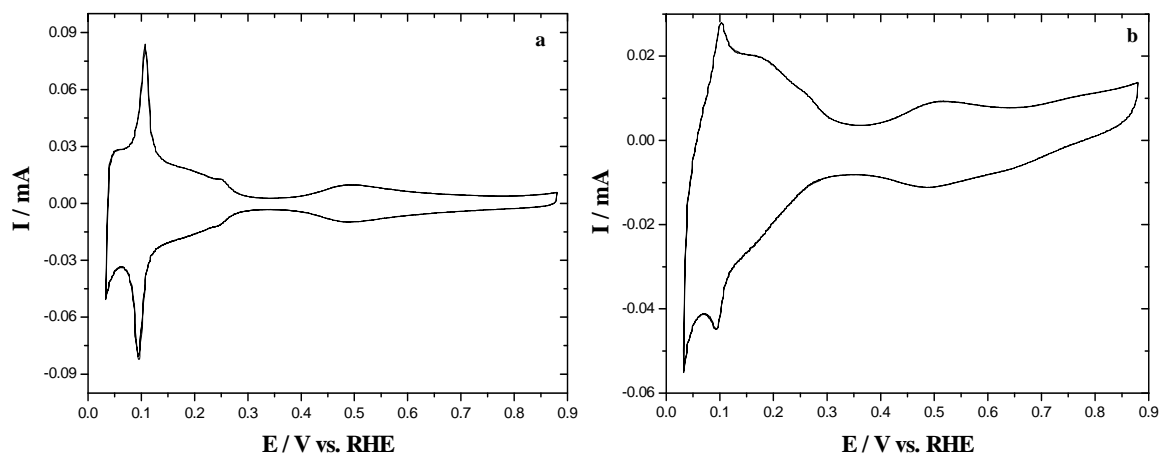


Figure 2-10: Typical characteristic CV for Pt(332) in 0.1 M $H_2SO_4$ + 0.5 M $HClO_4$ at 50 mV s$^{-1}$ a) in H-cell and b) in DEMS cell.

The difference in shape of the CVs shown above (Fig. 2-10) is partially caused by the flow in the dual flow through cell, and the transport of the evolved hydrogen away from the electrode, but also by unavoidable impurities from the DEMS cell material as well as the Teflon ring spacer (Böhme-Kunststofftechnik GmbH & Co. KG Schwarzenbek Germany).

### 2.2.6 The a conventional electrochemical glass cell "H-cell"

For the preparation of the stepped Pt single crystals electrodes in Ar/$H_2$ atmosphere by cyclic voltammetry, a conventional electrochemical glass cell "H-cell" was used. The typical glass cell "H-cell" consists of three glass compartments as shown in Fig. 2-11, the working electrode kept in hanging meniscus configuration in contact with the supporting electrolyte in the central one. In this part of the cell, there are additional inlets for Ar/$H_2$ mixture, and the electrolyte. The second compartment contains a sheet of Pt as counter electrode immersed in supporting electrolyte, which is separated from the first by a glass

frit. The third glass compartment, which is separated from the central compartment by a stop cock, contains the reference electrode immersed in supporting electrolyte.
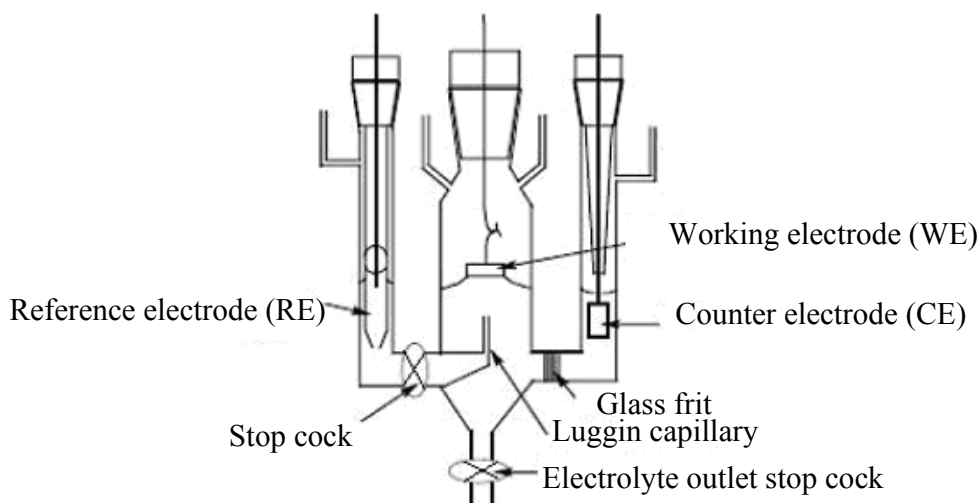


Figure 2-11: Cross section of an H-cell for the electrochemical experiments. Reprinted from ref. [6].

### 2.2.7 Preparation of the reference electrodes

#### *2.2.7.1 Reversible hydrogen electrode (RHE)*

The reference electrode that was used mostly in this work is a reversible hydrogen electrode (RHE) [7] as shown in Fig. 2-12.

To prepare a RHE, the electrode first was rinsed with Milli-Q water and then filled with supporting electrolyte according to the procedure indicated in Fig. 2-12. An extra platinum wire is dipped into the sulfuric acid and a voltage of 1.6 V was applied between the platinum wire (anode) and the reference electrode (cathode). Hydrogen evolution is observed at the cathode. When the hydrogen bubble covers about half of the Pt wire, the applied voltage is disconnected.
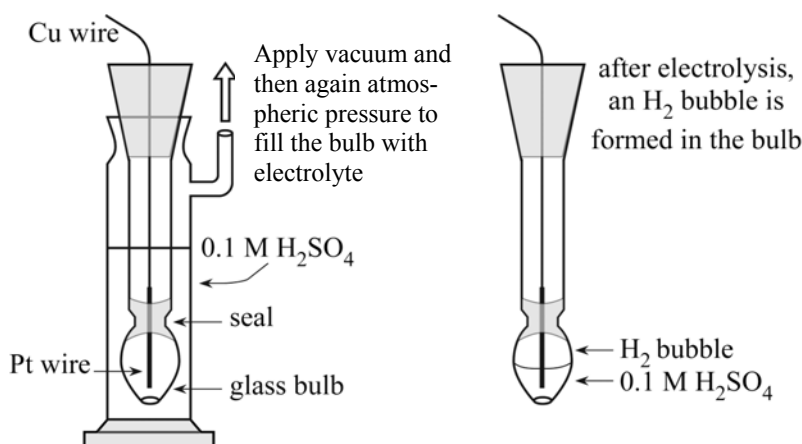
Figure 2-12: Construction of the reversible hydrogen electrode. Reprinted from ref. [8].

### 2.2.7.2 Pd/H electrode[*]

A palladium-hydrogen (Pd/H) reference electrode was used during the CVs of Ru quasi single crystal in supporting electrolyte (described in chapter 5). It consisted of a palladium wire (Goodfellows Ltd, Cambridge) spot-welded to a platinum wire and sealed in a glass holder. The palladium wire was heated in a Bunsen flame after the initial cleaning of the electrode in the green acid in order to oxidize and remove the surface contaminants. Then the charging procedure of the Pd wire was done by passage of hydrogen over the wire through the gas inlet of the reference compartment of the electrochemical cell for a period of 30 - 40 minutes. This allowed for the formation of a stable β-hydride phase, which exhibits a constant potential of 50 mV vs. RHE for several hours.

[*]Work in Cardiff University

### 2.2.7.3 Cu/CuSO$_4$ electrode

The Cu wire was cleaned first in the concentrated nitric acid and rinsed with Milli-Q water prior to usage. The cleaned Cu wire immersed in 1 mM CuSO$_4$ was used as reference electrode during the Cu-UPD.

## 2.3 DEMS setup and DEMS cells

For kinetic and mechanistic studies of methanol and ethanol electrooxidation at Pt surfaces with different orientation and at Ru modified Pt stepped surfaces under convec-

tion conditions, the on-line mass spectrometric detection of the volatile products and intermediates was used.

### 2.3.1 DEMS setup

The differential electrochemical mass spectrometry (DEMS) is a technique which allows qualitative and quantitative detection of electrochemical reaction products shortly after their formation. The DEMS setup involves the direct connection between an electrochemical cell and the quadrupole mass spectrometer (MS) (Balzer QMG-422). The volatile species that are produced during the electrochemical reaction will diffuse through a hydrophobic porous Teflon membrane (interface between electrochemical cell and MS) to the MS where they are detected.
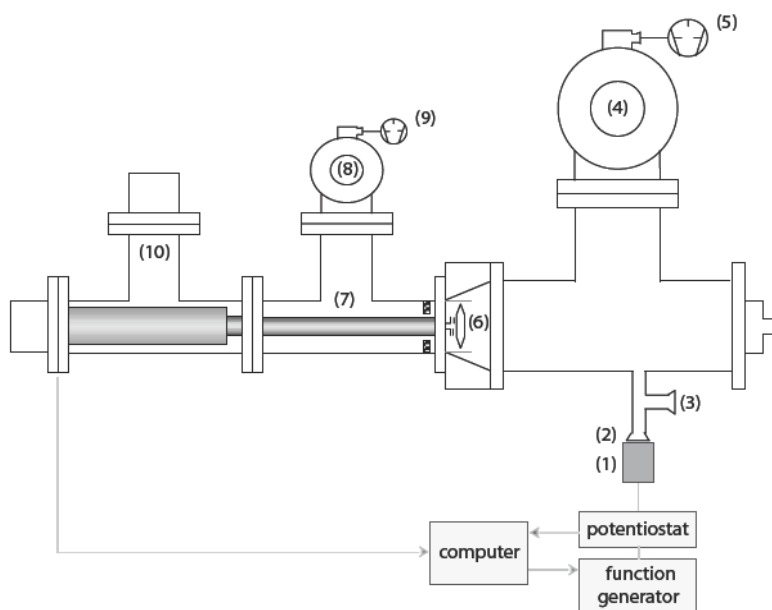


Figure 2-13: Schematic representation of a typical experimental DEMS setup; (1) electrochemical cell, (2) MS connection to the electrochemical cell, (3) connection to the calibration leak, (4) turbomolecular pump, (5) rotary pump, (6) ion source, (7) quadrupole rods, (8) turbomolecular pump, (9) rotary pump, (10) secondary electron multiplier [9].

## 2.3.2 The DEMS cells

### 2.3.2.1 Dual thin layer flow through cell
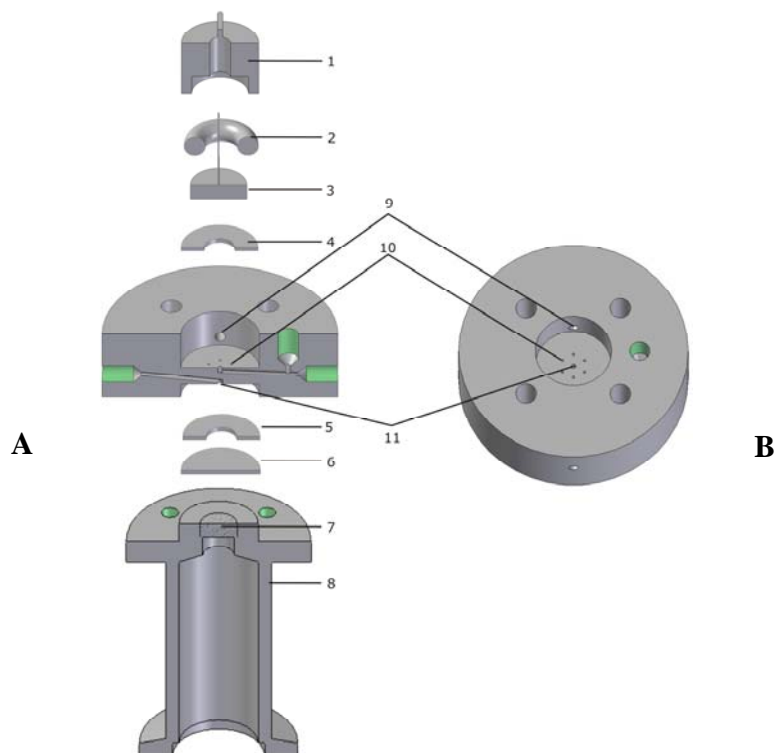


Figure 2-14: Sketch for the dual thin-layer flow through cell (Kel F) (1) Kel-F support; (2) Kalrez; (3) disc working electrode; (4), (5) Teflon gasket; (6) porous Teflon membrane; (7) stainless steel frit; (8) stainless steel connection to MS; (9) capillaries for flushing with Ar; (10) inlet-outlet capillaries; (11) connecting capillaries. (A) Side view of Kel-F body of the cell; (B) Top view of the cell.

A dual thin-layer flow cell, made of Kel-F, is connected to the mass spectrometer via a valve. The construction of this cell was described in detail in ref. [9]. There are two compartments: the upper one for electrochemical reactions and the lower one for mass spectrometric detection. The electrolyte flows from the upper compartment to the lower one through six capillaries. In the upper compartment, the working electrode was placed on a Teflon gasket (Böhme-Kunststofftechnik GmbH & Co. KG Schwarzenbek Germany) with a ≈ 130 μm thickness and an inner diameter of 6 mm. This leaves an electrolyte volume of ≈ 3.5 μL. In the lower compartment, a porous Teflon membrane (W. L.Gore &

Associates GmbH Putzbrunn Germany) - mean thickness of 50 μm, a mean pore size of 0.02 μm, and a porosity of 50%- was supported on a stainless steel frit and served as the interface between the electrolyte and vacuum. It was pressed against a Teflon gasket to create the lower thin layer with the same volume (3.5 μL).

Because the electrolyte volume of the DEMS cell is small (≈ 3.5 μL), the product concentration and thus the sensitivity for their detection is high. By ensuring a constant flow of electrolyte, products are transported from the working electrode surface to the mass spectrometer by convection, where the electrode and the mass spectrometer entrance are connected by six capillaries of a diameter of about 0.5 mm.

The electrolyte flows from the flask attached above the DEMS cell. The flow is adjusted by a peristaltic pump at the outlet. A reversible hydrogen electrode is used as the reference electrode connected to the electrolyte inlet. Two Pt wires at the inlet and outlet of the thin layer cell are used as counter electrodes connected through external resistances (100 kΩ and 1100 Ω at electrolyte inlet and outlet, respectively) to reduce the IR drop and create good current distribution.

### 2.3.2.2 New DEMS cell for bead crystal

In order to use small electrodes (bead crystals) as working electrodes under hanging meniscus configuration and under convection conditions, a new DEMS cell was designed. The general setup is shown in Fig. 2-15 with the following characterizations:

- Diameter of glass capillary 0.5 mm.
- Distance between the glass capillary and bead crystal in the range of a few micrometers.
- Two pumps for electrolyte flow: automatic vertical syringe pump for inlet and peristaltic pump for outlet.
- 3D crystal holder to adjust the position of bead crystal exactly on the center of glass capillary.
- Glass cell containing 6 opening (counter and reference electrodes, argon, electrolyte inlet, argon outlet and electrolyte exchange).
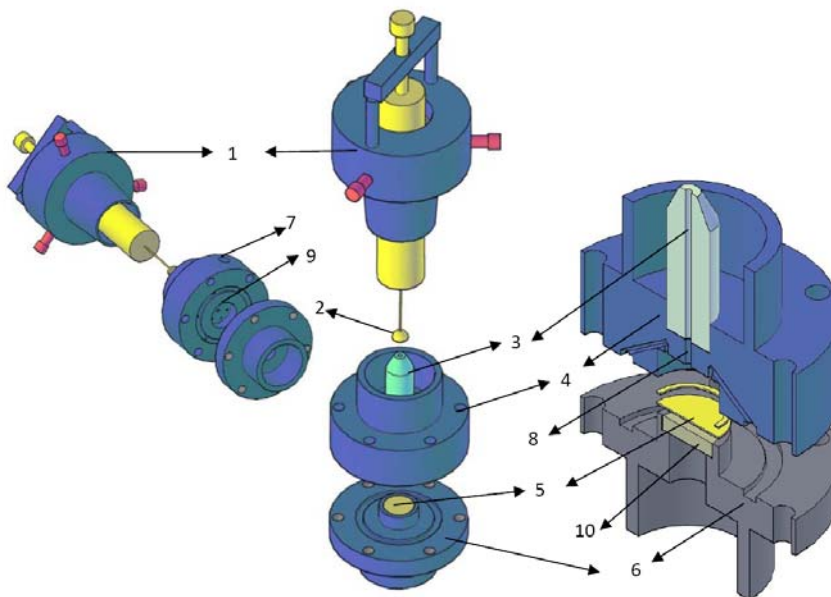
Figure 2-15: Sketch for bead crystal flow through cell (Kel F) (1) Kel-F 3D crystal holder; (2) bead crystal; (3) glass capillary; (4) Kel-F support; (5) hydrophobic porous Teflon membrane; (6) stainless steel connection to MS; (7) electrolyte outlet; (8) inlet capillary; (9) 6-outlet capillaries; (10) stainless steel frit.

## 2.4 Calibration of DEMS

### 2.4.1 DEMS calibration by electrooxidation of pre-adsorbed CO

Calibration of the DEMS setup was achieved at constant flow rate as follows: after cleaning the polycrystalline platinum electrode by sweeping the potential between 0.05 and 1.5 V in the supporting electrolyte at a scan rate 50 mV s$^{-1}$, the potential was held at a potential between 40-70 mV and the supporting electrolyte was replaced by a CO saturated solution ($\approx 10^{-3}$ mol L$^{-1}$) to form a monolayer of adsorbed CO on the Pt surface. After replacing it again with supporting electrolyte the potential was swept in anodic direction at a scan rate of 10 mV s$^{-1}$. The adsorbed CO was oxidized to $CO_2$, which was detected by MS, and the calibration constant ($K^*$) was calculated from the following relation:

$$K^* = z \frac{Q_{MS}}{Q_F} \tag{1}$$

Here $Q_{MS}$ and $Q_F$ are the mass spectrometric and the faradaic charges, respectively, and z is the number of electrons per one adsorbed CO molecule yielding $CO_2$.
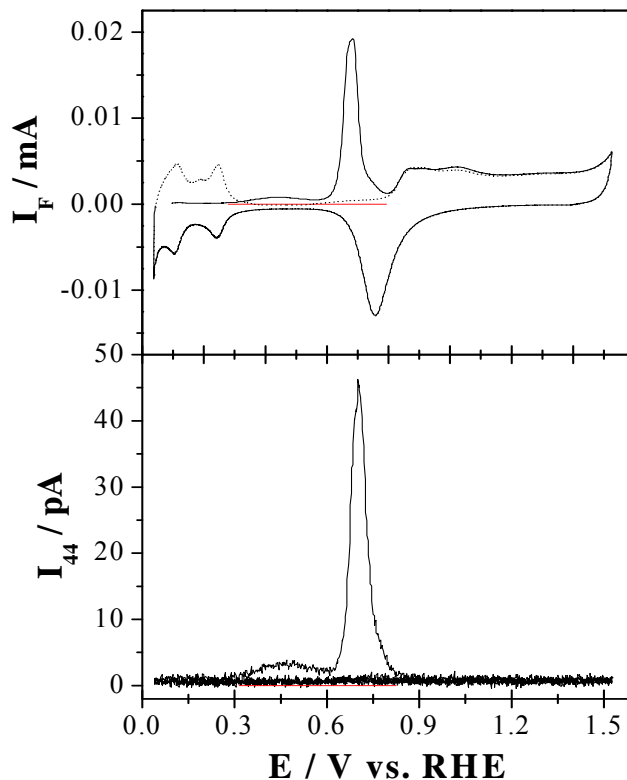


Figure 2-16: Simultaneously recorded faradic (a) and corresponding ion current (b) of $CO_2$ (m/z = 44) during the electrooxidation of pre-adsorbed CO at Pt(pc) in 0.5 M $H_2SO_4$ at scan rate 10 mV s$^{-1}$ and flow rate 5 µL s$^{-1}$. (solid line): 1$^{st}$ CV during $CO_{ad}$ electrooxidation, (dotted line): 2$^{nd}$ CV after $CO_{ad}$ electrooxidation.

In the first anodic sweep, no hydrogen desorption current can be seen because the surface is completely covered with $CO_{ad}$ as shown in Fig. 2-16. At a potential of about 0.4 V, $CO_{ad}$ starts to be oxidized to $CO_2$ with a current efficiency of 80% (after background subtraction), the remaining 20% being assigned to adsorption of anions like sulphate, bisulphate, hydroxide, …etc at the Pt surface.

### 2.4.2 Calibration curve for acetaldehyde (m/z = 29) and methylformate (m/z = 60)

Approximate calibration for acetaldehyde and methylformate was achieved using different concentrations of acetaldehyde (0.1 mM − 5 mM) and methylformate (1 mM − 0.1

M) solutions and monitoring the ionic signal of masses 15, 29 and 44 ($CH_3CHO$) and mass 60 ($HCOOCH_3$) for each concentration at different flow rates. A plot of the ion currents of x species vs. the concentration leads to a straight line with slope equal the calibration constant of these species ($°K_x$), which includes all the DEMS parameters.

$$I_x = °K_x \cdot C_x \qquad\qquad (2)$$

Where x = 29 (acetaldehyde) or 60 (methylformate)

The slope of a double logarithmic plot of $°K_x$ versus the electrolyte flow rate (u) showed that $°K_x \propto u^{0.3}$ suggesting partial diffusion limitation to the Teflon membrane [9].

Using this procedure, convert current efficiencies will be obtained only if a complete mixing of the electrolyte occurs before entering the detection compartment, i.e. if the product is homogenously distributed. This will only be the case for low flow rates (below $1\ \mu L\ s^{-1}$); at high flow rates the concentration of the product in the vicinity of the Teflon membrane will be higher, and therefore the ion currents will be too high.

## References:

[1]     S. Cramm, K. A. Friedrich, K. P. Geyzers, U. Stimming, and R. Vogel, Fresenius Journal of Analytical Chemistry 358:189 (1997).

[2]     S. E. Huxter and G. A. Attard, Electrochemistry Communications 8:1806 (2006).

[3]     S. R. Brankovic, J. X. Wang, and R. R. Adzic, Surface Science 474:L173 (2001).

[4]     J. Clavilier, D. Armand, S. G. Sun, and M. Petit, Journal of Electroanalytical Chemistry 205:267 (1986).

[5]     J. Clavilier, K. Elachi, M. Petit, A. Rodes, and M. A. Zamakhchari, Journal of Electroanalytical Chemistry 295:333 (1990).

[6]     T. Nagel, in Institute für Physikalische und Theoretische Chemie, Abteilung Elektrochemie, Vol. Ph.D., Rheinische Friedrich-Wilhelms Universität Bonn, Germany, 2007.

[7]     F. G. Will, Journal of the Electrochemical Society 133:454 (1986).

[8]     F. Hernandez, in Mathematisch-Naturwissenschaftliche Fakultät, Rheinische-Friedrich-Wilhelms-Universität Bonn, Bonn, 2006.

[9]     H. Baltruschat, Journal of the American Society for Mass Spectrometry 15:1693 (2004).

# Chapter 3: Electrooxidation of methanol and the mechanism of methylformate formation

## 3.1 Introduction

This chapter aims at determining the role of methylformate as a product of methanol electrooxidation. Whereas old data on the equilibrium constant of methylformate were available, astonishingly kinetic data is not found [1, 2]. I investigated the effect of methanol concentration (0.1 M and 0.2 M) and convection on the current efficiency of $CO_2$ and methylformate formation during the electrooxidation of methanol at smooth polycrystalline Pt. (The usable concentration range is very limited: at lower concentrations, the amount of methylformate formed is too low. At high concentrations, too much methanol evaporates into the ion chamber at the mass spectrometer, and the lifetime of the filaments is too much reduced). Using a potential step program, the steady state coverages of $CO_{ad}$ are determined as a function of potential and flow rate.

For highly stepped Pt surfaces vicinal to the (111) plane, the specific catalytic activity and the effect of Ru coverage on the electrooxidation of adsorbed monolayer of CO and bulk 0.01 M methanol were studied.

Finally, by comparing the experimental conditions and the kinetic parameters of methanol esterification, a new mechanism for direct methylformate formation at Pt surface is postulated.

## 3.2 Results and discussion

### 3.2.1 Kinetics of methanol esterification

#### 3.2.1.1 Calibration for methylformate

Calibration for methylformate was obtained by preparation of different concentrations of methylformate solutions in water (1 mM to 0.1 M) and monitoring the ionic signal of m/z = 60 during flow through for each concentration until $I_{60}$ became stable. The plot of

the mass signal vs. the methylformate concentration as shown in Fig. 3-1 shows a linear relationship with a slope equal to the calibration constant ($^oK_{60}$) as described in Eq. 1.

$$I_{60} = {}^oK_{60}. \text{[methylformate]} \tag{1}$$
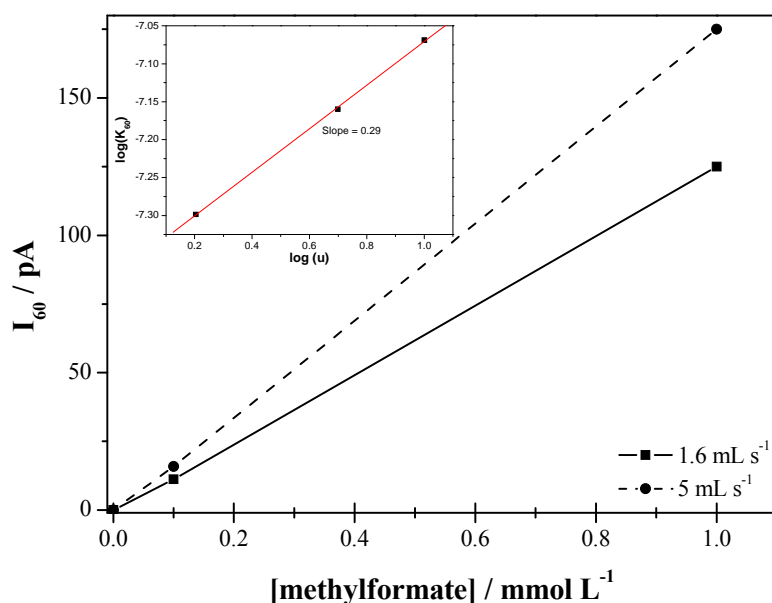


Figure 3-1: The calibration curve of methylformate by measuring the ionic current of mass 60 at different concentrations of methylformate at different flow rate. Inset: the flow rate dependence on calibration constant of methylformate.

The inset of Fig. 3-1 shows that the calibration constant of methylformate is dependent on the flow rate of the electrolyte according to $^oK_{60} \propto u^x$ relationship, with x = 0.29. Wang found a dependence of ionic signal of methylformate with flow rate with x = 0.29 at u > 1 μL s$^{-1}$ [3], but at u < 1 μL s$^{-1}$ the ionic signal is directly proportional to the flow rate [4] because at very low flow rate, the residence time is large enough and all of incoming molecules reach the Teflon membrane, the collection efficiency of the cell is 100%.

Recently, Wang et al. [5] used an aqueous solution of methylformate (10 mM) saturated with $CO_2$ for the methylformate calibration. From the ionic currents of mass 44 and 60 and $^*K_{44}$ they calculated $^*K_{60}$ assuming that the behaviour of methylformate is identical to that of $CO_2$. However the flow rate dependence of the diffusion limited ion currents

for gases like $CO_2$ follows a power law with a power of x > 0.5, suggesting that the evaporation of methylformate (with x ≈ 0.3) is not alone limited by diffusion [6-8]. Therefore calibration as described above is more appropriate.

### 3.2.1.2 Methanol esterification in acidic media

The hydrolysis rate ($k'_1$) of methylformate was determined by monitoring the decrease of ionic signal of mass 60 for a 1 mM methylformate solution in 0.5 M $H_2SO_4$ until reaching equilibrium (steady signal of m/z = 60); the electrolyte was continuously flowing through the dual compartment cell.

$$HCOOCH_3 + H_2O \underset{k_{-1}}{\overset{k'_1}{\rightleftharpoons}} CH_3OH + HCOOH \qquad (2)$$
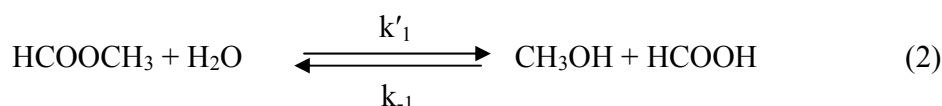
The hydrolysis reaction is a pseudo first order reaction and the hydrolysis rate constant ($k_1 = k'_1 \cdot [H_2O]$) was determined according to the following integrated equation for the first order reaction [9].

$$\ln[C] = \ln[C_o] - k_1 t \qquad (3)$$

Here $C_o$ is the initial concentration of methylformate (at t = 0) and C is the concentration at varied measuring time.

The methylformate concentration is calculated from equation 1 as shown in Fig. 3-2a. Using the integrated equation of the first order reaction (Eq. 3), a linear relationship between the logarithm of methylformate concentration and the measuring time is obtained as shown in the inset of Fig. 3-2a. The slope of the straight line equals -$k_1$ (the rate constant of methylformate hydrolysis). The rate constant value was calculated as $2.26 \times 10^{-3}$ $s^{-1}$, and the time constant for methylformate hydrolysis is about 440 s.

The rate constant of methylformate formation ($k_{-1}$) in acid media was determined by monitoring the mass signal of m/z = 60 until reaching to the equilibrium state in homogenous solution, starting with 0.2 M methanol and 0.2 M formic acid in 0.5 M sulfuric acid.

The methylformate formation is second order reaction and the formation rate constant was determined using the integrated rate equation [9]:

$$t = \frac{C_{eq}}{k_{-1}\left(C_o^2 - C_{eq}^2\right)} \cdot \ln \frac{\left[C_{eq}\left(C_o^2 - CC_{eq}\right)\right]}{\left[C_o^2\left(C_{eq} - C\right)\right]} \tag{4}$$
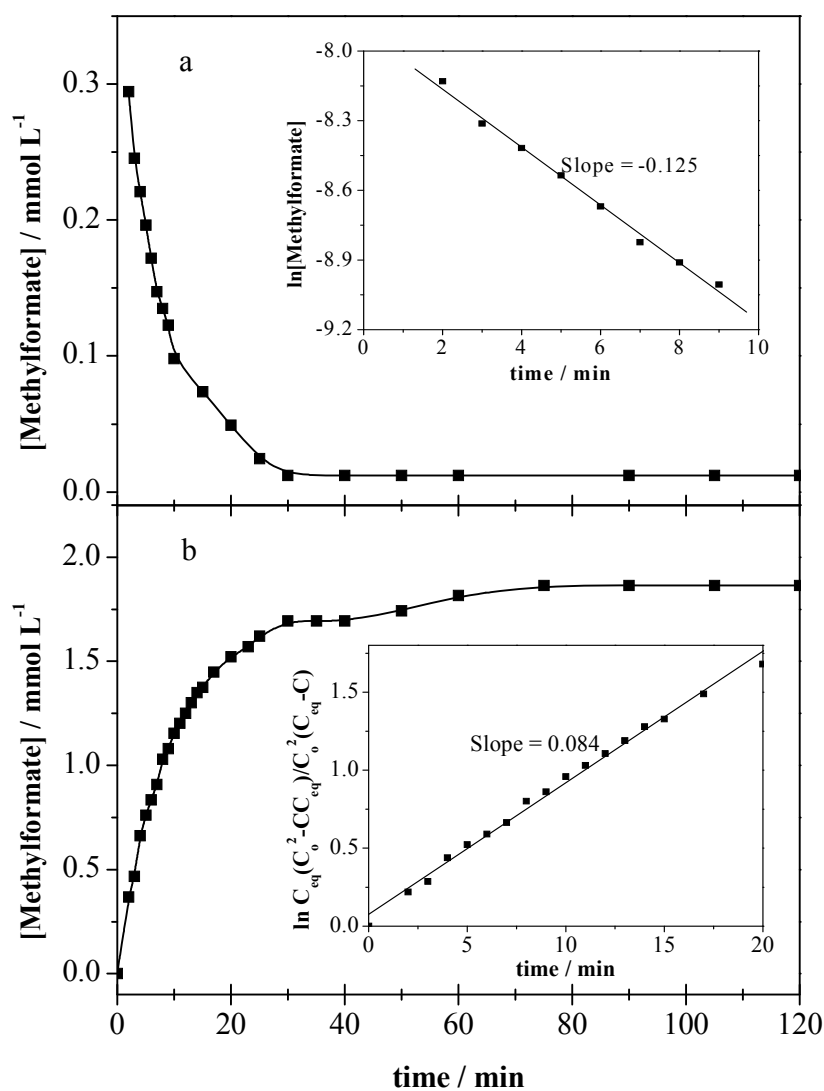


Figure 3-2: (a) Hydrolysis of 1 mM methylformate in 0.5 M $H_2SO_4$. Inset: Linear relationship between logarithm of methylformate concentration and time. (b) Formation of methylformate during esterification reaction of 0.2 M methanol with 0.2 M formic acid in 0.5 M $H_2SO_4$ at flow rate = 5 µL s$^{-1}$. Inset: Linear relationship between the logarithm of methylformate concentration and time according to the integrated equation of second order reaction.

The inset of Fig. 3-2b shows the linear relationship between the logarithm of concentration parameter and the time of measurement according to Eq.4 with

$$\frac{1}{slope} = \frac{C_{eq}}{k_{-1}\left(C_o^2 - C_{eq}^2\right)}$$
(5)

Where the slope is equal $0.084$ min$^{-1}$, the rate constant of methylformate formation is $6.57 \times 10^{-5}$ L mol$^{-1}$ s$^{-1}$.

From the final concentration of methylformate and methanol, the equilibrium constant is calculated using Eq. 6:

$$K_{eq} = \frac{[CH_3OH]^2}{([HCOOCH_3]\cdot[H_2O])} = \frac{(0.198)^2}{(55 \times 0.00187)} = 0.38$$
(6)

And from that k$'_1$ = K$_{eq}$·k$_{-1}$ = $2.5 \times 10^{-5}$ L mol$^{-1}$s$^{-1}$ is calculated, in reasonable amount with that value obtained from the hydrolysis experiment. (A determination of the equilibrium constant from the final concentration of the hydrolysis experiments is not meaningful because of the low final methylformate concentration).

Schultz [1] found that the equilibrium constant value depends on the solution compositions, especially the molar ratio of water and he found K$_{eq}$ = 0.24 in 0.05 M HCl. Indu et al. [2] investigated the effect of sulfuric acid concentration on the K$_{eq}$ of methylformate, and they found that K$_{eq}$ value decreases with increasing the sulfuric acid concentration from 0 to 5 M and at 0.5 M H$_2$SO$_4$, K$_{eq}$ = 0.25.

At high concentration of methanol (0.1 M) assuming pseudo first order reaction with esterification rate constant = $6.6 \times 10^{-6}$ s$^{-1}$; so the time constant for the methylformate formation is about $150 \times 10^3$ s. From this value of the time constant and also from the equilibrium constant it is clear that methylformate is not formed in a homogenous reaction from formic acid.

| Kinetic parameter | Hydrolysis exp. | Esterification exp. |
|---|---|---|
| k$'_1$ = k$_1$/[H$_2$O] | $4 \times 10^{-5}$ L mol$^{-1}$s$^{-1}$ | $2.5 \times 10^{-5}$ L mol$^{-1}$s$^{-1}$ |
| K$_{eq}$ | | 0.38 |
| k$_{-1}$ | | $6.57 \times 10^{-5}$ L mol$^{-1}$s$^{-1}$ |

### 3.2.2 Electrooxidation of bulk methanol *at a polycrystalline platinum electrode*

#### *3.2.2.1 Cyclic voltammetry*

*Effect of methanol concentration and flow rate*



Figure 3-3: Simultaneously recorded CV and MSCVs for m/z = 44 ($CO_2$) and m/z = 60 ($HCOOCH_3$) during the electrooxidation of bulk methanol at smooth Pt(pc) in 0.5 M $H_2SO_4$ solution + (a) 0.1 M and (b) 0.2 M methanol. Dotted line: in supporting electrolyte. Scan rate: 10 mV s$^{-1}$. Electrolyte flow rate: 1.6 μL s$^{-1}$. 3 cycles are shown. Inset: Expanded view of faradaic current in the first and second anodic sweep.

Figure 3-3 shows the cyclic voltammograms for the electrooxidation of 0.1 M and 0.2 M methanol, respectively, on polycrystalline platinum and the corresponding mass spectrometric cyclic voltammograms (MSCV) for m/z = 44 ($CO_2$) and m/z = 60 ($HCOOCH_3$) at a flow rate of 1.6 μL s$^{-1}$. The anodic peak around 0.25 V in the first anodic sweep does

not only correspond to hydrogen desorption, but also to the oxidative adsorption of methanol as $CO_{ad}$, which only takes place above 0.1 V after replacing the supporting electrolyte by the methanol containing electrolyte [10]. At 0.45 V the faradaic current starts to increase during the anodic sweep, leading to a sharp peak with its maximum at 0.83 V followed by the second anodic peak in the oxygen region at 1.3 V [11-13]. During the cathodic sweep, an oxidation peak is present at 0.74 V after the complete desorption of oxygen from the Pt-surface.

In the second sweep the hydrogen desorption peak is suppressed due to the blocking of the Pt-surface by the adsorbed intermediate ($CO_{ad}$) formed in the preceding cathodic sweep (cf. Inset of Fig. 3-3 and 3-4) and the first anodic peak at 0.83 V is also decreased because of this adsorbate, which is only oxidized around this potential [6, 14]. The signal shape of $m/z = 44$ is similar to that of faradaic current, its peak is shifted by 50 mV in both of the anodic and cathodic going sweep due to the delay time at the low flow rate (1.6 µL s$^{-1}$). A comparison of Fig. 3-3A and B shows that doubling the methanol concentration hardly has any influence on the faradaic current and $CO_2$ formation rate. Peak currents in the first sweep are even diminished due to faster poisoning at higher concentration. However, the methylformate rate is doubled.

While at low flow rates, more reliable current efficiencies are obtained, at higher flow rates such as 10 µL s$^{-1}$ (Fig. 3-4) the delay time of less than 1 s leads to a negligible potential shift, and the potential dependence of $CO_2$ and methylformate formation can be compared. The onset of the faradaic current at 0.45 V is not paralleled by an ionic current for $CO_2$ (the onset potential for $CO_2$ is 0.63 V and for $HCOOCH_3$ is 0.57 V). The current below 0.6 V is due to the formation of $CO_{ad}$ at Pt surface [14-16]. The shape of the faradaic current peak and the ion current peak for $m/z = 60$ (but not that for $m/z = 44$) during the anodic sweep at 10 µL s$^{-1}$ suggests that it consists of 2 peaks, one (a shoulder) at 0.75 V and the main peak at 0.88 V. Therefore, at low potentials, the relative amount of methylformate is high, and the current efficiency for $CO_2$ is lower than that at high potentials. This was described before for carbon supported Pt [5, 17-19].
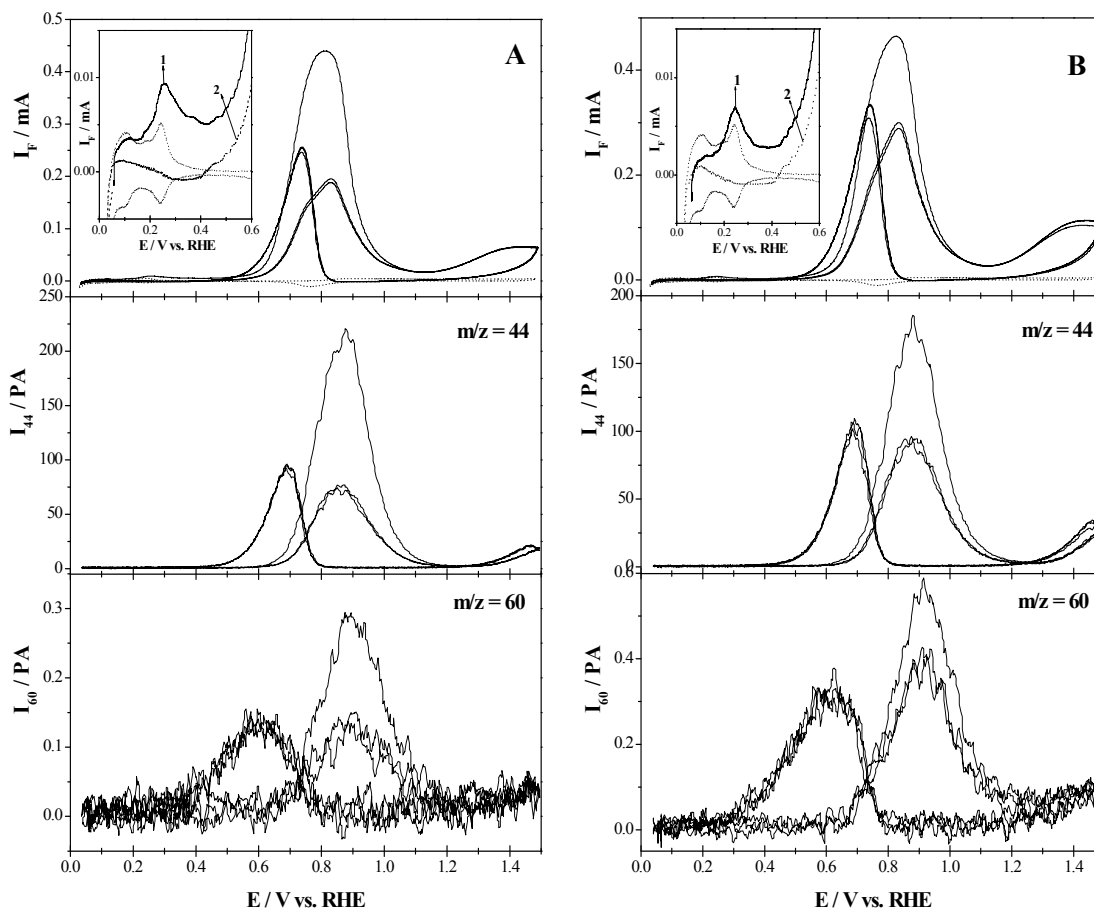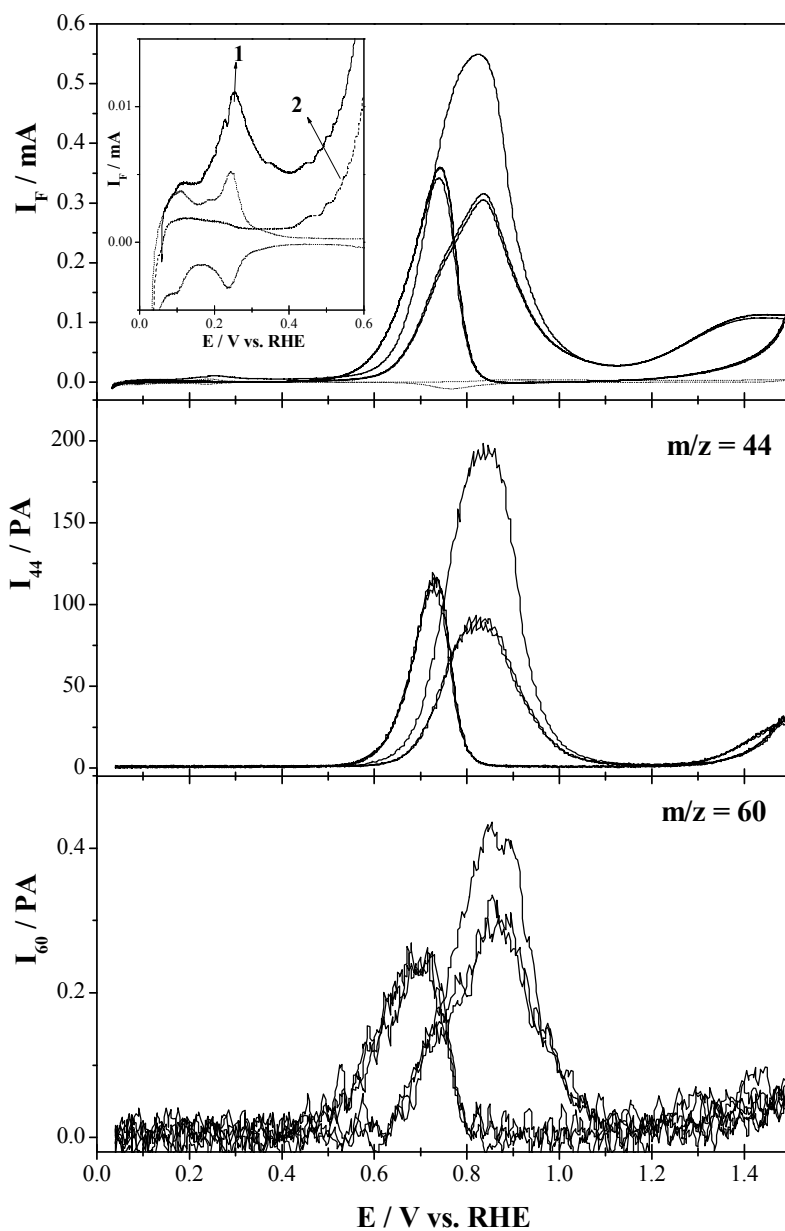
Figure 3-4: Simultaneously recorded CV and MSCVs for m/z = 44 ($CO_2$) and m/z = 60 ($HCOOCH_3$) during the electrooxidation of bulk methanol at smooth Pt(pc) in 0.2 M methanol + 0.5 M $H_2SO_4$ solution. Dotted line: CV in supporting electrolyte. Scan rate: 10 mV s$^{-1}$. Electrolyte flow rate: 10 μL s$^{-1}$. 3 cycles are shown. Inset: expanded view of faradaic current in the first and second anodic sweep.

*Current efficiency of oxidation product*

The faradaic peak current ($I_F$) and the signal peaks current of masses 60 and 44 were determined. $I_F$ is the summation of the corresponding faradaic current of many product species:

$$I_F = I_F^{CO_2} + I_F^{HCOH} + I_F^{HCOOH} + I_F^{Methylformate} \qquad (7)$$

So, the current efficiency for $CO_2$ formation ($A_{CO_2}$) was determined by the following equation:

$$A_{CO_2} = \frac{6 \cdot I_{CO_2}}{K * \cdot I_F} \qquad (8)$$

Here, 6 is the number of electrons transferred during the complete oxidation of one methanol molecule, $I_{CO_2}$ is the ionic signal of m/z = 44 corresponding to the peak potential at faradaic current.

In the same way, the current efficiency of methylformate ($A_{60}$) can be obtained according to eq (1) and the following equations:

$$A_{60} = \frac{I_F^{Methylformate}}{I_F} \qquad (9)$$

$$I_F^{Methylformate} = \left(\frac{I_{60}}{\circ K_{60}}\right) zFu \qquad (10)$$

Here, u is the flow rate in L s$^{-1}$ and F is the faradaic constant in C mol$^{-1}$. Equation (10) only holds, if the product of the electrochemical reaction is homogeneously distributed in the solution entering the mass spectrometric compartment, i.e. if complete mixing occurs. This is only the case for low flow values [4].

Table 3-1 shows the current efficiencies with respect to $CO_2$ and methylformate for different concentrations of methanol at four different flow rates and three potential cycles voltammograms at the anodic oxidation peak. The current efficiency with respect to $CO_2$ hardly depends on the flow rate. The increase of the apparent current efficiency with respect to methylformate with flow rate is due to the incomplete mixing as discussed above; only the values for u = 1.6 μL s$^{-1}$ are absolute values.

Table 3-1: Current efficiencies at the peak potential of the faradaic current with respect to $CO_2$ and methylformate formed during the electrooxidation of 0.1 M and 0.2 M methanol at Pt(pc) surface.

| u / ($\mu$L s$^{-1}$) | CV No. | 0.1 M CH$_3$OH | | 0.2 M CH$_3$OH | |
|---|---|---|---|---|---|
| | | A$_{44}$ % | A$_{60}$ % | A$_{44}$ % | A$_{60}$ % |
| **1.6** | 1 | 40.5 | 0.67 | 30.9 | 1.2 |
| | 2 | 31.8 | 0.72 | 24.9 | 1.4 |
| | 3 | 31 | 0.7 | 25.3 | 1.3 |
| **5** | 1 | 38 | (1) | 32.9 | (2.34) |
| | 2 | 32 | (1.2) | 27.9 | (2.62) |
| | 3 | 31.8 | (1.14) | 27.5 | (2.72) |
| **10** | 1 | 37.2 | | 33 | (2.93) |
| | 2 | 31.1 | n. d. | 27 | (3.8) |
| | 3 | 31.3 | | 26.6 | (3.6) |
| **30** | 1 | 37.9 | | 25.3 | |
| | 2 | 30.6 | n.d. | 23.9 | n.d. |
| | 3 | 30.4 | | 23.3 | |

Since the current efficiency values for $CO_2$ are between 23 and 40 %, other products (formic acid and formaldehyde) are formed to a large degree under all conditions. The increase of current efficiency for methylformate with methanol concentration is as expected, because 2 methanol molecules are necessary for its formation.

Since the formation of methylformate from formic acid and methanol in solution can be excluded because of the large time constant of that reaction, it is obvious that methylformate is formed in a direct reaction during methanol oxidation. The decrease of the current efficiency for $CO_2$ with methanol concentration and the concentration independence of the ionic current for $CO_2$ suggest that the oxidation path via adsorbed CO is not much dependent on concentration, whereas that leading to dissolved intermediates is.
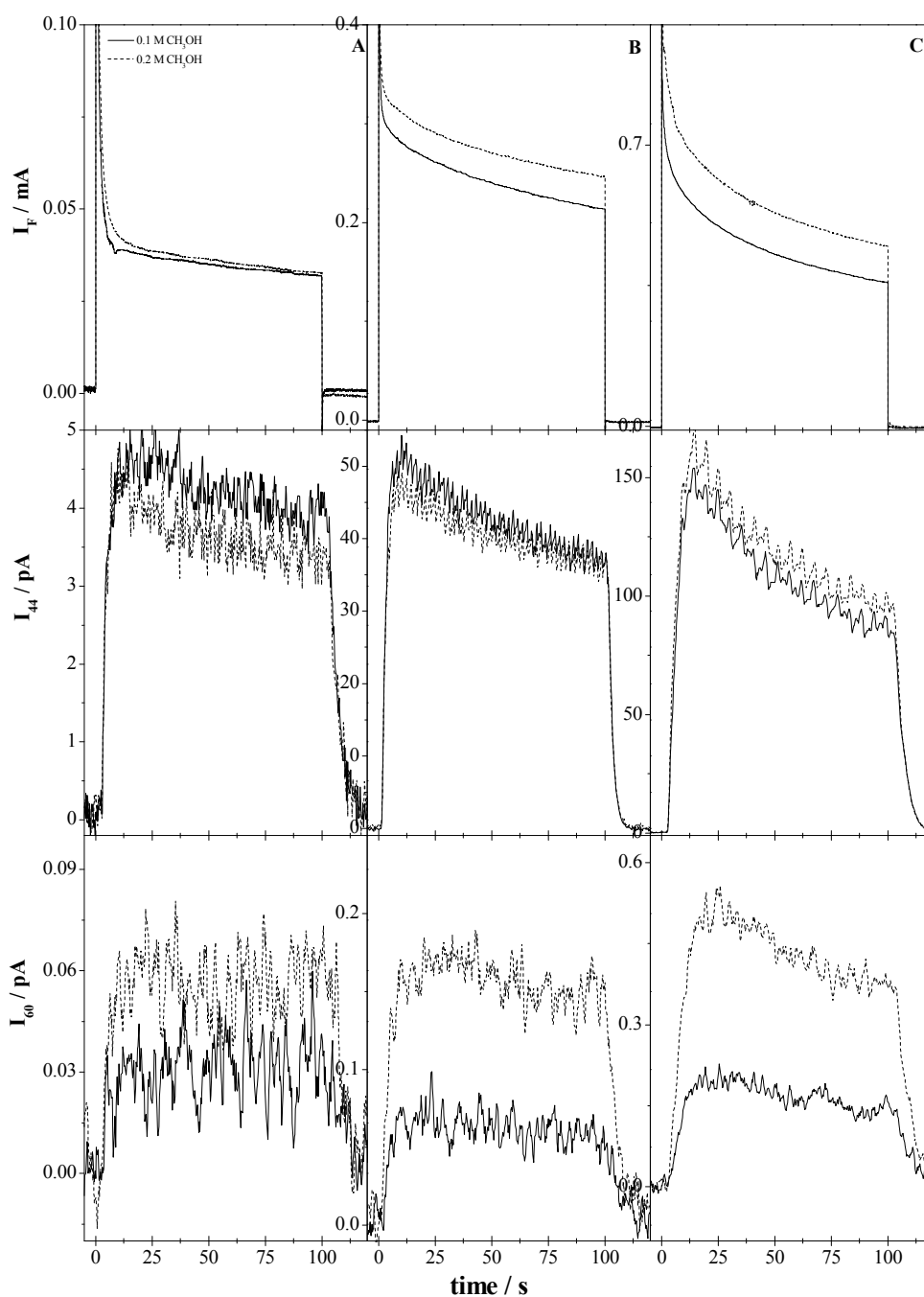
### 3.2.2.2 Potential step experiments



Figure 3-5: Simultaneously recorded transients of faradaic current and ion currents m/z = 44 and m/z = 60 on smooth Pt(pc) in  0.1 M methanol (solid) and 0.2 M methanol (dashed) + 0.5 M $H_2SO_4$ solution after the step of potential from 0.05 V to (A) 0.6 V, (B) 0.7 V and (C) 0.8 V. Electrolyte flow rate: 1.6 μL s$^{-1}$.

63

Potential step experiments were performed to start the reaction at constant potential at an un-poisoned electrode. To do so, after cleaning the electrode by cycling voltammetry in the supporting electrolyte, the potential was stopped at 50 mV, where the methanol containing electrolyte was introduced. Then the potential was stepped to 0.6, 0.7 and 0.8 V for oxidation (cf. the potential program in chapter 2, Fig. 2-2). The faradaic current and the corresponding mass spectrometric currents of m/z = 44 and m/z = 60 were simultaneously recorded. After 100 s, the potential was stepped back to around 50 mV to perform another electrolyte exchange. The degree of poisoning with CO was then evaluated in a potential sweep in the supporting electrolyte. Typical potential step experiments are shown in Fig. 3-5 for 0.1 M and 0.2 M methanol at smooth Pt(pc) in 0.5 M $H_2SO_4$ solution at 1.6 $\mu$L s$^{-1}$. The current at 0.6 V is essentially constant after 10 s, whereas at high potentials the current decrease over the whole oxidation period. A more pronounced current decay with time at more positive potential had also be observed in Seidel et al. [19].

Table 3-2 shows the current efficiencies with respect to both $CO_2$ and methylformate during the electrooxidation of bulk methanol on Pt(pc) for different step potentials and different flow rates. Whereas the current efficiency with respect to $CO_2$ increases with increased adsorption potential due to faster oxidation of $CO_{ad}$ at high potential (0.8 V), it decreases with increasing methanol concentration. As in cyclic voltmmetry, the flow rate of the electrolyte at a given adsorption potential hardly has an influence. The current efficiency with respect to methylformate increases with decreasing the adsorption/oxidation potential or increasing methanol concentration, which corroborates the results of cyclic voltammetry. A detailed comparison of the transients shows that the current efficiency for $CO_2$ does not change with time, contrary to the observation in ref. [19], where a decrease was observed over a period of 300 s.

The current efficiencies with respect to methylformate for 0.1 M methanol at 0.6 V is about 6-10 % of that of $CO_2$, but at higher potentials (0.8 V) the ratio is about 1-5 %. For 0.2 M methanol the amount of methylformate is higher, at 0.6 V is about 20-35 % and at 0.8 V is about 5-10 % relative to the amount of $CO_2$.

Table 3-2: Current and current efficiencies with respect to $CO_2$ and methylformate during the electrooxidation of bulk methanol and the corresponding CO coverages at different applied potential and at different flow rate in current transient and potential hold experiments.

| u / (µL s⁻¹) | $E_{ads}$ / V vs. RHE | 0.1 M MeOH | | | | | | 0.2 M MeOH | | | | | |
|---|---|---|---|---|---|---|---|---|---|---|---|---|---|
| | | $I_F$ / mA | $I_F^{44^*}$ /(µA) | $A_{44}$ % | $I_F^{60^{**}}$ /(µA) | $A_{60}$ % | $\vartheta_{CO}$ | $I_F$ / mA | $I_F^{44^*}$ /(µA) | $A_{44}$ % | $I_F^{60^{**}}$ /(µA) | $A_{60}$ % | $\vartheta_{CO}$ |
| 1.6 | 0.6 V | 0.03 | 5.58 | 17.5 | 0.45 | 1 | 31.2 | 0.033 | 4.8 | 14.7 | 1.07 | 3.2 | 32.3 |
| | 0.7 V | 0.25 | 70.8 | 28 | 1.85 | 0.74 | 20.5 | 0.29 | 69.36 | 23.7 | 4.94 | 1.7 | 24.8 |
| | 0.8 V | 0.36 | 126 | 35 | 2.5 | 0.7 | 14.4 | 0.45 | 139.8 | 31.2 | 6.84 | 1.5 | 14.5 |
| 5 | 0.6 V | 0.025 | 5 | 19.2 | 0.66 | (2.4) | 26 | 0.03 | 2.7 | 10.7 | 0.9 | (3.7) | 32.6 |
| | 0.7 V | 0.2 | 62.4 | 30.5 | 2.58 | (1.3) | 20 | 0.27 | 63.6 | 23.2 | 6.23 | (2.3) | 25 |
| | $E_h = 0.7$ | 0.097 | 30 | 30.9 | 1.58 | (1.6) | 15 | 0.13 | 31.8 | 24.4 | 4.7 | (3) | 20.8 |
| | 0.8 V | 0.37 | 135.6 | 36 | 4.72 | (1.3) | 8.5 | 0.45 | 141 | 31.3 | 11.2 | (2.5) | 12.4 |
| 30 | 0.7 V | 0.25 | 69 | 27.6 | 2.3 | (1) | 19.9 | 0.276 | 57.6 | 20 | 3 | (1.2) | 23 |
| | $E_h = 0.7$ | 0.1 | 31.2 | 25 | 1.16 | (1.13) | n.d | 0.14 | 33.8 | 24.8 | 3.28 | (2.33) | n.d |

$* I^{44}{}_F = 6.I_{44}(µA)/K^*$, $** I^{60}{}_F = zFu.I_{60}(µA)/{}^oK_{60}$

Table 3-3: The estimated reaction order for faradaic and ionic currents in different methanol oxidation experiments and at different flow rate.

| u / (µL s$^{-1}$) | E | $I_F$ | $I_{44}$ | $I_{60}$ |
|---|---|---|---|---|
| **1.6** | Ps 0.7 | 0.22 | 0 | 1.4 |
| | Ps 0.8 | 0.315 | 0.15 | 1.5 |
| | Peak CV | 0.636 | 0.34 | 1.52 |
| **5** | Ps 0.7 | 0.4 | 0.024 | 1.3 |
| | Ps 0.8 | 0.3 | 0.05 | 1.3 |
| | Peak CV | 0.717 | 0.5 | 2 |
| | Ph at 0.7 | 0.42 | 0.085 | 1.6 |
| **10** | Peak CV | 0.7 | 0.48 | n.d. |
| **30** | Ps 0.7 | 0.15 | 0.33 | n.d. |
| | Peak CV | 0.58 | 0.215 | n.d. |
| | Ph at 0.7 | 0.42 | 0.115 | n.d. |

Ps: potential step, Ph: potential hold and peak CV: in cyclic voltammetry

The reaction order of methanol oxidation with respect to the faradaic and ionic currents were estimated from the data obtained at the two different methanol concentrations as shown in table 3-3. The reaction order for methylformate is higher than 1.5 at the peak potential (in MSCV) and ≈ 1.3 in the ion transient experiments which is possible because the formation of methylformate involves two methanol molecules. The reaction order for the faradaic current (in CV and current transients) and for ionic current of mass 44 (in MSCV and ion current transients) is much less than one. This agrees with the previous results of Wang [17] where a wider concentration range of methanol from 1 mM to 0.1 M was applied, but where the reaction order for methylformate formation could not be determined.

### 3.2.2.3 Electrooxidation of methanol adsorbate
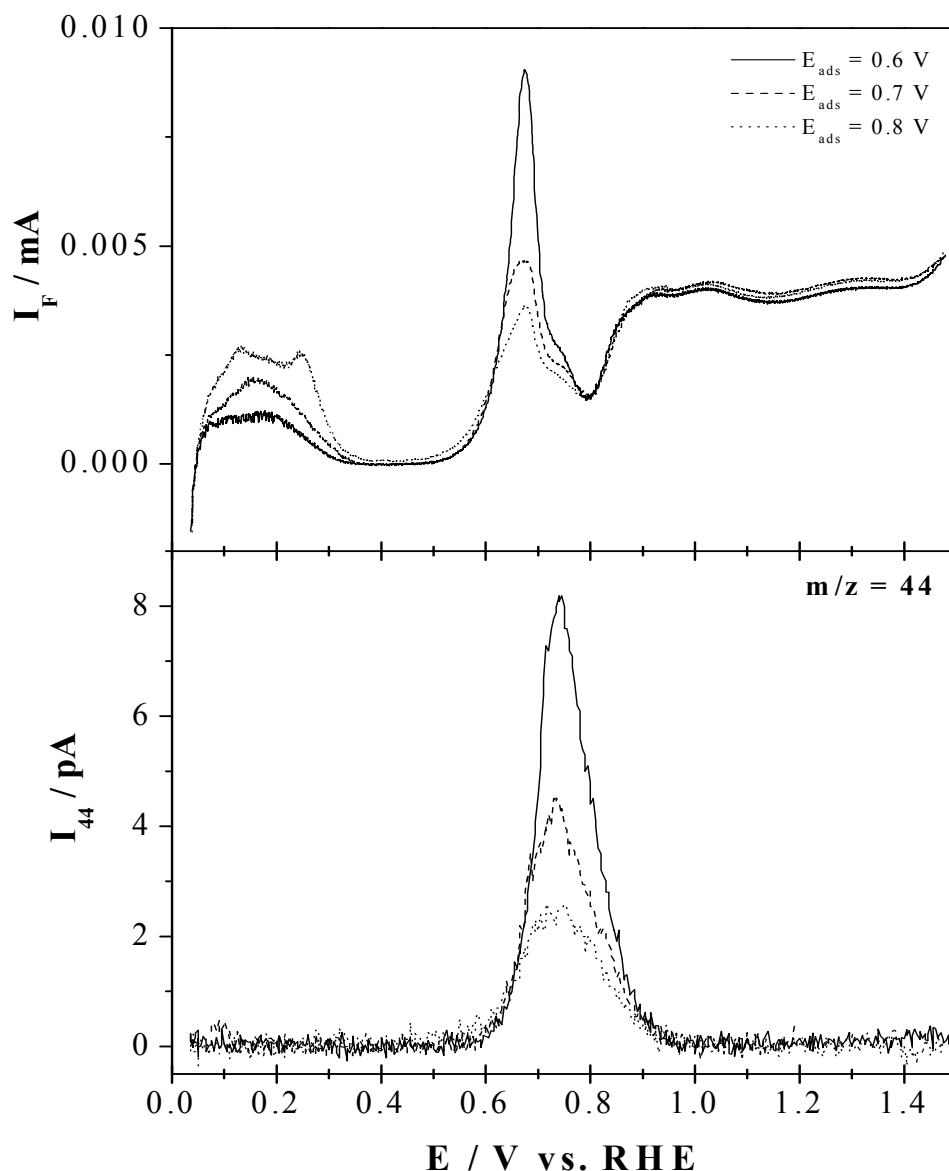


Figure 3-6: CVs and MSCVs of m/z = 44 ($CO_2$) during electrooxidation of methanol adsorbate on Pt(pc) in 0.5 M $H_2SO_4$ solution. Methanol adsorbed from 0.1 M methanol + 0.5 M $H_2SO_4$ for 100 s. Scan rate: 10 mV s$^{-1}$. The electrolyte flow rate: 1.6 μL s$^{-1}$. At the potential: (—) 0.6 V, (-----) 0.7 V and (······) 0.8 V.

After the potential step experiment, the potential was stepped back to 0.05 V and an electrolyte exchange with supporting electrolyte was performed. The cyclic voltammograms and the mass spectrometric cyclic voltammograms of $CO_2$ during oxidative strip-

ping of methanol adsorbate after potential step experiments at different applied potentials for adsorption time about 100 s are shown in Fig. 3-6. At this time steady state coverage is achieved [20]. Whereas the peak potential of oxidation shifts to higher potential with increasing coverage, the onsets of the oxidation peaks overlap, and the oxidation rate of methanol adsorbate is independent of the coverage of methanol adsorbate (zero order with respect to adsorbate coverage in agreement with ref. [20]).

In order to determine the relative coverage of methanol adsorbate ($\vartheta_{CO}$) to the surface concentration of Pt atoms, the ion current in the MSCV of $CO_2$ for the oxidation of methanol adsorbate was integrated ($Q_i^{44}$) and $\vartheta_{CO}$ was calculated according to:

$$\vartheta_{CO} = N_{CO} \big/ N_H \tag{11}$$

Here $N_{CO}$ is the number of adsorbed CO from methanol at Pt surface, and $N_H$ represents the number of surface sites as determined from adsorbed hydrogen in the characteristic CV in supporting electrolyte according to equation 12.

$$N_H = \frac{Q_H}{z \cdot F} \tag{12}$$

Where $Q_H$ is the integrated charge of adsorbed hydrogen atoms at Pt surface. It is determined by comparing the integrated charge of hydrogen desorption region between 0.05 and 0.4 V (the potential at the beginning of the double layer region) during the potential sweep in the supporting electrolyte [21, 22], and z is the number of electron exchange per H-atom.

The surface coverage with methanol adsorbate for 0.1 M and 0.2 M methanol after potential step experiments at different step potentials and at different flow rates are shown in table 3-2. It is observed that the coverage of methanol adsorbate somewhat increases with the increase of methanol concentration and decreases with the increase of adsorption potentials from 0.6 to 0.8 V due to the increased rate of adsorbate oxidation during potential step experiments. $\vartheta_{CO}$ is independent of electrolyte flow rate. Formation of adsorbed CO from intermediates (formaldehyde and formic acid) is therefore negligible. If it were not, more adsorbed CO would be formed at lower flow rates due to large residence times.

### 3.2.2.4 Potential hold experiments

In order to compare the degree of poisoning and the reaction rate during potential sweep with that of the potential step experiments, the potential sweep was stopped at 0.7 V and held the potential constant for 100 s as shown in Fig. 3-7.



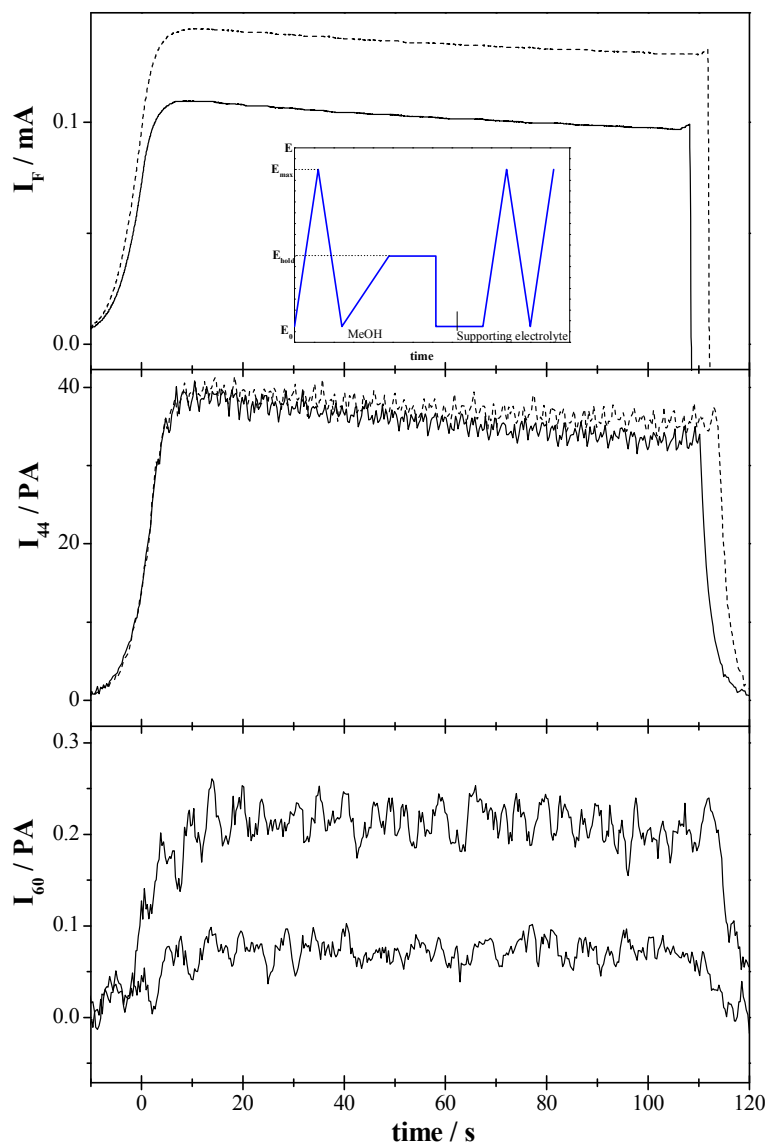Figure 3-7: Simultaneously recorded transients of faradaic current and ion currents m/z = 44 and m/z = 60 on smooth Pt(pc) in 0.1 M methanol (solid) and 0.2 M methanol (dashed) + 0.5 M $H_2SO_4$ solution at potential hold at 0.7 V for 100 s during the positive going sweep. Electrolyte flow rate: 5 $\mu L$ $s^{-1}$. Inset: The potential program for potential hold experiment and electrooxidation of adsorbed methanol.

Currents and ion currents stayed constant during this period (after double layer charging), contrary to the above potential step experiments. Then, the potential was stepped to 50 mV, and after the electrolyte exchange the coverage with CO was determined by a potential sweep as after the potential step experiments described above and as shown in Fig. 3-8. Astonishingly, the CO coverage is lower by one fifth although the lower current suggests a higher degree of poisoning. The difference in the currents closely reflects the difference between the first and subsequent sweeps in cyclic voltammetry. A possible origin could be a different amount of adsorbed formate, which also might inhibit the reaction to some degree [23-25]. Although this might well explain the different currents in the potential step and potential hold experiment, it does not explain the difference in the first and subsequent potential sweeps, because no formate is adsorbed in the hydrogen region [23]. As another possibility one would have to discuss different states of the adsorbed CO, such as islands of closely packed CO with CO-free parts on the surface versus a homogenous distribution of the adsorbed CO molecules. Such different states of adsorbed CO are supposed to be formed when sub-monolayer amounts of CO are adsorbed at different potentials [26, 27]. It is also known that adsorbed CO formed from methanol is not identical to an adsorbate layer of the same coverage formed from CO adsorption [28-30]. Such an effect might also cause the decrease of the current in the potential step experiments. As mentioned above, this decay with time is much more pronounced at 0.8 V than at 0.6 V. Therefore, an increasing degree of CO poisoning is unlikely to be the cause, because CO poisoning is slower at low potentials [20, 31].
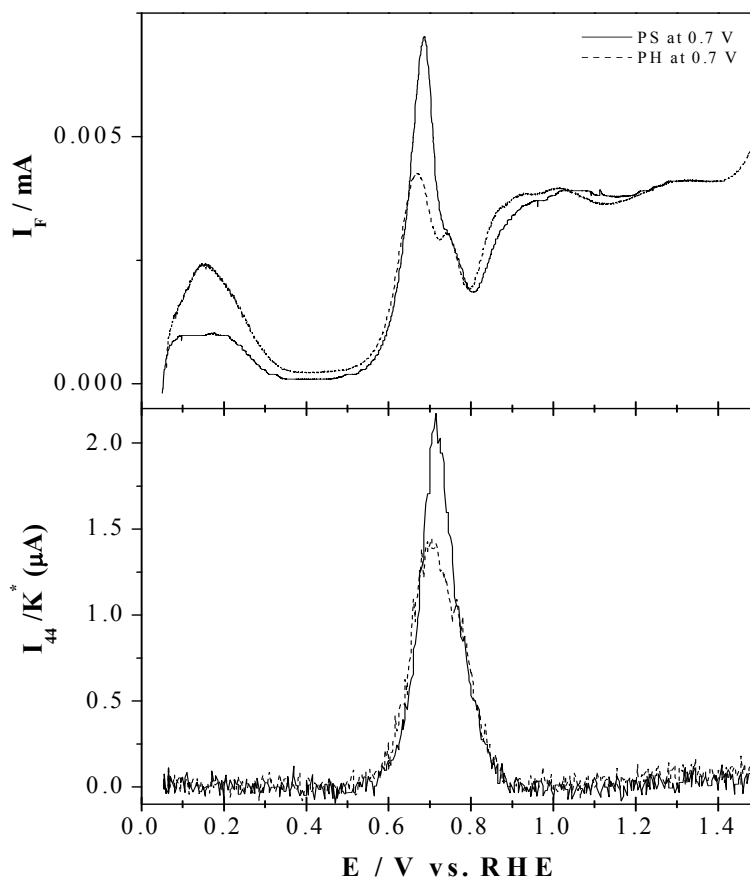
Figure 3-8: CVs and MSCVs of m/z = 44 ($CO_2$) during electrooxidation of methanol adsorbate on Pt(pc) in 0.5 M $H_2SO_4$ solution at 0.7 V and at 5 µL $s^{-1}$. Scan rate: 10 mV $s^{-1}$. Methanol adsorbed from 0.2 M methanol + 0.5 M $H_2SO_4$ (—) potential step for 100 s and (-----) potential hold.

### 3.2.2.5 Effect of supporting electrolyte

Because methanol oxidation is a surface sensitive reaction, it is generally believed that strongly adsorbed anions can inhibit methanol oxidation by blocking surface sites. Sulfate/bisulfate anions are more strongly adsorbed at Pt surfaces than perchlorate, their thus affect methanol adsorption and its oxidation rate. Fig. 3-9 shows the CV and corresponding MSCVs of $CO_2$ and methylformate during the electrooxidation of 0.1 M $CH_3OH$ on smooth Pt(pc) in a mixture of 0.5 M $HClO_4$ + 0.1 M $H_2SO_4$ solution as a supporting

electrolyte. The reason behind using perchloric acid is to reduce the specific adsorption without decreasing the conductivity of the electrolyte.
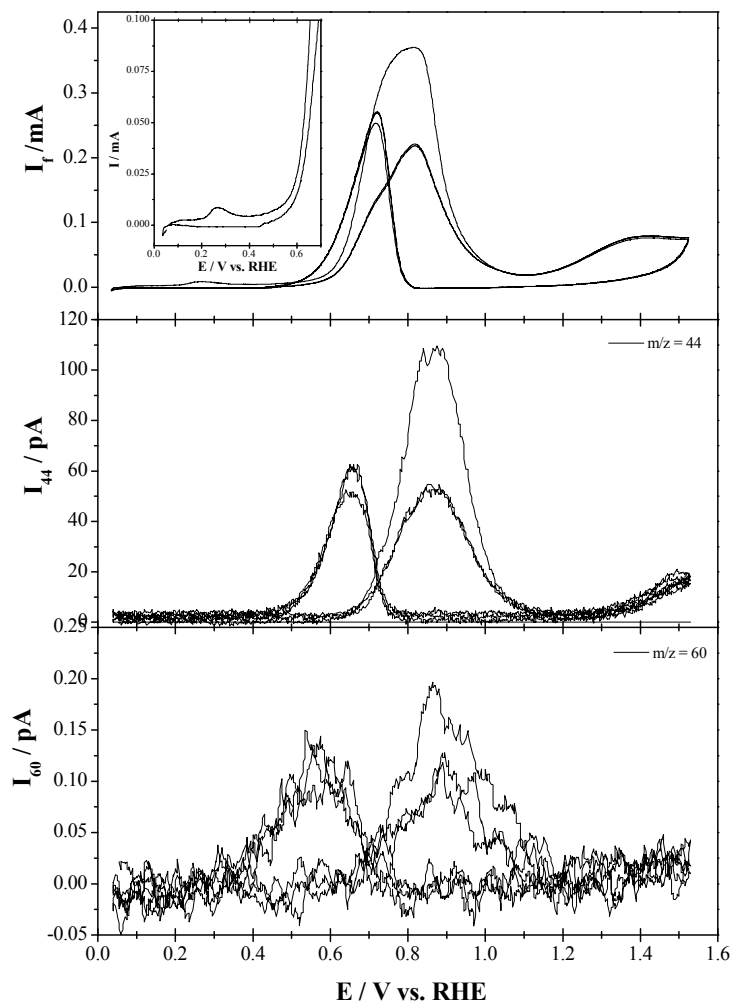


Figure 3-10: Simultaneously recorded CV and MSCVs for m/z = 44 ($CO_2$) and m/z = 60 ($HCOOCH_3$) during the electrooxidation of bulk methanol at smooth Pt(pc) in 0.1 M methanol + 0.5 M $HClO_4$ + 0.1 M $H_2SO_4$ solution. Scan rate: 10 mV $s^{-1}$. Electrolyte flow rate: 1.6 µL $s^{-1}$. 3 cycles are shown. Inset: Expanded view of faradaic current in the $H_{ad}/H_{des}$ region.

In the second CV, the onset potential of methanol oxidation and the faradaic and ionic peak currents are similar to that in Fig. 3-3A. The average current efficiency for $CO_2$ in 0.1 M $H_2SO_4$ + 0.5 M $HClO_4$ is 20% lower than that in pure 0.5 M $H_2SO_4$ solution as

summarized in table 3-4. For methylformate the current efficiency is the same as in 0.5 M $H_2SO_4$.

During the electrooxidation of 0.2 M methanol at Pt/C in different sulphuric acid concentration, Wang et al. [5] observed a slight increase in the peak current with increasing concentration of sulphuric acid from 0.1 to 0.5 M. The average current efficiencies with respect to $CO_2$ and methylformate were slightly changed. As the sulphuric acid concentration was increased to 2 M, the catalytic activity for methanol oxidation significantly suppressed as well as the current efficiencies. However, Schell and Kumara Swamy reported that the rate of methanol and formic acid oxidation was substantially increased by replacing a small amount of the supporting electrolyte (perchloric acid) with either sulfuric acid or tetrafluoroboric acid [32, 33].

In this work, however, decreasing the sulfuric acid / sulfate concentration from 0.5 M to 0.1 M had hardly any influence.

Table 3-4: The current efficiencies with respect to $CO_2$ and methylformate during the electrooxidation of 0.1 M methanol in 0.1 M $H_2SO_4$ + 0.5 M $HClO_4$ on Pt(pc) at flow rate 1.6 and 5 $\mu L/s$.

| CV No. | 1.6 $\mu L \ s^{-1}$ | | 5 $\mu L \ s^{-1}$ | |
|---|---|---|---|---|
| | $A_{44}$ | $A_{60}$ | $A_{44}$ | $A_{60}$ |
| 1a | 33.5 | 0.58 | 32.4 | 1.2 |
| 2a | 27 | 0.67 | 28.2 | 1.5 |
| 1c | 24 | 0.5 | 25 | 0.94 |
| 2c | 26 | 0.6 | 26.8 | 0.96 |

### 3.2.2.6 Discussions of methanol oxidation at Pt(pc)

The current efficiency for methylformate of about 1 % is similar to the value recently reported by Wang et al. [5] for carbon supported Pt nanoparticles. As demonstrated by the low rate constant determined here in this work, its origin is not a reaction between methanol and the product formic acid as is usually assumed [12, 18, 34-38]. The time

constant for methylformate formation from the reaction between the formic acid and me-thanol ($\approx$ 40 h at 0.1 mol L$^{-1}$ methanol) is many orders of magnitude longer than the time constant of dual-thin layer flow through cell (5 s at 1.6 µL s$^{-1}$). Rather, it is directly formed during oxidation of methanol at the surface. Both the indirect pathway via ad-sorbed CO and the direct pathway involve dehydrogenation of the methanol molecule.
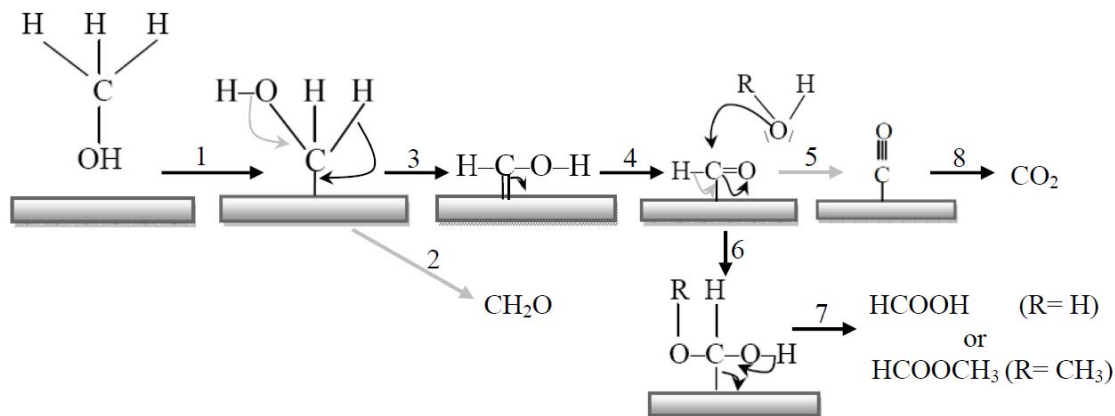


Figure 3-10: The mechanism of methanol oxidation and methylformate formation.

Formation of formic acid at some stage involves the nucleophilic attack of a water molecule to introduce a second oxygen atom into the molecule. This could happen at the stage 6 of the reaction path (Fig. 3-10). However, the nucleophilic power of the oxygen in methanol is larger than that of water, and therefore it is probable that the nucleophilic attack is by another methanol molecule instead of water. This methanol molecule might well be physisorbed or weakly chemisorbed (possibly also a methoxy species).

At the onset of methanol oxidation, the current efficiency for $CO_2$ is smaller than that at higher potentials. This is accompanied by the opposite potential dependence of the current efficiency for methylformate, as shown by both potential step experiments and the comparison of the ion currents for $CO_2$ and methylformate. Since methylformate ac-counts only for 1 to 3 % of the current, it is obvious that most of the dissolved interme-diates is formaldehyde or formic acid. The situation changes most likely for higher me-thanol concentrations: Extrapolating the estimated reaction orders to higher concentra-tions, the current efficiencies of 10 to 20 % for a 1 M concentration of methanol is ex-pected. (Note that methylformate itself is not electrochemically reactive and the first step

before oxidation is hydrolysis to formic acid and methanol [39, 40]). If the nucleophilic attack to the dehydrogenated methanol molecule is by a water molecule or methanol molecule from solution, the ratio of methylformate to formic acid among the products should only be given by the ratio of the nucleophilic power, and the potential dependence of their formation should be identical. This is supported by the opposing potential dependence of the current efficiency for methylformate and $CO_2$. Here, an unknown factor, however, is the amount of formaldehyde formed. If adsorbed species (methoxy and hydroxide) are involved in the nucleophilic attack, the situation is more complicated.

The low current efficiency for $CO_2$ at the onset potentials of oxidation shows that the indirect oxidation path is limited by the oxidation of adsorbed CO. Both the adsorbate oxidation experiments and the coverage data show that at 0.6 V the surface is largely covered by CO. Formation of dissolved intermediates is less affected by this catalyst blockage than formation and oxidation of CO. Seidel et al. [19] determined the current efficiencies as a function of flow rate and, contrary to the previous measurements of Baltruschat group [3, 14], found a slight decrease of the current efficiency for $CO_2$ for flow rates between 1 and 30 μL s$^{-1}$. They interpreted this decrease as being due to formation, desorption and subsequent re-adsorption of intermediates such as formaldehyde and formic acid. This model is identical to Baltruschat model used to explain the high current efficiencies at rough, porous or carbon supported Pt [17]. My measurements presented here, however, confirm the previous result of [3, 14] that such a flow rate dependence is negligible at smooth Pt. In particular, the CO coverage data confirm that re-adsorption is negligible in this case, i.e. at smooth Pt. At rough electrodes, however, a flow rate dependence of the CO coverage can be expected.

### 3.2.3 Electrooxidation at Pt single crystal electrodes

#### 3.2.3.1 Electrooxidation of adsorbed CO

*Effect of step density*

Two different regions can be distinguished in the voltammetric profiles associated with hydrogen and (bi)sulfate adsorption/desorption for Pt(332) and Pt(331) electrodes in 0.1 M $H_2SO_4$ + 0.5 M $HClO_4$ as shown in Fig. 3-11. For platinum stepped single crystals, the Pt(s)[n(111)x(111)] equivalent to [(n-1)(111)x(110)] surfaces are composed of (n–1)

atoms wide terraces with (111) orientation, separated by monoatomic steps with (110) orientation.

In the potential range between 50 and 350 mV, in the hydrogen adsorption region, the sharp peak at 100 mV corresponds to hydrogen adsorption/desorption at the step sites, whereas adsorption on the terrace sites gives a broad and featureless signal between 50 and 350 mV. The characteristic signals in the potential range between 350 and 850 mV is related to the adsorption of anions ((bi)sulfate) at the terrace sites [41, 42].
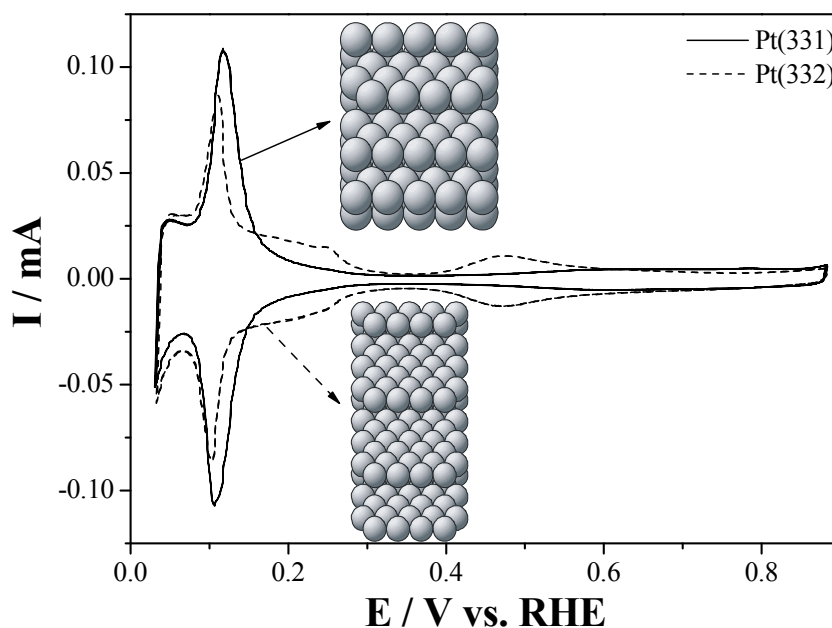


Figure 3-11: CVs of the clean Pt(332) and Pt(331) surfaces in 0.5 M HClO$_4$ + 0.1 M H$_2$SO$_4$. Scan rate: 50 mV s$^{-1}$.

After its transfer to DEMS cell, the Pt single crystal electrode was cleaned by adsorption and subsequent electrooxidation of CO. The CVs and MSCVs for the electrooxidation of CO$_{ad}$ at Pt(332), Pt(331) and the limiting case Pt(111) are shown in Fig. 3-12. The onset potential for CO adlayer oxidation shifts to less positive potentials at the higher step density surface. Whereas the difference between the onset potentials of the pre-peak for Pt(331) and Pt(111) is 250 mV, the potential difference for the main peak is 100 mV. The effect of promoting the oxidation of CO$_{ad}$ in presence of step sites has been explained by

the more favorable formation of oxygen-containing species at the step sites as compared to the terrace sites [36, 43, 44].
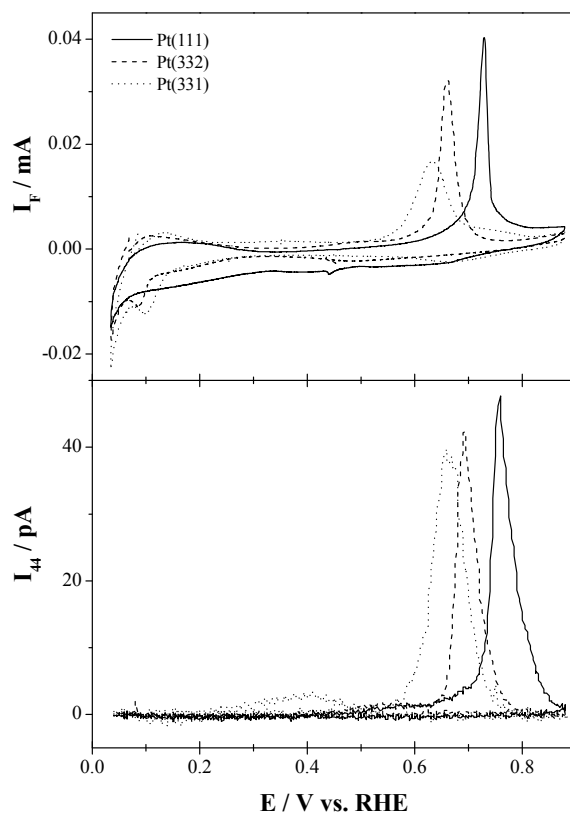


Figure 3-12: Simultaneously recorded CVs and MSCVs for m/z = 44 ($CO_2$) during the electrooxidation of adsorbed CO layer on Pt(111) (solid line), Pt(332) (dashed line) and Pt(331) (dotted line) in 0.1 M $H_2SO_4$ + 0.5 M $HClO_4$ solution. Scan rate: 10 mV $s^{-1}$. Electrolyte flow rate: 5 $\mu$L $s^{-1}$.

*Effect of Ru coverage*

Figure 2-5 represents typical CVs of Pt(331) and Pt(332) in 0.1 M $H_2SO_4$ + 0.5 M $HClO_4$ solution before and after Ru deposition as described in the experimental section (chapter 2). Ru deposition leads to partial suppression of hydrogen adsorption at the step sites (sharp peak at 100 mV), whereas the broad feature between 0.05 and 0.35 V, which is due to hydrogen adsorption at terraces sites, is not much influenced. This is in agree-

77

ment with step decoration in accordance with references [42, 45, 46]. The high current in the range of 350–800 mV is due to the hyroxide adsorption at Ru atoms.
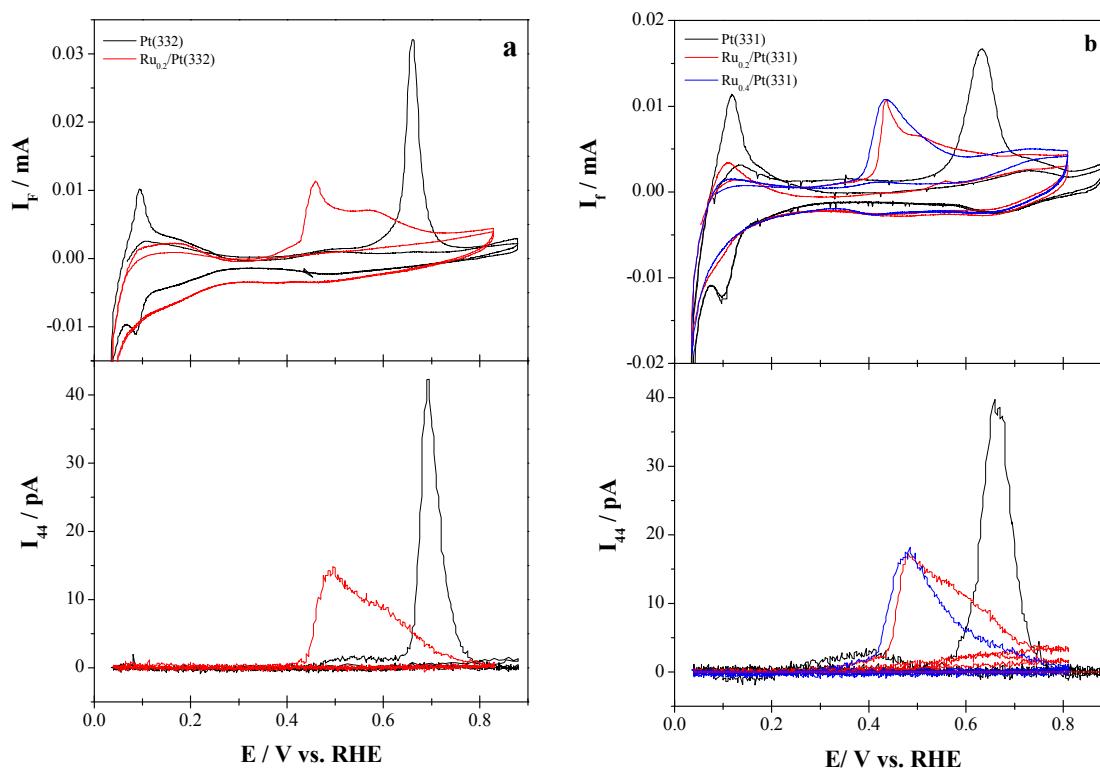


Figure 3-13: Electrooxidation of the pre-adsorbed CO on Ru free and Ru decorated the step sites of Pt single crystals with different coverage in 0.1 M $H_2SO_4$ + 0.5 M $HClO_4$ at 10 mV s$^{-1}$ and 5 μL s$^{-1}$ a) Pt(332) and b) Pt(331).

The CVs and corresponding MSCVs of $CO_{ad}$ oxidation at Ru-free and Ru-decorated step sites of Pt(332) (a) and Pt(331) (b) are shown in Fig. 3-13. The CV for $CO_{ad}$ oxidation at Ru-free Pt(332) shows that the pre-peak of adsorbed CO oxidation starts at 0.4 V with a symmetric main peak at 0.66 V. At the Ru-modified Pt(332), there are two peaks present at low potential, one at 0.45 V and the other one at 0.57 V. With increasing the step density of the Pt surface, at Ru free Pt(331), the pre-peak of CO adlayer oxidation starts at 0.2 V and the main peak present at 0.63 V. At Ru-half coverage of the step sites of Pt(331), the main peak is shifted to lower potential (0.43 V) with a new peak (or shoulder) appearing at 0.5 V. Thus, it overlaps with the pre-peak. All of these results are in agreement with previous work at Pt(665) [31, 45, 46].
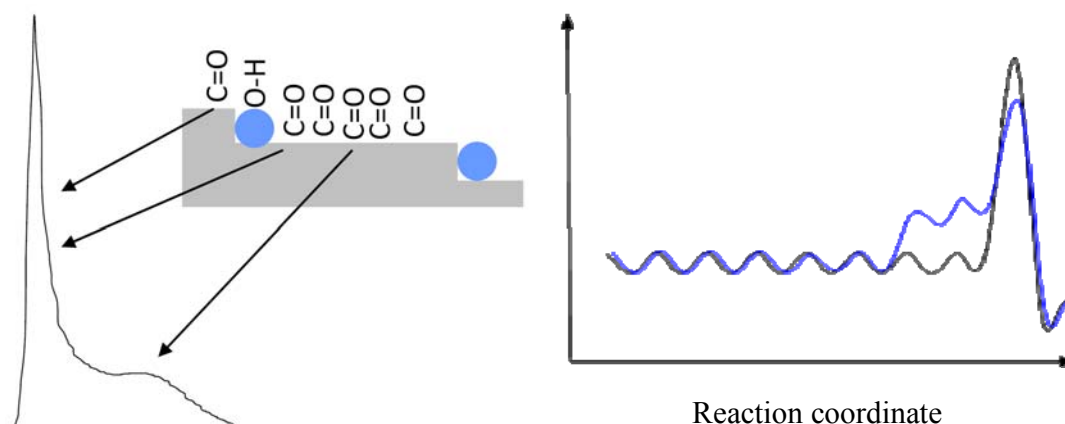
Figure 3-14: Influence of Ru step decoration on adsorption enthalpy of CO with respect to the reaction coordinate (schematically). (blue) Ru-decorated step; (black) Ru-free surface [46].

Baltruschat and co-workers attributed the separate oxidation of $CO_{ad}$ in two oxidation peaks at Pt(665) and Pt(332) (fac) to a different enthalpy of adsorption sites. The adsorption enthalpy of Pt atoms adjacent to Ru is increased owing to the electronic effect leading to a destabilization and this influence is extended over at least four rows of atoms. 1/3 of the terrace sites of Pt(665) are not influenced by this effect and diffusion of CO from these to the step sites is slow due to the higher adsorption enthalpy at those sites, cf. Fig. 3-14. Therefore, the two different oxidation peaks are due to the oxidation of adsorbed CO at different adsorption sites relative to Ru atoms on Pt surface. The first peak is due to the oxidation of $CO_{ad}$ molecules which are directly influenced by Ru. The second peak present at higher oxidation potential is due to the electrooxidation of $CO_{ad}$ at terraces far away from the Ru atoms which decorate the step sites but still the potential of this peak is lower than at the Ru-free surface due to the bifunctional effect.

### 3.2.3.2 Electrooxidation of bulk methanol at Pt(331)

*Effect of surface structure*

After the electrooxidation of $CO_{ad}$ (experiment shown in Fig. 3-12), the potential was held at 50 mV and the supporting electrolyte was changed with the methanol containing solution. Fig. 3-15a shows the CV and MSCV of m/z = 44 for the electrooxidation of

0.01 M methanol at smooth Pt(331) in 0.1 M $H_2SO_4$ + 0.5 M $HClO_4$ solution. In the first anodic sweep, the hydrogen desorption peak is not completely suppressed because the adsorption of methanol at the Pt surface does not take place at 50 mV. During the positive going sweep, one anodic oxidation peak is observed at 0.75 V with an onset potential at 0.42 V. During the negative going sweep, there is an oxidation peak at 0.63 V. The simultaneously recorded ionic current for m/z = 44 shows the anodic peak at 0.83 V and the cathodic peak at 0.56 V, these shifts in the ionic peak potentials with respect to those of the CV are due to the delay time in dual thin layer flow through cell ($\approx$ 5 s at 1.6 µL $s^{-1}$). Whereas the current efficiency with respect to $CO_2$ is 29 % for the electrooxidation of 0.01 M methanol at smooth Pt(331), this methanol concentration is not sufficient to produce a detectable amount of methylformate.



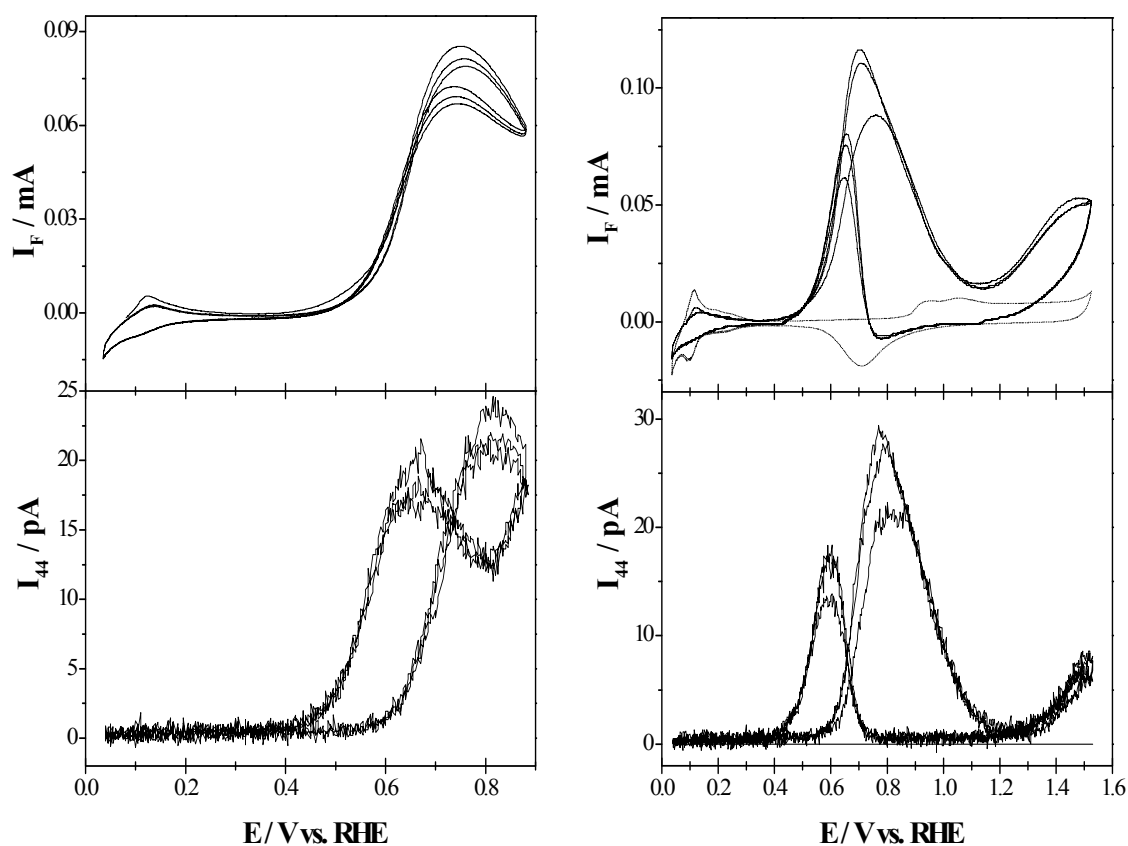Figure 3-15: Simultaneously recorded CV and MSCV m/z = 44 on (a) smooth Pt(331) (b) roughened Pt(331) in 0.01 M methanol + 0.5 M $HClO_4$ + 0.1 M $H_2SO_4$ solution. Scan rate: 10 mV $s^{-1}$. Electrolyte flow rate: 1.6 µL $s^{-1}$. 3 cycles are shown.

Three potential cycles with an upper limit of 0.85 V were followed by another three cycles with an upper limit of 1.5 V. The last 3 cycles and corresponding MSCV of m/z = 44 for the electrooxidation of 0.01 M methanol are shown in Fig. 3-15b. The first cycle of this series starts with a smooth surface, while during the next ones, the surface was roughened.

The onset potential for methanol oxidation at Pt (331) is 0.42 V in the positive going sweep followed by two anodic oxidation peaks. The first one is at 0.75 V and the second anodic oxidation peak is parallel to oxygen adsorption region. During the negative going sweep after oxygen reduction, there is an oxidation peak at 0.63 V. After the anodic potential sweep to 1.5 V (roughened surface), both faradaic and ionic currents in the second CV are higher than the smooth surface ($1^{st}$ CV) by 25 %. The current efficiency still is in the range of 27%, so the roughened Pt(331) has a higher catalytic activity towards methanol oxidation than smooth surface due to more defects induced during the sweep to the upper potential limit.

*Effect of Ru coverage*

The effect of Ru decorating the Pt(331) (half and complete coverage of the step sites) on the electrooxidation of methanol was studied as shown in Fig. 3-16a. As the Ru coverage increases, the catalytic activity of Pt(331) towards methanol oxidation decreases due to the blocking of the step sites by Ru. This means that the free step sites are most important for methanol adsorption and oxidation. In addition, the Ru modified Pt(331) has a 1.5 atoms wide terrace. That is not sufficient for the steps of methanol adsorption and further oxidation. Markovic et al. found that the methanol adsorption/dehydrogenation occurs on three-fold Pt atoms [47, 48]. Recently, Cuesta reported that an atomic ensemble of at least three contiguous Pt atoms is required for the decomposition of methanol to yield adsorbed CO on Pt(111) surfaces [49]. Extending this concept to Ru decorated Pt(331) surface, the number of free Pt atoms at steps and terraces is not enough for the formation of $CO_{ad}$ and their further oxidation to $CO_2$. For half coverage of the step sites of Pt(331) with Ru, the current efficiency with respect to $CO_2$ is half of that of the free Pt(331) ($A_{44}$ at Ru-free surface is 25% and at Ru decorated the step sites is 14%). This is in contradiction to the effect of Ru at Pt(pc) on methanol oxidation, where the faradaic current de-

creases with increasing Ru coverage and the current efficiency reaches its maximum value at $\theta_{Ru} = 0.4$ and then hardly decreases with increasing the Ru coverage [6]. Therefore, the formation of soluble intermediates (HCHO and HCOOH) dominates over $CO_2$ formation as shown in reaction pathways scheme (Fig. 3-17).
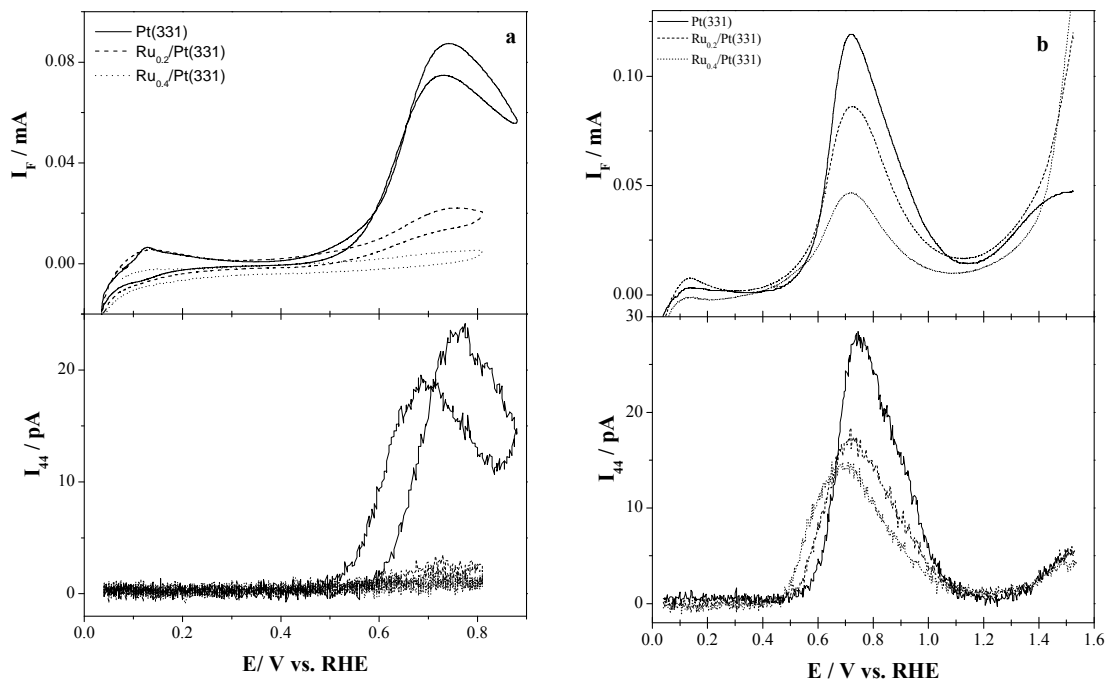


Figure 3-16: Electrooxidation of $10^{-2}$ M methanol at (a) smooth and (b) roughened Pt(331) with different Ru coverage in 0.1 M $H_2SO_4$ + 0.5 M $HClO_4$ at 10 mV s$^{-1}$ and flow rate 5 μL s$^{-1}$.

In conclusion, methanol dissociation to $CO_{ad}$ on half or completely Ru decorated step sites of Pt(331) surface is likely inhibited due to lack of adsorption sites. Methanol oxidation via adsorbed CO becomes slow, relative to methanol oxidation via soluble intermediates that can occur on the ensembles of less than three adjacent Pt atoms. Thus, the rds changes from the oxidative removal of $CO_{ad}$ to formation of $CO_{ad}$. As a result, this leads to a decrease in both of the faradaic current and the current efficiency of $CO_2$ formation.

By dissolving some Ru atoms by sweeping the potential anodically to 1.5 V to form Ru sub-monolayer at the step sites of Pt(331), the onset oxidation potential shifted to less positive and both the faradaic and ionic currents increase (cf. Fig. 3-16b). Wang et al.

found that the catalytic activity of PtRu/C electrodes can be further enhanced by partial dissolution of surface Ru atoms to create a Pt-rich surface [5].
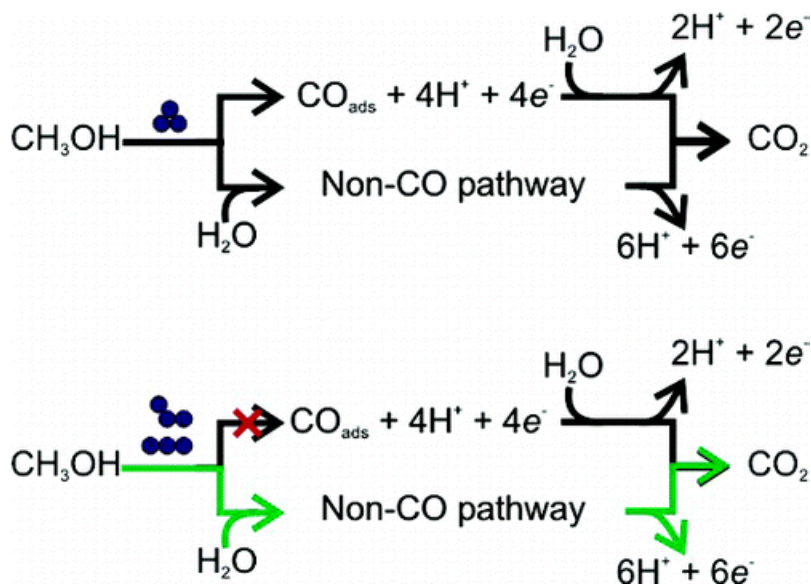


Figure 3-17: Dependence of methanol oxidation pathways at Pt(111) on atomic ensemble. Reprinted from ref. [49]

## 3.3 Conclusions

Electrooxidation of methanol proceed via dual pathway mechanism, the formation of soluble intermediates such as formaldehyde and formic acid is considered as the direct pathway, while the decomposition of methanol to adsorbed CO is referred to as indirect pathway. Methylformate is one of the volatile products formed during the electrooxidation of methanol at Pt surface. In all published articles assumed that, the detection of methylformate is an indirect way to calculate the amount of formic acid produced during the oxidation reaction.

In the present thesis, the simple kinetics of methanol esterification with formic acid and methylformate hydrolysis in acid media is monitored by mass spectrometry. The time constant for methylformate formation (pseudo first order) from the reaction between the formic acid and methanol was determined to be $\approx 40$ h (for 0.1 mol L$^{-1}$ methanol). This time constant is many orders of magnitude longer than the time constant of the dual-thin layer flow through cell (5 s at a flow rate of 1.6 $\mu$L s$^{-1}$).

During the electrooxidation of 0.1 M methanol at polycrystalline Pt, the current efficiency with respect to methylformate is about 1 % at low electrolyte flow rate; most of the dissolved intermediate is HCHO and HCOOH. As demonstrated by the low rate constant determined here in this work, its origin is not a reaction between methanol and the product formic acid as is usually assumed [12, 18, 34-38]. Rather, it is directly formed during oxidation of methanol at the electrode surface, not in the solution phase as believed before.

In agreement with previous results of Baltruschat group for methanol oxidation at Pt surface, the current efficiency with respect to $CO_2$ is independent of the electrolyte flow rate; also the surface coverage with $CO_{ad}$ does not depend on convection. These results confirm the parallel pathway mechanism.

At Pt stepped single crystals vicinal to the (111) plane (Pt(111), Pt(332) and Pt(331)), the step sites accelerate the electrooxidation of CO adlayer. The Ru decorated Pt stepped surfaces promotes the electrooxidation of $CO_{ad}$ according to electronic and bifunctional mechanisms. Whereas the complete coverage of the step sites with Ru has an inhibiting effect for methanol oxidation due to the blockage of the most active sites, i.e. the free step sites are necessary to the first step of methanol adsorption and oxidation.

# References:

[1]     R. F. Schultz, Journal of the American Chemical Society 61:1443 (1939).

[2]     B. Indu, W. R. Ernst, and L. T. Gelbaum, Industrial & Engineering Chemistry Research 32:981 (1993).

[3]     H. Wang, Vol. PhD, Beijing Normal University, Beijing, 2001.

[4]     H. Baltruschat, Journal of the American Society for Mass Spectrometry 15:1693 (2004).

[5]     H. Wang, L. R. Alden, F. J. DiSalvo, and H. D. Abruna, Langmuir 25:7725 (2009).

[6]     H. Wang, Beijing Normal University, Beijing, 2001.

[7]     T. Löffler, in Institut für Physikalische und Theoretische Chemie, Universität Bonn, Bonn, 1997, p. 93.

[8]     H. Baltruschat, in Interfacial Electrochemistry (A. Wieckowski, ed.), Marcel Dekker, Inc., New York, Basel, 1999, p. 577

[9]     P. Atkins and J. de Paula, Atkins' Physical Chemistry, Oxford University Press Inc., New york, 2002.

[10]    M. Krausa and W. Vielstich, Journal of Electroanalytical Chemistry 399:7 (1995).

[11]    J. Willsau and J. Heitbaum, Electrochimica Acta 31:943 (1986).

[12]    T. Iwasita and W. Vielstich, Journal of Electroanalytical Chemistry 201:403 (1986).

[13]    T. Iwasita-Vielstich, in Advances in Electrochemical Science and Engineering, Vol. 1 (H. Gerischer and C. W. Tobias, eds.), VCH, Weinheim, New York, 1990, p. 127.

[14]    H. Wang, T. Löffler, and H. Baltruschat, Journal of Applied Electrochemistry 31:759 (2001).

[15]    W. Vielstich and X. H. Xia, Journal of Physical Chemistry 99:10421 (1995).

[16]    T. Iwasita, Electrochimica Acta 47:3663 (2002).

[17]    H. S. Wang, C. Wingender, H. Baltruschat, M. Lopez, and M. T. Reetz, Journal of Electroanalytical Chemistry 509:163 (2001).

[18]    Z. Jusys, J. Kaiser, and R. J. Behm, Langmuir 19:6759 (2003).

[19]    Y. E. Seidel, A. Schneider, Z. Jusys, B. Wickman, B. Kasemo, and R. J. Behm, Langmuir 26:3569 (2010).

[20]    B. Lanova, H. Wang, and H. Baltruschat, Fuel Cells 6:214 (2006).

[21]    T. Iwasita, W. Vielstich, and E. Santos, Journal of Electroanalytical Chemistry 229:367 (1987).

[22]    S. Wilhelm, T. Iwasita, and W. Vielstich, Journal of Electroanalytical Chemistry 238:383 (1987).

[23]    Y. X. Chen, A. Miki, S. Ye, H. Sakai, and M. Osawa, Journal of the American Chemical Society 125:3680 (2003).

[24]    M. Nakamura, K. Shibutani, and N. Hoshi, ChemPhysChem 8:1846 (2007).

[25]    K. Kunimatsu, H. Hanawa, H. Uchida, and M. Watanabe, Journal of Electroanalytical Chemistry 632:109 (2009).

[26]    K. Kunimatsu, W. G. Golden, H. Seki, and M. R. Philpott, Langmuir 1:245 (1985).

[27]    K. Kunimatsu, H. Seki, W. G. Golden, J. G. Gordon, and M. R. Philpott, Langmuir 2:464 (1986).

[28]    J. Lu and A. Bewick, Journal of Electroanalytical Chemistry 270:225 (1989).

[29]    A. Hamnett, Catalysis Today 38:445 (1997).

[30]    F. Seland, D. A. Harrington, and R. Tunold, Electrochimica Acta 52:773 (2006).

[31]    B. Lanova, in Institute für Physikalische und Theoretische Chemie, Abteilung Elektrochemie, Vol. Ph.D., Rheinische Friedrich-Wilhelms Universität Bonn, Germany, 2009.

[32]    B. E. Kumara Swamy and M. Schell, The Journal of Physical Chemistry B 110:5139 (2006).

[33]    M. Schell and B. E. Kumara Swamy, Journal of Electroanalytical Chemistry 584:157 (2005).

[34]    K.-I. Ota, Y. Nakagawa, and M. Takahashi, Journal of Electroanalytical Chemistry 179:179 (1984).

[35]    M. Krausa and W. Vielstich, Journal of Electroanalytical Chemistry 379:307 (1994).

[36]    S. C. S. Lai, N. P. Lebedeva, T. H. M. Housmans, and M. T. M. Koper, Topics in Catalysis 46:320 (2007).

[37]    K. Otsuka, T. Ina, and I. Yamanaka, Applied Catalysis A: General 247:219 (2003).

[38]    N. Nakagawa, K. Sekimoto, M. S. Masdar, and R. Noda, Journal of Power Sources 186:45 (2009).

[39]    A. R. Kucernak, G. T. Burstein, C. J. Barnett, and K. R. Williams, Electrochimica Acta 43:1705 (1998).

[40]    P. J. Barczuk, K. Miecznikowski, and P. J. Kulesza, Journal of Electroanalytical Chemistry 600:80 (2007).

[41]    J. Mostany, E. Herrero, J. M. Feliu, and J. Lipkowski, Journal of Physical Chemistry B. 106:12787 (2002).

[42]  V. Del Colle, A. Berna, G. Tremiliosi-Filho, E. Herrero, and J. M. Feliu, Physical Chemistry Chemical Physics 10:3766 (2008).

[43]  N. P. Lebedeva, M. T. M. Koper, E. Herrero, J. M. Feliu, and R. A. van Santen, Journal of Electroanalytical Chemistry 487:37 (2000).

[44]  H. Massong, S. Tillmann, T. Langkau, E. A. Abd El Meguid, and H. Baltruschat, Electrochimica Acta 44:1379 (1998).

[45]  H. Massong, H. S. Wang, G. Samjeske, and H. Baltruschat, Electrochimica Acta 46:701 (2000).

[46]  G. Samjeské, X.-Y. Xiao, and H. Baltruschat, Langmuir 18:4659 (2002).

[47]  H. A. Gasteiger, N. Markovic, P. N. Ross, and E. J. Cairns, Journal of Physical Chemistry 97:12020 (1993).

[48]  N. M. Markovic and P. N. Ross, Surface Science Reports 45:117 (2002).

[49]  A. Cuesta, Journal of the American Chemical Society 128:13332 (2006).

# Chapter 4: Electrooxidation of ethanol

## 4.1 Introduction

For fuel cell application, ethanol is a more attractive fuel than hydrogen and methanol because it is produced in a high quantity from biomass, easier to handle than hydrogen, less toxic than methanol and it has a high mass energy density. In all the papers cited in chapter 1 (section 1.5.4), in particular those on the effect of monoatomic steps, high concentrations of ethanol and a stagnant electrolyte were used. Whereas such conditions apply to practical conditions, this may lead to complications in the interpretation, when one is interested in the main fundamental questions: slow follow up reactions cannot be separated from the initial process, and poison formation becomes more important at high concentrations. In this chapter, the catalytic activity of Pt stepped single crystals and polycrystalline platinum towards ethanol oxidation (10 mM) was studied under controlled convection similar to practical conditions. DEMS was used for a semi-quantitative analysis of the volatile products formed during the electrochemical reaction and for an estimate of the current efficiency. Also the effect of Ru decorating the Pt step sites on ethanol oxidation was investigated.

## 4.2 Results and discussion

### 4.2.1 Electrooxidation of bulk ethanol on Pt(Pc)

#### *4.2.1.1 Effect of supporting electrolyte*
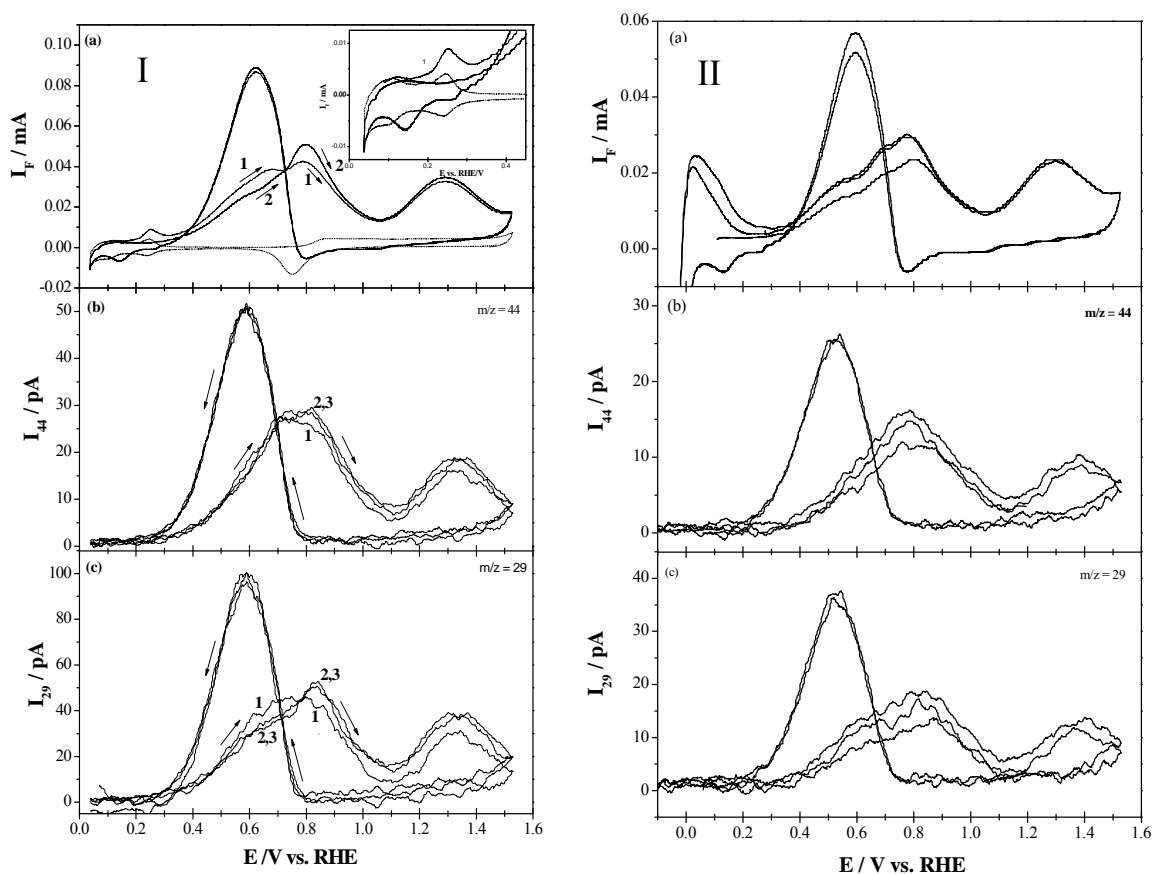


Figure 4-1: Simultaneously recorded CV (a) and MSCV for m/z = 44 (b) and m/z = 29 (c) during the electrooxidation of bulk ethanol on smooth polycrystalline platinum in (I) 0.01 M ethanol + 0.1 M $H_2SO_4$ + 0.5 M $HClO_4$ solution and (II) 0.01 M ethanol + 0.5 M $H_2SO_4$ solution. Scan rate: 10 mV $s^{-1}$. Electrolyte flow rate: 5 μL $s^{-1}$. 3 cycles are shown. Dashed line: CV in supporting electrolyte. Inset: Expanded view of faradaic current in the $H_{ads}/H_{des}$ region.

Figure 4-1 shows the cyclic voltammograms for the electrooxidation of 0.01 M ethanol on polycrystalline platinum and the corresponding mass spectrometric cyclic voltammograms (MSCV) for m/z = 44 ($CH_3CHO$ + $CO_2$) and m/z = 29 (acetaldehyde) at flow rate 5 μL $s^{-1}$. In the first anodic sweep in the cyclic voltammogram (Inset of Fig. 4-

90

1a), the faradaic current starts to increase at 100 mV with a peak at 250 mV. The height of this peak is higher than that of hydrogen desorption peak in supporting electrolyte and the corresponding ionic current is not observed. This current may be due to the adsorption of ethanol on Pt surface in that potential range or due to the overlapping between the hydrogen desorption and ethanol adsorpate currents. The onset of the oxidation at about 300 mV is followed by two peaks at 0.65 V and 0.8 V and a third anodic peak in the oxygen region at 1.3 V [1, 2]. During the cathodic sweep, an oxidation peak is present at 0.6 V after the complete desorption of oxygen from the Pt surface.

In the second sweep the hydrogen desorption peak is suppressed due to the blocking of Pt-surface by the adsorbed intermediates formed in the preceding cathodic sweep. The first anodic peak is also decreased because of these adsorbates, which are only oxidized at higher potentials.

Figure 4-1.I(b and c) show the mass spectrometric cyclic voltammetry of ionic signals of m/z = 44 and m/z = 29. The shape of the ionic signal for mass 29 is similar to the faradaic current for both the first and subsequent sweeps. This means that the current efficiencies for the production of acetaldehyde during ethanol oxidation at polycrystalline Pt is independent of the applied potential and it is produced over the whole potential range. Also, the ionic signal of mass 44 follows the ionic signal of mass 29 in the third anodic peak. However, at the first faradaic peak at 0.6 V, both the faradaic current and the ionic peak of mass 29 are lower than that in the second peak at 0.8 V, whereas, the ionic peak of mass 44 is higher. At 0.8 V the ion current for m/z = 44 is that expected for the molecular peak of acetaldehyde ($I_{44} \approx 55\%$ of $I_{29}$ as shown in acetaldehyde spectrum in Fig. 4-2). However, at 0.6 V, the ion current of m/z = 44 obviously is higher, and a part of this current is due to the formation of $CO_2$. Thus, the main product at 0.8 V is acetaldehyde, but at 0.6 V there is some amount of $CO_2$ produced from the oxidation of adsorbed species like $CO_{ad}$ resulting from the breaking of C–C bond at low potential (E < 0.5 V) [3].
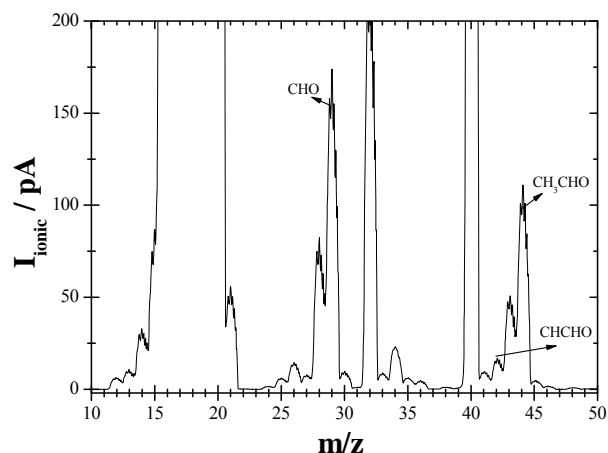
Figure 4-2: Mass spectrum of the acetaldehyde in DEMS under experimental conditions.

In order to study the effect of the supporting electrolyte, the electrooxidation of 0.01 M ethanol was performed at polycrystalline Pt in 0.5 M $H_2SO_4$ (Fig. 4-1.II) under the same conditions as Fig. 4-1.I. The general behaviour of CV and MSCVs of masses 44 and 29 are typical to that in perchloric acid and sulphuric acid electrolyte but the faradaic and ionic currents are two-fold lower than that in Fig. 4-1.I.

The reduction in the Pt activity towards ethanol electrooxidation in the presence of high concentration of sulphuric acid is due to the specific adsorption of sulfate and bisulfate at the Pt surface. The inhibition effect of sulfate was investigated at basal plane Pt using FTIR by Iwasita et al. [4]. They concluded that sulfate has an ability to attain the maximum coordination. Sulfate has a triple coordination at Pt(111) and double coordination at Pt(100) and Pt(110).

### 4.2.1.2 Electrooxidation of deuterated ethanol

In order to better distinguish between $CO_2$ and fragments of acetaldehyde, $d_6$-ethanol was used. The most abundant fragment of $d_4$-acetaldehyde is then CDO at m/z = 30. On m/z = 44 there is a contribution of $C_2D_2O$ which should have an intensity of 7% of that of the m/z = 30 signal. ($C_2H_2O$ has an abundance of 7% of the m/z = 29 signal in the case of $h_4$-acetaldehyde).

Figure 4-3 shows the CV and MSCV of mass 44 ($C_2D_2O + CO_2$) and m/z = 30 (CDO of $d_4$-acetaldehyde) for the electrooxidation of $d_6$-ethanol on polycrystalline Pt at flow

rate 5 μL s$^{-1}$. The CV is similar to that of Fig. 4-1a, but all currents are nearly two times lower than that of normal ethanol due to the kinetic isotope effect.

The shape of ionic signals for m/z = 30 is similar to that for m/z = 29 in Fig. 4-1. In the anodic sweep, the ion current for m/z = 44, however, is drastically decreased at 0.6 V and only shows a peak at 0.8 V.
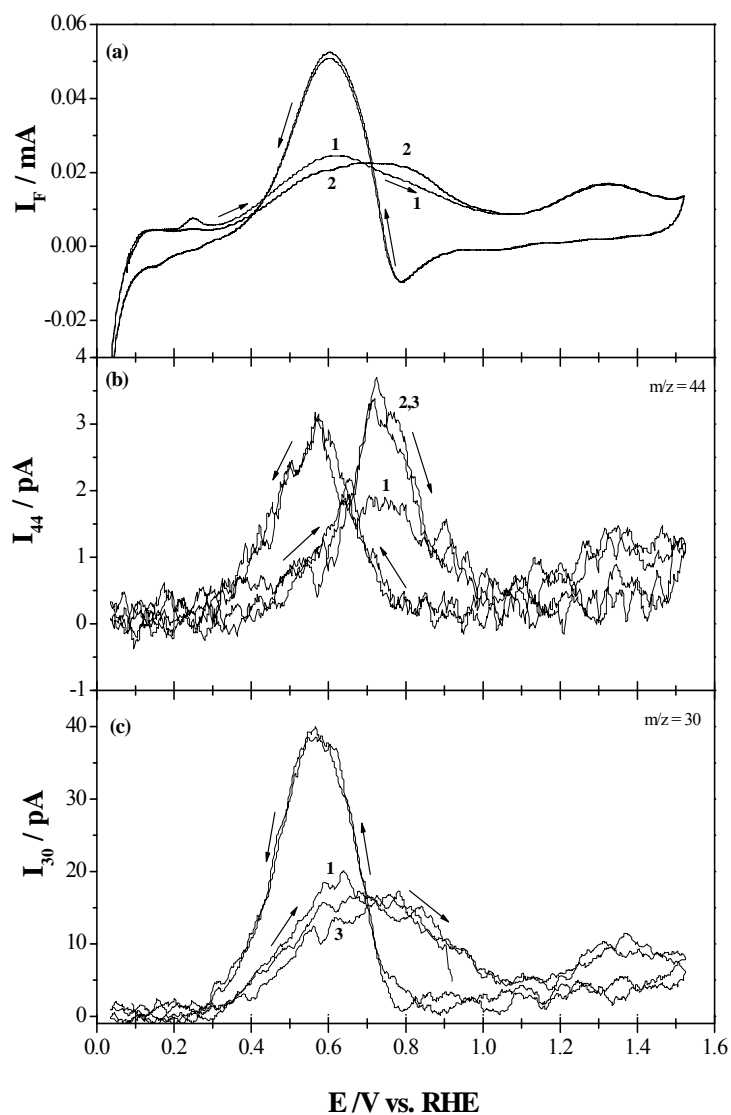


Figure 4-3: Simultaneously recorded CV (a) and MSCV for m/z = 44 (b) and m/z = 30 (c) during the electrooxidation of bulk d$_6$-ethanol on smooth polycrystalline platinum in 0.01M d$_6$-ethanol + 0.1 M H$_2$SO$_4$ + 0.5 M HClO$_4$ solution. Scan rate: 10 mV s$^{-1}$. Electrolyte flow rate: 5 μL s$^{-1}$. 3 cycles are shown.

93

Table 4-1: The current efficiencies with respect to $CO_2$ during the electrooxidation of bulk $d_6$-ethanol on smooth polycrystalline platinum in 0.01 M $d_6$-ethanol + 0.1 M $H_2SO_4$ + 0.5M $HClO_4$ solution at different flow rate and peak potential. Scan rate 10 mV s$^{-1}$.

| u / µL s$^{-1}$ | $E_{peak}$ / V vs. RHE | 1st cycle | | | | 2nd cycle | | | |
|---|---|---|---|---|---|---|---|---|---|
| | | $I_F$ / mA | $I_{44}$ / pA | $A_{30}\%$ | $A_{44}\%$ | $I_F$ / mA | $A_{30}\%$ | $I_{44}$ / pA | $A_{44}\%$ |
| 1.6 | 0.6$^a$ | 0.023 | 0.78 | 114 | 0 | 0.018 | 139 | 1.5 | 4 |
| | 0.8$^a$ | 0.016 | 1.6 | 130 | 4 | 0.019 | 114 | 3.5 | 15 |
| | 1.3$^a$ | 0.016 | 1 | 111 | 0 | 0.016 | 119 | 1.3 | 8 |
| | 0.62$^c$ | 0.045 | 2.3 | 134 | 0 | 0.045 | 131 | 3.2 | 0 |
| 5 | 0.6$^a$ | 0.024 | 1.5 | 230 | 1 | 0.021 | 263 | 1.8 | 5 |
| | 0.8$^a$ | 0.018 | 1.6 | 270 | 4 | 0.022 | 250 | 3 | 13 |
| | 1.3$^a$ | 0.017 | 1.4 | 237 | 5 | 0.017 | 214 | 1.3 | 6 |
| | 0.62$^c$ | 0.051 | 3.1 | 283 | 0 | 0.053 | 247 | 3.1 | 0 |

a: anodic   c: cathodic

In the oxidation peak during the cathodic sweep, the ion current for m/z = 44 is 7% of that for m/z = 30 and thus results from acetaldehyde. In the first anodic sweep, the ion current for m/z = 44 is 10% of that for m/z = 30, in the subsequent sweeps even 20% at 0.8 V. The higher ionic current of m/z = 44 in the second and third sweep as compared to that in the first sweep above 0.7 V is due to the oxidation of adsorbed intermediate which were formed in the previous sweeps. The summary of these results in Table 4-1 shows that current efficiencies for $CO_2$ are negligible in the first sweep; higher efficiencies in the second sweep are due to these adsorbed intermediates.

### 4.2.1.3 Potential hold experiments

These experiments were done to determine exactly the current efficiency of acetaldehyde formed during oxidation of ethanol in order to circumvent the problem of the dual thin layer flow through cell. In the potential hold experiments, first the potential was swept in positive direction starting from 50 mV and the potential was held at $E_1$ for 2 min, then the potential was swept again in negative and positive direction to oxidize the

formed adsorbates, then it was held again at $E_2 > E_1$ for 2 min. This procedure was repeated in the potential hold range of 0.3 to 0.9 V as shown in Fig. 4-4. The faradaic and ionic currents did not decrease with time due to the higher degree of poisoning formed during the previous CVs.
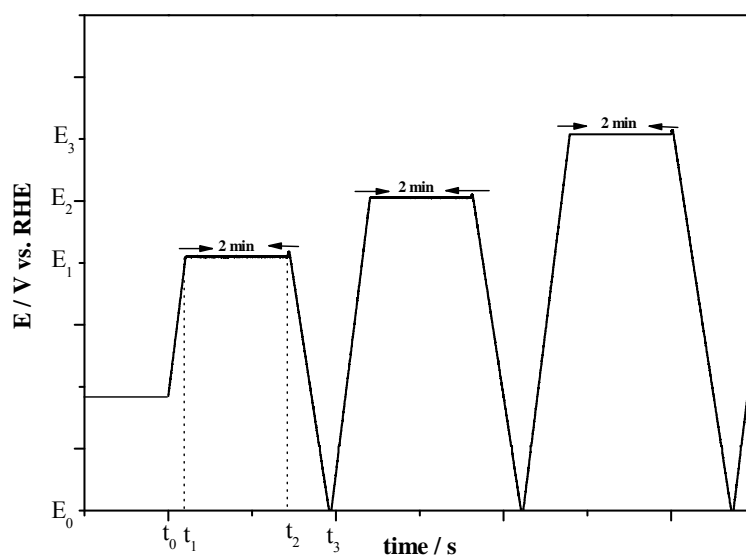


Figure 4-4: The potential program for potential hold experiments.

Approximate calibration for acetaldehyde was achieved using different concentrations of acetaldehyde solutions in the range of 0.1 mM to 5 mM and monitored the ionic signal of masses 15, 29 and 44 for each concentration for different flow rates. The ion currents were plotted vs. the acetaldehyde concentration. The slope of the linear relationship is the calibration constant ($°K_{29}$) which includes all the DEMS parameters.

$$I_{29} = °K_{29} \, [\text{Acetaldehyde}] \tag{1}$$

A double logarithmic plot showed that the slope ($°K_{29}$) depends on the electrolyte flow rate (u) according to $°K_{29} \propto u^{0.3}$ suggesting diffusion limitation to the Teflon membrane [5].

The faradaic current is given by the sum of the oxidation current to the various product species.

$$I_F = I_F^{CO_2} + I_F^{ald} + I_F^{acac} \tag{2}$$

The current efficiency of $CO_2$ was calculated as shown before in chapter 3 and for acetaldehyde ($A_{29}\%$) was calculated according to equation 1 and the following equations:

$$I_F^{29} = (\frac{I_{29}}{{}^{\circ}K_{29}})zFu \qquad\qquad (3)$$

$$A_{29} = \frac{I_F^{29}}{I_F} \qquad\qquad (4)$$

Here, u is the flow rate in L s$^{-1}$ and F is the faradaic constant in C mol$^{-1}$

The apparent current efficiencies of acetaldehyde are similar to those calculated in potential step experiments (next section) at 1.6 and 5 µL s$^{-1}$ as shown in Table 4-2.

Table 4-2: The current efficiency with respect to acetaldehyde during the electrooxidation of ethanol at different flow rate in potential hold experiments.

| $E_{hold}$ / V vs. RHE | 1.6 µL s$^{-1}$ (0.5 M $H_2SO_4$) | | 5 µL s$^{-1}$ (0.5 M $H_2SO_4$ + 0.5 M $HClO_4$) | |
|---|---|---|---|---|
| | $I_f$ / mA | $A_{29}\%$ | $I_f$ / mA | $A_{29}\%$ |
| 0.5 | 0.0045 | 120 | 0.0117 | n.d. |
| 0.6 | 0.019 | 112 | 0.0237 | 310 |
| 0.7 | 0.0283 | 122 | 0.032 | 296 |
| 0.8 | 0.0227 | 111 | 0.0275 | 269 |
| 0.9 | 0.00855 | 108 | n.d. | n.d. |

### 4.2.1.4 Potential step experiments

Figure 4-5 shows a typical potential step experiment for d$_6$-ethanol at smooth poly-crystalline platinum in 0.01 M d$_6$-ethanol + 0.1 M $H_2SO_4$ + 0.5 M $HClO_4$ solution. The potential was stepped from 0.05 to 0.7 V and the faradaic current and the corresponding mass spectrometric currents of m/z = 30 (acetaldehyde-CDO) and m/z = 44 ($C_2D_2O$ + $CO_2$) were simultaneously recorded.

The apparent current efficiencies for acetaldehyde and $CO_2$ which were formed during the potential step experiments at different applied potentials and two different flow rates are presented in Table 4-3. Again, in the cyclic voltammetry experiments, the ion

current for m/z = 44 is approximately 7% of that for m/z = 30, and therefore due to the acetaldehyde fragment, the corrected current efficiency for $CO_2$ is in the range of 1% and therefore does not exceed the error which originates from noise and the necessity to correct for the contribution of acetaldehyde on m/z = 44.
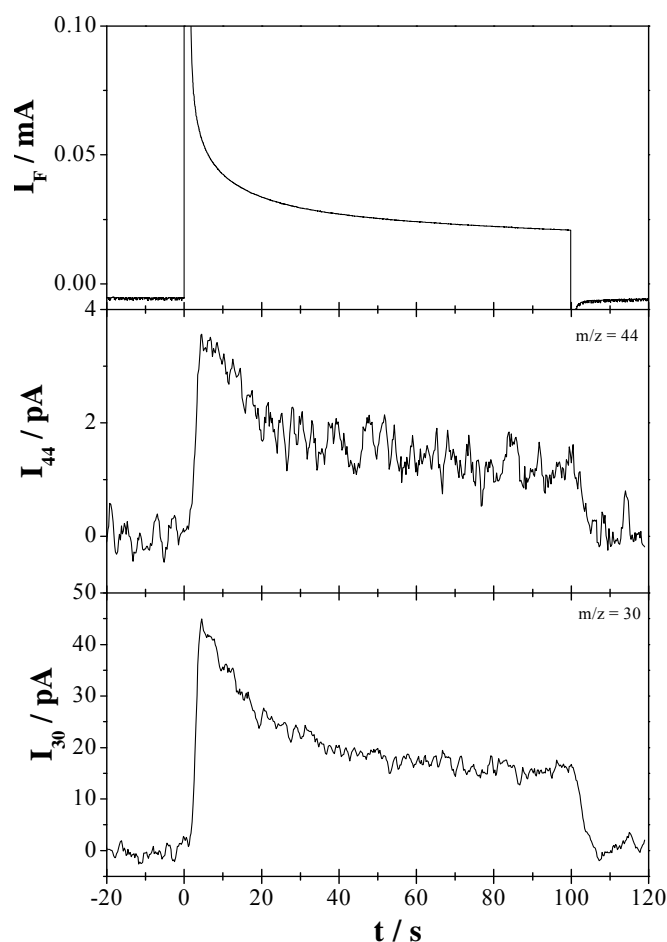


Figure 4-5: Simultaneously recorded faradaic current and ionic current for m/z = 44 and m/z = 30 during potential step experiment at 0.7 V for $d_6$-ethanol on smooth polycrystalline Pt in 0.01 M $d_6$-ethanol + 0.1 M $H_2SO_4$ + 0.5 M $HClO_4$ solution. Electrolyte flow rate: 5 $\mu$L s$^{-1}$.

The apparent current efficiencies for acetaldehyde are all larger than the maximum possible value of 100%. These too high values are due to the incomplete mixing between the first thin layer compartment and the detection compartment [5]. A volume element of

the electrolyte which is close to electrode in the first compartment and therefore containing a high acetaldehyde concentration will be closest to the Teflon membrane in the detection compartment. Calibration, however, is done with a solution in which the concentration is identical everywhere at the entrance of the detection compartment. Correspondingly the apparent current efficiency increases with flow rate due to the smaller residence time of the electrolyte in the capillaries.

Table 4-3: The apparent current efficiencies for $CO_2$ and acetaldehyde during the potential step experiment of bulk 0.01 M $d_6$-ethanol and 0.01 M $h_6$-ethanol on smooth polycrystalline platinum in 0.1 M $H_2SO_4$ + 0.5 M $HClO_4$ solution at different flow rate and adsorption potential.

| u / μL s$^{-1}$ | E$_{ad}$ /V vs. RHE | CD$_3$CD$_2$OD | | CH$_3$CH$_2$OH | |
|---|---|---|---|---|---|
| | | A$_{44}$% | A$_{30}$% | A$_{44}$% | A$_{29}$% |
| 1.6 | 0.6 | 0 | 120 | 0 | 113 |
| | 0.7 | 0.2 | 70 | 0 | 104 |
| | 0.8 | 0.5 | 116 | 0 | 103 |
| 5 | 0.6 | 0 | 245 | 0 | 260 |
| | 0.7 | 0 | 250 | 0 | 236 |
| | 0.8 | 0 | 177 | 0 | 250 |

From the characterization of a dual thin layer cell a flow rate dependant measurements with $Fe^{2+}/Fe^{3+}$, CO and $H_2$ [6], it is roughly expected an ionic current which is too large by a factor of 1.4 at a flow rate of 1.6 μL s$^{-1}$; this factor should increase with $\sqrt{u}$, and therefore we expect for a true current efficiency of 100% an apparent current efficiency of ≈ 120% at 1.6 μL s$^{-1}$ and 250% at 5 μL s$^{-1}$, in rough agreement with values of Table 4-3. (This incomplete mixing is not a problem for $CO_2$, because calibration is also done with $CO_2$ formed at the electrode surface, i.e. under condition of incomplete mixing). Therefore, the current efficiency for the formation of acetaldehyde on polycrystalline Pt is roughly 100% is concluded, i.e. the amount of acetic acid is negligible under convective conditions in the flow through cell.

### 4.2.2 Ethanol adsorbate species

#### *4.2.2.1 Oxidation of ethanol adsorbate*

What are the steady state coverages with adsorbed intermediates? After recording current transients such as those shown in Fig. 4-5, during which ethanol was allowed to adsorb at different applied potential of adsorption for two minutes, an electrolyte exchange with the supporting electrolyte was performed and the potential was swept in positive direction (Fig. 4-6a). $CO_2$ is formed at a potential where usually $CO_{ad}$ is oxidized. In the experiments of Fig. 4-6b, where deuterated ethanol is used, there are two separated peaks (Fig. 4-6b); the peak around 0.8 V again is typical for $CO_{ad}$ ($\alpha$-carbon).
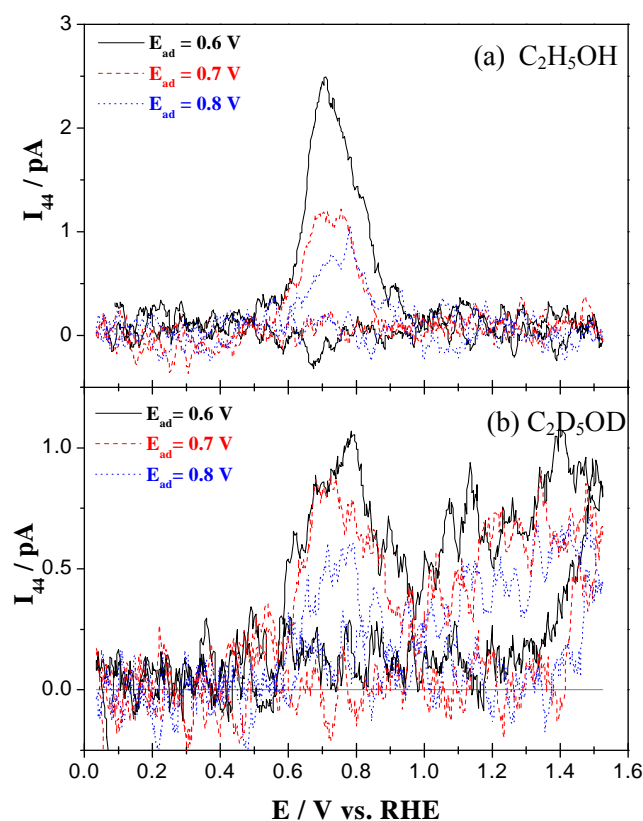


Figure 4-6: The recorded MSCVs for m/z = 44 during the electrooxidation of pre-adsorbed ethanol (a) and $d_6$-ethanol (b) after a potential step experiment at different potential on smooth polycrystalline Pt in 0.1 M $H_2SO_4$ + 0.5 M $HClO_4$ solution. Electrolyte flow rate: 1.6 $\mu$L s$^{-1}$.

At more positive potentials, i.e. in the oxygen region, where typically hydrocarbons are oxidized, the formation of $CO_2$ signifies that the carbon atom from the methyl group (β-carbon) is only oxidized in this potential region. These data confirm the previous results of the formation of $CH_x$ species as adsorbate [3, 7], which recently also was identified by SERS on Pt electrodeposited on Au electrodes [8].

Important is the fact, that some of the methyl groups are oxidized to adsorbed CO. This is probably a slow follow up reaction from $CH_x$ to CO, as indicated in the reaction scheme in Fig. 4-7. Only in the case of deuterated ethanol, the $CD_x$ species is not oxidized faster than it is formed (due to the kinetic isotope effect), whereas the oxidation of $CH_x$ species to $CO_{ad}$ is faster than its formation at the chosen condition.

Therefore, in the case of deuterated ethanol, the steady state coverage with $CD_x$ may well be higher than that of $CO_{ad}$.

$$CH_3CH_2OH \xrightarrow{\phantom{xx}k_{ad}\phantom{xx}} CO_{ad} + CH_{x,ad} \xrightarrow[k_{CO}]{} CO_2$$

with $k_{CH}$ loop from $CH_{x,ad}$ back.
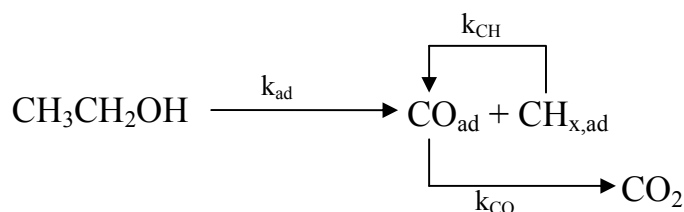
Figure 4-7: Schematic pathways for the oxidation of adsorbed ethanol.

### 4.2.2.2 Reduction of ethanol adsorbate

The adsorbed methyl group may be reduced to methane in the negative going sweep or oxidized at higher potential to $CO_2$. Fig. 4-8 shows first the reduction of pre-adsorbed ethanol at 0.3 V on Pt(332) to methane (m/z = 15) during the negative going sweep to –0.1 V, implying that the $CH_x$ species can be reduced to $CH_4$ at sufficient negative potential. On the other hand, the transformation of the rest of $CH_x$ species into $CO_{ad}$ takes place only at potential higher than 0.5 V during the positive going sweep [3, 9].
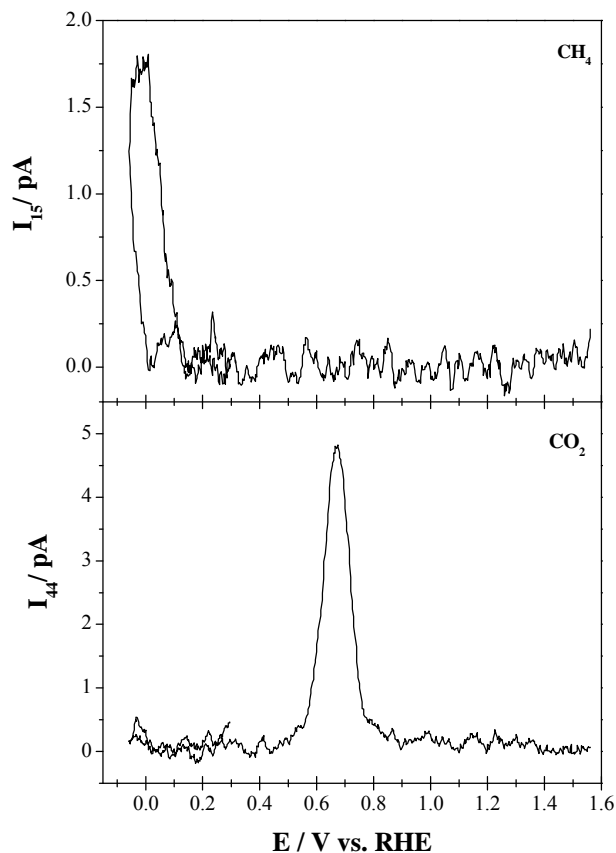
Figure 4-8: The recorded MSCVs for m/z = 15(methane) and 44($CO_2$) during the electrooxidation of pre-adsorbed ethanol at 0.3 on Pt(332) in 0.1 M $H_2SO_4$ + 0.5 M $HClO_4$ solution. Electrolyte flow rate: 5 $\mu$L $s^{-1}$. Negative going sweep followed by positive going sweep.

Figure 4-9 shows the summary of ethanol adsorbate oxidation-reduction pathways dependence on the applied potential: the adsorption of the ethanol molecule occurs at potentials as low as 0.5 V and creates two adsorbates: $-CH_2OH$ ($\alpha$–carbon) and $-CH_3$ ($\beta$–carbon). The $\alpha$–carbon adsorbate is immediately transformed to $CO_{ad}$ that is further oxidize at 0.7 V to carbon dioxide. Whereas the transformation of the $\beta$–carbon adsorbate to $CO_{ad}$ occurs slowly at 0.7 V then oxidize to $CO_2$ or directly oxidize to $CO_2$ in the hydrocarbon oxidation region potential. At potential lower than 0.2 V, the $\beta$–carbon adsorbate will be reduced to methane.

101
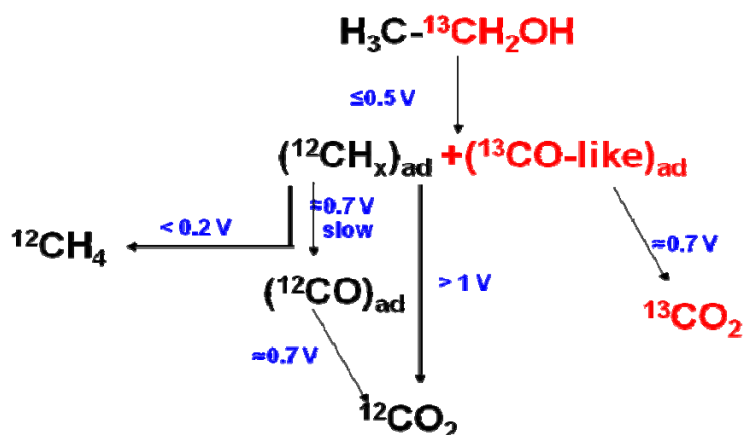
Figure 4-9: The reaction scheme for ethanol adsorbate at Pt surface [3, 9].

### 4.2.2.3 Coverage of ethanol adsorbate

After the electrooxidation of adsorbed species from ethanol and deuterated ethanol on polycrystalline platinum, the total coverage of these adsorbed species was determined. The coverage of adsorbed species is dependent on the flow rate and the adsorbed potential. The amount of $CO_{ad}$ decreases with increasing potential from 8% to 5% in the case of $h_6$-ethanol (cf. Table 4-4a) and from 5% to 2.5% for $d_6$-ethanol and hardly depends on the flow rate (1.6 and 5 $\mu L\ s^{-1}$) (cf. Table 4-4b). This is as expected because the adsorption potential is in the region of the oxidation peak of $CO_{ad}$. The amount of $CD_x$, oxidized above 1 V, is around 10% and not influenced by the adsorption potential.

Table 4-4a: Influence of adsorption potential and flow rate on the coverage of ethanol at polycrystalline Pt. Adsorption of ethanol was done in 0.01 M $C_2H_5OH$ + 0.1 M $H_2SO_4$ + 0.5 M $HClO_4$ solution.

| Ethanol | $E_{ads}$ / V | 1.6 µL s$^{-1}$ | | 5 µL s$^{-1}$ | |
|---|---|---|---|---|---|
| | | $Q_{CO_2}$ / mC | $\theta_{CO}$ | $Q_{CO_2}$ / mC | $\theta_{CO}$ |
| | 0.6 | $3.5\times10^{-8}$ | 8.4 | $2.85\times10^{-8}$ | 7.3 |
| | 0.7 | $2.11\times10^{-8}$ | 5.1 | $1.5\times10^{-8}$ | 3.8 |
| | 0.8 | $2\times10^{-8}$ | 4.8 | $1.2\times10^{-8}$ | 3.1 |

Table 4-4b: Influence of adsorption potential and flow rate on the coverage of $d_6$-ethanol at polycrystalline Pt. Adsorption of $d_6$-ethanol was done in 0.01 M $C_2D_5OD$ + 0.1 M $H_2SO_4$ + 0.5 M $HClO_4$ solution.

| $d_6$-ethanol | $E_{ads}$ / V | 1.6 µLs$^{-1}$ (0-1 V) | | 5 µLs$^{-1}$ | | 1.6 µLs$^{-1}$ (1-1.5 V) | | 5 µLs$^{-1}$ (1-1.5 V) | |
|---|---|---|---|---|---|---|---|---|---|
| | | $Q_{CO_2}$ / mC | $\theta_{CO}$ | $Q_{CO_2}$ / mC | $\theta_{CO}$ | $Q_{CO_2}$ / mC | $\theta_{CO}$ | $Q_{CO_2}$ / mC | $\theta_{CO}$ |
| | 0.6 | $2.3\times10^{-8}$ | 5.2 | $1.25\times10^{-8}$ | 3 | $4.3\times10^{-8}$ | 9.7 | $3.6\times10^{-8}$ | 9 |
| | 0.7 | $2.4\times10^{-8}$ | 2.3 | $7.87\times10^{-9}$ | 2 | $2.8\times10^{-8}$ | 6.3 | $3.7\times10^{-8}$ | 9 |
| | 0.8 | $1.1\times10^{-8}$ | 2.5 | $6.4\times10^{-9}$ | 1.6 | $3.37\times10^{-8}$ | 7.6 | $3.93\times10^{-8}$ | 9.8 |

## 4.2.3 Effect of surface structure

Figure 4-10 shows a comparison of the CVs of the electrooxidation of 0.01 M ethanol at different Pt-single crystals. It is observed that the Pt(111) surface is catalytically un-reactive towards ethanol oxidation, but with increasing the step density from 20% [Pt(332)] to 50% [Pt(331)] the electrocatalytic activity increased as reported before in literature [10]. It is clear from the CVs that the maximum faradaic current of Pt(331) is two-fold higher than that of Pt(332) which has a similar activity as the polycrystalline Pt (cf. Fig. 4-1). In addition, the onset of peak potential of ethanol oxidation shifts towards less positive potential with increasing the step density of Pt-surfaces. So, the presence of

free step sites on Pt(111) is very necessary for ethanol adsorption and oxidation processes at the surfaces.

For Pt(19 1 1) = Pt(s)[10(100)x(111)], the onset oxidation potential is nearly 300 mV higher than that of Pt(332). Such a higher onset potential as compared to polycrystalline Pt or surfaces vicinal to the (111) plane has been noted before for the Pt(100) surface and ascribed to the ability of (100) surface to support the formation of carbon monoxide and other partial oxidation species as strongly adsorbates [11-13].
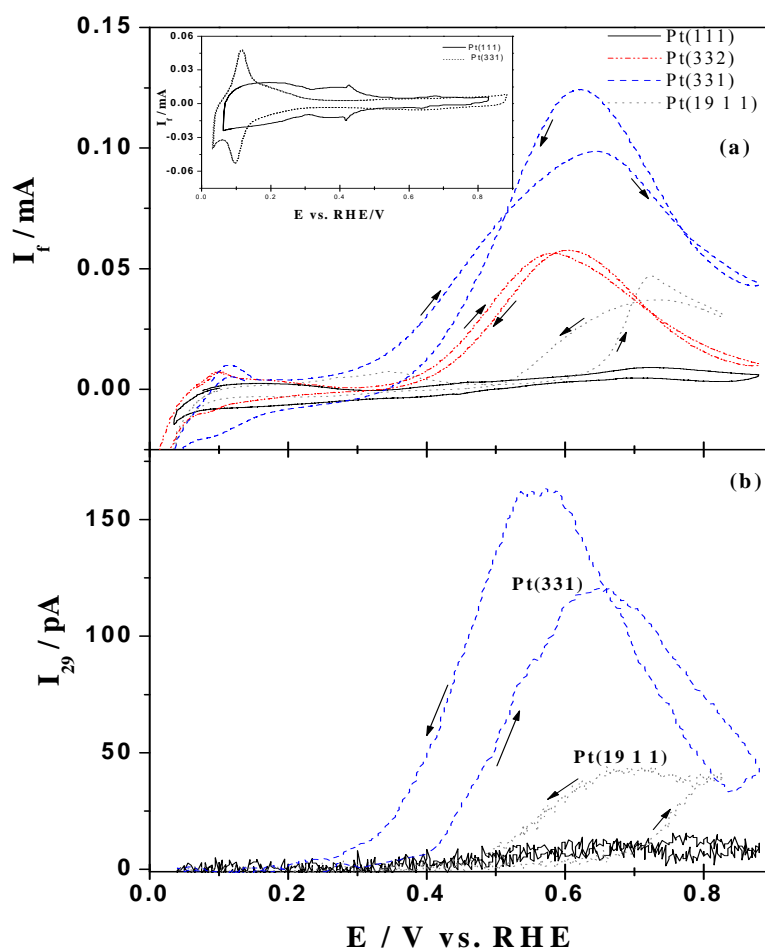


Figure 4-10: Simultaneously recorded CV (a) and MSCV for m/z = 29 (b) during the electrooxidation of bulk ethanol on smooth Pt(111), Pt(332), Pt(331) and Pt(19 1 1) in 0.01 M ethanol + 0.1 M $H_2SO_4$ + 0.5 M $HClO_4$ solution. Scan rate: 10 mV $s^{-1}$. Electrolyte flow rate: 5 µL $s^{-1}$. First CV is shown. Inset: typical CVs for Pt(111) and Pt(331) in supporting electrolyte in DEMS cell.

Fig. 4-11 shows the CV and the corresponding MSCVs for m/z = 29 and 44 during the electrooxidation of ethanol at a Pt(332) electrode.
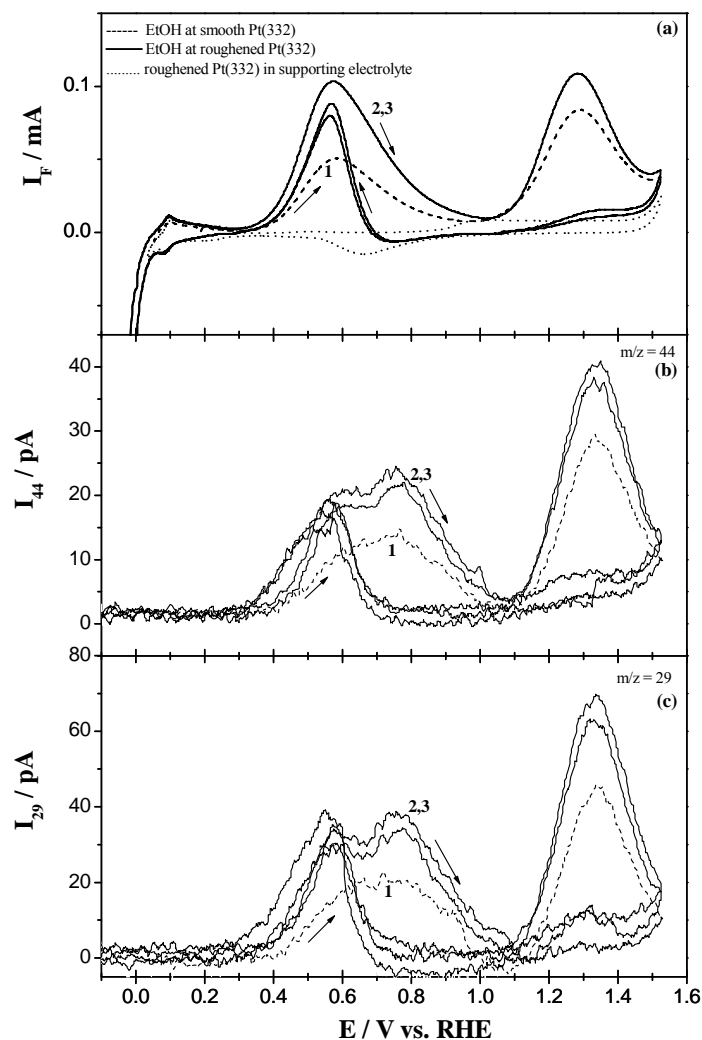


Figure 4-11: Simultaneously recorded CV (a) and MSCV for m/z = 44 (b) and m/z = 29 (c) during the electrooxidation of bulk ethanol on Pt(332) in 0.01 M ethanol + 0.5 M $HClO_4$ + 0.1 M $H_2SO_4$ solution. Scan rate: 10 mV s$^{-1}$. Electrolyte flow rate: 5 μL s$^{-1}$. Dashed line: first sweep to 1.5 V, corresponding to the smooth Pt(332), solid line: roughened Pt(332) and dotted line: roughened Pt(332) in supporting electrolyte.

Clearly, the oxidation rate increases after the first extension of the sweep into the oxygen region due to the introduction of defects into the surface. Whereas the activity of the smooth Pt(332) comparable to that of the polycrystalline surface, after roughening it

105

is twice as high. Differently from the case of the polycrystalline electrode (Fig. 4-1), there is only one peak in the CV at 0.6 V (where there is only a shoulder at polycrystalline Pt); the peak at 0.8 V is missing in the CV, but present in the MSCVs. Obviously, at 0.6 V an oxidation reaction is taking place that does not lead to acetaldehyde. The asymmetric shape of the current peak at 0.6 V may signify that it contains a small peak at 0.8 V. The identical shape of the ion currents as well as the value of the ion current ratio signifies that there is no appreciable formation of $CO_2$. Therefore, the only possible oxidation product formed at 0.6 V is acetic acid.

Also, the corresponding experiment with deuterated ethanol (Fig. 4-12) which shows a better distinction of $CO_2$ and acetaldehyde does not reveal any features of $CO_2$ except for the first sweep into the oxygen region.

In Fig. 4-12 the ion currents for both m/z = 44 and m/z = 30 closely follow the faradaic current with a two-fold increase in the 2$^{nd}$ sweep, i.e. after roughening. However, in the oxygen region, the ion current for acetaldehyde is lower than one would expect from the faradaic current, which is twice as large as that at 0.6 V. This points to an additional formation of acetic acid. The difference to the above result with non deuterated ethanol is due to the fact that the higher electrolytes flow rate was used there, resulting in a lower time constant for detection, and also due to the kinetic isotope effect.

Similar experiments with a Pt(111) electrode showed that the activity is negligible in the first sweep (cf. Fig. 4-13). After several extensions of the potential into the oxygen region and the corresponding roughening, the shape of the CV and of the MSCVs for m/z = 29 and m/z = 44 were qualitatively similar to that of Fig. 4-11. However, after only one potential sweep into the oxygen region, two peaks are clearly resolved in the faradaic current, only the second of which corresponds to formation of acetaldehyde. The amount of acetaldehyde formed at 0.6 V, however increases with roughening. This is similar to the case of the Pt(331) (Fig. 4-14), where also only after roughening a peak of acetaldehyde is clearly visible around 0.6 V; before roughening, only its width suggests that also some acetaldehyde is formed at 0.6 V at this highly stepped surface.
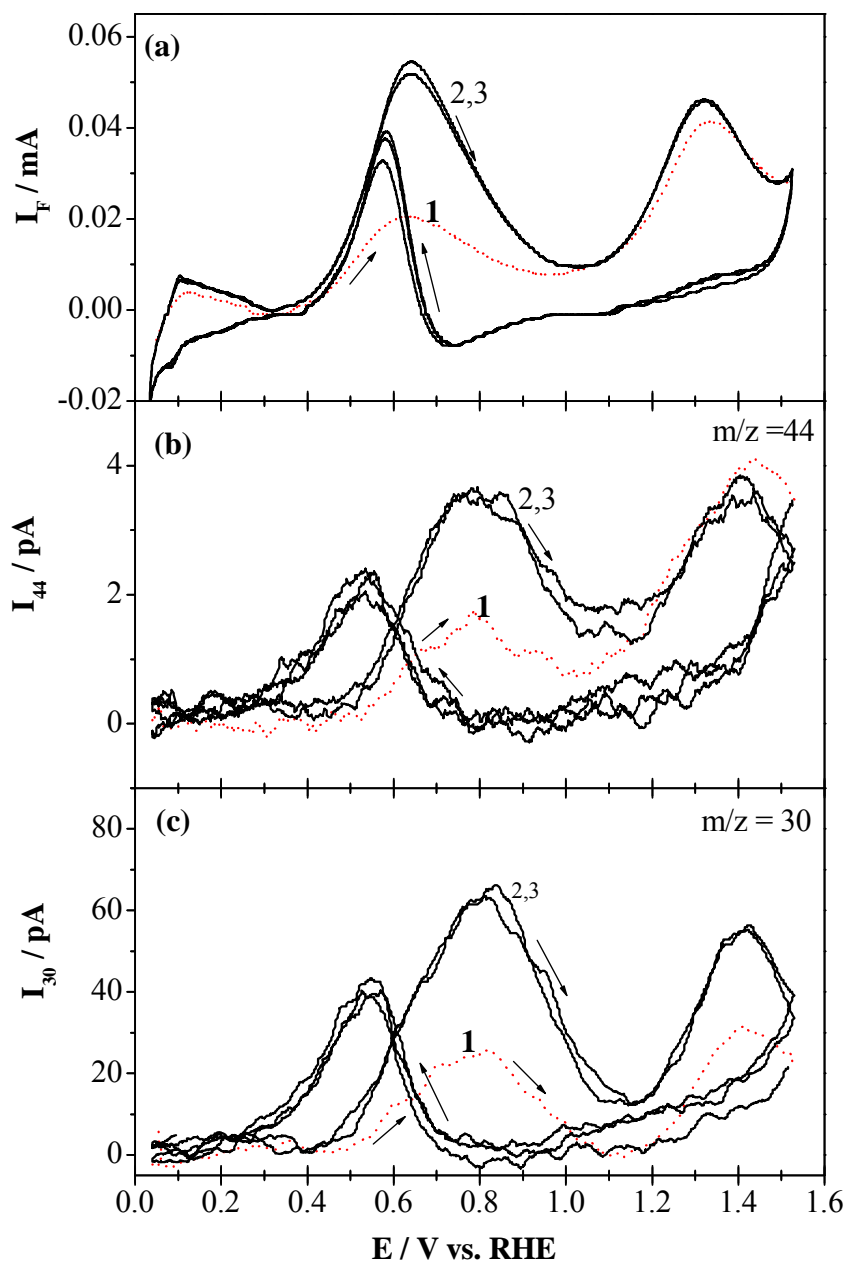
Figure 4-12: Simultaneously recorded CV (a) and MSCV for m/z = 44 ($CD_2O + CO_2$) (b) and MSCV m/z = 30 (CDO) (c) during the electrooxidation of bulk $d_6$-ethanol on smooth Pt(332) in 0.01 M $d_6$-ethanol + 0.1 M $H_2SO_4$ + 0.5 M $HClO_4$ solution. Scan rate: 10 mV $s^{-1}$. Electrolyte flow rate: 1.6 µL $s^{-1}$, dotted line: first sweep to 1.5 V, corresponding to the smooth Pt(332) and solid line: roughened Pt(332).
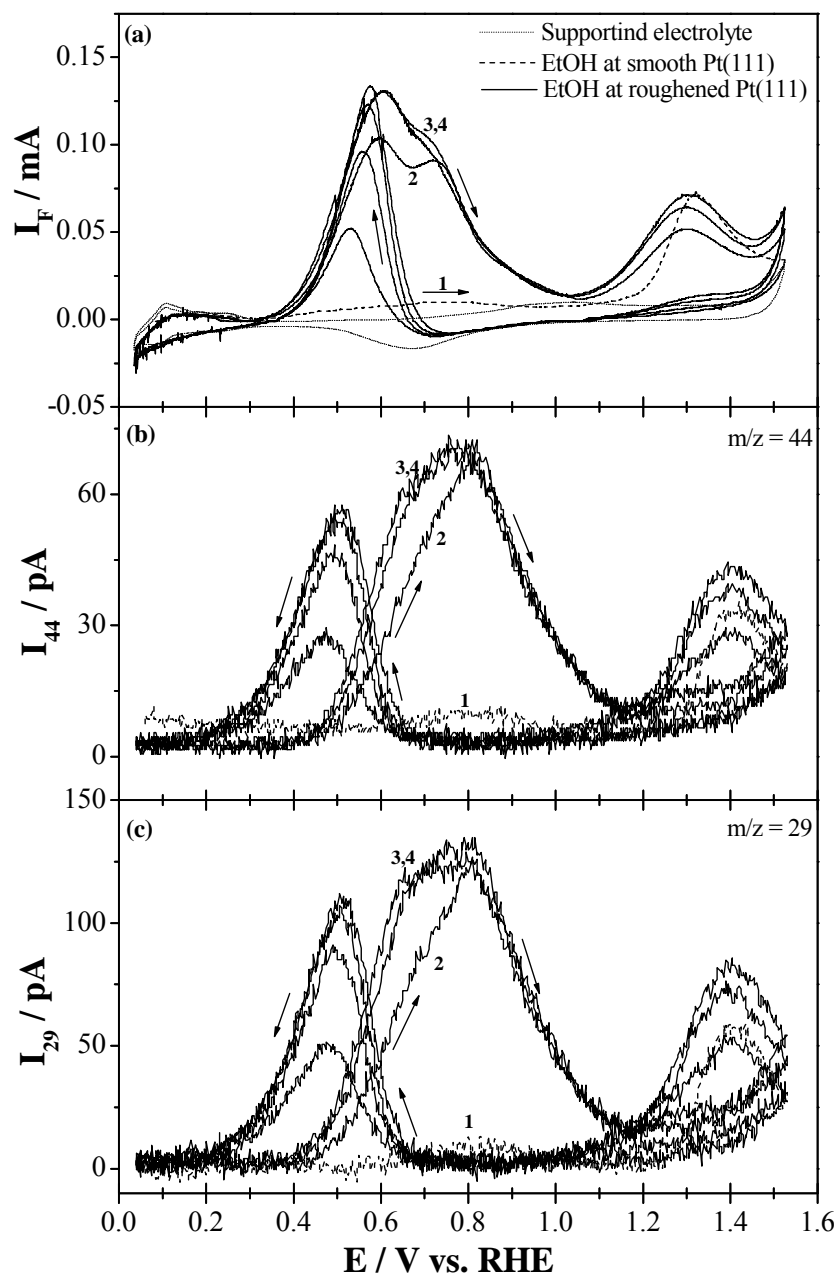
Figure 4-13: Simultaneously recorded CV (a) and MSCV for m/z = 44 (b) and MSCV m/z = 29 (c) during the electrooxidation of bulk ethanol on Pt(111) in 0.01 M ethanol + 0.1 M $H_2SO_4$ + 0.5 M $HClO_4$ solution. Scan rate: 10 mV $s^{-1}$. Electrolyte flow rate: 1.6 µL $s^{-1}$. Dashed line: first sweep to 1.5 V, corresponding to the smooth Pt(111), solid line: roughened Pt(111) and dotted line: roughened Pt(111) in supporting electrolyte.
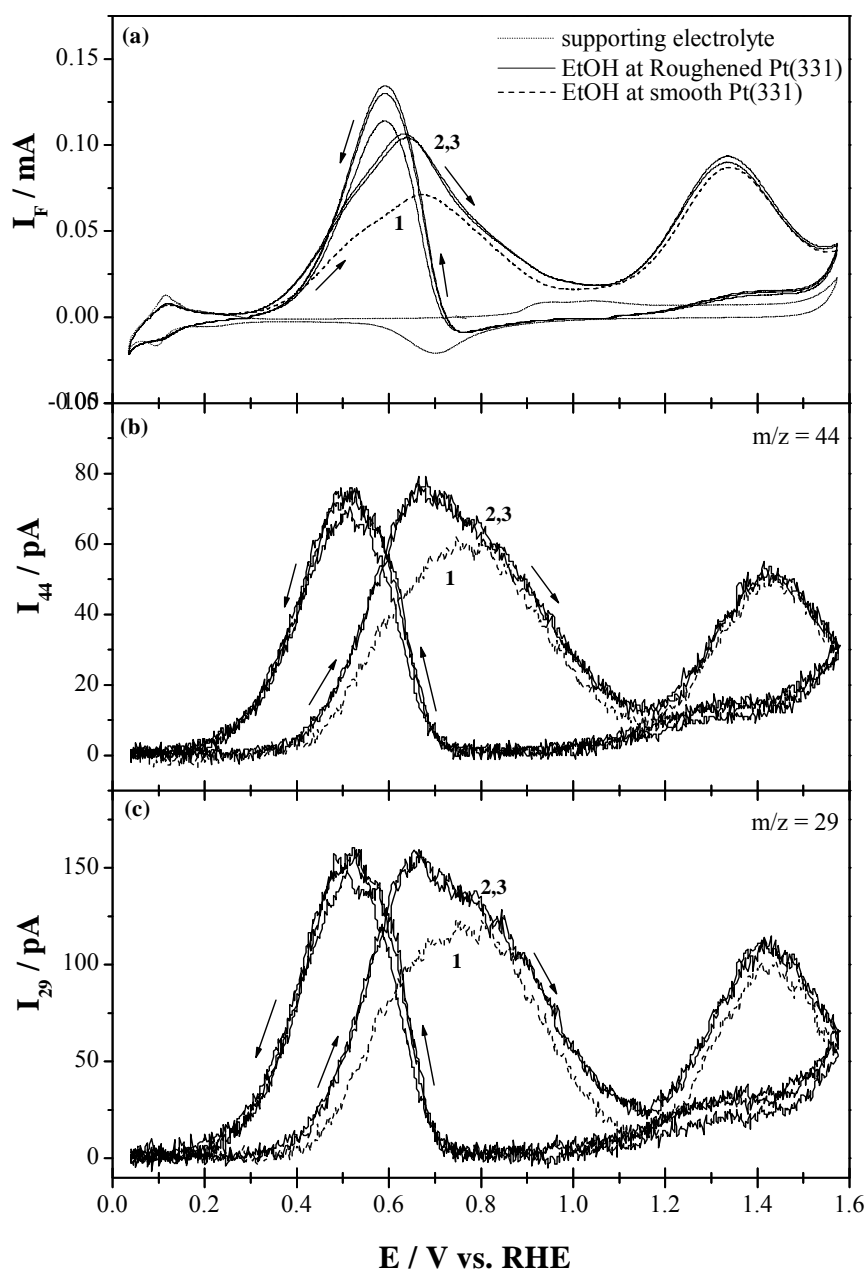
Figure 4-14: Simultaneously recorded CV (a) and MSCV for m/z = 44 (b) and MSCV m/z = 29 (c) during the electrooxidation of bulk ethanol on Pt(331) in 0.01 M ethanol + 0.1 M $H_2SO_4$ + 0.5 M $HClO_4$ solution. Scan rate: 10 mV s$^{-1}$. Electrolyte flow rate: 1.6 μL s$^{-1}$. Dashed line: first sweep to 1.5 V, corresponding to the smooth Pt(331), solid line: roughened Pt(331) and dotted line: roughened Pt(331) in supporting electrolyte.
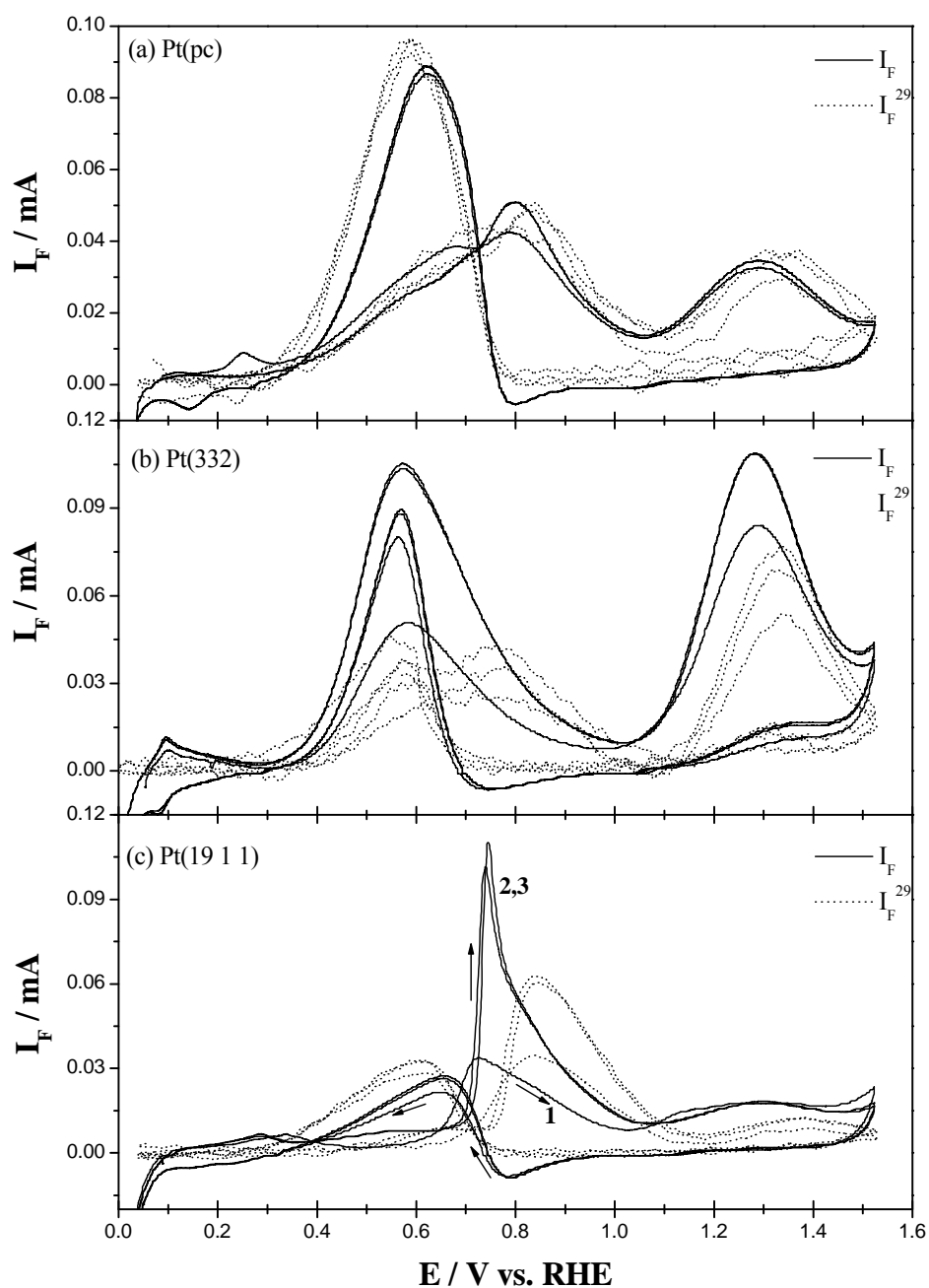
Figure 4-15: Comparison of the faradaic-current (solid line) with the corresponding ion current (dotted line) for acetaldehyde after conversion to faradaic current units on poly-crystalline Pt (a), Pt(332) (b) and Pt(19 1 1) (c) in 0.01 M ethanol + 0.1 M $H_2SO_4$ + 0.5 M $HClO_4$ solution. Scan rate: 10 mV s$^{-1}$. Electrolyte flow rate: 5 µL s$^{-1}$.

The amount of acetic acid cannot be directly determined by DEMS, but it can be estimated indirectly from the amount of acetaldehyde. On polycrystalline Pt, the apparent current efficiencies of 120% from the ion current at flow rate of 1.6 $\mu$L s$^{-1}$ corresponding to a true current efficiency of 100% was calculated (cf. the discussion of the Table 4-3).

Figure 4-15 shows the ion currents for m/z = 29 after conversion to faradaic current values, plotted together with the faradaic current. On polycrystalline Pt, both curves closely overlap. On Pt(332) however, where the same conversion factor was used, the current due to the formation of acetaldehyde is lower than the faradaic current. Only at around 0.8 V, both currents are similar. In spite of some incertitude in the calibration factor, it is clear that the true current efficiency cannot exceed 100%. Obviously, in the current peak another product is formed.

Since the ion current for m/z = 44 closely follows that of acetaldehyde and is mainly determined by acetaldehyde, $CO_2$ cannot be the origin of this discrepancy. Rather, acetic acid is formed in the current peak, but no more at higher potentials. Certainly, it is somewhat astonishing that the product with the higher oxidation state is formed at a lower potential than that with the lower oxidation state. But it has to be kept in mind that also at the higher potentials acetaldehyde cannot be oxidized further in a follow up reaction if there is strong convection that leads to a fast transport away from the electrode. Therefore, the formation of acetic acid seems to be due to a direct reaction at the electrode surface without acetaldehyde as an intermediate. In Fig. 4-15c, the preliminary results for Pt(19 1 1) again using the same conversion factor for the ion current are shown. Oxidation only starts above 0.6 V (cf. Fig. 4-10), which is much more positive than on the other surfaces. Only after roughening by the potential extension into the oxygen region, a small oxidation current becomes visible around 0.5 V. The steep increase in oxidation rate at 0.7 V renders a comparison to the ion current difficult because of the slow response of the ion current. The charges under the peaks of the faradaic current and the converted ion current are identical also for the second sweep. Therefore, on this surface only acetaldehyde is formed and no acetic acid. These results are summarized in the reaction scheme shown in Fig. 4-16a.

Hence, the adsorbed CO and $CH_x$ species is formed from an adsorbed acetyl species, as suggested before for the adsorption of ethene [3, 14, 15]
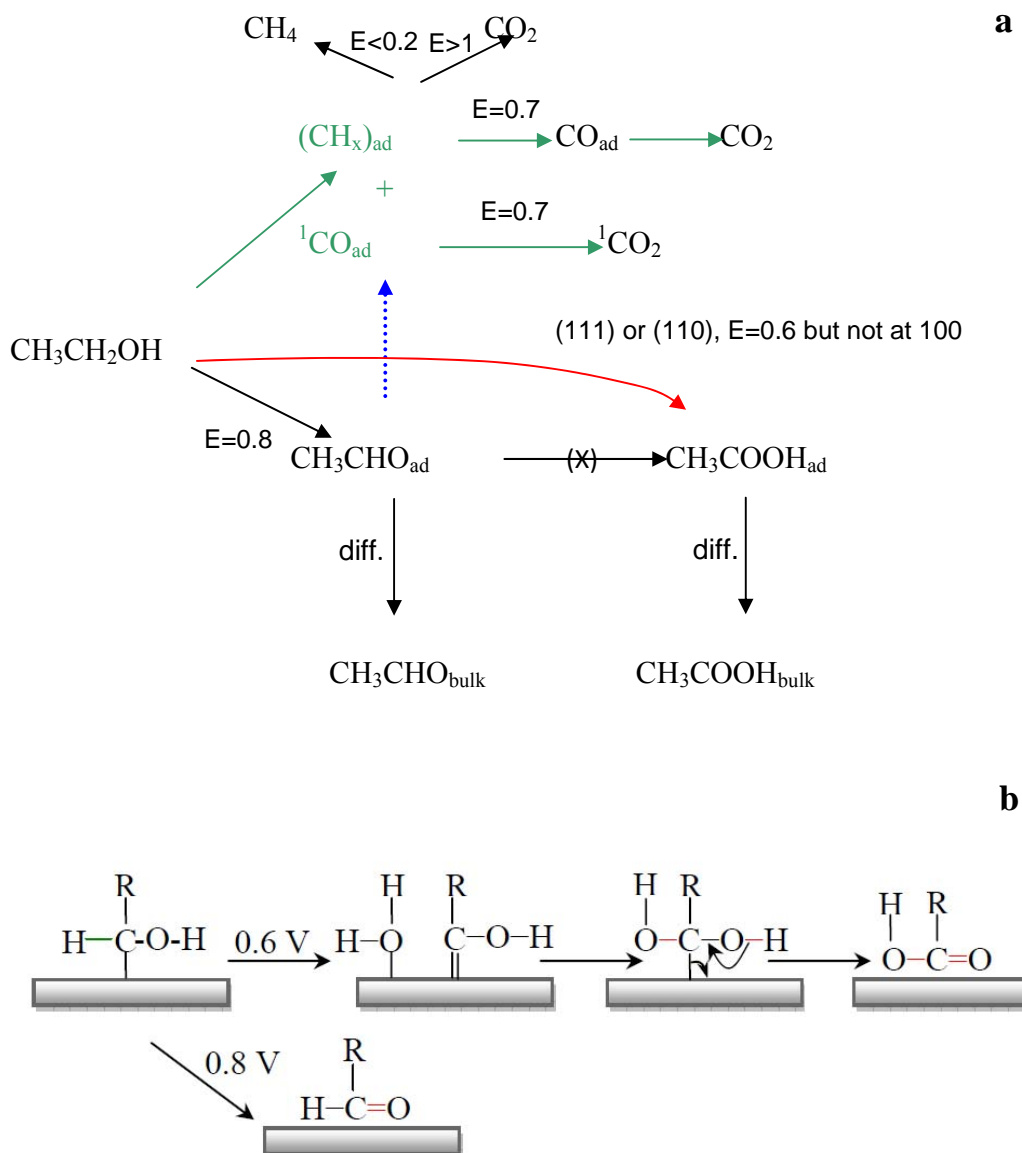
Figure 4-16: (a) Schematic pathways for ethanol oxidation. (b) Schematic mechanism for acetic acid formation during ethanol electrooxidation.

From the crystal structure dependence, the following points are concluded:

- The reactivity of Pt(111) is extremely low and probably is completely determined by defects.

- At stepped surfaces with (111) terraces, the reactivity is largely determined by the step density. A reaction channel directly leading to acetic acid is available at these surfaces, but only at potentials around and below 0.6 V. At higher potentials, (around 0.8 V) acetaldehyde is formed, which, under the convection flow conditions, does not react further because transport away from the electrode is faster. The reaction channel leading to acetic acid requires both step sites and (111) terraces, because it is absent at polycrystalline Pt and Pt(19 1 1). Whereas the reaction leading to acetaldehyde is a simple dehydrogenation, the formation of acetic acid involves also a reaction with ad-sorbed oxygen or OH from water (cf the mechanism in Fig. 4-16b). Although at first sight one might assume that the availability of surface bound OH or activated water increases with potential, this is not true for the surfaces considered here. (bi)sulphate adsorption takes place in the potential range below 0.6 V at the (111) terraces and is completed between 0.6 and 0.7 V. Therefore, the adsorption of an activated water or hydroxide species might be impeded this way. Acetate formed as an intermediate is similarly strongly adsorbed and might block the surface above a potential of 0.7 V. Above this potential, therefore, terraces are blocked (making further oxidation slower than diffusion away from the surface) and only dehydrogenation may take place at step sites. Below this potential, dehydrogenation also takes place at step sites, and a further reaction to acetic acid is possible after a (admittedly speculative) spill over to the terraces sites.

- At Pt(19 1 1), oxidation only starts around 0.7 V. Whether this is due to an inherently lower reactivity at 100 surfaces remains to be shown, it may also be due to a faster poisoning of this surface by intermediates. Comparison to a Pt(100) under similar conditions will be necessary.

- Oxidation at the polycrystalline surface starts at the same potential as at the Pt(332) surface, but only leads to acetaldehyde, Obviously, (111) terraces are a prerequisite for the fast formation of acetic acid.

## 4.2.4 Effect of Ru
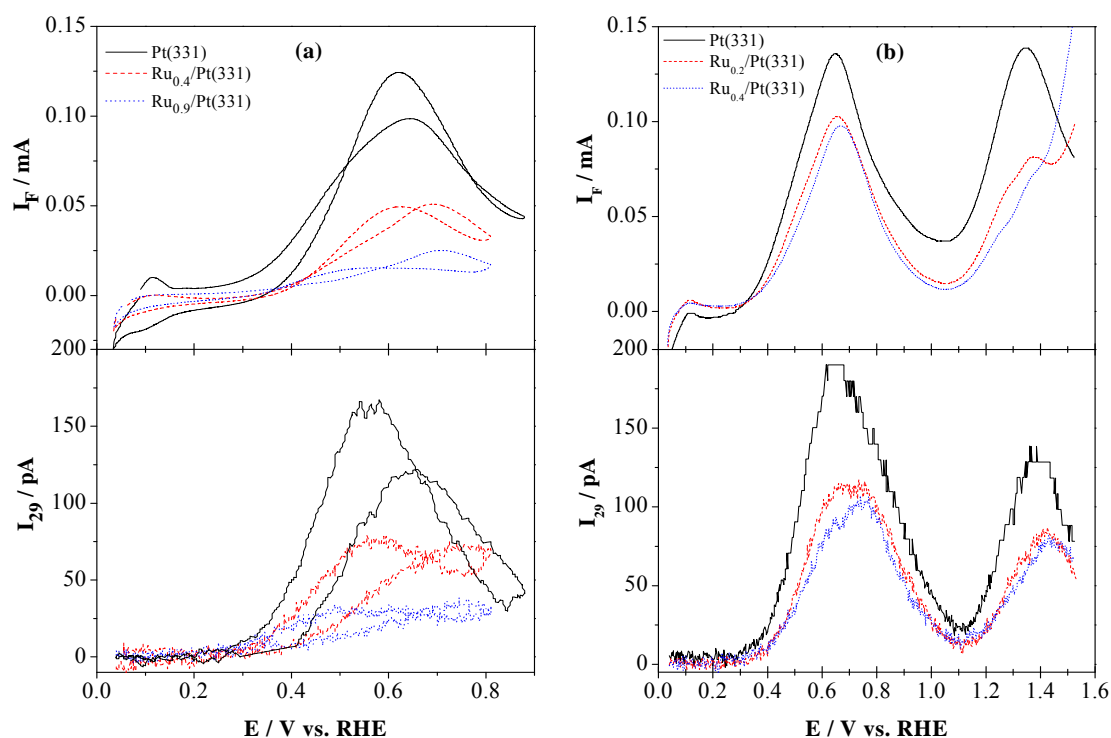


Figure 4-17: Simultaneously recorded CV and MSCV for m/z = 29 during the electrooxidation of bulk ethanol on (a) smooth Pt(331) and Ru modified Pt(331) (b) roughened Ru-modified Pt(331) in 0.01 M ethanol + 0.1 M $H_2SO_4$ + 0.5 M $HClO_4$ solution. Scan rate: 10 mV $s^{-1}$. Electrolyte flow rate: 5 µL $s^{-1}$.

The faradaic current and the ionic current of m/z = 29 during the electrooxidation of ethanol on Ru-modified Pt(331)- with  half coverage of the step sites- is half of that on Ru-free Pt(331) as shown in Fig. 4-17. This signifies that the free step sites at Pt(331) are very significant for the initial adsorption and oxidation processes for ethanol oxidation. Decorating 40% (corresponding to total Ru coverage of 20%) of the step sites by Ru leads to blocking of these active sites on the surface and inhibits the ethanol oxidation. Upon further deposition of Ru on the step sites until the full coverage, the electrocatalytic activity towards ethanol oxidation decreases considerably.

114
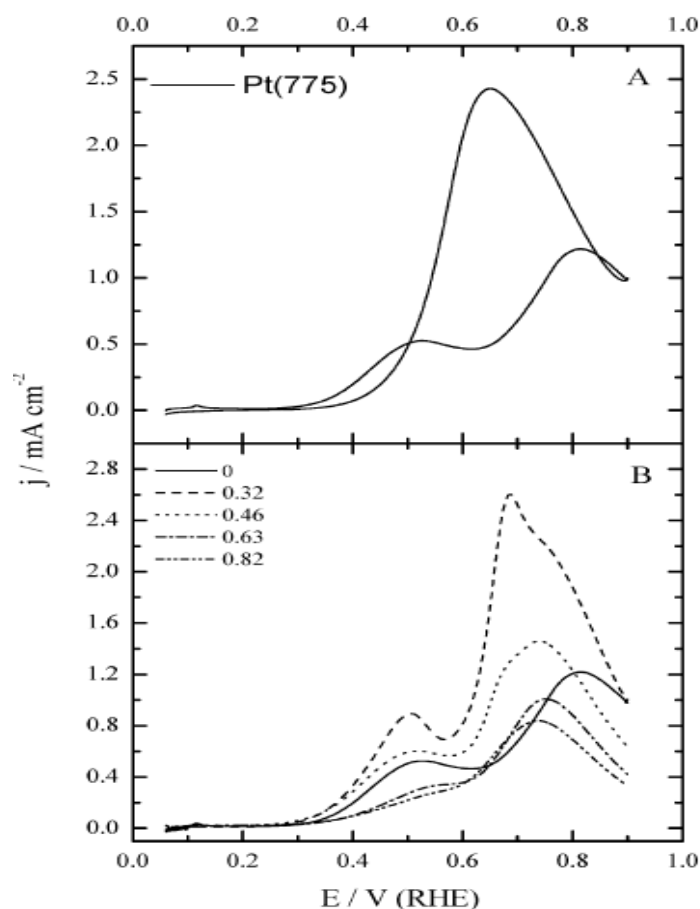
Figure 4-18: (A) Voltammetric profile for the Pt(775) electrode in 0.1 M $C_2H_5OH$ + 0.1 M $H_2SO_4$. (B) Positive going scan for the Pt(775) electrode in 0.5 M $C_2H_5OH$ + 0.1 M $H_2SO_4$ with different Ru coverages on the step. Scan rate: 50 mV $s^{-1}$. Reprinted from ref. [16].

Complete step decoration leads to a nearly complete suppression of the electrocatalytic activity since key sites (step sites) for ethanol oxidation is blocked by ruthenium, in agreement with results of Feliu and co-workers [16]. However, differently from the present results an increase in reactivity towards ethanol oxidation at Pt(775) had been found when steps were covered by 46% Ru as shown in Fig. 4-18. This difference could be due to the difference in step density (terraces width) and the stagnant electrolyte due to which the slow oxidation of acetaldehyde is possible; its oxidation might be catalyzed more by Ru.

## 4.3 Conclusions

Under flow through conditions, at polycrystalline Pt the only oxidation product of ethanol is acetaldehyde. The same is true for single crystal surfaces with (100) terraces; at these however; the onset potential is considerably shifted to positive potentials. At stepped surfaces with (111) terraces, at the onset of oxidation acetic acid is directly formed. At more positive potentials, acetaldehyde is the only oxidation product also at these surfaces, possibly because adsorbed anions (sulfate or the acetate ion) prohibit reaction of an ethanol oxidation intermediate with a second oxygen species. The question remains why at polycrystalline Pt "only" acetaldehyde is formed at low potentials. Obviously (111) sites are necessary for this reaction to occur directly at the surface (and not only via a slow further oxidation step of dissolved acetaldehyde).

For fuel cell applications, the formation of acetic acid is a dead end, because of its inertness. C–C bond splitting is necessary to form $CO_2$ (and thus get the maximum number of electrons out of one ethanol molecule). This might be easier achieved from acetaldehyde [8, 10], therefore, acetic acid formation should be avoided. Since nanoparticles consist to a large degree of (111) facets, this effect of direct acetic acid formation may also play a role in practical applications, i.e. fuel cells. Whether this effect is responsible for the high current efficiency for acetic acid of 70% at such carbon supported catalysts (as compared to nearly 30% for acetaldehyde) remains to be shown [2].

Ru as a co-catalyst, up to a surface composition of 40%, usually increases the reactivity also for ethanol oxidation [16, 17]. In the case of step decoration, however, the effect of blocking the reactive step sites seems to be larger than the co-catalytic effect. Already at a coverage of 20% (corresponding to a step decoration of 40%) the reactivity is considerably decreased.

## References:

[1]    G. A. Camara and T. Iwasita, Journal of Electroanalytical Chemistry 578:315 (2005).

[2]    H. Wang, Z. Jusys, and R. J. Behm, Journal of Physical Chemistry B 108:19413 (2004).

[3]    U. Schmiemann, U. Müller, and H. Baltruschat, Electrochimica Acta 40:99 (1995).

[4]    T. Iwasita and A. R. F.C. Nart, E. Pastor, M. Weber, Electrochimica Acta 40:53 (1995).

[5]    H. Baltruschat, Journal of the American Society for Mass Spectrometry 15:1693 (2004).

[6]    H. Wang, Vol. PhD, Beijing Normal University, Beijing, 2001.

[7]    T. Iwasita and E. Pastor, Electrochimica Acta 39:531 (1994).

[8]    S. C. S. Lai, S. E. F. Kleyn, V. Rosca, and M. T. M. Koper, The Journal of Physical Chemistry C 112:19080 (2008).

[9]    J. Souza-Garcia, E. Herrero, and J. M. Feliu, Chemphyschem 11:1391 (2010).

[10]   S. C. S. Lai and M. T. M. Koper, Faraday Discussions 140:399 (2008).

[11]   S.-C. Chang, L.-W. H. Leung, and M. J. Weaver, Journal of Physical Chemistry 94:6013 (1990).

[12]   D. J. Tarnowski and C. Korzeniewski, Journal of Physical Chemistry B 101:253 (1997).

[13]   F. Colmati, G. Tremiliosi-Filho, E. R. Gonzalez, A. Berna, E. Herrero, and J. M. Feliu, Faraday Discussions 140:379 (2008).

[14]   T. Löffler, R. Bussar, X. Xiao, S. Ernst, and H. Baltruschat, Journal of Electroanalytical Chemistry 629:1 (2009).

[15]   T. Löffler and H. Baltruschat, Journal of Electroanalytical Chemistry 554-555:333 (2003).

[16]   V. Del Colle, A. Berna, G. Tremiliosi-Filho, E. Herrero, and J. M. Feliu, Physical Chemistry Chemical Physics 10:3766 (2008).

[17]   N. Fujiwara, K. A. Friedrich, and U. Stimming, Journal of Electroanalytical Chemistry 472:120 (1999).

## **Chapter 5: Cu UPD at Ru quasi single crystal**

## **5.1 Introduction**

Ruthenium is a metal of considerable importance, in electrocatalysis and electrochemical technology because of its specific catalytic properties [1]. The cheapest and most convenient method - flame annealing and cooling down in argon/hydrogen atmosphere or quenching process, successfully used to handle platinum [2], Iridium [3], gold [4], silver [5], rhodium [6] and palladium [7]  single crystal electrodes - does not work for massive ruthenium electrodes, because they are rapidly oxidized by atmospheric oxygen even at high temperature. In UHV, after cleaning by cycles of Ar-ion bombardment and high temperature annealing e.g. by resistive heating to temperatures above 1500 K and cooling, it is possible to reproducibly prepare clean, well-defined and ordered oxygen-free Ru surfaces, which can be used as electrodes after clean transfer in an electrochemical cell [8-11]. El-Aziz and Kibler [12] recently reported that the inductive heating to prepare the Ru(0001) single crystal in an argon stream gives more reproducible results while being simpler to use than the heating in a hydrogen furnace. Recently, Attard et al. [13] found that it is possible to prepare quasi single crystalline Ru films on Pt(111), Pt(100) and stepped single crystal surfaces vicinal to these planes by resistive heating of Ru deposited on Pt single crystal surfaces in a nitrogen atmosphere. For Ru-films prepared on a Pt(111) single crystal electrode, voltammetric peaks are similar to those reported for single crystal Ru(0001) electrodes. The advantage of this new preparation procedure for electrocatalytic studies is that the well-established preparation methods for Pt single crystals can be used to prepare defined Ru surfaces. Unfortunately, until now there is still a lack of information concerning the surface structure of these very interesting quasi single crystalline electrode surfaces, which are also attractive model systems for catalytic studies, especially when modified by Pt.

This chapter aims at obtaining some information about the surface structure by Cu UPD. A further question is whether step decoration occurs, i.e. will the Cu UPD start at steps or at terraces?. On stepped Pt surfaces vicinal to (111) terraces, Cu is preferentially

deposited at steps sites [14]. Recently Francke et al. found that on surfaces with (100) oriented terraces Cu is preferentially deposited at the terrace [15]. In the present study, Cu UPD as a tool for characterization of Ru-film surfaces is explored. More interesting is the study of the stepped surfaces because of their importance for fundamental electrocatalytic studies. Different behaviour for Cu stripping from terrace and step sites is expected, as observed before on stepped Pt single crystals [14, 15]. To my knowledge, there are only a few articles concerning electrochemical copper deposition on bulk Ru surfaces, despite of its importance in the damascene process [16-20]. Electrochemical Cu UPD on polycrystalline Ru in sulphuric acid was first reported in 1983 by Barbier et al. [21]. Gonzales Tejera et al. [22] investigated the influence of the upper potential limit and chloride anions on the Cu UPD. They found that extending the upper potential to high potential limit, i.e. with increasing the amount of the oxide at the surface, the peak potential of Cu UPD peak shifts to less negative values and the amount of Cu deposit decreases. They also found that the presence of chloride seemed to have an inhibitive effect on Cu UPD due to the strong adsorption of chloride. To my knowledge there are only a few papers that report electrochemical Cu UPD on Ru(0001) single crystals. EC-UHV transfer experiments for Cu UPD on Ru(0001) were performed by Stuve et al. [23, 24]. They studied the surface both with cyclic voltammetry and in UHV with AES and thermal desorption spectroscopy (TDS). Comparison of UHV and electrochemically deposited Cu in perchloric acid showed that Cu forms a pseudomorphic overlayer structure on the Ru(0001) and the peak for Cu UPD dissolution occurs at around 150 mV vs. SCE in perchloric acid. The charge density for the oxidation/dissolution of the first Cu layer was found to be $600 \pm 40$ $\mu C$ $cm^{-2}$. The group of Kelber et al. [25-27] studied the growth kinetics and nucleation behaviour of Cu deposited on Ru(0001) and polycrystalline Ru with XPS, and the influence of chloride and iodide on Cu deposition. Chloride was found to induce the formation of a Cu(I) species on top of Ru. For the influence of iodide they found that the iodine adlayer protects the Ru(0001) surface against the oxidation during exposure to air as well as it works as a surfactant for Cu electrodeposition.

In the present chapter, I follow up the method of Ru quasi single crystals preparation by forced deposition and resistive heating processes [13]. The Ru quasi single crystals are prepared on Pt basal plane surfaces as well as on stepped electrodes vicinal to the (100)

surface plane with a terrace width of n = 2 , . . 7 (Pt(s)[n(100)x(111)]) and on Ru/ Pt(533) = Pt(s)[4(111)x(100)]. The Ru quasi film is characterized by Cu UPD and as well as Cu OPD. Whereas the deposition of Pt by UPD on Ru film is not possible, a formation of Pt sub-monolayer at Ru film by galvanic replacement reaction of Cu UPD monolayer on Ru film is achieved.

## 5.2 Results and discussion

### 5.2.1 Characterization of Pt stepped single crystals

#### *5.2.1.1 Blank voltammograms*
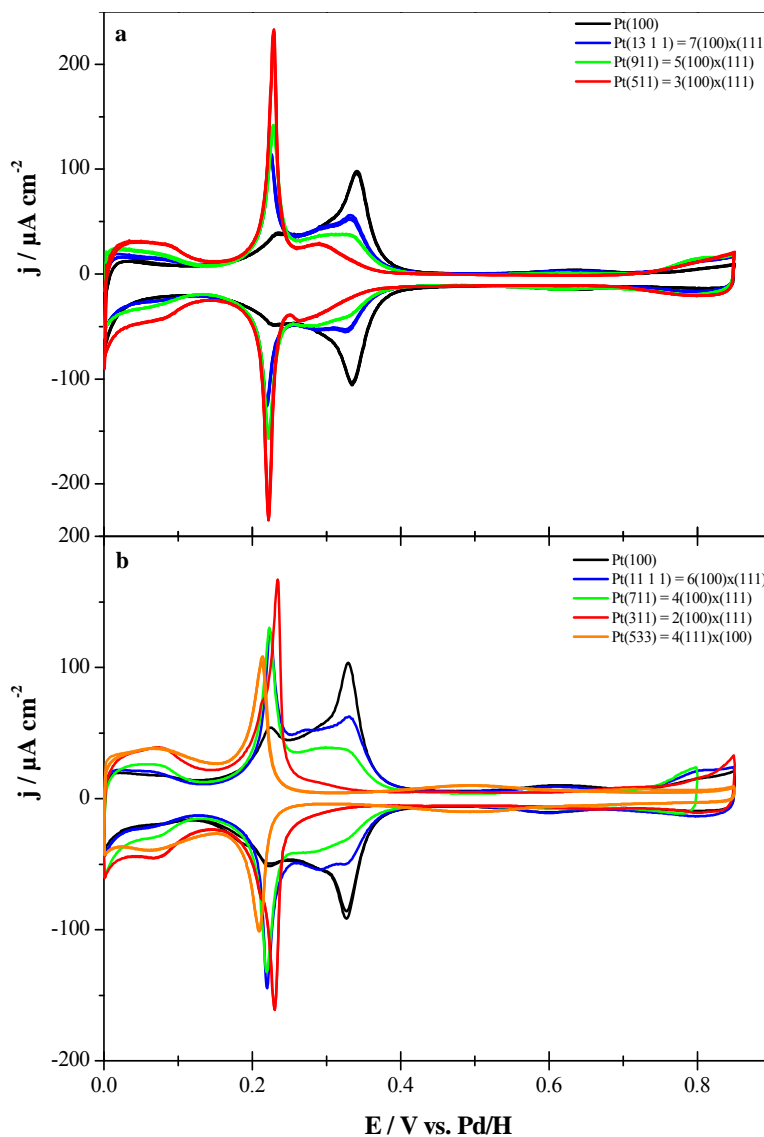


Figure 5-1: CVs of the clean Pt(s)[n(100)x(111)] surfaces in 0.1 M $H_2SO_4$. Scan rate: 50 mV $s^{-1}$. (a) n = 3, 5, 7 and (b) n = 2, 4, 6, Pt(533) and Pt(100).

The voltammetric profiles in 0.1 M $H_2SO_4$ at a scan rate of 50 mV $s^{-1}$ corresponding to the platinum bead single crystal electrodes used in this study are shown in Fig. 5-1 in agreement with the previous studies [13, 15]. The current of all the CVs presented in this

chapter were normalized to the geometric surface area of the electrode. Stable current-potential profiles in Fig. 5-1a and b show many features and clear reversibility between hydrogen/anions adsorption and desorption at different sites of Pt surface. The intensity and the potential of the peaks are depending on the geometry of the surfaces.

A variation of the peak intensity in the potential region between 0 and 0.4 V is observed with increasing the step density. Compared to the profile of Pt(100), as the step density is increased at Pt surface, the intensity of the peaks at 0.22 V and below 0.15 V increase and the intensity in the region between 0.25 and 0.45 V diminishes. While the increase of the current with growing step density in the region between 0 and 0.15 V is an indication for an adsorption processes at the (111) step sites, the current increase of the peak at 0.22 V has been ascribed to hydrogen and anion adsorption on terrace atomic rows adjacent to step sites (terrace edge at 2 and 4 position have a different energy than the rest of terrace as shown in Fig. 5-2). Additionally, the decrease of the current in the region above 0.25 V is an indication to the adsorption processes at (100) terrace sites.
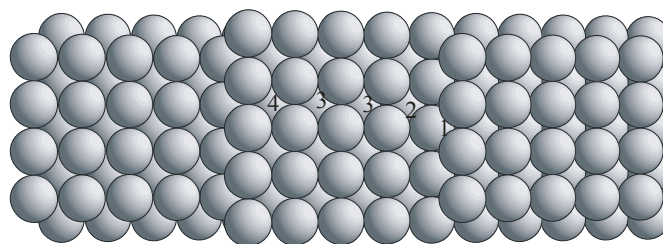


Figure 5-2: The model of the Pt(911) surface. The marked sites involve terrace (3), terrace edge (2 and 4) and step sites (1).

### 5.2.1.2 Cu UPD

The voltammetric behaviour for Cu UPD and bulk deposition on Pt(111) and Pt(100) in 1 mM $CuSO_4$ + 0.1 M $H_2SO_4$ with a scan rate of 10 mV s$^{-1}$ is shown in Fig. 5-3. In the positive going scan, the peak at around 25 mV vs. Cu/Cu$^{2+}$ is related to Cu stripping from more than a monolayer (bulk copper).

In the first positive going scan, the Cu UPD on Pt(100) shows two sharp peaks present at 450 and 475 mV which could be attributed to Cu stripping from the unreconstructed Pt(100)-(1x1) [28]. The integrated charge after double layer correction for the

UPD stripping is about 390 $\mu C \; cm^{-2}$, which is in good agreement with the theoretical value of 420 $\mu C \; cm^{-2}$ and the value of 446 $\mu C \; cm^{-2}$ was found by Alakl et al. [28].
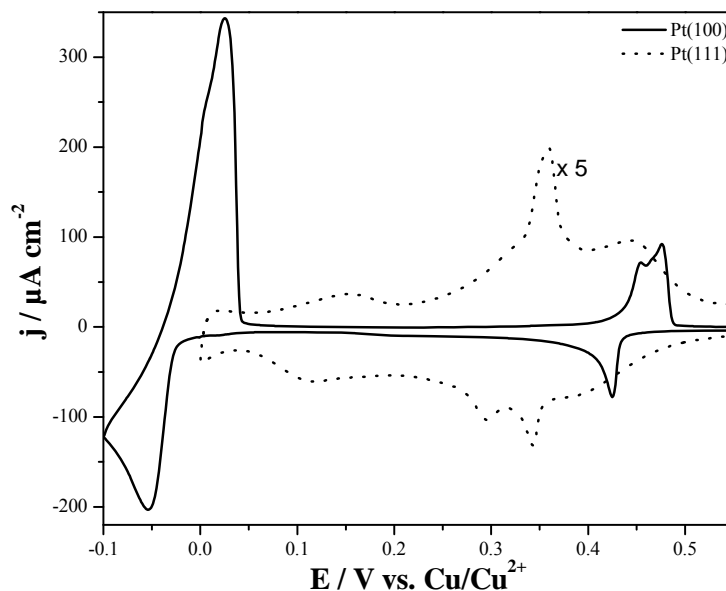


Figure 5-3: Cyclic voltammograms for Cu UPD on the Pt (111) and Pt(100) single crystals. Electrolyte: 0.1 M $H_2SO_4$ + 1 mM $CuSO_4$. Scan rate 10 mV $s^{-1}$.

The CV for Cu UPD on the Pt(111) shows a two peaks between 250 mV and 470 mV vs. $Cu/Cu^{2+}$ in the positive going scan. The first sharp one is at 370 mV and the second broad one is at 450 mV. Whereas in the negative going scan, a two Cu UPD deposition peaks with a charge of 428 $\mu C \; cm^{-2}$ are present. The stripping peak for the Cu UPD in the positive going scan is much sharper in 0.5 M $H_2SO_4$ according to literature [29-33].

The CVs for the Cu UPD on the stepped Pt(s)[n(100)x(111)] single crystals, Pt(533) and, for comparison, the CV for Cu UPD on Pt(100) are shown in Fig. 5-4. Except for Pt(100), three Cu stripping peaks are visible in the anodic going scan. A broad peak at 240 mV (peak A) and another two sharper peaks (B and C) in the region from 350 - 480 mV are observed. With increasing the step density of the Pt stepped single crystals with (100) terraces, the peaks B and C are shifted to less positive potentials. The intensity of peak C decreases with increasing the step density; this is an indication that this peak is due to Cu UPD at terraces (100). The intensity of peaks A and B increase with increasing the step density, they are assigned to Cu stripping from the step sites. The CV for Cu

UPD on the Pt(311) electrode shows two distinct peaks corresponding to stripping from (111) and the (100) sites, the more positive peak corresponding to stripping from the (100) sites [34]. Similarly, for Cu UPD on Pt(533) which has large terraces with (111) orientation, the charge of the first peak at 0.33 V is higher than that at 0.48 V. Here, the first and the second peak are assigned to Cu stripping from terraces with (111) orientation and the step sites with (100) orientation, respectively.
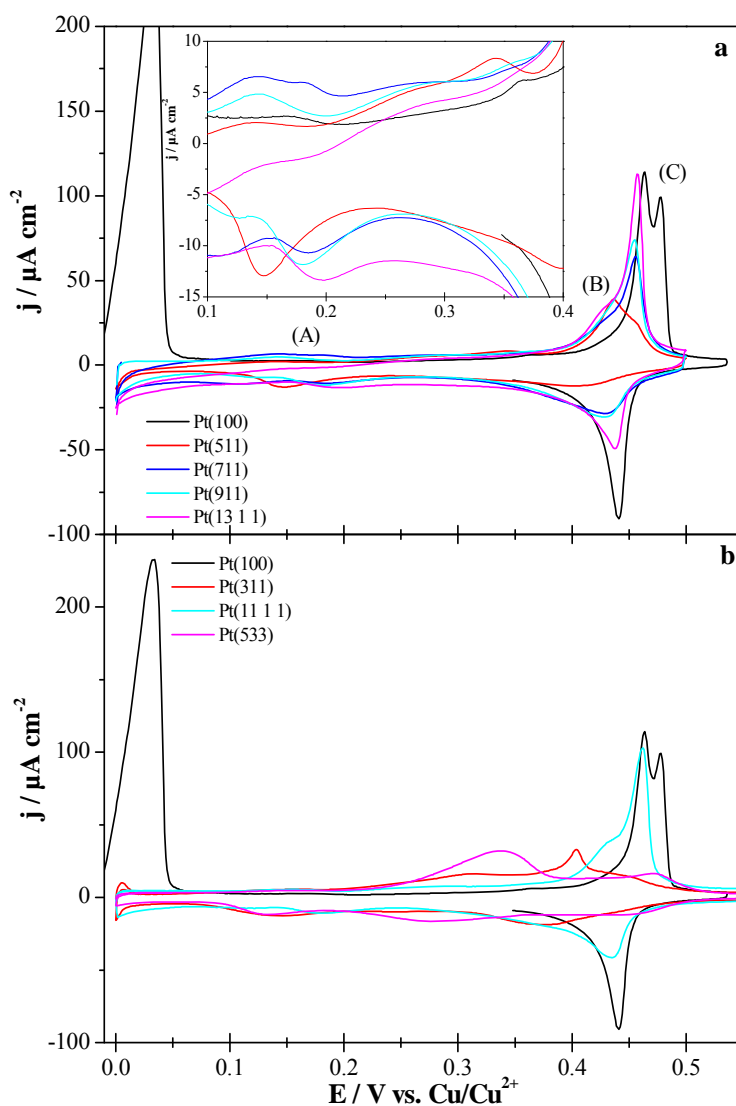


Figure 5-4: Cyclic voltammograms for Cu UPD on the Pt stepped single crystals. Electrolyte: 0.1 M $H_2SO_4$ + 1 mM $CuSO_4$. Scan rate 10 mV s$^{-1}$. (a) n = 3, 4, 5, 7 and (b) n = 2, 6, Pt(533) and Pt(100). Inset: the magnification of the deposition peak at 200 mV.

For Cu on Pt(s)[n(111)x(100)] and Pt(s)[n(110)x(100)], it was found that copper preferentially adsorbs at the step sites [14]. In contrasts to these surfaces, at Pt(s)[(100)x(111)] Cu UPD takes place first at the (100) terraces due to the higher activity of the (100) plane of the fcc system relative to the (111) plane. This mean that Cu atom at (100) plane is coordinated by four Pt atoms, while at (111) only by three due to the hexagonal symmetry.

### 5.2.2  Characteristic CV of Ru quasi single crystal film

#### 5.2.2.1 Blank voltammograms for Ru/Pt basal planes

Figure 5-5 shows the voltammetric profiles for the Ru/Pt(100), Ru/Pt(110) and Ru/Pt(111) quasi single crystalline Ru-film electrodes in 0.1 M $H_2SO_4$ prepared using forced deposition followed by resistive heating [13]. In the forced deposition method, the Ru ions are reduced in a hydrogen atmosphere on the Pt surface followed by resistive heating in a nitrogen atmosphere to 800-900 K. (For more details see section 2.1.4). First, there is no indication of any platinum like electrosorption features in the CVs. In case of Ru/Pt(111), the voltammetric result show a series of electrosorption peaks that are closely similar to those found for Ru(0001) [12, 13, 35, 36]. Huxter and Attard reported that the annealed ruthenium film supported on Pt(111) exhibits hexagonal symmetry and therefore mimics the adsorption properties of Ru(0001); it retains a quasi fcc structure that is epitaxial with the underlying platinum substrate [13].

The cyclic voltammogram of Ru/Pt(110) shows two peaks in the positive going scan: one sharp peak at around 30 mV, and one broad peak at around 400 mV. In the negative going scan, several smaller peaks and a large sharp peak at around -30 mV are visible. By comparison with Ru(0001) single crystal measurements were performed on literature [11, 12, 35, 37], the peaks at low potentials are related to hydrogen- or hydroxide-adsorption/desorption, and the peaks at high potentials are related to sulphate adsorption/desorption.
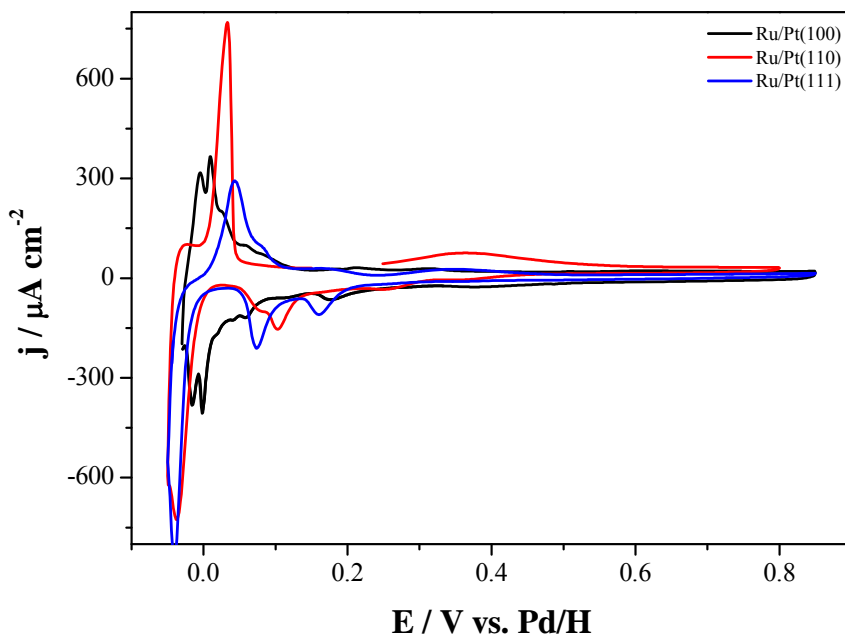
Figure 5-5: Voltammetric profiles for the Ru/Pt(100), Ru/Pt(110) and Ru/Pt(111) quasi-single crystalline Ru-film electrodes in 0.1 M $H_2SO_4$. Scan rate: 50 mV s$^{-1}$.

For Ru/Pt(100), it can be observed two main features. The first one is the presence of a sharp doublet at approximately 0 V [13, 38] which has not been reported previously for any ruthenium single crystal. There are in addition some minor peaks between 0.05 and 0.2 V that were ascribed to OH adsorption [13]. Second, the electrosorption for the ruthenium film charge in the potential range between 0.05 and 0.3 V is greater than that of the Pt(100) electrode between 0 and 0.5 V (363 and 210 $\mu C$ cm$^{-2}$ respectively). Attard ascribed this behavior, depending on the previous publication concerning Ru(0001) [12, 35, 36], to stronger interaction of ruthenium relative in comparison to platinum with electrolyte species such as $SO_4^{-2}/HSO_4^-$, OH and possibly also hydrogen [13].

### 5.2.2.2 Blank voltammograms for Ru/Pt stepped single crystals

Figure 5-6 shows the recorded voltammetric profiles of the quasi single crystal Ru-film electrodes on stepped Pt(s)[n(100)x(111)] single crystals with n = 2,...,7 vicinal to the (100) plane and the profile for Ru/Pt(100) film electrode in 0.1 M $H_2SO_4$. As reported in reference [13], the peak pair observed in the positive going scan at around 0 mV for

the (100) stepped substrates on the Ru films decreases with increasing step density that was ascribed to adsorption/desorption at (100) terraces, and a new peak at around 0.05 V appears was ascribed to processes on the (111)x(100) step sites as described by Attard group [13].



Figure 5-6: Voltammetric profiles of Ru/Pt(100) and Ru/Pt(s)[n(100)x(111)] electrodes with n = 2, 4 and 6 (a) and n = 3, 5 and 7 (b) in 0.1 M $H_2SO_4$. Scan rate 50 mV s$^{-1}$.

### 5.2.2.3 Cu UPD on Ru /Pt basal planes
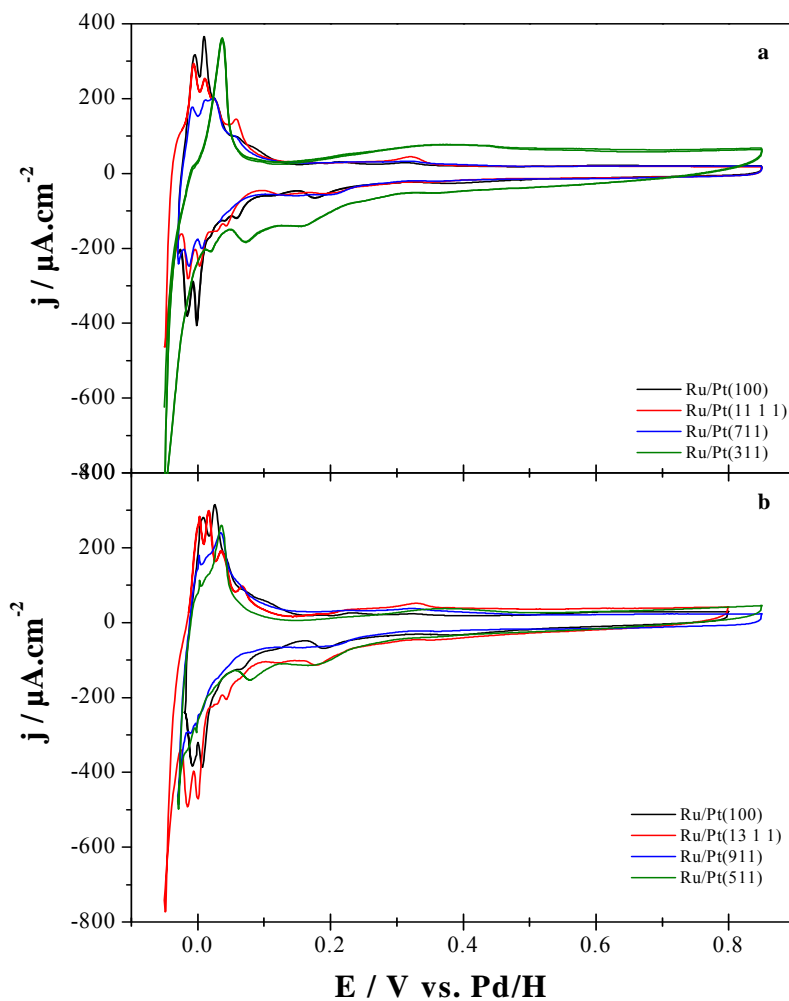
Figure 5-7 show the cyclic voltammograms for Cu underpotential deposition on the low index Ru/Pt(100), Ru/Pt(110) and Ru/Pt(111) quasi single crystal Ru-film electrodes

in 1 mM $CuSO_4$ in 0.1 M $H_2SO_4$ at a scan rate 10 mV $s^{-1}$. First, there is not any indication for Cu UPD on free Pt sites like Pt domains on the Ru-film electrodes, that are usually visible at higher potentials around 0.45 V as shown in Fig. 5-3.
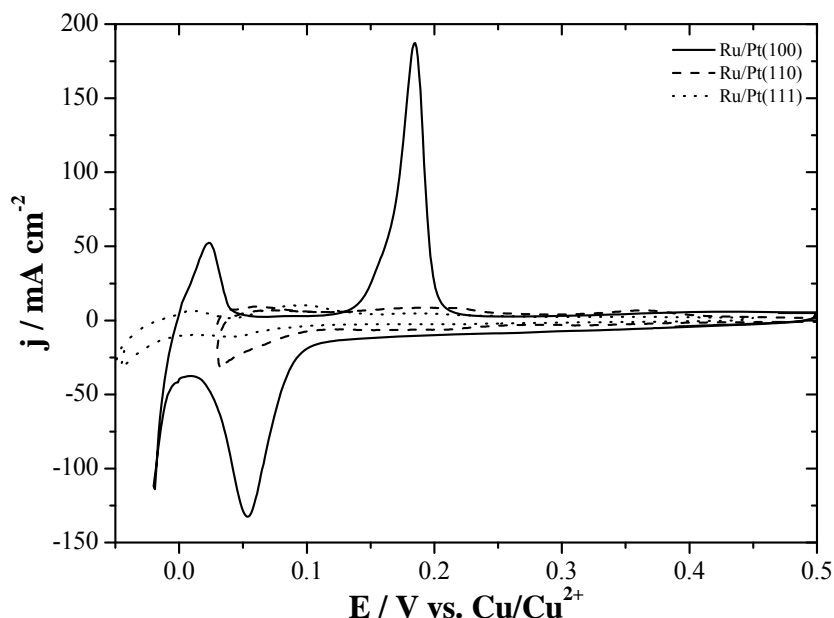


Figure 5-7: Cyclic voltammograms for Cu UPD on the low-indexed Ru/Pt(100), Ru/Pt(110) and Ru/Pt(111) quasi single crystal film electrodes in 1 mM $CuSO_4$ + 0.1 M $H_2SO_4$. Scan rate 10 mV $s^{-1}$.

During the Cu UPD on the Ru/Pt(100) film electrode surface, two different peaks are observed. A large peak with a small shoulder at around 185 mV vs. Cu/$Cu^{2+}$ for the Cu stripping is seen. It is believed that this peak is related to Cu UPD stripping from (100) sites. The peak at around 0 V related to stripping of bulk deposited Cu (from more than a monolayer). The charge density of Cu UPD stripping from the terrace sites (peak at 185 mV) of Ru/Pt(100) film electrode after subtraction of the baseline from the beginning to the end of the peak is 443 $\mu C$ $cm^{-2}$, which is close to theoretical value of 420 $\mu C$ $cm^{-2}$ for (1x1) Cu overlayer on Pt(100) [28].

For Cu stripping from Ru/Pt(110) and Ru/Pt(111), besides bulk Cu stripping around 0 V, only small, broad peaks between 0.05 and 0.12 V and at around 185 mV can be observed under these experimental conditions. The integrated charge densities found in the cyclic voltammograms for Cu UPD on the Ru/Pt(110) and Ru/Pt(111) are clearly far too

small for a copper monolayer. I believe this is due to a blockage of the (111) and (110) sites by an oxygen containing species as described for Cu UPD on bulk Ru surfaces [22] and Ru deposited on polycrystalline Pt [39]. It seems, that the oxygen species adsorbed on the Ru/Pt(100) sites is not as stable as it is on the other low indexed crystal surfaces, and can be displaced by Cu. This can also be seen from the voltammetric profiles in Fig. 5-5. Recently, El-Aziz et al. found that Cu UPD takes place on Ru(0001) surface [40]. This difference to the results described here is attributed to the difference in the lattice constants in both surfaces. The peaks for hydrogen/hydroxide adsorption and desorption appear less pronounced, at more positive potential and more reversibly as compared to the Ru/Pt(110) and Ru/Pt(111) film electrodes. A higher stability of Cu on (100) sites may be also help in this displacement.

### 5.2.2.4 Cu UPD on Ru /Pt stepped single crystals

Cu UPD experiments performed on the quasi single crystal Ru film surfaces on stepped Pt(s)[n(100)x(111)] single crystal electrodes show a clear trend for the anodic peaks found at 185 mV vs. $Cu/Cu^{2+}$, as can be seen in the cyclic voltammograms in Fig. 5-8. The charge densities of the Cu UPD stripping peaks at 0.185 V and the corresponding deposition peaks in the potential range between 0.05 V and 0.08 V decrease with increasing the step density. On the other hand the charge density of the second peak at around 70 mV vs. $Cu/Cu^{2+}$ seems to increase somewhat with increasing number of (111) x (100) step sites, which might be associated with Cu UPD on (111) x (100) step sites, but in contrast to the peak at 185 mV no clear trend is visible. Obviously Cu UPD is more strongly adsorbed on (100) terrace sites than on (111) step sites. This was also recently reported by Francke et al. [15] for Cu underpotential deposition on "clean", stepped Pt(s)[n(100)x(111)] single crystal surfaces, where a tentative explanation based on the different coordination of copper on both sites was proposed (cf. discussion of Fig. 5-3).

It should be mentioned here that the stripping peak of Cu UPD at 185 mV on the Ru/Pt(11 1 1) seems to consist of two peaks which overlap, resulting possibly from imperfections of the Ru-film, which can also be inferred from the small extra peak at around 80 mV vs. Pd/H in the CV of the Ru-film electrode in sulphuric acid in Fig. 5-6. The in-

tegrated charge densities for the anodic Cu stripping peaks on the Ru/Pt(100) and Ru/Pt(s)[n(100)x(111)] film electrodes are summarized in Table 5-1.
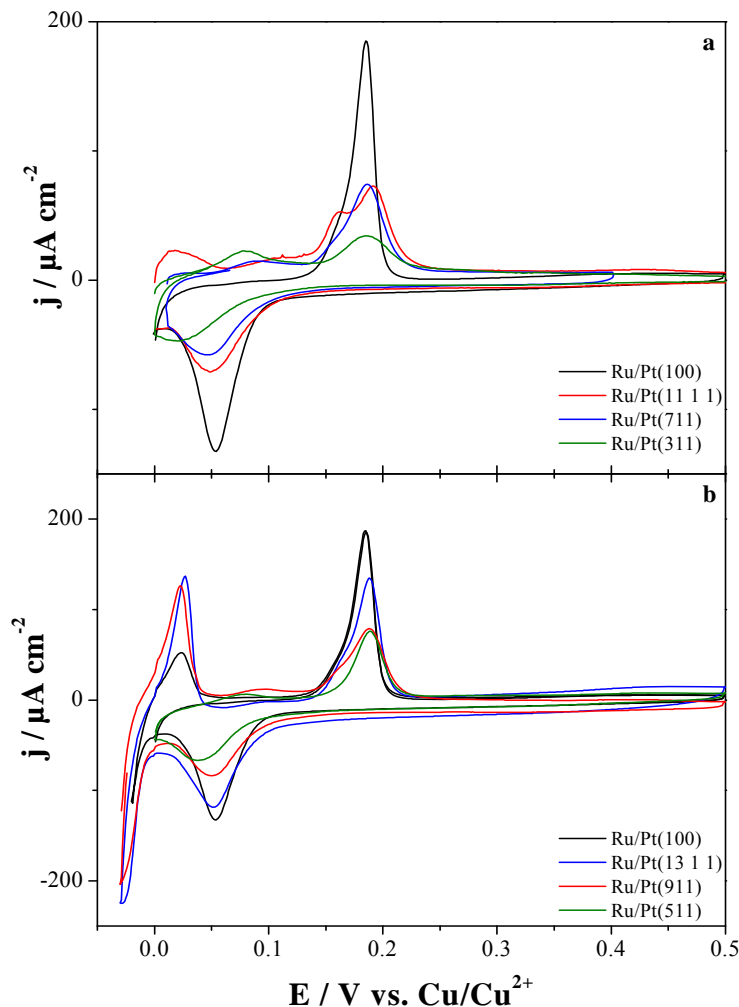


Figure 5-8: Cyclic voltammograms for the Cu UPD on the Ru quasi single crystal Ru/Pt(100) and the Ru-film electrodes prepared on stepped Pt(s)[n(100)x(111)] with (a) n = 2, 4 and 6 and (b) n = 3, 5 and 7 in 1 mM $CuSO_4$ in 0.1 M $H_2SO_4$. Scan rate 10 mV s$^{-1}$.

A plot of the charge densities $Q_{185mV}$ from Table 5-1 divided by $\cos(\alpha)$ vs. the step density of Pt surfaces ($1/(n-1/2)$) originally proposed by Clavilier et al. for hydrogen adsorption on stepped Pt(s)[n(111)x(111)] [41] and Pt(s)[n(111)x(100)] [42] single crystal surfaces shows a linear relationship of these charge densities and $1/(n-1/2)$ (cf. Fig. 5-9).

Where the term $\cos(\alpha)$ represents the cosine of the angle $\alpha$ between the (100) plane and the surface plane, and is given by:

$$\cos(\alpha) = \frac{(n - 1/2)}{\sqrt{(n - 1/2)^2 + 1/2}} \qquad (1)$$

Table 5-1: Integrated charge densities for Cu dissolution peaks on the Ru/Pt(100) and Ru/Pt(S)[n(100)x(111)] film electrodes with terrace width n = 2, ..7 for the peaks at around 70 ($Q_{70mV}$) and 185 mV ($Q_{185mV}$) vs. Cu/Cu$^{2+}$ and values for $\cos(\alpha)$ (see Fig. 5-8).

| Ru-film electrode | n | Charge $Q_{70mV}$ / $\mu C\ cm^{-2}$ | Charge $Q_{185mV}$ / $\mu C\ cm^{-2}$ | Charge $Q_{70mV}$ + $Q_{185mV}$ / $\mu C\ cm^{-2}$ | $\cos(\alpha)$ |
|---|---|---|---|---|---|
| Ru/Pt(100) | ∞ | - | 443 | 443 | 1.000 |
| Ru/Pt(13 1 1) | 7 | 10 | 413 | 423 | 0.994 |
| Ru/Pt(11 1 1) | 6 | 31 | 342 | 373 | 0.992 |
| Ru/Pt(911) | 5 | 43 | 334 | 377 | 0.988 |
| Ru/Pt(711) | 4 | 41 | 287 | 328 | 0.980 |
| Ru/Pt(511) | 3 | 19 | 241 | 260 | 0.962 |
| Ru/Pt(311) | 2 | 25 | 102 | 127 | 0.906 |

As can be derived from the hard sphere model [15, 41, 42] for the Pt(s)[n(100)x(111)] surface, (n-1/2) indicates the terrace atomic width and N = 1/d(n-1/2) therefore represents the number of step sites per unit length perpendicular to the step (step density) with d as the atomic diameter of Pt (0.277 nm [41]). (n-1) atom wide rows of the terrace are freely accessible; a further row is half covered by a row of step atoms as shown in Fig. 5-9 for Pt(711). The area of the projection on (100) terraces plane of the surface unit cell is given by S = d$^2$(n-1/2) and therefore the electric charge for fully populated step ($q_s$) is given by:

$$q_s = \frac{z \cdot \theta_{step} \cdot e}{d^2 \cdot (n - 1/2)} = z \cdot \theta_{step} \cdot q_{100} \cdot d \cdot N \qquad (2)$$

Where z is the formal number of transferred electrons per elemental reaction, $\theta_{step}$ is the maximum coverage attained at step sites, e the elemental charge (1.602 x 10$^{-19}$ C) and $q_{100} = (e/d^2)$ is the charge corresponding to the transfer of 1 e$^-$ per surface site on the ideal Pt(100)(1x1) surface.

The theoretical slope depends on the number of rows being deposited on a terrace. If only one row of terrace is either uncovered by Cu or the corresponding Cu is desorbed at a different potential, the theoretical charge density due to adsorption on the terrace sites, according to ref [15], is given by:

$$q_{terrace} = \frac{(n-1)z \cdot e \cdot \theta_{terrace}}{d^2(n-1/2)} = z \cdot \theta_{terrace} \cdot q_{100} - \frac{(1/2) \cdot z \cdot \theta_{terrace} \cdot q_{100}}{(n-1/2)} \tag{3}$$

where $\theta_{terrace}$ is the maximum coverage attained at terrace sites. The expected theoretical slope in that case is -220 µC cm$^{-2}$ at a Cu coverage $\theta_{terrace} = 1$ on the terrace sites, z = 2 for the oxidation of Cu$^0$ to Cu$^{2+}$ and the experimental value of q$_{100}$ = 443 µC cm$^{-2}$.

Assuming that two rows of the n rows per terrace are missing, the theoretical charge density due to adsorption on the terrace sites was calculated as -662 µC cm$^{-2}$, according to ref. [15], should be given by :

$$q_{terrace} = \frac{(n-2) \cdot z \cdot \theta_{terrace} \cdot e}{d^2 \cdot (n-1/2)} = z \cdot \theta_{terrace} \cdot \left(\frac{e}{d^2}\right) - \left(\frac{(3/2)}{n-1/2}\right) \cdot z \cdot \theta_{terrace} \cdot \left(\frac{e}{d^2}\right) \tag{4}$$

$$q_{terrace} = z \cdot \theta_{terrace} \cdot q_{100} - \frac{(3/2) \cdot z \cdot \theta_{terrace} \cdot q_{100}}{(n-1/2)} \tag{5}$$

These two rows could be the rows in direct contact to either side of the steps, which differ most in adsorption energy from terrace sites (indicated as broken lines in Fig. 5-9).

From the linear decrease of the charge for the anodic Cu stripping peaks at around 185 mV vs. Cu/Cu$^{2+}$, the slope of -513 µC cm$^{-2}$ and the intercept at 453 µC cm$^{-2}$ are found. The linear behaviour and the obtained current density value of the intercept strongly supports the assumption that the (100) terraces (and steps) of the underlying Pt substrate are preserved on top of the Ru film, although fcc(100) adsorption sites are normally not existing for hcp metals. The results also suggest that the Cu coverage $\theta_{Cu}$ on terraces is 1 for Cu UPD on the Ru-films. Obviously, the experimentally found slope of -513 µC cm$^{-2}$ is closest to that of the model with two missing rows at the step sites (-662 µC cm$^{-2}$). It has to be remarked that the adsorption of (bi)sulphate and its contribution to the charge density in this system could also be responsible for some deviation from the hard sphere model. In addition, the uncertainty in the double layer contribution can affect the value of the slope. Some distribution of the true terrace width around the nominal

value and imperfections of the film may also lead to some additional deviation from the theoretical slope.

From the plot of the charge densities $Q_{70mV}$ from Table 5-1 divided by $cos(\alpha)$ vs. $1/(n-1/2)$ no clear dependence on step density can be deduced (Fig. 5-9).
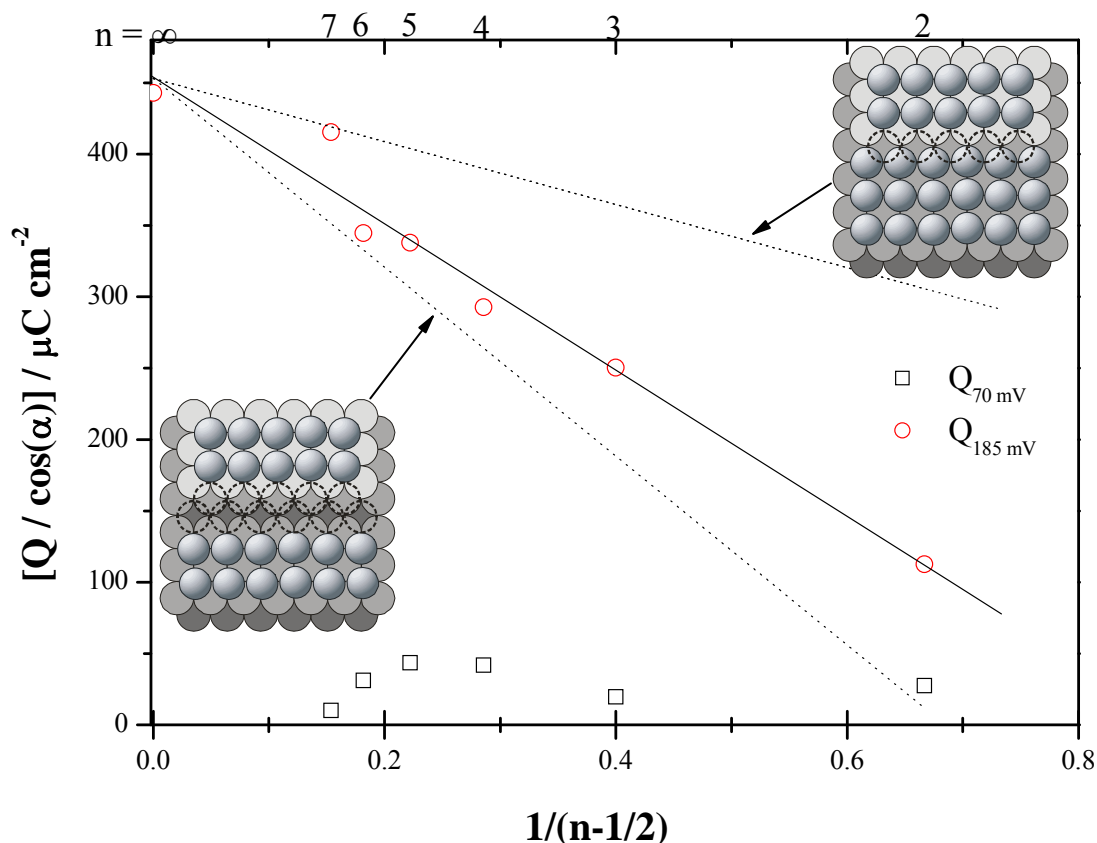


Figure 5-9: Plot of integrated charge densities $Q_{185mV}$ divided by $cos(\alpha)$ for the anodic Cu dissolution peaks at 185 mV vs. $Cu/Cu^{2+}$ from Table 5-1 for Cu UPD on the Ru/Pt(100) and the film electrodes on Ru/Pt(s)[n(100)x(111)] film electrodes with n = 2, .. 7 vs. $1/(n-1/2)$. The linear regression for the charge density is indicated by a dotted line; theoretical lines having the same intercept with a slope of -662 (two rows uncovered by the adsorbate) and -220 $\mu C$ $cm^{-2}$ (one row uncovered by the adsorbate) are indicated by a dashed and a dash-dotted line. The two graphs of a stepped (711) surfaces (circles, number of the layer indicated by the brightness of the colour) represent models for Cu adsorption (grey balls), if (n-2) or (n-1) surface rows (missing rows indicated by dotted circles) are accessible for Cu deposition at 185 mV.

Assuming coverage of 1 for Cu deposited at the step sites, the slope to be around +420 $\mu C\ cm^{-2}$ would be expected, which is obviously not the case. A peak in this potential region can also be found for Cu stripping from polycrystalline (bulk) Ru [33]. Therefore, it is believed that this peak is related to Cu stripping from polycrystalline Ru domains or defects of the Ru quasi single crystal films. As for Cu UPD on Ru/Pt(111), the step sites seem to be blocked for Cu UPD under these experimental conditions. In the next section, it will be shown that Cu can be forced to adsorb at (111) sites, however, the corresponding dissolution peak is observed around 300 mV and not at 70 mV, corroborating the above interpretation

### 5.2.3 Electrodeposition of Cu under diffusion control

The diffusion controlled progressive deposition of Cu on Ru-film surfaces at very negative potentials was performed in order to achieve monolayer deposition of Cu on the Ru/Pt(111) quasi single crystal film electrode, that may be blocked by strongly adsorbed oxygen species (cf. Discussion of Fig. 5-7).

Using a very low concentration of $Cu^{2+}$ ion containing solution ($10^{-5}$ M $CuSO_4$), the potential can be swept far below the $Cu/Cu^{2+}$ equilibrium potential in order to reduce the surface oxide or the adsorbed oxygen species. Because of the diffusion limitation, extensive multi-layer deposition of copper will only occur after prolonged deposition. Figure 5-10 shows an example for diffusion controlled copper deposition on Ru/Pt(111) film electrode by sweep the potential between -250 and 100 mV vs. $Cu/Cu^{2+}$ in a very dilute Cu solution, using a scan rate of 50 mV $s^{-1}$. The peaks of hydrogen/hydroxide adsorption and desorption on the Ru-film electrode surface, are more and more suppressed with increasing number of potential cycles in the potential range.

Figure 5-11 show the dissolution of Cu layer from Ru/Pt(111), Ru/Pt(311) and Ru/Pt(511) film during scanning the potential in the positive going direction to + 450 mV after the complete suppression of H/OH adsorption/desorption peaks and changing the scan rate to 10 mV $s^{-1}$. For the Ru/Pt(111) surface, two peaks at around 0 and 320 mV were observed.
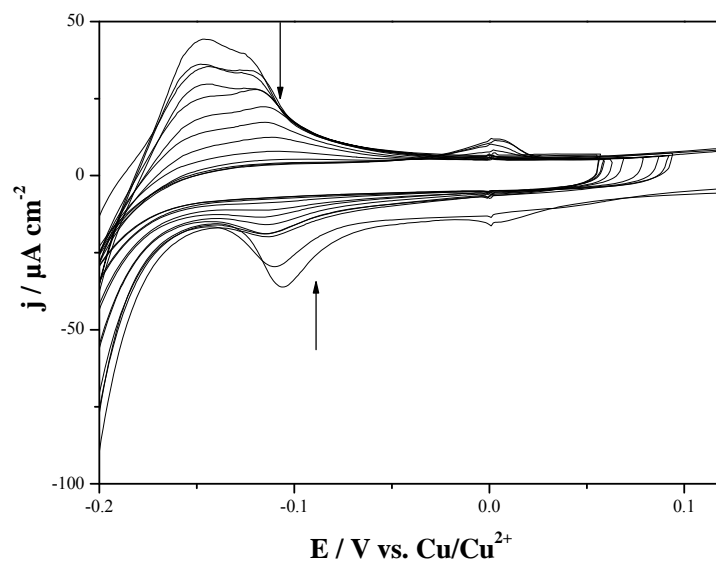
Figure 5-10: Cyclic voltammogramms for the progressive diffusion controlled Cu OPD on a Ru/Pt(111) film electrode in $10^{-5}$ M $CuSO_4$ in 0.1 M $H_2SO_4$. Arrows indicate changes in the voltammogram with increasing amount of Cu adsorbed. Scan rate 50 mV $s^{-1}$.
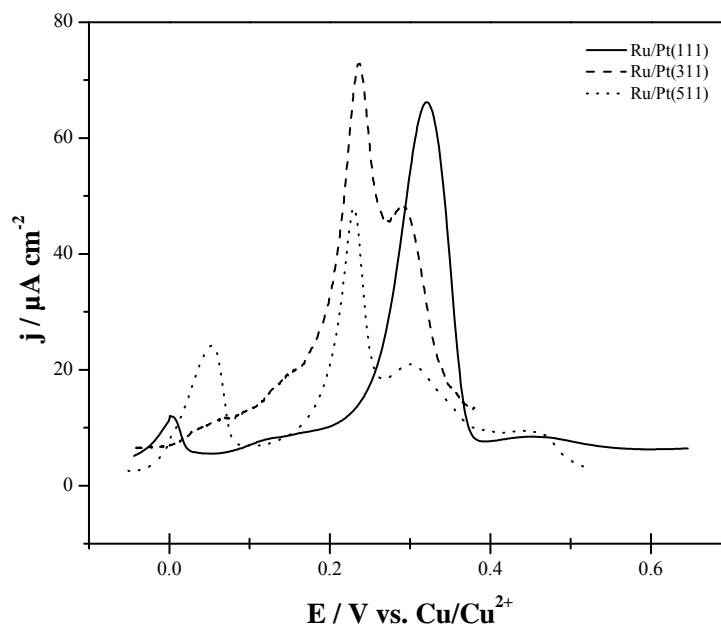


Figure 5-11: First anodic sweeping for the Cu desorption on the Ru/Pt(111), Ru/Pt(311) and Ru/Pt(511) film electrodes after progressive Cu OPD in $10^{-5}$ M $CuSO_4$ in 0.1 M $H_2SO_4$. Scan rate 10 mV $s^{-1}$.

The first small peak is attributed to the dissolution of bulk Cu. The second broad peak at 300 mV vs. Cu/Cu$^{2+}$ for the dissolution of Cu from the Ru/Pt(111) surface. For these the charge density of about 475 $\mu C$ cm$^{-2}$ was obtained, but the unknown background charge makes it very hard to give an exact value. For Cu stripping from Ru/Pt(311) and Ru/Pt(511) film electrodes, the intensity of the stripping peak at 300 mV decrease with decreasing the number of (111) step sites per unit length with a little shift in potential to less positive potential, this peak is therefore attributed to Cu dissolution from (111) sites. This indicates that Cu desorption around 300 mV is not only related to terrace sites with local (111) geometry, but also to step sites with local (111) geometry. A new peak at around 220 mV was observed for the Ru/Pt(311) and Ru/Pt(511) related to the Cu desorption from the (100) terrace sites, see Fig. 5-8. Unfortunately, this comparison can only be qualitative, since displacement of the adsorbed oxygen species possibly is not complete. Some Cu might rather be deposited in 3D islands, cf. the large peak for bulk Cu dissolution around 0 V for Ru/Pt(511) and the comparatively small peak at +200 mV. It should be emphasized that the peak at the high potential around 300 mV could not be observed for Cu dissolution from the Ru/Pt(100) and Ru/Pt(s)[n(100)x(111)] films in the previous experiments (where the lowest potential was limited to values around zero volts vs. Cu/Cu$^{2+}$). The peak at around +185 mV for Cu dissolution from (100) terrace sites were always observed. The potential found for Cu UPD stripping on the Ru/Pt(111) film electrode differs from the value of +140 mV reported for Cu UPD stripping from Cu on Ru(0001) in HClO$_4$ by Stuve et al. [23]. For Cu UPD on a Ru sub-monolayer deposited on Pt(111), the peak potential of about +200 mV was found [33]. A possible reason for these differences is, that the lattice constant of the surface unit cell for Ru deposited epitaxially on Pt(111) is that for Pt(111) (0.277 nm instead of 0.271 nm for bulk Ru(0001)). A difference between the present values and that of Stuve et al. might also be due to the different supporting electrolyte (specific adsorption of sulphate). Nevertheless, the fact that Cu UPD on the hexagonal "(111)/(0001)" surface is more stable than on the quadratic "(100)" face is astonishing, because on Pt it is less stable on the hexagonal face.

**5.2.4 Pt sub-monolayer on Ru quasi single crystal film**

Behm and co-workers found that the presence of small amounts of Pt monolayer islands catalyze the $OH_{ad}$ and $H_{ad}$-UPD exchange reaction [35, 43, 44]. Whereas the OH and H adsorption are taking place simultaneously at Ru surface, it occurs separately on Pt.

In this section, the preliminary experiments for galvanic replacements are performed to obtain a Pt sub-monolayer at a Ru quasi single crystal film and to characterize it by voltammetry and Cu UPD.

*5.2.4.1 Why not UPD deposition of Pt on Ru(ijkl)?*

UPD is usually observed when the work function ($\Phi$) of substrate surface is higher than the work function of the adsorbate. The underpotential deposition of Pt on the Ru as a substrate is not possible because the $\Phi_{Pt}$ is higher than $\Phi_{Ru}$ as shown in Table 5-2.

Table 5-2: The work function of different metal surface.

| Surface | $\Phi/eV$ |
|---------|-----------|
| Pt-poly | 5.64 |
| Pt(111) | 5.93 |
| Cu(111) | 4.94 |
| Au(111) | 5.31 |
| Pd-poly | 5.22 |
| Pd(111) | 5.6 |
| Ru-poly | 4.71 |
| Tl-poly | 3.84 |
| Pb-poly | 4.25 |

Another choice is the metal deposition by galvanic replacement, that was first introduced by Adzic et al. for Pt/Au(111) [45]; in that method the deposition of noble metal occurs as a spontaneous irreversible redox process in which a monolayer of Cu obtained by UPD is oxidized by the noble metal cation, which is reduced simultaneously and de-

posited as shown in Fig. 5-12. In that method, there is no preferential deposition on steps or defect sites like other deposition methods, because it occurs far from equilibrium.

### 5.2.4.2 Galvanic replacement of $Cu_{ML}$ with Pt

In order to obtain Pt deposited at a Ru quasi single crystal electrode prepared at a Pt(s)[n(100)x(111)] substrate by forced deposition and resistive heating process as described in the previous chapter, the following steps are proceeded:

- Formation of Cu monolayer by UPD on Ru quasi single crystals.

- The Cu UPD monolayer is replaced with a more noble metal (Pt) when the $Cu_{ML}$/Ru film was immersed in a solution containing 1 mM $PtCl_6^{2-}$. (Note that, the $Cu_{ML}$/Ru film is transferred through air to Pt ion containing solution that leads to dissolution of some of Cu ).

- Leave the crystal in contact with $PtCl_6^{2-}$ solution for 3 min to ensure the complete replacement of Cu with Pt.

- Wash the crystal with Millipore water and check the $Pt_{0.5}$/Ru/Pt(s)[n(100)x(111)] by cyclic voltammetry in 0.1 M $H_2SO_4$ and Cu UPD.
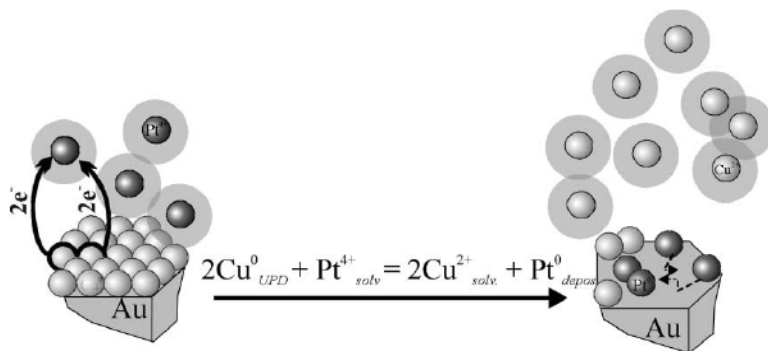


Figure 5-12: Schematic of the replacement of Cu by Pt in a charge transfer process via direct $Cu^0$ adatom-$Pt^{4+}$ ion interaction. Pt atom: dark gray and Cu atom: light gray. Reprinted from ref. [45].

In agreement with the behaviour of Pt at Au(111) [45], the amount of Pt deposited by galvanic replacement of Cu UPD monolayer is limited to half a monolayer, because $Pt^{4+}$ ions from the solution oxidize two Cu UPD adatoms:

$$2 \text{ Cu}^0 / \text{Ru}_{QSC} + \text{PtCl}^{2-} \longrightarrow \text{Pt}^0/\text{Ru}_{QSC} + 2 \text{ Cu}^{2+} + 6 \text{ Cl}^-$$
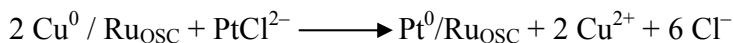
### 5.2.4.3 Characterization of Pt/Ru/Pt single crystals

*Blank voltammograms for Pt/Ru/Pt single crystals*

The electrochemical behaviour of the Pt modified Ru quasi single crystal film was checked by cyclic voltammograms in 0.1 M $H_2SO_4$ and by Cu UPD experiments. Fig. 5-13a shows the characteristic CV for Pt/Ru/Pt(100) in 0.1 M $H_2SO_4$ and its comparison with free Pt(100) and Ru/Pt(100) surfaces. The characteristic sharp doublet peak for Ru/Pt(100) at 0 V diminished and two new peaks were present in the hydrogen adsorption/desorption region. Again, similar to the Pt(100) surface, the characteristic peaks for Ru/Pt(13 1 1) in 0.1 M $H_2SO_4$ decreased after replacement of the Cu monolayer with Pt (Fig. 5-13b).



Figure 5-13: Voltammetric profiles for (a) Pt/Ru/Pt(100), Ru/Pt(100) and Pt(100) and (b) Pt/Ru/Pt(13 1 1), Ru/Pt(13 1 1) and Pt(13 1 1) electrodes in 0.1 M $H_2SO_4$. Scan rate: 50 mV s$^{-1}$.

*Cu UPD for Pt/Ru/Pt single crystals*

The characterization of Pt sub-monolayer at Ru quasi single crystal film was achieved by Cu UPD experiments. Fig. 5-14 show the Cu UPD on Pt/Ru/Pt(13 1 1) in 1 mM CuSO$_4$ + 0.1 M $H_2SO_4$ with a scan rate 10 mV s$^{-1}$. In the positive going scan, there are two Cu stripping peaks, the first one at 30 mV and the other one at 225 mV vs. Cu/Cu$^{2+}$. The second peak with a charge density of 315 μC cm$^{-2}$ is shifted positively with respect to the Cu UPD stripping peak on Ru/Pt(13 1 1). (The charge density for Cu stripping from clean

140

Pt(13 1 1) and Ru/Pt(13 1 1) are 270 and 450 $\mu C$ cm$^{-2}$ respectively). Because the Pt atoms are distributed on the surface without preferential deposition sites (steps or terraces) but Cu should be deposited preferentially on Pt or Ru or between Pt and Ru atoms. The Cu UPD stripping peak is present in the potential range between Cu UPD on pure Pt and on Ru/Pt film indicate the higher stability of Cu on the Pt/Ru/Pt surface than that on Ru film at Pt electrode.



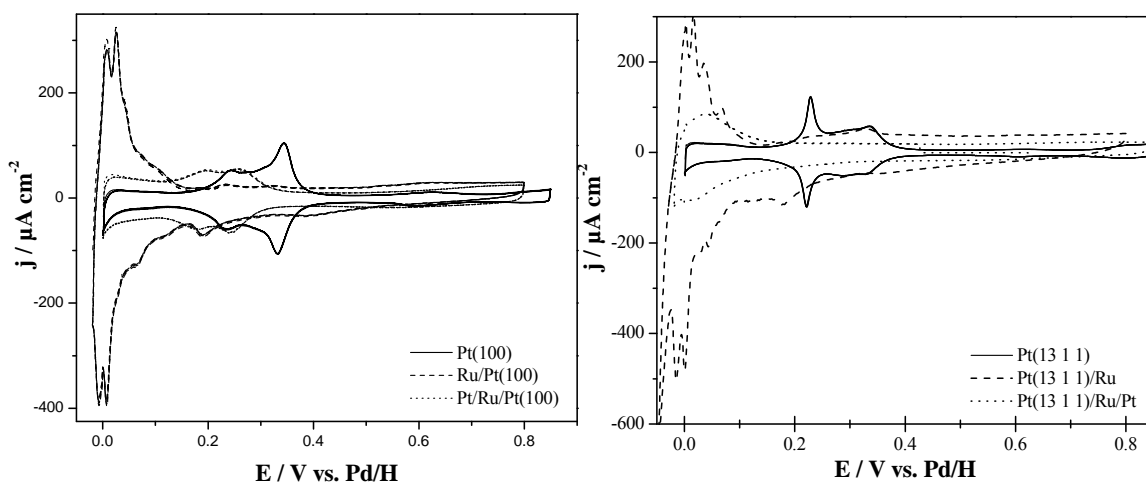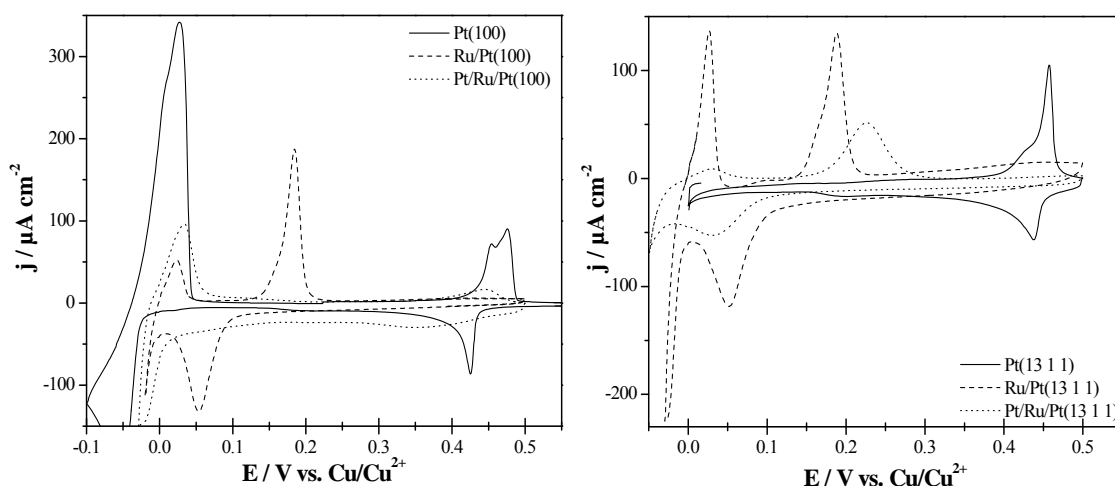Figure 5-14: Cyclic voltammograms for the Cu UPD on (a) Pt/Ru/Pt(100), Ru/Pt(100) and pt(100) and (b) Pt/Ru/Pt(13 1 1), Ru/Pt(13 1 1) and pt(13 1 1) electrodes in 1 mM CuSO$_4$ + 0.1 M H$_2$SO$_4$. Scan rate 10 mV s$^{-1}$.

Figure 5-10 shows the Cu deposition at the Ru/Pt(111) surface under diffusion limited condition. After complete suppression of H/OH adsorption/desorption peaks (as an indication for Cu monolayer formation), the potential was held to keep only a monolayer of Cu, then the galvanic replacement with Pt was applied as described before. The characteristic CVs in 0.1 M H$_2$SO$_4$ are shown in Fig. 5-15a. The H/OH adsorption/desorption peaks at Pt/Ru/Pt(111) are shifted with respect to that at Ru/Pt(111) film. This is an indication for sub-monolayer of Pt formed on Ru film. Fig. 5-15b shows a qualitative comparison between Cu stripping from Pt/Ru/Pt(111) and Ru/Pt(111). The Cu dissolution peaks are present at 400 and 300 mV respectively with corresponding charge density 340

and 440 $\mu C$ cm$^{-2}$. Again, this is an indication of the stability of Cu layer on Pt/Ru/Pt(111) relative to that on Ru/Pt(111) film.



Figure 5-15: Voltammetric profiles for (a) Pt/Ru/Pt(111), Ru/Pt(111) and Pt(111) in 0.1 M $H_2SO_4$. Scan rate 50 mV s$^{-1}$. (b) cyclic voltammograms for the Cu stripping from Pt/Ru/Pt(111) and Ru/Pt(111) electrodes in 10$^{-5}$ 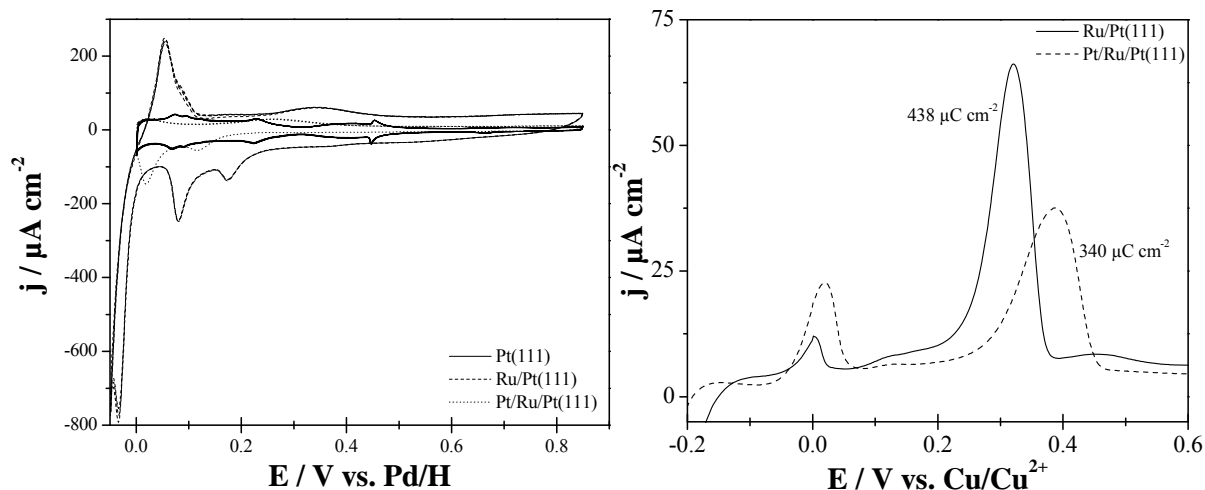M $CuSO_4$ + 0.1 M $H_2SO_4$ after formation of a Cu monolayer by diffusion limited deposition. Scan rate 10 mV s$^{-1}$.

## 5.3 Conclusions

Cu UPD experiments were achieved in order to characterize the low index Ru quasi single crystal Ru/Pt(100), Ru/Pt(110) and Ru/Pt(111) electrodes as well as on stepped electrodes vicinal to the (100) surface plane with a terrace width of n = 2 , . . . , 7 (Ru/Pt(s)[n(100)x(111)]) and on Ru/Pt(s)[4(111)x(100)]. Because of the strong adsorption of hydroxide/oxide at Ru/Pt(111) and Ru/Pt(110) films, the surfaces were blocked for Cu UPD deposition and there is no indication for Cu deposition on these surfaces during Cu UPD experiments. However, monolayer deposition on these surfaces was performed under diffusion limited monolayer deposition.

During Cu UPD experiments, Cu stripping from Ru/Pt(100) electrode occurs in a single peak with its maximum at around 185 mV vs. Cu/Cu$^{2+}$ with a charge density of 443 $\mu C$ cm$^{-2}$; that is in agreement with the theoretical value of 420 $\mu C$ cm$^{-2}$ for a (1x1) Cu overlayer on Pt(100). For the anodic Cu UPD stripping on Ru films deposited on stepped Pt single crystal vicinal to the (100) surface plane the charge density for the peak related

to Cu desorption from terrace sites decreases with increasing the step density of the Pt single crystal substrate. A smaller peak at 70 mV is related to Cu desorption from poly-crystalline Ru-domains (defects of the Ru quasi single crystal film). The linear relationship of the charge density with the step density suggests that after the Ru film preparation the terrace and step sites of the underlying Pt single crystal substrate are preserved, whereas free Pt domains are absent i.e. the Pt surface is completely covered by Ru.

The preliminary Cu UPD experiments are achieved to characterize the Pt sub-monolayer formed on the Ru film by galvanic replacement method. Cu UPD experiments showed that the Cu layer on the Pt/Ru/Pt single crystal surface is more stable than that on Ru film electrode since the Cu stripping peak is present at higher potential.

Finally, Cu UPD on Ru/Pt(hkl) and Pt/Ru/Pt(hkl) is very beneficial technique to characterize the surface structure.

# References:

[1]    H. A. Gasteiger, N. Markovic, P. N. Ross, and E. J. Cairns, Journal of Physical Chemistry 97:12020 (1993).

[2]    J. Clavilier, R. Faure, G. Guinet, and R. Durand, Journal of Electroanalytical Chemistry 107:205 (1980).

[3]    S. Motoo and N. Furuya, Journal of Electroanalytical Chemistry 167:309 (1984).

[4]    A. Hamelin, in Modern Aspects of Electrochemistry, Vol. 16 (B. E. Conway, R. E. White, and J. O. M. Bockris, eds.), Plenum Press, 1985, p. 4.

[5]    A. Hamelin, L. Doubova, D. Wagner, and H. Schirmer, Journal of Electroanalytical Chemistry 220:155 (1987).

[6]    M. Hourani and A. Wieckowski, Journal of Electroanalytical Chemistry 227:259 (1987).

[7]    K. Sashikata, N. Furuya, and K. Itaya, J. Vac. Sci. Technol. B 9:457 (1991).

[8]    W. F. Lin, M. S. Zei, Y. D. Kim, H. Over, and G. Ertl, Journal of Physical Chemistry B 104:6040 (2000).

[9]    W. F. Lin, P. A. Christensen, A. Hamnett, M. S. Zei, and G. Ertl, Journal of Physical Chemistry B 104:6642 (2000).

[10]   M. S. Zei and G. Ertl, Physical Chemistry Chemical Physics 2:3855 (2000).

[11]   N. S. Marinkovic, J. X. Wang, H. Zajonz, and R. R. Adzic, Journal of Electroanalytical Chemistry 500:388 (2001).

[12]   A. M. El-Aziz and L. A. Kibler, Electrochemistry Communications 4:866 (2002).

[13]   S. E. Huxter and G. A. Attard, Electrochemistry Communications 8:1806 (2006).

[14]   C. Nishihara and H. Nozoye, Journal of Electroanalytical Chemistry 386:75 (1995).

[15]   R. Francke, V. Climent, H. Baltruschat, and J. M. Feliu, Journal of Electroanalytical Chemistry and Interfacial Electrochemistry 624:228 (2008).

[16]   L. D. Burke, N. S. Naser, and R. Sharna, Journal of Applied Electrochemistry 38:377 (2008).

[17]   T. P. Moffat, M. Walker, P. J. Chen, J. E. Bonevich, W. F. Egelhoff, L. Richter, C. Witt, T. Aaltonen, M. Ritala, M. Leskela, and D. Josell, Journal of the Electrochemical Society 153:C37 (2006).

[18]   L. Guo, A. Radisic, and P. C. Searson, Journal of the Electrochemical Society 153:C840 (2006).

[19]   S. K. Cho, S. K. Kim, H. Han, J. J. Kim, and S. M. Oh, Journal of Vacuum Science & Technology B 22:2649 (2004).

[20]   D. Josell, D. Wheeler, C. Witt, and T. P. Moffat, Electrochemical and Solid State Letters 6:C143 (2003).

[21]   M. A. Quiroz, Y. Meas, E. Lamypitara, and J. Barbier, Journal of Electroanalytical Chemistry 157:165 (1983).

[22]   C. N. Nguyen Van Huong and M. J. Gonzalez-Tejera, Journal of Electroanalytical Chemistry 244:249 (1988).

[23]   E. M. Stuve, J. W. Rogers, D. Ingersoll, D. W. Goodman, M. L. Thomas, and M. T. Paffett, Chemical Physics Letters 149:557 (1988).

[24]   K. R. Zavadil, D. Ingersoll, and J. W. Rogers, Journal of Electroanalytical Chemistry 318:223 (1991).

[25]   J. Lei, S. Rudenja, N. Magtoto, and J. A. Kelber, Thin Solid Films 497:121 (2006).

[26]   J. Liu, J. Lei, N. Magtoto, S. Rudenja, M. Garza, and J. A. Kelber, Journal of the Electrochemical Society 152:G115 (2005).

[27]   J. Kelber, S. Rudenja, and C. Bjelkevig, Electrochimica Acta 51:3086 (2006).

[28]   A. Alakl, G. Attard, R. Price, and B. Timothy, Journal of the Chemical Society-Faraday Transactions 91:3585 (1995).

[29]   R. Michaelis, M. S. Zei, R. S. Zhai, and D. M. Kolb, Journal of Electroanalytical Chemistry 339:299 (1992).

[30]   N. M. Markovic and P. N. Ross, Journal of Vacuum Science & Technology a-Vacuum Surfaces and Films 11:2225 (1993).

[31]   H. Ogasawara, J. Inukai, and M. Ito, Surface Science 311:L665 (1994).

[32]   R. Gomez, H. S. Yee, G. M. Bommarito, J. M. Feliu, and H. D. Abruna, Surface Science 335:101 (1995).

[33]   T. Nagel, N. Bogolowski, and H. Baltruschat, Journal of Applied Electrochemistry 36:1297 (2006).

[34]   G. Gómez, J. M. Feliu, and H. D. Abruna, Langmuir 10:4315 (1994).

[35]   H. Hoster, B. Richter, and R. J. Behm, Journal of Physical Chemistry B 108:14780 (2004).

[36]   S. R. Brankovic, J. X. Wang, Y. Zhu, R. Sabatini, J. McBreen, and R. R. Adzic, Journal of Electroanalytical Chemistry 524:231 (2002).

[37]   J. X. Wang, N. S. Marinkovic, H. Zajonz, B. M. Ocko, and R. R. Adzic, Journal of Physical Chemistry B 105:2809 (2001).

[38]   N. Bogolowski, S. Huxter, A.-E.-A. A. Abd-El-Latif, G. A. Attard, and H. Baltruschat, Journal of Electroanalytical Chemistry 646:68 (2010).

[39]   C. L. Green and A. Kucernak, Journal of Physical Chemistry B 106:11446 (2002).

[40]   A. M. El-Aziz, R. Hoyer, and L. A. Kibler, Chemphyschem 11:2906 (2010).

[41]  J. Clavilier, K. E. Achi, and A. Rodes, Journal of Electroanalytical Chemistry 272:253 (1989).

[42]  A. Rodes, K. Elachi, M. A. Zamakhchari, and J. Clavilier, Journal of Electroanalytical Chemistry 284:245 (1990).

[43]  H. E. Hoster, A. Bergbreiter, P. M. Erne, T. Hager, H. Rauscher, and R. J. Behm, Physical Chemistry Chemical Physics 10:3812 (2008).

[44]  H. E. Hoster, M. J. Janik, M. Neurock, and R. J. Behm, Physical Chemistry Chemical Physics 12:10388 (2010).

[45]  S. R. Brankovic, J. X. Wang, and R. R. Adzic, Surface Science 474:L173 (2001).

## Chapter 6: New DEMS cell applicable to different electrode sizes

### 6.1  Introduction

The dual thin layer flow through cell for differential electrochemical mass spectrometry (DEMS) presented in chapter 2 can be used only for relatively large electrodes (diameter $\approx$ 1 cm) [1, 2]. On the other hand, bead electrodes with a diameter of 2-3 mm have become very popular in electrochemistry, because they are cheaper and more easily prepared. They can be easily used in the hanging meniscus arrangement. Kita and co-workers [3] developed an interface for on-line electrochemical mass spectrometry for bead single crystals in a hanging meniscus configuration based on a small Teflon tip that is used as inlet. A disadvantage of this setup is a long delay time $(10 - 15 \text{ s})$; also, it cannot be used for experiments under convection.

In the present chapter, a new DEMS cell design will be introduced that allows using the bead single crystal electrode surfaces with a small diameter in the usual arrangement of hanging meniscus under convective conditions.

The quality of the DEMS cell was checked by: a) the characteristic cyclic voltammograms of Pt single crystals, b) the reproducible calibration constant of DEMS ($K^*$) ($K^*$ was determined by the electrooxidation of a monolayer of $CO_{ad}$ or bulk oxidation of formic acid at different Pt surfaces) and c) the detected signal of the volatile products that are formed during the electrooxidation of small organic molecules at Pt bead crystals.

### 6.2 Description of the new cell

The new DEMS flow cell is mounted in combination with a Balzers quadrupole mass spectrometer (Balzer QMG-422) as shown in Fig. 6-1. For more details about the cell construction, see Fig. 2-15 in chapter 2. The distance between the electrode and the glass capillary should be very small (in the range of few micrometers). Thus, the bead crystal is fixed first at a special 3-D movable Teflon holder to control the position of the electrode centered at the glass capillary. The distance and the electrode position relative to the glass capillary are controlled using a magnifying lens before and during the experiments. In

147

this construction, it is important to ensure an identical flow rate of inlet and outlet electrolyte in order to keep electrolyte level constant and thus have a stable hanging meniscus for long time. The electrolyte was introduced into the cell by using vertical syringe pump (microlab®500, Hamilton). The redox products are transported from the working electrode surface through the glass capillary to the mass spectrometer compartment by convection, and then only the volatile products diffuse through the hydrophobic Teflon membrane (W. L. Gore & Associates GmbH Putzbrunn Germany) that is supported on a stainless steel frit and serve as the interface between electrolyte and vacuum. The electrolyte outlet is adjusted using peristaltic pump.
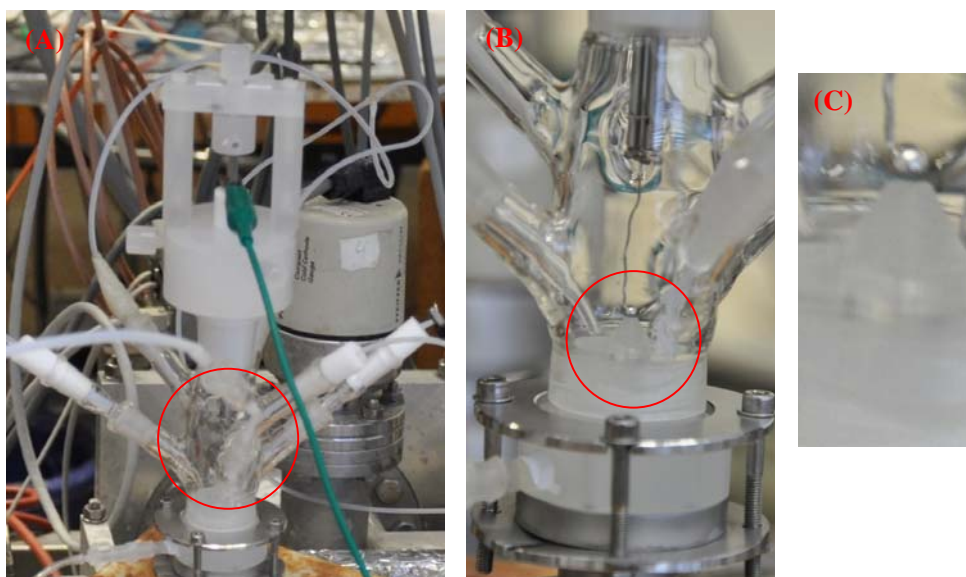


Figure 6-1: Photographs of a typical A) complete new DEMS cell connected to the mass spectrometer. B) and C) magnifications of A), the position of bead single crystal electrode directly centered on the glass capillary.

The construction of the electrochemical glass cell is shown in Fig. 6-1. The electrolyte volume is small (1-2 ml). The electrolyte is deaerated by argon in a separate glass bubbler before its introduction into the syringe pump and its further transfer to the glass cell. Two argon tubes are connected inside the glass cell, one introduced a bubble of argon directly underneath the electrolyte drop introduced with a flow rate 5 μL s$^{-1}$ and

another one with a moderate stream of argon above the electrolyte level to keep the electrode surrounding free from air.

## 6.3 Results and discussion

### 6.3.1 Characteristic CVs of Pt single crystal electrodes in DEMS cell

Before the electrooxidation experiments, the purity of the electrode surface is tested after annealing by recording the cyclic voltammogram in the base electrolyte in the conventional glass cell (H-cell). Keeping the electrode surface covered by a drop of a base electrolyte saturated with argon to protect the electrode surface from air, the crystal is transferred very fast to the DEMS cell and the CV is recorded in the base electrolyte and both CVs were compared as shown in Fig. 6-2.
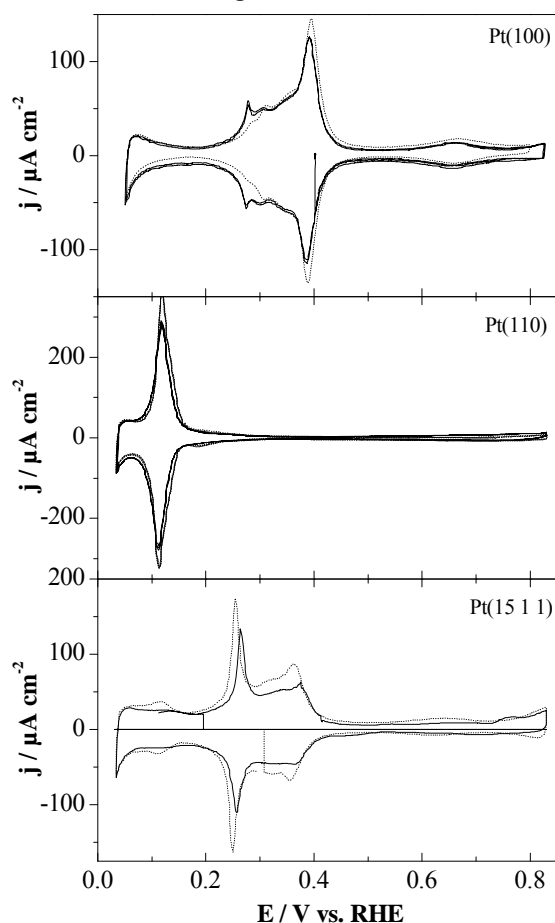


Figure 6-2: Cyclic voltammetry of Pt(100), Pt(110) and Pt(15 1 1) electrodes in 0.1 M $H_2SO_4$ in the new DEMS cell at u = 5 µL s$^{-1}$ (black line) and in a typical glass cell (dotted line) at sweep rate 50 mV s$^{-1}$.

The effects of electrolyte flow rate, distance between the electrode surface and the glass capillary and cleanliness of DEMS cell are performed. Fig. 6-2 shows the reproducible typical voltammetric profiles for different bead Pt single crystal electrodes in a hanging meniscus arrangement in 0.1 M $H_2SO_4$ at electrolyte flow rate of 5 µL $s^{-1}$ in DEMS cell and a glass cell (without convection), for comparison. The difference between the CVs for each single crystal depends on the velocity of transfer of the crystal from the glass cell to the DEMS cell in air environment. The CVs obtained are the typical ones for the respective single crystals in their quality and they are better than that observed in dual thin layer flow through cell.

### 6.3.2 Calibration of DEMS setup

#### *6.3.2.1 DEMS calibration by CO adlayer electrooxidation*

Adsorption and oxidation of CO adlayer at Pt surface is the standard experiment to check the quality of the DEMS setup and to calibrate the system [2, 4]. The electrooxidation of an adlayer of $CO_{ad}$ at Pt(pc) surface is performed at sweep rate 10 mV $s^{-1}$ and a flow rate 5 µL $s^{-1}$ according to the procedure mentioned before in chapter 2.

Figure 6-3 shows the CV and the MSCV for $CO_2$ during the stripping of $CO_{ad}$ from Pt(pc). For the oxidation of $CO_{ad}$, the potential was held at a potential between 40 and 70 mV and the supporting electrolyte was replaced by a CO saturated solution to form a monolayer of adsorbed CO; then it was replaced again with supporting electrolyte. The potential was swept in the positive direction with a scan rate of 10 mV $s^{-1}$, to oxidize the adsorbed CO to $CO_2$. The recorded CV and MSCV for CO adlayer oxidation are in agreement with the previous published results for different DEMS cells [2, 4-7]. The main characteristic feature for this new cell is the difference between the location of the peak potential in the CV and the MSCV, which indicates to the short delay time in the range of 2 s. The calibration constant ($K^* = 3.35E-6$) is nearly the same as calibration constant in dual thin layer flow through cell ($K^* = 4E-6$). Both experiments are done on the same day.
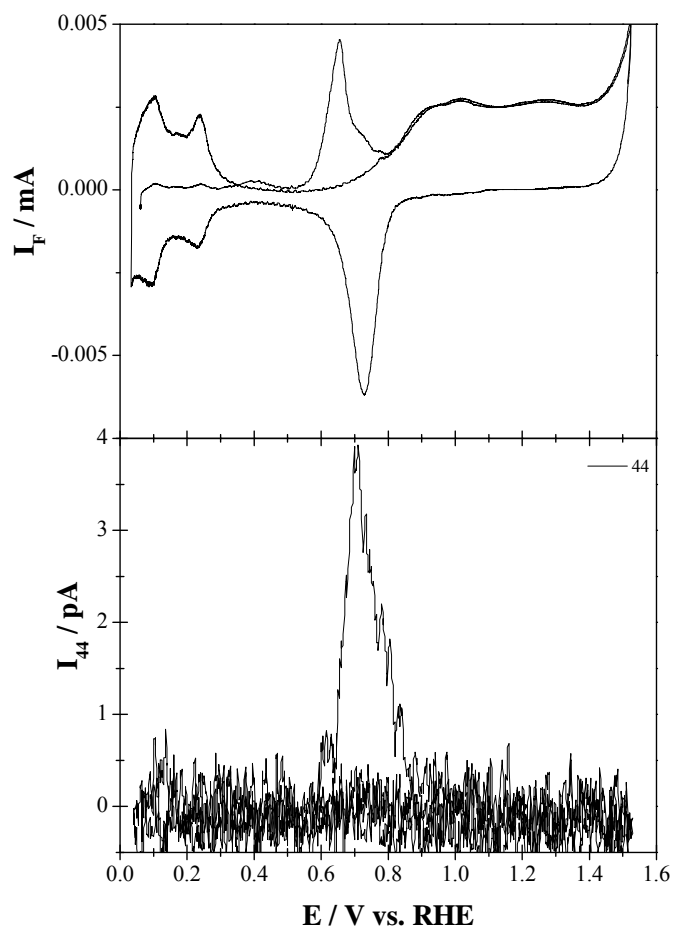
Figure 6-3: Simultaneously recorded CV and MSCV for m/z = 44 during the stripping of CO adlayer in 0.1 M $H_2SO_4$ on Pt(pc) electrode at sweep rate 10 mV $s^{-1}$ and a flow rate 5 $\mu L\ s^{-1}$.

### 6.3.2.2 DEMS calibration by formic acid electrooxidation

The main disadvantages of DEMS setup calibration with $CO_{ad}$ oxidation are as follows: first, the small corresponding ionic current of $CO_2$ due to the small surface area of the electrode and second, the position of the electrode used in DEMS calibration (polycrystalline Pt) and working electrode of organic molecule oxidation (Pt single crystal) relative to glass capillary is not identical. The possible influence of this position on the calibration constant, in particular the transfer efficiency, has to be elucidated.

To overcome these problems and calculate the accurate calibration constant, the electrooxidation of formic acid is performed after each organic compound oxidation under

the same experimental conditions. The electrooxidation of 0.1 M formic acid at different Pt surface was done assuming the complete oxidation of formic acid to carbon dioxide.

Figure 6-4 shows an example for this calibration procedure after the electrooxidation of methanol at a roughened Pt(15 1 1). The calculated $K^*$ value from the electrooxidation of bulk formic acid on roughened Pt(15 1 1) is 1.7E-6. This calibration constant is much lower than that was obtained from the electrooxidation of $CO_{ad}$ at Pt(pc) due to the difference of the Pt surface orientation, the relative position to glass capillary, the oxidant species and finally the difference in the filament efficiency due to long period between both experiments.
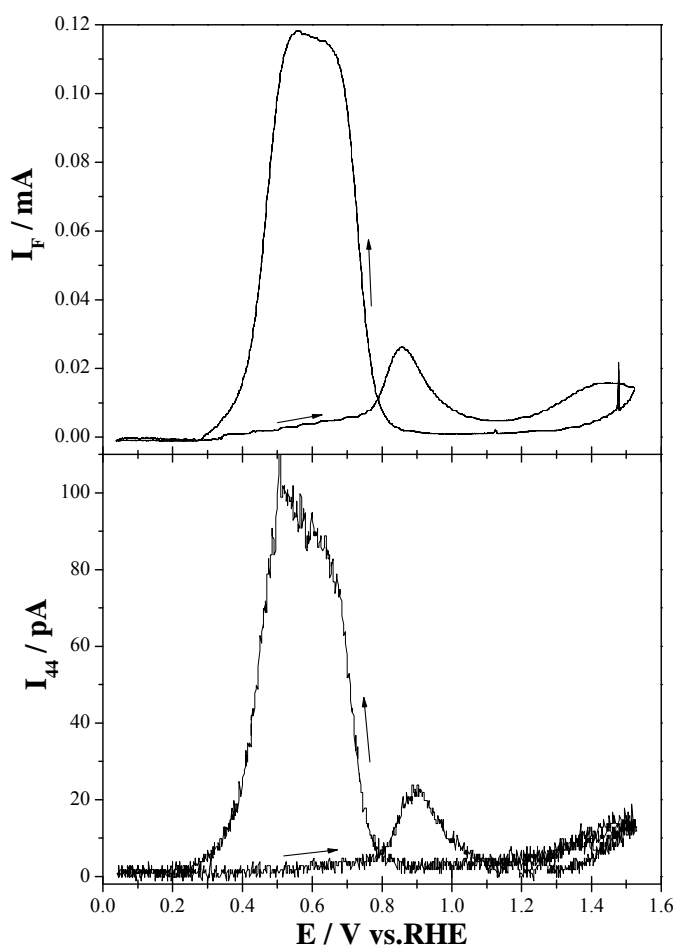


Figure 6-4: Simultaneously recorded CV and MSCV for m/z = 44 during the electrooxidation of bulk 0.1 M formic acid in 0.1 M $H_2SO_4$ on roughened Pt (15 1 1) electrode at scan rate 10 mV s$^{-1}$ and a flow rate 5 µL s$^{-1}$.

152

### 6.3.2.3 DEMS calibration by hydrogen evolution

Another way to check the cleanliness and calibration of DEMS setup is the hydrogen evolution at Pt surface. Fig. 6-5 shows the typical potential program and the recorded faradaic current and the corresponding ionic current of m/z = 2 during the potential scan and potential hold at -30 and -40 mV for 30 s in 0.1 M $H_2SO_4$ at Pt(15 1 1). The applied potential is swept in the negative going potential to potential lower than the Nernest equilibrium potential of hydrogen. The calculated calibration constant is very similar to that for formic acid oxidation on the same Pt surface (1.64E-6). The investigated delay time is about 2 s at a flow rate 5 µL s$^{-1}$.
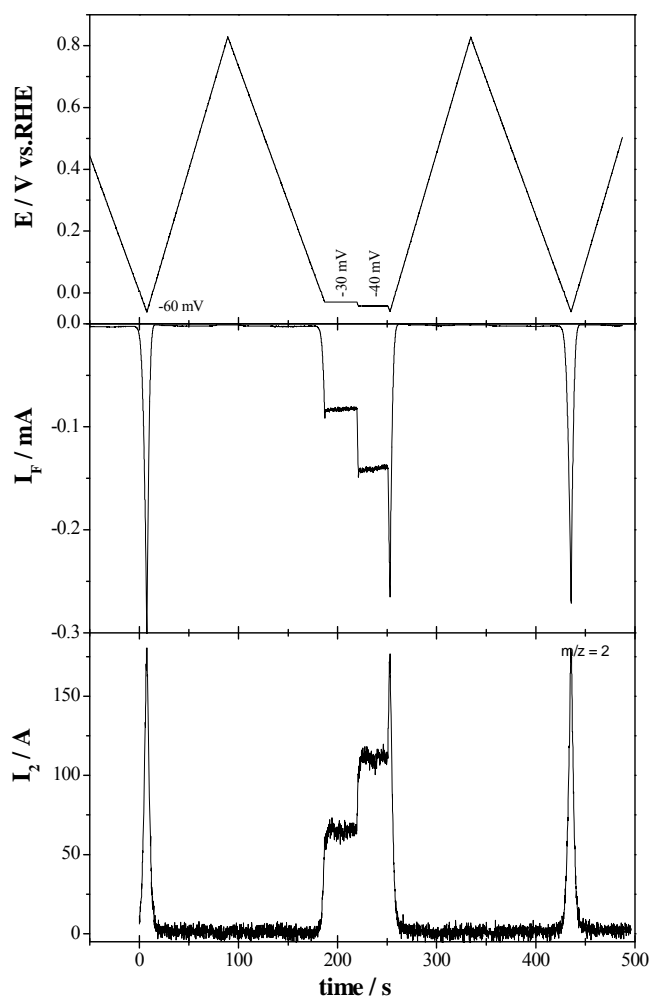


Figure 6-5: Simultaneously recorded faradaic and ionic currents for m/z = 2 during the evolution of $H_2$ in 0.1 M $H_2SO_4$ on Pt(15 1 1) electrode at sweep rate 10 mV s$^{-1}$ and a flow rate 5 µL s$^{-1}$.

153

### 6.3.3 Electrooxidation of small organic molecules

In order to test the performance of DEMS cell, the electrooxidation of small organic molecules (formic acid, formaldehyde and methanol) at Pt(15 1 1) are performed.

#### *6.3.3.1 Electrooxidation of formic acid*

Figure 6-6a shows CV and MSCV for the electrooxidation of 0.1 M formic acid at smooth Pt(100), Pt(15 1 1) and Pt(711). In the positive going scan, a low oxidation current is visible above 0.3 V due to the blocking of the surface by adsorbed CO at low potentials and the strongly bound water species at 0.8 V [8-11]. In the negative going sweep, the oxidation current increased due to the desorption of previously bound water structures and the oxidation of previously adsorbed CO until the highest current value (potential peak at 0.45 V). At potential lower than 0.45 V, the current diminishes again due to the further accumulation of CO.
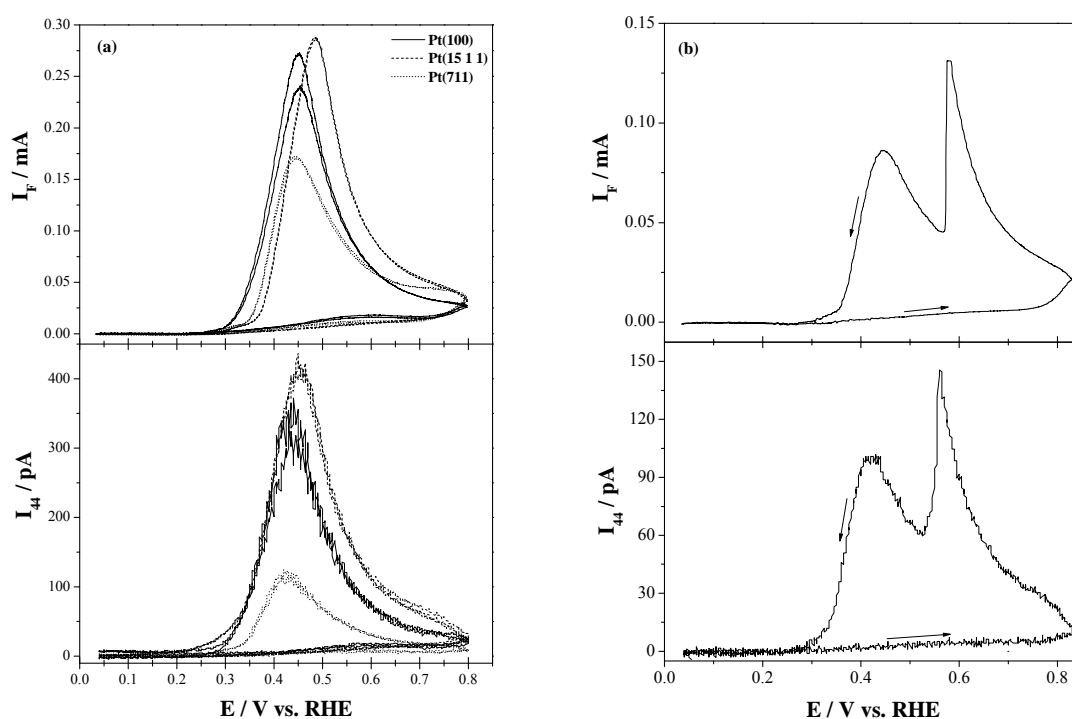


Figure 6-6: Simultaneously recorded CV and MSCV for m/z = 44 ($CO_2$) during the electrooxidation of bulk formic acid at (a) Pt(100), Pt(15 1 1) and Pt(711) and (b) other experiment for Pt(15 1 1) in 0.1 M HCOOH + 0.1 M $H_2SO_4$ solution. Scan rate: 10 mV s$^{-1}$. Electrolyte flow rate: 5 μL s$^{-1}$.

The electrooxidation of formic acid is proceeds through dual pathways; the direct pathway that involves the direct oxidation of formic acid to $CO_2$ via adsorbed formate as an active intermediate [12] is given by Eq.1

$$HCOOH \longrightarrow \text{active intermediate} \longrightarrow CO_2 + 2H^+ + 2e^- \qquad (1)$$
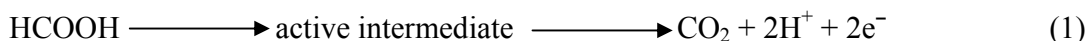
The formation of adsorbed CO at the surface was donated as indirect pathway according to Eq. 2.

$$HCOOH \longrightarrow CO_{ad} + H_2O \qquad (2)$$

Fig. 6-6a shows that the catalytic activity of Pt(15 1 1) towards formic acid oxidation is similar to that for Pt (100). For the small terraces width electrode, Pt(711), the catalytic activity for HCOOH oxidation is diminished in agreement with the results of Feliu and co-workers obtained for Pt(s)[n(100)x(111)] electrodes with n = 2 to n = 20 as shown in Fig. 6-7 [11]. They attributed the similar activity of Pt(100) and Pt(15 1 1) towards formic acid oxidation to the lifting of the reconstruction of Pt(100) in contact with solution. The surface with a wide (100) terrace, the reconstruction does not take place until n = 7. At n < 7, the catalytic activity of formic acid oxidation at high stepped Pt surfaces is decreased due to the faster poisoning of these surfaces [11].
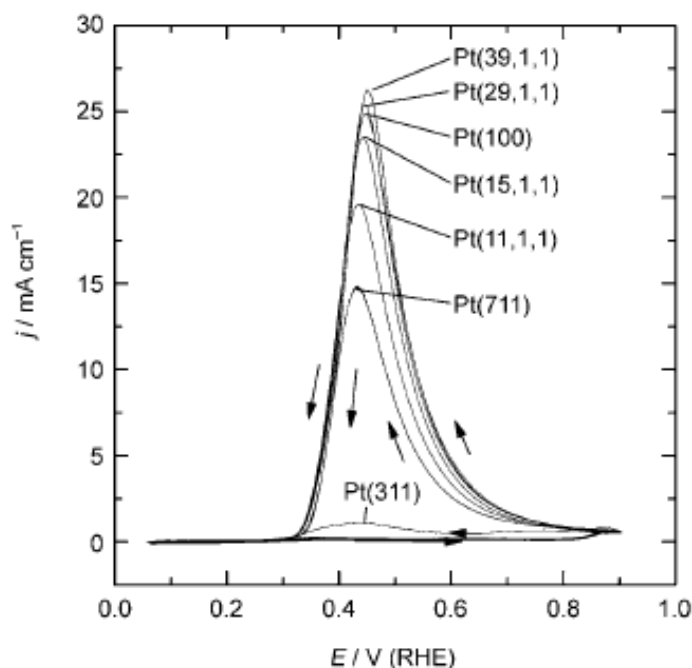


Figure 6-7: The voltammetric profile of the Pt(2n-1,1,1) electrodes in 0.5 M $H_2SO_4$ + 0.1 M HCOOH. Scan rate: 50 mV s$^{-1}$. Reprinted from ref. [11].

Figure 6-6b shows an other experiment for the electrooxidation of 0.1 M HCOOH at Pt(15 1 1) surface. During the negative going sweep, the splitting of the oxidation peak into separate two peaks at 0.44 and 0.58 V is observed, which is caused by oscillatory instabilities due to a high electrolyte resistance [13, 14]. The identical peak shape even of the sharp peak is an indication for the suitability of the setup.

### 6.3.3.2 *Electrooxidation of formaldehyde*



Figure 6-8: Simultaneously recorded CV and MSCVs for m/z = 44 (CO$_2$) during the electrooxidation of bulk formaldehyde at smooth Pt(15 1 1) in 0.1 M formaldehyde + 0.1 M H$_2$SO$_4$ solution. Scan rate: 10 mV s$^{-1}$. Electrolyte flow rate: 5 µL s$^{-1}$.

Figure 6-8 shows the CV and MSCV for m/z = 44 for the electrooxidation of 0.1 M HCHO in 0.1 M H$_2$SO$_4$ at smooth Pt(15 1 1). The faradaic and ionic currents are negligible at potentials lower than 0.4 V due to the blocking of the surface by the strongly adsorbed CO on the steps and the terraces of Pt(15 1 1) in the positive going sweep. The indirect pathway of formaldehyde oxidation reduces the catalytic activity of the Pt surface. The onset potential of the CO$_{ad}$ oxidation is about 0.4 V and the main oxidation

156

peak is present at 0.65 V with further increase in the current until upper potential limit. During the negative going sweep, the oxidation peak is present at 0.6 V.

The calculated current efficiency with respect to $CO_2$ is 10%. This means that the rest of oxidation product only is formic acid is agreement with previous literature [15, 16]. However, since the calibration constant was obtained by the electrooxidation of $CO_{ad}$ on polycrystalline Pt at position not identical to that of the Pt(15 1 1), the above value for the current efficiency is only a rough estimate.

### 6.3.3.3 Electrooxidation of methanol
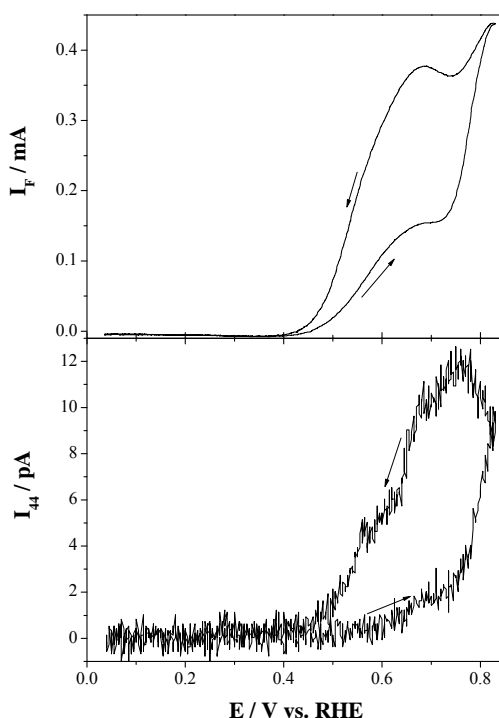


Figure 6-9: Simultaneously recorded CV and MSCV for m/z = 44 ($CO_2$) during the electrooxidation of bulk methanol at smooth (a) Pt(100) and (b) Pt(15 1 1) in 0.1 M $CH_3OH$ + 0.1 M $H_2SO_4$ solution. Scan rate: 10 mV $s^{-1}$. Electrolyte flow rate: 5 μL $s^{-1}$.

Figure 6-9 shows the CV and the corresponding MSCV of m/z = 44 for the electrooxidation of 0.1 M methanol in 0.1 M $H_2SO_4$ at smooth Pt (100) and Pt(15 1 1). In the positive going scan, both surfaces are blocked by the strongly adsorbed methanol adsorbate species like $CO_{ad}$, the faradaic and ionic currents are negligible below 0.7 V. At a

potential higher than 0.7 V the currents start to increase sharply due to the electrooxidation of this adsorbates at that potential, after that the currents diminish again because of the strongly interaction of water structures ($OH_{ad}$) with Pt surface formation [11, 17]. In the negative going scan, the increase of faradaic and ionic currents are ascribed to the desorption of the strongly bound water and the continuous oxidation of methanol.

The calculated current efficiency with respect to $CO_2$ at a peak potential is 48 % for Pt(100) and 60% for Pt(15 1 1). The methylformate is not detected by mass spectrometry because the sensitivity of mass spectrometry is not high enough to detect the small amount of methylformate produced at such small surface area.
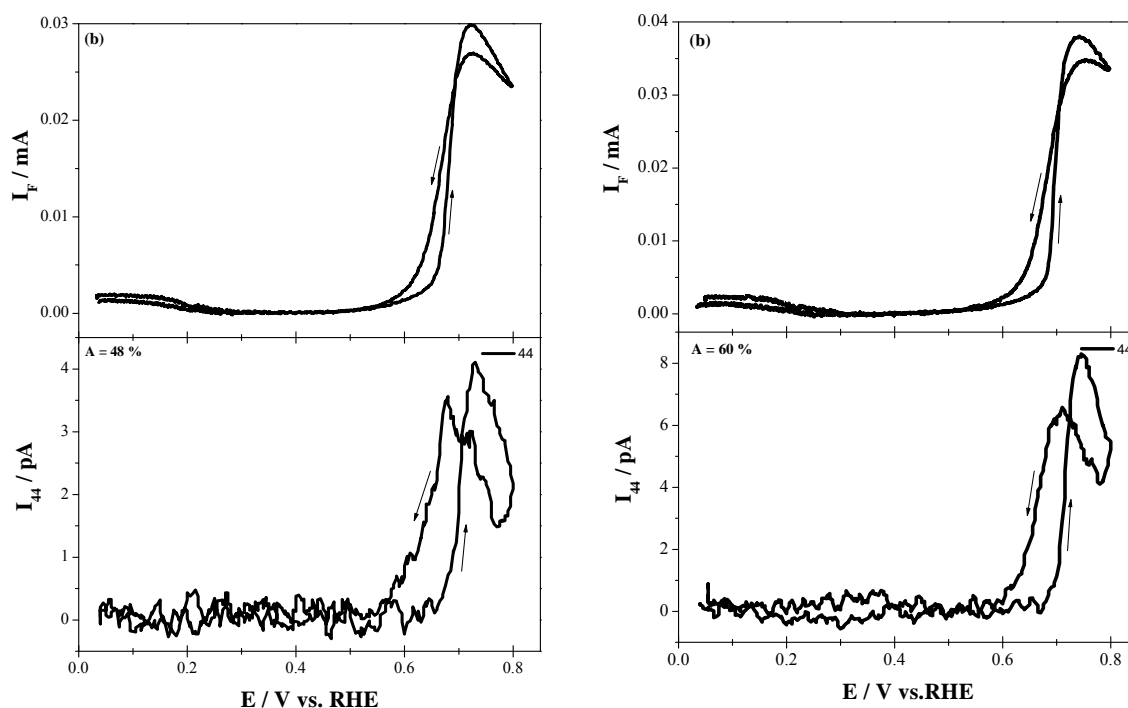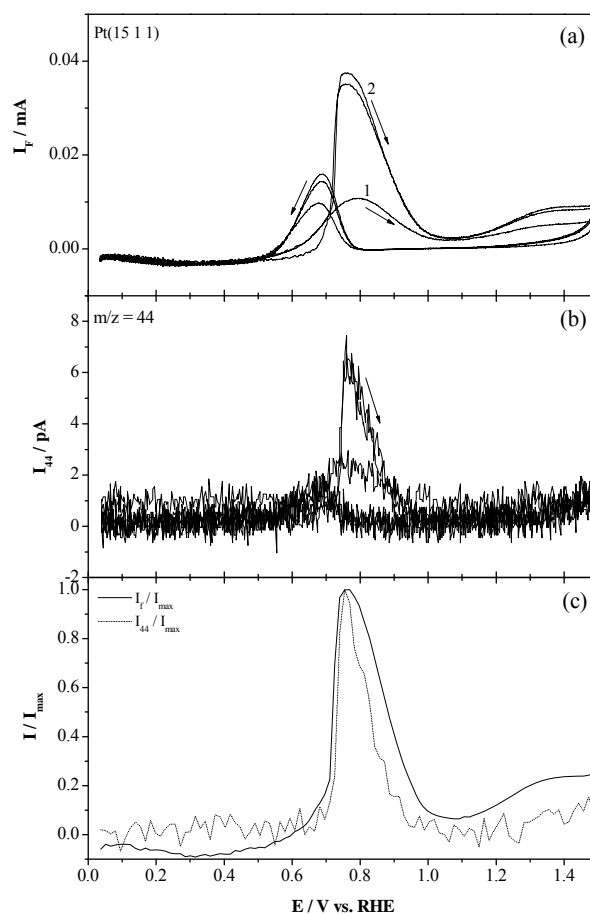


Figure 6-10: Simultaneously recorded (a) CV and (b) MSCV for m/z = 44 ($CO_2$) during the electrooxidation of bulk methanol at Pt(15 1 1) in 0.1 M $CH_3OH$ + 0.1 M $H_2SO_4$ solution. Scan rate: 10 mV s$^{-1}$. Electrolyte flow rate: 5 $\mu$L s$^{-1}$. (c) The normalized faradaic and ionic currents in the second anodic sweep.

Figure 6-10 shows the CV and the corresponding MSCV for m/z = 44 during the electrooxidation of methanol at Pt(15 1 1) electrode with an upper potential limit of 1.5 V. Both the faradaic and ionic currents increase after the first extension of the sweep into the oxygen region due to the introduction of defects into the surface. The calculated current efficiency with respect to $CO_2$ at a peak potential is 49 %. The normalized faradaic and ionic currents (Fig. 6-10c) show that the ionic current of $CO_2$ diminishes prior to the faradaic current at the positive side of the oxidation peak. It is believed that this difference is due to the formation of non-volatile products in that potential range (mainly formaldehyde and formic acid). This confirms the results of chapter 3 where the formation of formaldehyde and formic acid were suggested during the electrooxidation of methanol at Pt(pc). A comparison of the sweep before the extension into the oxygen adsorption region and thereafter shows that roughening shifts the onset of oxidation to higher potentials: poisoning of the surface is more severe for the roughened surface.

## 6.4 Conclusions

In this chapter, a new DEMS cell, which is applicable for bead single crystal electrodes in hanging meniscus arrangement under convection conditions with short delay time, is introduced.

The performance of the new cell was tested by recording the cyclic voltammograms of different Pt bead single crystals in 0.1 M $H_2SO_4$ as a supporting electrolyte. The characteristic CVs of these electrodes are in agreement with those obtained in the conventional glass cell and in agreement with literature profiles.

The calibration of the DEMS setup was done by electrooxidation of CO adlayer or electrooxidation of bulk formic acid. Calibration by electrooxidation of formic acid has the advantage that it can be done after the experiment itself without changing the electrode position. The most important parameters in the new setup are how to control: a) the flow rate of electrolyte (identical at inlet and at outlet) to keep the connection and hanging meniscus arrangement of the working electrode, b) the position and distance of the crystal relative to the glass capillary.

The $K^*$ values are reproducible and typical to those of the dual thin layer flow through cell under the same conditions. The current efficiency with respect to $CO_2$, during the

electrooxidation of bulk methanol at Pt(pc) in the new flow cell, is higher than that in the previous cell design. The reason might be the further oxidation of the soluble intermediates (formic acid and formaldehyde) because of a less efficient electrolyte flow in the thin layer between the electrode surface and the glass capillary. Also, the ionic signal of methylformate is not detected under the same experimental conditions due to the small surface area of the working electrode resulting in a small amount of product.

## References:

[1] Z. Jusys, H. Massong, and H. Baltruschat, Journal of the Electrochemical Society 146:1093 (1999).

[2] H. Baltruschat, Journal of the American Society for Mass Spectrometry 15:1693 (2004).

[3] Y. Gao, H. Tsuji, H. Hattori, and H. Kita, Journal of Electroanalytical Chemistry 372:195 (1994).

[4] H. Baltruschat, in Interfacial Electrochemistry (A. Wieckowski, ed.), Marcel Dekker, Inc., New York, Basel, 1999, p. 577

[5] O. Wolter and J. Heitbaum, Ber. Bunsenges. Phys. Chem. 88:6 (1984).

[6] Z. Jusys and R. J. Behm, Journal of Physical Chemistry B 105:10874 (2001).

[7] A. H. Wonders, T. H. M. Housmans, V. Rosca, and M. T. M. Koper, Journal of Applied Electrochemistry 36:1215 (2006).

[8] K. Kunimatsu, Journal of Electroanalytical Chemistry 213:149 (1986).

[9] J. Clavilier, Journal of Electroanalytical Chemistry 236:87 (1987).

[10] S.-C. Chang, L.-W. H. Leung, and M. J. Weaver, Journal of Physical Chemistry 94:6013 (1990).

[11] V. Grozovski, V. Climent, E. Herrero, and J. M. Feliu, ChemPhysChem 10:1922 (2009).

[12] Y. X. Chen, A. Miki, S. Ye, H. Sakai, and M. Osawa, Journal of the American Chemical Society 125:3680 (2003).

[13] P. Strasser, M. Lubke, F. Raspel, M. Eiswirth, and G. Ertl, Journal of Chemical Physics 107:979 (1997).

[14] K. Krischer, N. Mazouz, and P. Grauel, Angewandte Chemie-International Edition 40:851 (2001).

[15] E. A. Batista and T. Iwasita, Langmuir 22:7912 (2006).

[16]   G. Samjeske, A. Miki, and M. Osawa, Journal of Physical Chemistry C 111:15074 (2007).

[17]   I. C. Yeh and M. L. Berkowitz, Journal of Electroanalytical Chemistry 450:313 (1998).

# Chapter 7: Summary and outlook

Pt is considered as a model for fuel cell electrocatalysts. In the present thesis, I studied the electrooxidation mechanisms of methanol (chapter 3) and ethanol (chapter 4) on different Pt surfaces, using a dual thin-layer flow through cell combined with the mass spectrometer. In chapter 5, Ru quasi single crystal films on different bead Pt surfaces were formed using the resistive heating in a stream of nitrogen. The Ru films were examined by cyclic voltammetry in sulfuric acid and by structure-sensitive underpotential deposition of Cu. Finally, in chapter 6, in order to use bead single crystal in the right arrangement (hanging meniscus) on DEMS, a new DEMS flow cell was manufactured and improved for that purpose.

The electrooxidation of methanol proceeds via the dual pathway mechanism. The path involving the formation of soluble intermediates such as formaldehyde and formic acid is the direct pathway, while the dehydrogenation of methanol to adsorbed CO followed by its oxidation to $CO_2$ is referred to as indirect pathway. Methylformate is one of the volatile products formed during the electrooxidation of methanol at Pt surfaces. In all previous articles it is assumed that methylformate formation results from the reaction of formic acid and the excess of methanol, i.e. the detection of methylformate is an indirect way to determine the amount of formic acid produced during the oxidation reaction. However, the probability of esterification reaction is very small because the fast diffusion of the soluble products away from DEMS cell under effect of continuous electrolyte flow. A simple kinetic study of methanol esterification and methylformate hydrolysis in acid media was performed since literature data for the rate of this esterification reaction were not available. The reaction rate constant of methylformate formation was found to be far too low ($\tau \approx 40$ h at 0.1 mol $L^{-1}$ methanol), while the time constant of dual-thin layer flow through cell at 1.6 $\mu$L $s^{-1}$ is 5 s. Methylformate therefore is directly formed during oxidation of methanol at the electrode surface and not in the solution phase as believed before, with a current efficiency about 1%.

The suggested mechanism for methylformate formation, as shown in Fig. 7-1, is the nucleophilic attack of adsorbed methanol with another methanol molecule from the solu-

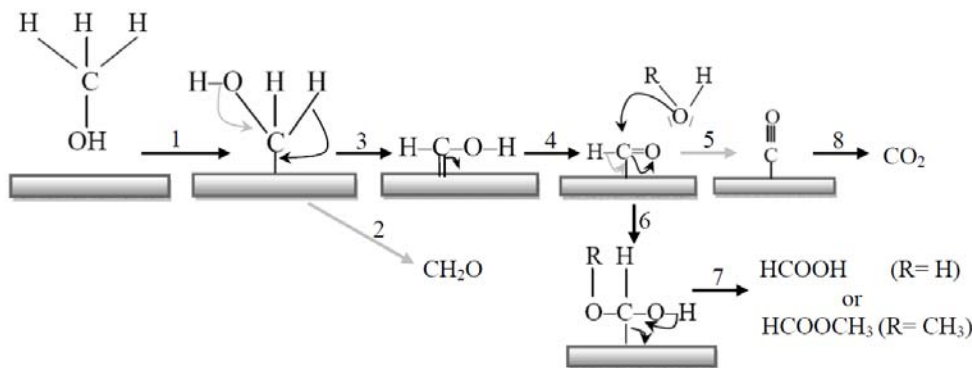tion; note that the nucleophilic power of the oxygen in methanol is higher than that in the water molecule.



Figure 7-1: The mechanism of methanol oxidation and methylformate formation

The current efficiency with respect to $CO_2$ and the surface coverage with methanol adsorbate ($CO_{ad}$) have been shown to be independent of the electrolyte flow rate (from 1.6–30 $\mu L\ s^{-1}$); this confirms the parallel pathway mechanism.

Poisoning of the catalyst with adsorbed CO is one of the main problems in fuel cells. Ru as a catalyst with Pt promotes the electrooxidation of adsorbed CO according to bifunctional and the electronic mechanism. On such bimetallic surfaces, Ru is preferentially deposited at steps. Using deliberately stepped Pt surfaces as model electrodes, it could be shown that the complete coverage of the step sites with Ru has an inhibiting effect for methanol and ethanol oxidation due to the blockage of the most active sites, i.e. the free step sites are necessary for the first step of $C_1$ and $C_2$ alcohols adsorption and oxidation.

For ethanol, the cleavage of C–C bond is the most difficult step in the complete oxidation of ethanol to $CO_2$. Also ethanol electrooxidation at Pt surfaces occurs according to different pathways depending on the surface structure. During the electrooxidation under controlled convection, where there is no further oxidation of soluble products at the surface, acetaldehyde is the main product at polycrystalline Pt and Pt stepped single crystal surfaces vicinal to the (100) plane. Acetaldehyde is formed at these surfaces over the potential range with a current efficiency close to 100%.

At Pt stepped single crystals vicinal to the (111) plane, the formation of acetic acid proceeds at lower potentials than that of acetaldehyde production due to the direct reac-

164

tion between adsorbed ethanol and adsorbed hydroxide species (cf. the reaction mechanism in Fig. 7-2). At higher potentials, due the blockage of the surface with adsorbed anions, e.g. acetate and sulfate, only the dehydrogenation of ethanol takes place at (111) planes to produce acetaldehyde.
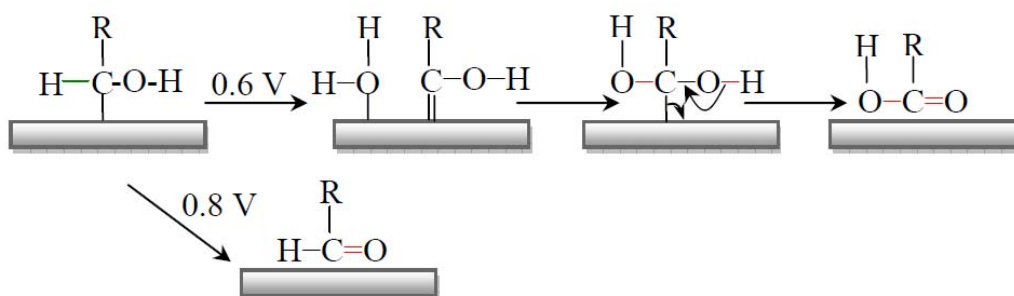
Figure 7-2: Schematic mechanism for acetic acid formation during ethanol oxidation.

In practical applications, the formation of acetic acid should be avoided because of its inertness whereas, in principle, acetaldehyde can be oxidized to $CO_2$. Therefore, it might be advantageous to use nanoparticles without a large degree of (111) facets as electrocatalyst in fuel cells.

Another kind of model electrode would be Ru single crystals modified by Pt. However, since Ru is oxidized by atmospheric oxygen very fast, the usual flame annealing method in air does not work. Attard and co-workers developed a new method for Ru quasi single crystal preparation by forced deposition of Ru multilayer on Pt single crystals followed by resistive heating in a nitrogen atmosphere. In order to characterize this Ru film on different Pt single crystals, Cu UPD is the suitable technique.

For Pt(100), the charge density of Cu UPD stripping from Ru quasi-single-crystal electrode is in agreement with the charge density of Cu UPD stripping from clean Pt(100); this suggests the formation of an epitaxial Ru film on the Pt(100) electrode. For the Ru films formed on Pt(111) and Pt(110) surfaces, Cu UPD deposition is inhibited due to strongly adsorbed oxygen species.

For Ru films deposited on stepped Pt single crystal vicinal to the (100) plane, it was found that:

- Because the characteristic Cu UPD stripping peak related to the free Pt sites is absent, the stepped Pt single crystal surfaces are completely covered with Ru film.

- The charge density for the peak at 185 mV related to Cu UPD stripping from (100) terrace sites decreases linearly with increasing the step density of the Pt single crystal substrate, which confirms the formation of epitaxial Ru films on the Pt surfaces.

Preliminary results show that the deposition of a Pt sub-monolayer on the Ru film is possible by galvanic replacement of Cu UPD.

In order to be able to use bead single crystals in the hanging meniscus configuration, a new DEMS cell was constructed. The recorded cyclic voltammogrames for different bead Pt single crystals in supporting electrolyte, under hanging meniscus arrangement and at constant flow of electrolyte, are in agreement with literature profiles. This and the calibration constant and corresponding ionic signals for organic molecules oxidation suggest that this new cell is well suited for bead single crystals. Compared with the dual thin layer flow through cell, it has the advantage that cleanliness is easier achieved and that less expensive single crystals can be used.

The $K^*$ values are reproducible and typical to that of the dual thin layer flow through cell under the same experimental conditions. For the electrooxidation of bulk methanol at polycrystalline Pt in the new flow cell, the current efficiency with respect to $CO_2$ is higher than that in the previous cell design. The reason might be the further oxidation of the soluble intermediates because of a less efficient electrolyte flow in the thin layer between the electrode surface and the glass capillary. Also, the ionic signal of methylformate is not detected under the same experimental conditions due to the small surface area of the working electrode resulting in a small amount of product.

For future work, the following experiments would be most interesting:

- While the Ru film was characterized in this study only by CV in supporting electrolyte and Cu UPD, more direct information about the surface structure and the topography of this film will be obtained by STM and AFM studies.

- Also the Pt sub-monolayer on Ru quasi single crystal electrode obtained by forced deposition or galvanic replacement has to be characterized by STM to know how Pt is distributed on the surface.

- The electrocatalytic activity of Ru quasi-single crystal films (Ru/Pt(hkl)) and the Pt sub-monolayer deposit on these films toward the electrooxidation of CO as well as the electrooxidation of $C_1$ and $C_2$ alcohols should be studied. Those experiments should be done under stagnant conditions (in H-cell) and at electrolyte flow using the new DEMS cell.

- Improve the construction of the new DEMS cell by:

  - Direct attachment of the electrolyte vessel to the DEMS cell to reduce the time of electrolyte change as well as to reduce the electrolyte path to diminish the amount of dissolved oxygen.

  - Use glass windows in the cell to adjust the position and height of electrode surface relative to the glass capillary.

  - Use a reflected laser beam to monitor the position of the electrode surface.

## Acknowledgement

I would like to express my sincere gratitude and appreciation to my research advisor, **Prof. Helmut Baltruschat**. I am greatly indebted to Prof. Baltruschat for his support, guidance, and assistance in all the work that I have accomplished. His leadership and dedication inspire us all to excel in everything that we do.

My gratitude and appreciation is also extended to the other member of my thesis committee, Prof. Wandelt, Prof. Waldvogel and Prof. Maier. I would like to thank them for their willingness to take the time to oversee the development and evaluation of this thesis.

Special thanks are due to Prof. Gary Attard and his group in Cardiff University for providing collaboration and instrumentation for a considerable part of the work presented in this thesis. His knowledge and technical expertise have been invaluable resources, and his help is greatly appreciated.

I would also like to extend my sincere thanks to Nicky Bogolowski for his collaboration on Cardiff work, working assistance whenever necessary, and for sharing his scientific knowledge (some of his working figures are included in chapter 5). I thank Dr. Ernst (my old brother) for his valuable discussions and knowledge pertaining to this research and other areas of chemistry.

All my great thanks to my colleagues Ana and Mehdi for checking my thesis and spending time on it. My thanks are also for the former and present members of electrochemistry department. Micheal, Barbora, Wang, Nikolay, Sevda, Ehab, Sabina, Johannes, Xu, Jan, Shahed, Christoph and as well as Frau Kleine for their friendship and help.

Thanks are also given to the members of mechanical, electronic and glass workshops, especially Mr. Königshoven, Mr. Backhausen, Mr. Bömher and Mr. Langen, for their supporting, helping and constructing the fine cells and repairing devices.

I thank the Egypt Government for funding this research for four years. I extend my sincere thanks to the staff of the Egypt Cultural Bureau in Berlin, especially, Prof. Tag-Eldin and Mrs. Thanaa for support and assistance.

I would like to thank my immediate and extended family and friends for loving, supporting, and encouraging me throughout my educational career.

I acknowledge my gratitude to my wife, for her endless patience, emotional, and motivational support that helped me reach all my goals so far.

**Finally, this study would not have been completed without the help of ALLAH.**

Abd El Aziz

## Publications

1. Critical pitting temperature of Type 254 SMO stainless steel in chloride solution, Corros. Sci. 49 (2007) 263-275.
2. Crevice corrosion of Type 254 SMO stainless steel in seawater, EUROCORR 2005 Annual conference, Portugal.
3. Electrochemical and SEM study on Type 254 SMO stainless Steel in chloride solutions, Corros. Sci. 46 (2004) 2431-2444.
4. Copper underpotential deposition on Ru quasi-single-crystal films; J. Electroanal. Chem., 646 (2010) 68-74.
5. Electrooxidation of ethanol at polycrystalline and platinum stepped single crystals: A study by differential electrochemical mass spectrometry; Electrochim. Acta, 55(2010) 7951-7960.
6. Formation of methylformate during methanol oxidation revisited: the mechanism; accepted in J. Electroanal. Chem.
7. New DEMS cell applicable to different electrode sizes; submitted to Electrocatalysis.

## Conferences and poster contribution

1. International Symposium" Templates in Chemistry and Beyond" SFB 624, 13-14 September 2007, Bonn, Germany.
2. 3$^{rd}$ Euregio Workshop-AGEF Seminar "Interfacial Electrochemistry" 2-3 June 2008, Roduc Abbey, Kerkrade, Netherlands.
3. **"Electrooxidation of ethanol on Pt(332) and Ru modifiedPt(332) electrodes: DEMS study"** GDCh, Electrochemistry: Crossing boundaries, 6$^{th}$ - 8$^{th}$ October 2008, Giessen, Germany.
4. **"Bimetallische Katalysatoren an vicinal gestufen Einkristalloberflächen"** Template Funktionale Chemische Schablonen SFB 624, 27-28.01.2009, Bonn, Germany.
5. **"Electrooxidation of ethanol on Pt(332) and Ru modifiedPt(332) electrodes: DEMS study"** Bunsentagung 2009, 21-23 May 2009, Koeln Universitaet.
6. **"Cu and Ag upd on stepped Pt surfaces vicinal to the (100) plane and Ru quasi single-crystal films"** Electrocatalysis: Molecular level approach to modern application; 22-25 August 2010, Kloster Irsee.

7. **"Electrooxidation Methanol and Ethanol: adsorption rates and rates of intermediate formation at Pt single crystal electrodes"** Electrochemistry 2010: From microscopic understanding to global impact, 13$^{th}$ -15$^{th}$ September 2010, RUHR Universitaet Bochum, Germany.

8. **"Oxidation reactions at Pt(s)[(100)x(111)] surfaces"** Electrochemistry from biology to physics, The 61st annual meeting of the international society of electrochemistry, 26 Sep.-1 Oct. 2010, Nice, France.

9. **"DEMS study on methanol electrooxidation at monocrystalline platinum electrodes: The effect of adsorption time, surface structure, Ru adatom and potential"** Electrochemistry from biology to physics, The 61$^{st}$ annual meeting of the international society of electrochemistry, 26 Sep.-1 Oct. 2010, Nice, France.

## Lecture contributions

1. **"Ethanol and methanol: Adsorption rates and rates of intermediate formation at Pt single crystal electrodes"** 216$^{th}$ ECS meeting, 4-9 October 2009, Vienna, Austria.

2. **"Electrooxidation of small organic molecules at platinum single crystal electrodes and BDD: DEMS study"** Winter school of electrochemistry, 6-11 Feb. 2010, Kleinwalseltal, Austria.

3. **"Electrooxidation of ethanol on Pt(332) and Ru modifiedPt(332) electrodes: DEMS study"** Recent Advances in Electrocatalysis and Photoelectrocatalysis, 7$^{th}$ spring meeting of ISE, 22-25 March, 2009, Szczyrk, Poland.

4. **"Stepped surfaces as templates for the generation of ordered bimetallic electrocatalyst"** Doktorandenworkshop, Template Funktionale Chemische Schablonen SFB 624, 09-10 October 2008, Bad Honnef, Germany.

5. **"Electrooxidation of ethanol on Platinum stepped single crystals"** 24-28 November 2008, Electrocatalysis @ Nanoscale, Leiden, Netherlands.

6. **"Alcohol adsorption and oxidation at modified stepped Pt electrodes"** Doktorandenworkshop, Template Funktionale Chemische Schablonen SFB 624, 17-18 June 2010, Bad Honnef, Germany.